PREDICTION OF IRRADIATION HARDENING IN METALS

A Thesis
Presented to
The Academic Faculty

by

Cameron Sobie

In Partial Fulfillment
of the Requirements for the Degree
Doctor of Philosophy in the
George W. Woodruff School of Mechanical Engineering

Georgia Institute of Technology
May 2016

PREDICTION OF IRRADIATION HARDENING IN METALS

Approved by:

Professor Laurent Capolungo, Advisor
George W. Woodruff School of Mechanical Engineering
Georgia Institute of Technology

Professor David L. McDowell
George W. Woodruff School of Mechanical Engineering
Georgia Institute of Technology

Professor Ting Zhu
George W. Woodruff School of Mechanical Engineering
Georgia Institute of Technology

Professor Tom Sanders
School of Materials Science and Engineering
Georgia Institute of Technology

Doctor Enrique Martinez
Materials Science and Technology Division
Los Alamos National Laboratory

Date Approved: 29 February 2016

ACKNOWLEDGEMENTS

I would like to thank my advisor Dr. Laurent Capolungo for his support, motivation and guidance as well as encouragement to grow as a research scientist. I would like to thank Dr. David McDowell and Dr. Enrique Martinez for their valuable insight, discussions, and contributions to the studies performed during this thesis, and the entire dissertation committee for their time and consideration of this work.

My four years spent in Metz have been unforgettable thanks to my labmates, thank you for both the discussions and collaborations, as well as coffee breaks and trips together. I wish you all the best and continued success in your careers.

Finally, I extend my deepest gratitude to my close friends and family, without whose unwavering support I could not have made it this far.

TABLE OF CONTENTS

LIST OF TABLES

LIST OF FIGURES

SUMMARY

The purpose of this thesis is to improve predictions of irradiation hardening in metals with a focus on coarse-graining via meso-scale simulations. Increasing hardness and decreasing in ductility in nuclear reactor pressure vessel steel is the limiting factor of nuclear reactor life, and accurately predicting reactor life is of the utmost importance for the safe operation of nuclear facilities. This is an inherently multi-scale problem with primary damage occurring at the atomic scale and its effects propagating across ten orders of magnitude in length and time scale to changes in macroscopic material properties, which must be reflected in its methods of prediction. To achieve this goal, this thesis develops two novel approaches to simulate the motion of dislocations in irradiated α-iron. First, a dislocation dynamics simulation coarse-graining insight from atomistic dislocation-defect simulations is used to guide the selection of proposed constitutive models. Several studies investigating the effect of size distribution show that the mean defect size can be used with the selected models to predict material hardening without a complex treatment for the defect size distribution. The hardening effect of the commonly observed defect types are found independently and a superposition principle is proposed for materials with both defect types. Second, a link to transition state theory and thermally activated reactions is established using a new method augmenting a discrete dislocation dynamics simulations with the nudged elastic band method to characterise the minimum energy pathways of dislocation reactions. This development enables calculations of activation energy for dislocation events using a continuum method as well as the numerical calculations of dislocation attempt frequency. The thesis concludes with an extension to the analysis of coarse-graining unit events to large scale dislocation-obstacle bypass

phenomena.

CHAPTER I

INTRODUCTION

Mastering atomic energy is one of the greatest accomplishments of mankind. Harnessing such power for peaceful applications provides the most environmentally sustainable, large-scale source of electricity to date in the form of nuclear fission power reactors, and developments regarding nuclear fusion show potential to further revolutionize energy production. Fission-based nuclear power provides an ideal pathway to transition from highly-polluting hydrocarbon based energy sources to future fusion energy. Such stable sources of electricity are necessary to augment far more volatile sustainable energy sources such as solar and wind energy. The near-term future of nuclear energy is clear and certain, with 440 reactors currently operating and 66 reactors under construction [2]. However, nuclear fission power reactors also present one of the most extreme environments for structural materials. With internal conditions characterised by high temperature (300°C), high internal pressure ($\approx$ 17 MPa) [158], complex water chemistry, and irradiation, the exceptional demands on structural materials in nuclear reactors are clear. The design objectives of the pressure vessel are equally exigent: operational lifetimes are expected to be on the order of 50 years and the pressure vessel must contain all nuclear material in the event of an accident. Even further, these two requirements are intrinsically linked; the operational lifetime of a nuclear reactor is tied directly to the degradation of mechanical properties caused by irradiation. When the pressure vessel is no longer guaranteed to remain intact in extenuating circumstances, the reactor must be decommissioned.

Irradiation has long been known to cause hardening and embrittlement in metals [40, 157]. Embrittlement poses a critical threat to reactor pressure vessels, and is

currently a limiting factor for reactor life [74]. In the event of a power excursion and steam explosion, the pressure vessel must deform to absorb energy rather than fracture and release radioactive material. Therefore, ductility and toughness are key properties governing the lifetime of the reactor pressure vessel. First generation nuclear reactors are now approaching their design lifetimes and because of their high capital cost, lifetime extension is of significant interest. Accurately predicting material properties and mechanical behaviour of an irradiated structure is an essential part of this process, as well as for the design of future nuclear facilities. This concept is the central theme of this thesis: starting from a bottom-up approach at the at scale approaching the atomic level for dislocation-defect interaction and moving to higher length and time scales to predict properties for engineering materials.

Nuclear energy can be harnessed to produce electricity by capturing the thermal energy produced during nuclear decay reactions, most often done using water as the principle coolant. The heat energy is used to produce steam, which is fed through turbines to produce mechanical followed by electrical energy. An archetypical modern power reactor is a pressurized water reactor (PWR), which contains two independent water circuits. The nuclear core is fully immersed in water maintained at high pressure (≈ 17 MPa) to prevent boiling and increase thermal efficiency. This water is circulated through a heat exchanger with a second loop of water under lower pressure, which is then boiled and the steam circulated through a turbine. Such a configuration compartmentalizes irradiated materials to a limited physical area. The principle nuclear reaction in light-water PWRs relies on uranium fission reactions. When a uranium-235 atom captures a neutron, it most often results in fission and produces an average of 2.4 neutrons and 200 MeV of energy [110]. The probability that a ballistic neutron interacts with a U235 nucleus is dependent on the interaction cross-section for neutron capture, which itself is dependent on neutron velocity. The interaction probability has a complex dependence on neutron energy and increases

significantly at thermal neutron energies (on the order of $\frac{3}{2}k_BT$, where k_B is the Boltzmann constant and T is the absolute temperature.). Thus, the balance between neutron energy and degree of uranium enrichment play a significant role on the nature of the nuclear reaction. PWRs use uranium that has been enriched from its natural concentration of 0.72% to 3-5% [106] with a light water coolant/moderator (typical water), whereas another design of reactor (CANDU type) uses a heavy water coolant/moderator (D_2O) to slow neutrons [98] enabling this reactor type to use natural uranium as the fuel. Reactors designed to operate with neutron energy greatly higher than the thermal range are referred to as "fast" reactors. The next generation of nuclear reactors favour fast reactors more heavily than the current generation because of more favourable nuclear reactions (such as fuel breeding and waste burning) as well has high thermal efficiency. The neutron energy is a characteristic of paramount importance for both the nuclear reaction as well as for interactions with the surrounding structure; the neutron energy spectrum has direct consequences on the damage caused by neutrons in a structural material and therefore must be taken into account in irradiation damage predictions.

1.1 Irradiation Damage

1.1.1 Primary Irradiation Damage

When an energetic particle such as a neutron, ion, or electron enters a crystal lattice and strikes a lattice atom, the lattice atom may be freed and become ballistic itself if the available energy in the reaction exceeds the threshold energy for displacement. If this atom is freed, it is known as the primary knock-on atom (PKA) and such an event occurs when the incident particle has sufficient energy to overcome the threshold energy to free the atom from its lattice site. The original particle and the newly freed lattice atoms continue to collide with and free additional lattice atoms until the particles' energy falls below the threshold displacement energy.

While collisions between the incoming particle and lattice atoms can often be approximated as elastic, ballistic atoms are subject to electronic interactions dissipating a significant amount of energy for even small kinetic energy levels [9]. This series of collisions and the resulting damage is referred to as a displacement cascade, because atoms are displaced from their lattice sites producing self-interstitial atom and vacancy pairs (Frenkel pairs) following a cascade of collisions. For neutrons with an energy on the order of 1 MeV, PKA energies are on the order of 20 keV and the process for a single cascade takes place over the course of approximately 20 ps [187]. During an individual cascade, the temperature in the local region of the cascade spikes and the material can be considered to be liquified during the cascade, but the material quickly solidifies thereby freezing the defects into the structure. Molecular dynamics simulations are well adapted to the length and time scales associated to irradiation damage cascades and have been used to predict cascade formation in numerous materials [12, 10, 125, 200]. Irradiation damage in materials science is quantified using displacements per atom (DPA), which is the average number of times every atom in the lattice has been displaced from its original lattice site. A material with a DPA of unity then indicates that every atom in the material has been displaced by irradiation. A typical PWR pressure vessel can be subjected to 1 DPA, whereas fusion reactors are expected to experience 50-200 DPA [258] during an operational lifetime.

Following numerous cascades and a period of time for thermally driven diffusion to occur, the point defects initially created in displacement cascades coalesce to form larger defect clusters. Predicting how the density and morphology of these defects evolve as a function of irradiation dose, dose rate, and temperature is beyond the feasible simulation scales of atomistic calculations, and therefore the data from atomistic cascade simulations must be coarse-grained and input into higher scale models. Coarse-graining can be accomplished by characterising the relevant defect statistics from displacement cascades and using these as inputs to higher scale models. Two

principle methods are used to simulate the annealing of cascade damage: object kinetic Monte Carlo (OKMC) and mean field rate theory (MFRT). OKMC is named as such because it tracks individual objects (e.g. interstitial atoms) as a function of time, and the kinetics are evolved using an Arrhenius type equation and a stochastic method to predict defect diffusion and agglomeration [53, 20, 204, 129]. MFRT techniques use a series of ordinary differential equations describing defect concentration evolution [161, 19, 250, 119, 57] to predict deterministically how defects move and combine to form larger defects. Both of these methods exist to predict the material damage state following realistic degree of irradiation for predicting material hardening. The defect sizes and densities must be validated against experiments, after which such simulations can be used to provide inputs to higher scale models at arbitrary irradiation levels. This input represents the second major step in scale transition for predicting irradiation hardening.

1.1.2 Irradiated Material State

Irradiation damage is a function of many variables including irradiation type, rate, and amount, temperature, and material. Representative experimental data is very challenging to produce for several reasons. Experiments aiming to replicate reactor conditions are ideally performed using neutron irradiation. However, producing neutron radiation itself is a challenge, and is most often realized using high-flux research reactors [37] or spallation [121] sources. Such experiments are costly, and render the sample radioactive, which engenders numerous associated precautions and problems. Self-ion irradiation [100] resolves concerns with radioactivity but results in different irradiation damage [253]. Dual-beam experiments or helium implantation experiments create even an even greater disparity from neutron irradiation, because voids are stabilised and promoted by internal helium pressure [49]. Interstitial helium also acts stabilise larger SIA clusters [123]. Spatially correlated void/bubble formation

was also observed under dual beam (Fe, He) irradiation as seen in Figure 1c [28]. The only truly representative samples for a nuclear pressure vessel must be extracted from the vessel itself. The studies used to inform the simulations in this thesis were all performed using high-flux research reactors, particularly the works of Eldrup *et. al.* [59], and Hernández-Mayoral and Gómez-Briceño [91].

The physical realization of irradiation damage following multiple displacement cascades and time for anneal create larger defects whose form is material dependent. For example, in FCC copper, stacking fault tetrahedra, voids, and self-interstitial atom loops are experimentally observed [69, 196, 44, 59], whereas in BCC α-iron, spherical voids and self-interstitial atom loops are observed (Figures 1a,1c) [59, 28, 91], and in HCP zirconium, only void and self-interstitial atom loops are seen as shown in Figure 1b [39].

The materials of greatest relevance for nuclear applications are α-iron, being the principle constituent material of reactor pressure vessel steel [158], and zirconium, because of its low neutron cross section. Zirconium is used as nuclear fuel cladding, so it is replaced during refuelling and is subject to less demanding in-service mechanical requirements. On the other hand, the integrity of the steel pressure is paramount to the safe functioning of the reactor for its entire lifetime. The reactor is constructed using several monolithic (>100 tons) forged components and large scale in-situ repairs are effectively impossible. Therefore, this thesis focuses on advancing predictions of the effect of irradiation on the mechanical properties of α-iron. First, the damage state unique to this material system must be well established from which one may consider its impact on mechanical behaviour. Experimental studies and atomistic calculations have provided insight into the defect types, populations, and formation mechanisms, which are crucial parameters to ensure that the studies in this thesis are applicable to a physically relevant system.

Experimental studies on neutron-irradiated α-iron reveal a disparity in the SIA

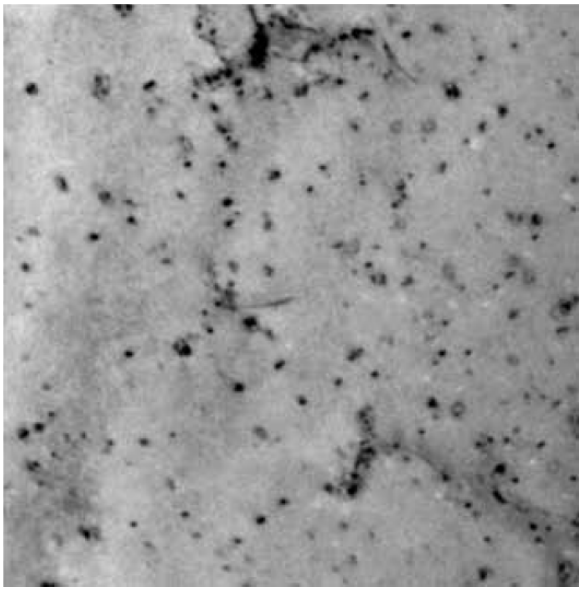

(a) SIA loops in α-iron under neutron irradiation [91].

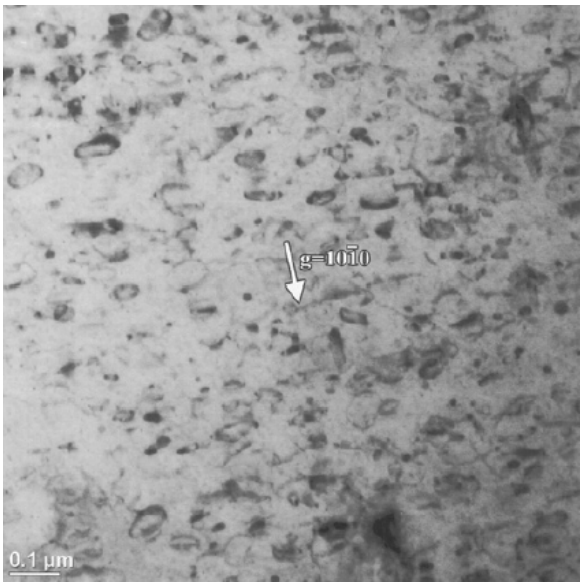

(b) Dislocation loops in Zr under neutron irradiation [39].

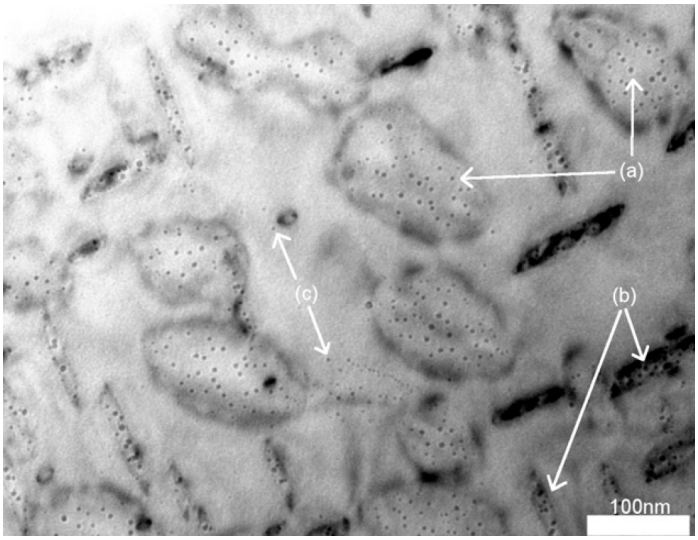

(c) Spatially correlated bubble formation in α-iron under dual beam irradiation [28].

Figure 1: Various irradiation defects in different material systems.

loop/void densities and sizes as seen in Figures 2a, 2b, and 2c. Voids are on the order of 100 times more numerous than SIA loops but much smaller in size. As shown in Figure 2c, SIA loop sizes can be well-characterized using transmission electron microscopy (TEM). However, the vast majority of voids at the given irradiation levels are below the TEM resolution threshold ($\approx$ 2nm), so Eldrup *et. al.* applied a technique known as positron annihilation spectroscopy (PAS). This experimental method injects positrons into the material, which penetrate up to 100 μm and annihilate with electrons at a rate proportional to the electron density [58]. The moment of position-electron annihilation can be precisely measured because it results in the production of two 0.511 MeV γ-rays and the annihilation rate is proportional to the electron density [58]. The positron population in a material containing voids will decay less rapidly, which is reflected in the rate of γ-ray production. This method best suited to materials subjected to neutron or self-ion irradiation, because any gas atoms (e.g. helium) trapped in the voids strongly influences the positron lifetime [58]. PAS is also complementary to TEM, because the positrons are localized to the void wall at larger void sizes and the lifetime becomes insensitive to void size.

The dislocation character of SIA loops in α-iron is dominated by the sessile $\langle 001 \rangle$ type [130, 152]. At 300°C under neutron irradiation, 86% of the loops are of $\langle 001 \rangle$ type [91] and the remainder of the loops are of the glissile $1/2\langle 111 \rangle$ type. Glissile dislocation loops have a low migration energy [246], and in the case of thin films, were suspected to rapidly migrate to the free surfaces [130]. In the case of a bulk materials, these loops may migrate to grain boundaries or other pinning points such as interstitial alloying atoms. In this work, only $\langle 001 \rangle$ loops are considered.

In addition to the properties of the irradiation source, several material properties also influence the degree of damage. Beyond the chemical composition and crystal structure, the internal material geometry can influence the damage state because internal interfaces can act as defect sinks and catalysts for defect recombination. New

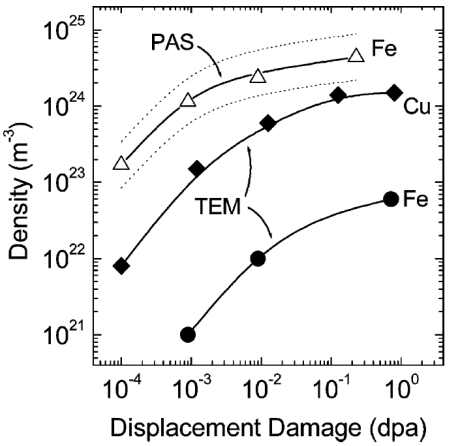

(a) Void and SIA loop densities as a function of dose in α-iron under neutron irradiation.

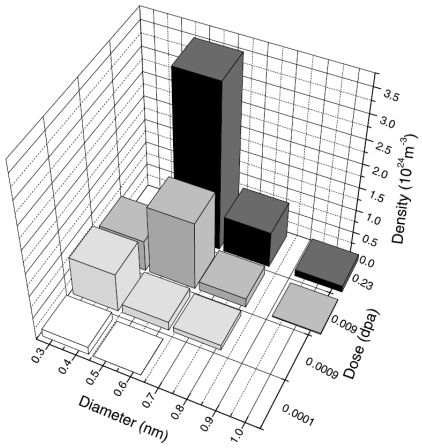

(b) Void sizes as observed using positron annihilation spectroscopy in α-iron under neutron irradiation.

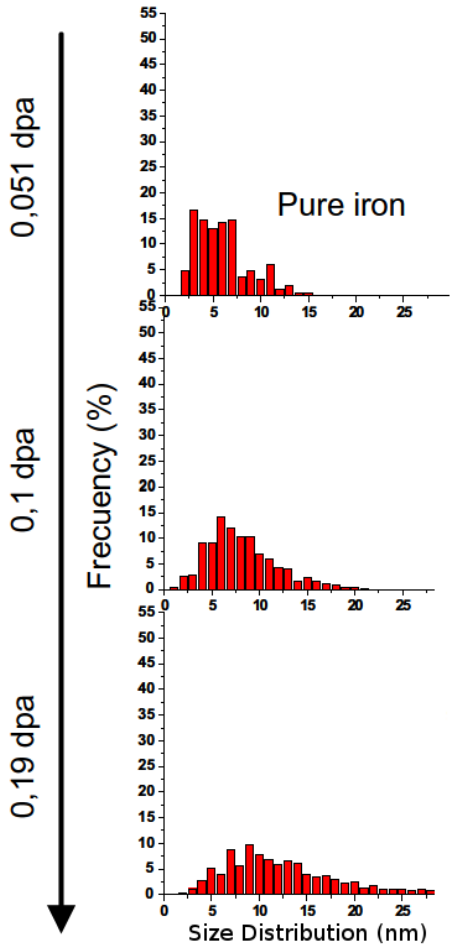

(c) SIA loop size distribution following neutron irradiation. [91].

Figure 2: Experimentally observed irradiated state in α-iron [59, 91].

classes of materials leveraging this self-healing phenomenon for high irradiation applications are under active research for both fission and future fusion reactors. Nano-structured materials have an inherently high interface area to bulk volume, which has spurred significant research into these materials. Oxide dispersion strengthened alloys (ODS steels) [224, 103] contain nanometric ($D \approx$ 3-5 nm) Y_2O_3 oxide particles acting as both defect recombination sites as well as barriers to dislocation motion, thereby increasing the yield strength of the material. Nano-grained tungsten [223, 75] is of particular interest for fusion applications given that it has the highest melting point of any metal, and multilayered metallic laminate (MML) materials have shown remarkable resistance to irradiation-induced damage in the case of ion irradiation [136, 48], and greatly improved mechanical properties compared to the constituent material bulk properties [239, 126]. A DDD study investigating the role of interfacial dislocations on Cu/Nb mechanical properties is performed for this thesis and is presented as an application of DDD in nano-structured material systems in Chapter 2.

1.2 Motivation and Objectives

Gliding dislocations are the principle carriers of plastic deformation in α-iron; consequently, their motion governs many material properties such as yield point, ductility, and fracture toughness. Irradiation defects on the nanometer length-scale interact with gliding dislocations and impede their motion. Such interactions have direct and profound consequences on the macroscopic material properties, as seen in Figure 3.

At even the lowest doses, 1000 times less than that of a fission reactor at the end of its lifetime, the yield point increases and ductility decreases by $\approx$15% and by 0.72 dpa, the change is on the order of 300%. Predicting this dramatic shift in yield point and ductility for any dose, dose rate, and temperature would be a revolutionary advance for nuclear structure design and nuclear safety in general.

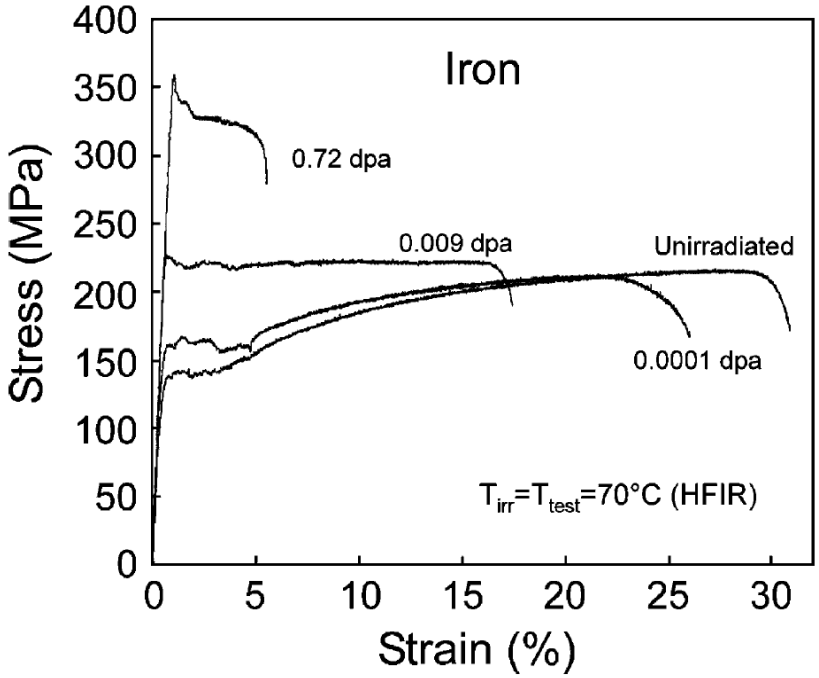

Figure 3: Experiments show that yield strength increases and ductility decreases with increasing irradiation dose in α-iron [59].

The microscopic interactions between irradiation-induced obstacles and gliding dislocations occur over nanometres and picoseconds, yet directly influence macroscopic mechanical properties such as yield point and fracture toughness evolving over the lifetime of a reactor. Spanning such a gulf of length and time scales requires a multi-scale approach and advanced coarse-graining techniques. Therefore, the purpose of this dissertation is to develop techniques enabling the prediction of mechanical properties for materials subject to irradiation damage, starting from the scale of single defect-dislocation interactions and moving towards creep predictions in bulk α-iron.

Dislocation-defect interactions represent a broad field of study in which irradiation damage is a small subset. Many models predicting hardening from various types of defects such as dislocation loops, attractive obstacles and non-attracting obstacles have been published [191, 68, 107, 13]. The validity and predictive capabilities of several models have been compared with mesoscopic simulations such line tension simulations

[54], but these simulations lack physical fidelity because of certain assumptions such as square arrays of defects or infinitesimal defect size [64, 54] in addition to excessive oversimplification of the physical process in line tension simulations. Discrete dislocation dynamics (DDD) studies with direct comparison to hardening models have been very limited in scope with a single application to screw dislocation motion in an atmosphere of 25nm glissile SIA loops [4]. Even further, comparison to a hardening law with combinations of different defect types has only been considered from a line tension perspective [54, 46]. Before parameters for these hardening models can be extracted from experimental results or applied to predict the strength of an irradiated structural material, the fundamental functional form of the models must be shown to be predictive across a wide range of defect sizes and densities. In this thesis, dislocation dynamics simulations are developed and informed using atomistic calculations of defect strength for SIA loops and voids in α-iron. The most commonly used hardening models are compared to DDD predictions in order to select the most accurate models as well as determine their parameters, and the validity of applying the mean size of a defect distribution to predict hardening is examined for both SIA loops and voids.

Constitutive laws predicting irradiation-induced hardening from first principles and hardening calculations performed by traditional dislocation dynamics simulations provide valuable insight into the effect of irradiation on structural metals, but both omit one crucial phenomenon: thermally activated processes. Thermal lattice vibrations can impart sufficient energy, in combination with the energy from driving stresses, that a dislocation can overcome an energy barrier for a characteristic process. Given that thermally activated processes occur proportionally to the exponential of the inverse of temperature [159], the temperature dependence for the activation of such reactions is extremely strong. Using transition state theory and the Arrhenius

equation, one can predict the rate of such reactions if the activation energy of the reaction is known. Several numerical simulations exploiting this technique have been verified experimentally [53, 129]. Predicting thermally activated events is therefore highly dependent on activation energy calculations. First-principles (analytical, DFT) and atomistic methods have been the only methods employed to rigorously compute activation energy barriers for microscopic state transitions such as dislocation-obstacle bypass. However, significant computational requirements limit simulations to processes involving small volumes and therefore restrict the possible range of phenomena that can be considered. Atomistic simulations have only been performed for a dislocation bypassing single defect in a periodic volume, which represents a square array of defects. Limiting atomistic simulations to this basic geometry omits any investigation regarding the effect of nearest-neighbor defect configurations, such as asymmetric spacing between defects and defects at different positions in the glide direction, that can be significant for dislocation migration. Even further, most atomstic simulations only consider a dislocation crossing the center of the defect or a highly limited number of configurations. Lastly, the activation energy for a dislocation-SIA loop/void bypass process has never been published. All of these effects and more will be investigated using a new computational method employing discrete dislocation dynamics (DDD) to represent the energy landscape of a dislocation interacting with SIA loops using the continuum theory of defects. When the necessary approximations are valid, simulations described using continuum formulations are desirable in terms of low computational requirements and a direct connection to constitutive models. With this method, it is possible to capture the evolution of activation energy for a unit process as a function of numerous parameters that have never before been investigated. Furthermore, the numerical methods that provide access to activation energy calculations inherently provide access to the relaxed and activated reaction complexes. Using the work of Vineyard [234], who extented the Arrhenius equation to N-body reactions

in solid state physics, the attempt frequency for a process can be derived from the modal frequencies of the relaxed and activated complexes. Determing the vibrational characteristics of these two configurations using a Hessian analysis provides direct access to the attempt frequency as well as the change in entropy for the reaction.

In a bulk material, a dislocation's motion is impeded by numerous different obstacles distributed in space, and simulating thermally activated motion demands incorporating the combined effect of an ensemble defects. Until now, simulations of dislocation-irradiation defect interactions have been limited to unit processes in confined environments, as atomistic calculations have been the only method capable of simulating such phenomena. However, these simulations omits the spatial distribution and correlation of defects arising in a complex heterogeneous microstructure. This thesis extends activation energy calculations for dislocation-SIA loop interactions using NEB simulations on large volumes and representative defect microstructures entirely unreachable using atomistic calculations. The calculated dislocation migration activation energies compared to the Kocks transition state theory model for activation energy stress dependence [104] and the distribution of expected activation energies is derived.

1.3 Scope of the Thesis

The present Ph.D. thesis is dedicated to advancing predictions of irradiation hardening for α-iron with an emphasis on coarse-graining and meso-scale material behaviour. Existing atomistics data for dislocation-irradiation defect interactions is coarse-grained to study the influence of ensemble an ensemble of obstacles on macroscopic material behaviour and analyze the predictive capabilities of several irradiation hardening models. The high temperature ranges seen in nuclear reactors motivates an investigation into the role of thermal activation on material behaviour, first in the unit case for dislocation-defect interactions followed by an investigation into if it is

possible to transition the insight gained from the unit case to ensemble behaviour with the goal of predicting macroscopic thermally activated material behaviour such as creep. The thesis is organized as follows:

Chapter 1 details the significant numerical developments required to accomplish the research goals set forth in this thesis. The studies performed herein rely on a nodal discrete dislocation dynamics (DDD) code developed during the course of this thesis. A review and analysis of atomistic dislocation-defect interaction simulations is presented and coarse-grained for use with DDD simulations, and the details of the integration with the DDD code are discussed. Simulating the reaction rates of processes sensitive to thermal activation requires a determination of minimum energy for the processes in question. Several established methods from the domain of atomistics are presented, and the steps to augment a DDD code with one of these methods is explained. A method to calculate the vibrational modes of a dislocation using DDD is also presented.

Chapter 2 aims to calculate hardening in the athermal regime caused by irradiation-induced defects and to use the results to evaluate the applicability of models developed to predict such hardening. An atomistically informed DDD simulation is applied to calculate the increase in yield strength caused by the presence of SIA loops and voids. Calculations of mechanical strength for various defect types, densities, and sizes are compared to strength predictions from three relevant hardening models, and a superposition principle is proposed for materials containing several types of defects. The validity of a mean size approach to predicting hardening caused by a distribution of defect sizes, which has been used in experimental determination of hardening law parameters [114, 21], is also considered.

In Chapter 3, a novel method for calculating the activation energy barriers for dislocation processes is developed using a DDD simulation is augmented with nudged elastic band method calculations. Applying a continuum formulation rather than

atomstic calculations to calculate energy barriers enables far larger simulation volumes as well as decreased computation times. The novel method is applied to characterise energy barriers and to produce activation energy maps for a dislocation bypassing an SIA loop in α-iron. The applicability of the phenomenological Kocks transition state theory model [104] with regards to dislocation-obstacle activation energy is also investigated. In addition to activation energy, the attempt frequency for a process must be determined to predict the rate of a thermally activated process with the Arrhenius equation. The vibrational behaviour of a dislocation is characterized, from which one can determine the attempt frequency associated to an activation energy barrier.

Chapter 4 presents a crucial step in scale transition to move from micro-scale unit processes to macroscopic material behaviour. Leveraging the developments and expertise gained in Chapter 3, the methods used to simulate dislocation unit processes are extended to a dislocation migrating through an ensemble of SIA loops. Large scale NEB simulations of a glide dislocation passing through an atmosphere of defects are used to produce probability distributions for activation energy barriers over a range of defect densities and sizes, which are compared to the distributions obtained using unit process calculations. The insight gained is used to move towards the development of a new constitutive equation.

Finally, Chapter 5 summarizes the results and developments accomplished in this thesis and presents possible future work and perspectives.

CHAPTER II

NUMERICAL METHODS

The tasks presented for this thesis are made possible with the development of several advanced numerical schemes and tools, which enable the simulation of certain dislocation phenomena at the mesoscale with greater physical fidelity than ever before. Discrete dislocation dynamics studies have existed for several decades, but the treatment of dislocations interacting with irradiation defects has been restricted to a very small number of studies. The concepts and formulations surrounding dislocations described by the continuum theory of defects are reviewed, and the numerical aspects of DDD are explained. The coarse-graining of atomistics data to produce an atomistics informed DDD simulation for irradiation defect hardening is detailed. Finally, two numerical methods used for activation energy calculations are presented and the possible link with DDD calculations is presented.

2.1 Dislocations

2.1.1 Continuum Theory of Dislocations

In the field of materials science, the term "dislocation" is used to refer to linear crystallographic defects associated with a displacement discontinuity. The notion of a dislocation was first introduced by Volterra [235]. The continuum theory of defects, the set of assumptions under which dislocations were originally formulated [47], approximates a solid as a continuous elastic medium. A dislocation is defined by the displacement discontinuity vector, or Burgers vector $\vec{b}$, and the line tangent $\vec{t}$ and from these two properties, the character of the dislocation is defined. Two linearly independent dislocation types exist: edge, corresponding to $\vec{b} \cdot \vec{t} = 0$, and screw, corresponding to $|\vec{b} \cdot \vec{t}| = |\vec{b}||\vec{t}|$. Figures 4 and 5 depict these dislocation types

pictorially.

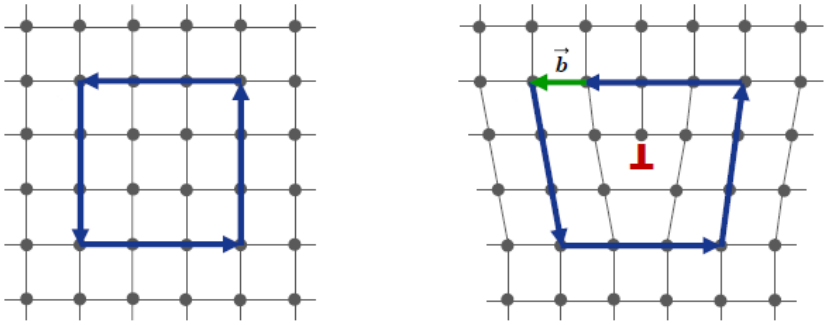

Figure 4: A perfect crystal (left) and a crystal with an edge dislocation (right) [23]. The edge dislocation tangent is into the page.

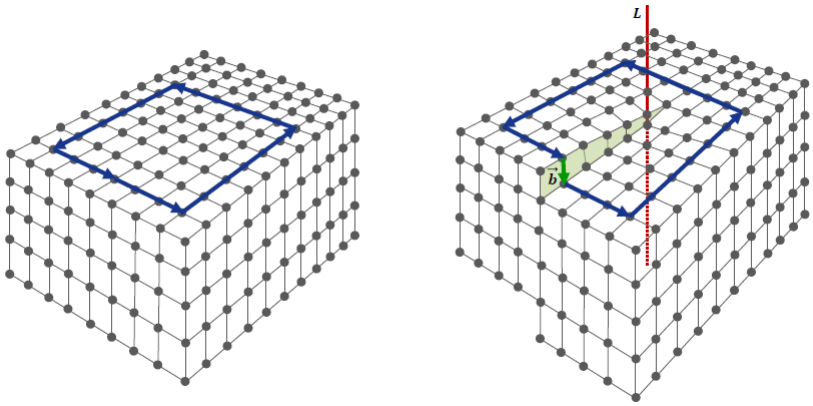

Figure 5: A perfect crystal (left) and a crystal with a screw dislocation (right) [23]. The dislocation tangent is along the red line.

Dislocations with a character between these two are also possible, and thus curved dislocation lines can exist in a material. As alluded to by Figures 4 and 5, dislocations cannot exist anywhere in a solid, but are restricted to exist in quantized locations because of the discrete, atomic nature of materials. Dislocation generally move in the close-packed directions, or the directions with the smallest distance between atoms. These directions are unique to each crystal type so that FCC, BCC and HCP crystals have different planes on which dislocations are most likely to glide.

The deformation of the crystal, which is clear in Figures 4 and 5, gives rise to strain and stress fields in the material. Because the dislocations are defined by the

displacement discontinuity, the displacement field in the material is known exactly and from this, the elastic field can be determined. Starting with the elastic small strain tensor defined as as $\varepsilon_{ij} = 1/2(u_{i,j} + u_{j,i})$ where u_i is the displacement vector, the stress tensor can be obtained using Hooke's Law $\sigma_{ij} = C_{ijkl}\varepsilon^e_{kl}$ where σ_{ij} is the Cauchy stress tensor and C_{ijkl} is the elastic stiffness tensor. Closed form expressions are possible for edge and screw dislocations, and for general curved dislocations can be written as [47, 148, 92, 149]

$$\sigma_{ij}(\vec{x}) = C_{ijkl} \oint_L \epsilon_{ijk} C_{pqmn} G_{kp,q}(\vec{x} - \vec{x'}) b_m dx'_h \tag{1}$$

where ϵ_{ijk} is the Levi-Civita tensor, $G_{kp,q}$ the first derivative of the static Green's function for an elastic medium, and b_m the Burgers vectors. In the case of isotropic elasticity, the Green's function can be written down exactly:

$$G_{kp}(\vec{R}) = \frac{1}{8\pi\mu}\left[\delta_{kp} R_{,qq} - \frac{1}{2(1-\nu)} R_{,kp}\right] \tag{2}$$

where $\vec{R} = \left|\vec{x} - \vec{x'}\right|$, δ_{ij} the Kronecker delta function, μ is the shear modulus, and ν Poisson's ration. If one expands the second derivative of the radius vector (or examines the stress fields for a pure edge/screw dislocation), a complication with this formulation becomes clear - the strain and stress fields are singular at the dislocation core ($R = 0$) and decay as $1/R$:

$$R_{,ij} = \left(\delta_{ij} - \frac{R_i}{R}\frac{R_j}{R}\right)\frac{1}{R}. \tag{3}$$

As a result, the strain energy $U = 1/2 \int \sigma_{ij}\varepsilon_{ij}\, dV$ is not defined or requires one to set an arbitrary cutoff around the dislocation core and at the upper limit of integration. Such complications arise because of the initial assumptions of continuum elasticity; defining the displacement jump with a Kronecker delta function creates an infinitely sharp displacement jump, which is non-physical if one considers the atomic

construction of a solid. Several attempts have been made to address the non-physical nature of the solution. The Peierls-Nabarro model of a solid [169, 150] smooths the jump in Burgers vector using a Lorentzian Burgers vector distribution:

$$\mathbf{g}(\mathbf{x}) = \frac{\mathbf{b}}{\pi} \frac{\zeta}{r^2 + \zeta^2}, \tag{4}$$

where ζ is a constant related to the width of the dislocation.

Cai *et. al.* proposed deriving an isotropic Burgers vector distribution enabling closed form integration of Equation 1. The authors were successful in this pursuit and while a closed form expression of the Burgers vector distribution does not exist owing to a convolution integral without a closed form solution, the distribution is well characterized by the following expression:

$$\mathbf{g}(\mathbf{x}) = \mathbf{b} \frac{15}{8\pi} \left[\frac{1-m}{a_1^3 \left[(r/a_1)^2 + 1 \right]^{7/2}} + \frac{m}{a_2^3 \left[(r/a_2)^2 + 1 \right]^{7/2}} \right], \tag{5}$$

where r is the distance to the dislocation axis, $a_1 = 0.9038a$, $a_2 = 0.5451$a, $m = 0.6575$ and a the dislocation core width parameter. While this differs from the core distribution of Peierls, a close agreement between the two can be reached with the correct choice of parameters. Therefore, the formulation explicitly includes non-linearities associated to the dislocation core within the approximations of the continuum theory of defects. The tremendous advantage of using the Burgers vector distribution in Equation 5 is that analytic expressions are available for all dislocation force, stress, and energy calculations for straight dislocation segments. Figures 6 and 7 show the non-zero stress components for two different configurations with an edge or screw dislocation. For the stress measured along a line through the dislocation core in Figure 7, the core width parameter has a clear and strong influence within a few lattice spacings of the core, but the differences are negligible at 5a from the core. For a line passing 2a above the core of a screw dislocation as shown in Figure 6, the differences between the singular and non-singular theory are less emphasized but still significant

at the positions closest to the core.

The non-singular formulation is undoubtedly a more physically realistic representation of a dislocation core than a singular solution, it also using a core spreading function chosen solely to enable close form integration rather than the best representation of the physical configuration. However, such assumptions are acceptable because the dislocation core structure is an ongoing subject of study for α-iron using density functional theory or other atomistic calculations [230, 120, 231].

Anisotropic elasticity presents significant theoretical and numerical challenges regarding dislocation formulations. To obtain the Green's function for anisotropic elasticity, one must solve the sextic eigenvalue problem as posed by Stroh [205, 206] and developed further by Ting and Lee [219]. Closed form solutions for the stress field of dislocation in transverse isotropy exist [38] and some numerically amenable forms for general anisotropy in a homogeneous medium [166], a composite medium [254], and at the interface of an anisotropic bimaterial [165]. Here, numerically amenable implies an expression that can be resolved using classical computing techniques; however, it does not speak to the computational demands. These formulations often require inverse fast Fourier transforms and numerical integration resulting in prohibitively computationally expensive calculations. The entirety of this thesis is performed assuming elastic isotropy.

2.1.2 Dislocation Dynamics

The details of dislocation nucleation, glide, and multiplication play a fundamental role in governing the mechanical properties of many engineering metals such as yield point and plastic behaviour [41, 67, 92]. The presence of a dislocation in a crystal contributes to the free energy of the crystal via its elastic fields. Other elastic fields, whether they are generated by the presence of other dislocations or a macroscopically applied stress, all interact to change the free energy. The classical mechanics definition

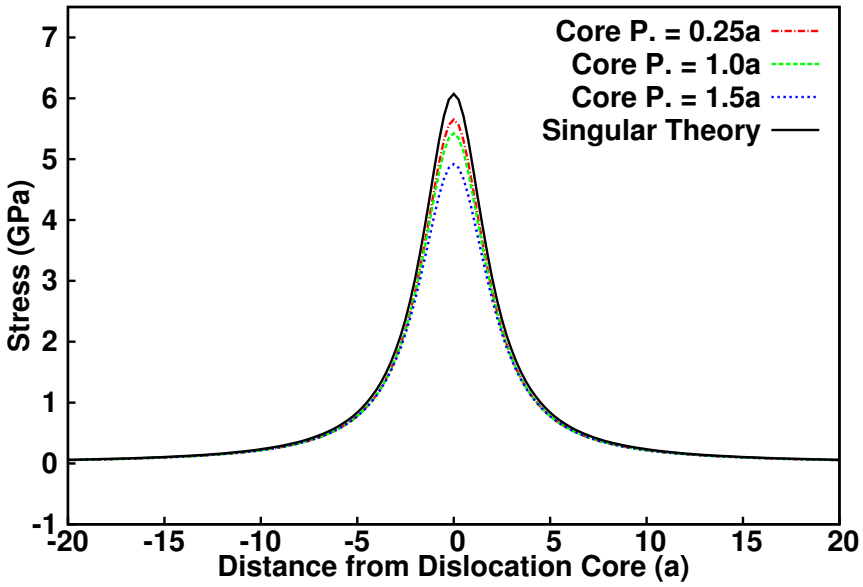

(a) Stress component σ_{xy} for several core width parameters.

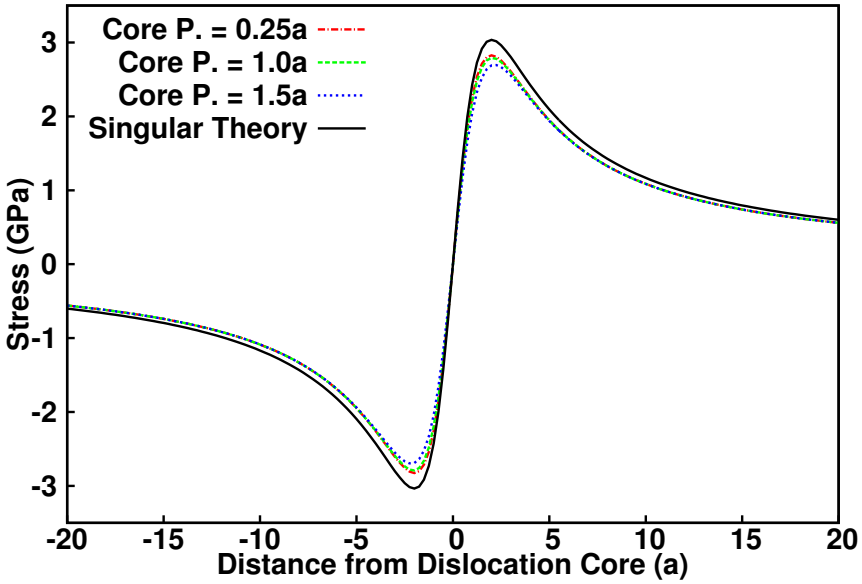

(b) Stress component σ_{xz} for several core width parameters.

Figure 6: Comparison of singular and non-singular dislocation theory for a straight infinite screw dislocation. Here, the stress is measured along a line crossing 2a above and perpendicular to the dislocation core

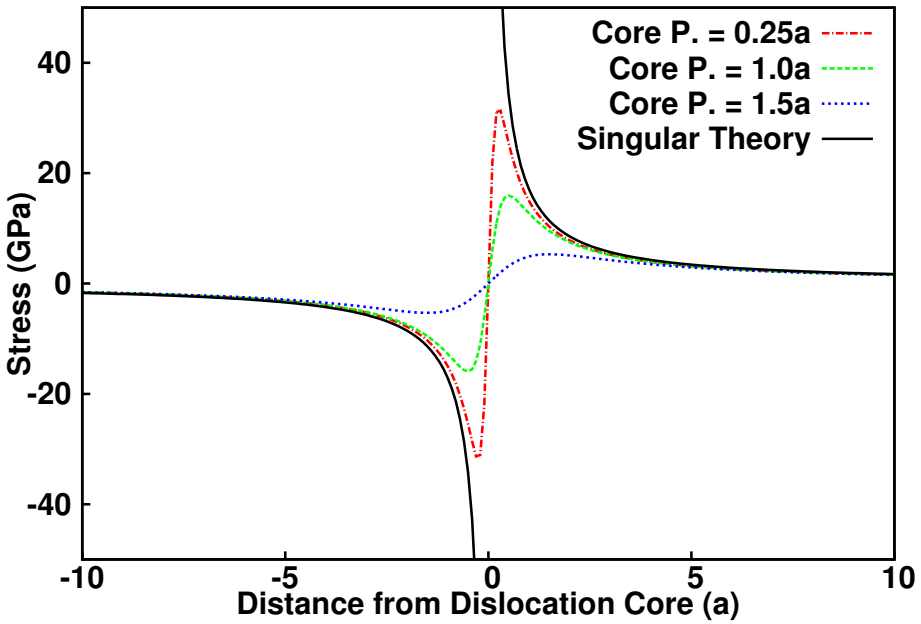

Figure 7: Stress component σ_{xy} measured along a line perpendicular to and crossing through the core of an edge dislocation. The line lies in the glide plane.

of a force $\vec{F}$ arising from a scalar potential, in this case the energy E, can be written as

$$\vec{F} = -\vec{\nabla} E. \tag{6}$$

In general, the force will two contributions. The first is known as the Peach-Koehler force [168] which is caused by interactions of elastic fields:

$$\vec{F}^{\mathrm{PK}} = \left(\boldsymbol{\sigma} \cdot \vec{b}\right) \times \vec{t}. \tag{7}$$

where $\vec{t}$ is equal to the dislocation line length. Alternatively, the unit vector of the tangent can be used to give the force per unit length for cases where the stress varies over the length of the segment. Equation 7 will be derived in Section 2.3, which details the calculation of enthalpy for a dislocated elastic solid.

The second force contribution is caused by chemical contributions that are manifested as osmotic forces. Vacancy content in a material can cause non-conservative

motion of a dislocation [52], particularly for edge dislocations: a vacancy in the vicinity of an edge dislocation has the possibility to recombine with a lattice site at the dislocation, in a phenomenon known as dislocation climb. This process can be accounted for with an osmotic force; however, this contribution is often neglected in dislocation dynamics simulations, and is also negated in this thesis.

Dislocation motion caused by an applied force is often modelled using a mobility function M:

$$\vec{v} = M\left(\vec{f}\right) \tag{8}$$

where $\vec{v} = \frac{d\vec{x}}{dt}$. Such a model was proposed based on experimental observations as well as atomistic simulations. The mobility function M is most often approximated using an overdamped equation of motions incorporating the viscous drag caused by dislocation-phonon interactions. If one neglects inertial effects, this equation of motion can be written as

$$\mathbf{B}\vec{v} = \vec{f} \tag{9}$$

where B is the matrix of drag coefficients. Figure 8 reveals the experimental justification for a viscous drag mobility law - a linear relationship between resolved shear stress and dislocation velocity is observed.

The motion of dislocations in BCC materials, such as α-iron in this thesis, and particularly for screw dislocations, can be a complex thermally activated motion driven by kink-jog movement. In the domain of continuum dislocation modelling such as in the case of DDD, atomistically-informed simulations [31, 143, 242] have been performed, but a far more common model for this movement is using a screw mobility 10-100 times less than that of an edge dislocation [79, 4]. This asymmetry in segment mobility is also entirely neglected in some cases [180, 213].

Dislocations are confined to glide on their slip planes as defined by the normal

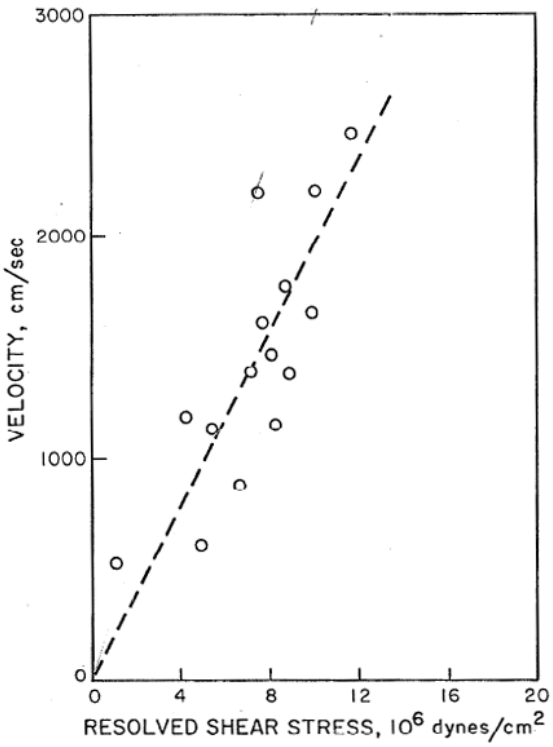

Figure 8: The velocity of dislocation migration is seen to be linearly proportional to resolved shear stress in high purity aluminum [77]. Such results motivated the development of an equation of motion as presented in Equation 9.

vector $\vec{n} = \frac{\vec{b}\times\vec{t}}{|\vec{b}\times\vec{t}|}$. As previously mentioned, a screw dislocation is defined by $\vec{b}\times\vec{t} = 0$ and therefore no slip plane can be defined. As a result, gliding screw dislocations can change close-packed planes in a process known as cross-slip. This processes is thermally activated, for which activation energies have been determined using atomistic calculations [229, 182]. Cross-slipping can be a method for dislocations to bypass hard obstacles, as the activation energy decreases with the dislocation driving force so a dislocation may cross-slip around the obstacle to continue gliding. This type of bypass is one process that enables strain-rate dependence as well as creep behaviour.

As a dislocation glides to accommodate an applied load, atom planes are permanently displaced with respect to one another and therefore give rise to a notion of strain caused by permanent displacements (rather than recoverable elastic displacements). Such permanent strain is called plastic strain, and the elementary plastic

shear strain γ is defined by the area shear by the dislocation, i.e.,

$$\gamma = \frac{bA}{V}, \tag{10}$$

where $b = |\vec{b}|$, A the area swept by the dislocation, and V the volume of the sheared crystal. Generalizing Equation 10 to all possible glide planes s with their associated projections, the expression for the plastic strain tensor ε_p can be written as:

$$\varepsilon_p = \frac{1}{2} \sum_s \frac{b^s A_s^i}{V} \left(b_i^s n_j^s + b_j^s n_i^s \right), \tag{11}$$

where n_i^s is the normal vector for glide plane s.

2.2 Discrete Dislocation Dynamics

2.2.1 Boundary Value Problem

Before developing a numerical methodology to predict the motion of dislocation according to the previously developed theories, one must defined the problem to be solved, which is the fundamental boundary value problem of continuum mechanics. At every point within a simulation volume V, mechanical equilibrium must be respected (assuming zero body forces) and satisfy the prescribed displacement and traction boundary conditions:

$$\sigma_{ij,j} = 0 \tag{12}$$

$$\sigma_{ij} = C_{ijkl} \varepsilon_{kl} \tag{13}$$

$$u_i = u_i^* \text{ on } \partial_1 R \tag{14}$$

$$\sigma_{ij} n_j = t_i^* \text{ on } \partial_2 R \tag{15}$$

where σ_{ij} is the Cauchy stress tensory, C_{ijkl} is the stiffness tensor, ε_{kl} is the elastic small strain tensor,u_i is the displacement vector, n_i is the normal vector on $\partial_2 R$, the displacement boundary condition u_i^* is applied on the portion $\partial_1 R$ of the boundary, and the traction boundary condition t_i^* is applied on the portion $\partial_2 R$ of the boundary. The most widely adopted method of solution to this boundary value problem is that proposed by Van der Giessen and Needleman [225]. Their approach considers the medium as elastic everywhere outside the dislocation cores and in doing so, it is possible to apply linear superposition and to decompose the system into the internal contributions from dislocation and the externally applied loading. Consequently, the two problems are as follows: one in which the dislocations exist in an unbounded elastic medium, and one in which the boundary conditions u_i and t_i^* have been modified to account for the influence from the dislocation fields. Doing so enables the stress in the material to be defined in terms of two contributions: the internally generated dislocation stress fields, and the stresses arising from the externally imposed boundary conditions:

$$\sigma_{ij} = \sigma_{ij}^{\text{int}} + \sigma_{ij}^{\text{ext}} \tag{16}$$

The application of σ_{ij}^{ext} ensures that equilibrium and the boundary conditions (Equations 12,14, and 15) are respected. As previously mentioned in section 2.1.1, the stress field for a dislocation as given by Equation 1, i.e.,

$$\sigma_{ij}(\vec{x}) = C_{ijkl} \oint_L \epsilon_{ijk} C_{pqmn} G_{kp,q}(\vec{x} - \vec{x'}) b_m dx'_h, \qquad \text{(1 repeated)}$$

is general; however, a numerically amenable and computationally efficient form of the Green's function G_{ij} exists only for isotropic elasticity in an infinite medium without external loading. By carefully choosing a Burgers vector spreading function, Cai *et. al.* [30] achieved a closed form solution for a non-singular dislocation stress field in an infinite medium. More importantly for DDD, the nodal forces for straight dislocation

segments is available in closed form, which avoids the highly costly calculation of the stress contribution from every dislocation segment at numerous points along each dislocation segment in order to perform numerical integration.

The external stress field contribution σ_{ij}^{ext} often arises as a method by which to extend the utility of DDD simulations from an unloaded infinite medium to include applied loads as well as finite simulation volumes and internal surfaces [233, 63, 245]. This external contribution is also important in simulations of bulk crystals using periodic boundary conditions (PBC). When simple displacement boundary conditions are applied, the external stress is given using a direct mean-field method because this loading type results in a uniform stress everywhere in the volume. The uniform applied stress/strain is given directly from Hooke's Law (Equation 13). Such simplifications are only true for a simulation volume far from the boundaries in a bulk material, and therefore PBC are required. In DDD, periodicity requires not only ensuring periodicity of the dislocations but their elastic fields as well. From a numerical standpoint, this is accomplished by creating 26 repetitions of the cuboid simulation volume around the principle volume. The elastic fields from these repeated volumes are included in the external stress contribution σ_{ij}^{ext}. Solving the boundary volume with complex boundary conditions such as a finite simulation volume or a simulation containing multiple materials require solving the boundary value problem directly using finite element method (FEM) [199] or other techniques such as Fourier transforms.

2.2.2 Dislocation Motion

With the dislocation static and dynamics formulations established in Sections 2.1.1 and 2.1.2, the boundary value problem fully defined and the stress state fully determined in section 2.2.1, the problem of simulation dislocation dynamics is established from the theoretical standpoint. First, the system must be represented in a numerical

form. At the most basic level, dislocations can be represented either continuously or discretely, both of which have seen success. Discretized dislocations are the favoured implementation in the literature. The simplest form of discretization is using pure edge and pure screw dislocation segments to represent a smooth line [233, 34]. The simplicity of the implementation results in a lower burden in creating the simulations and well as low computational complexity, but have been shown to be insufficient when complex junction morphologies are possible [51]. Some studies adopted more possible geometries (such as 45° segments) but nevertheless a finite number. A significantly improved discretization with regards to physical fidelity is possible using a nodal discretization. Using this method, a series of nodes are distributed along a dislocation segment and a shape function is used to interpolate the dislocation line between these points [71, 29]. Continuous representations including level set methods [247, 179, 36, 237] and phase field methods [241, 186, 97] can represent dislocation as smooth curves, but a high cost: a complex and costly calculation is necessary to represent the dislocation lines, and junction formation cannot be treated explicitly. Consequently, small time-steps are required to allow elastic interactions to form junctions.

In this thesis, a nodal based scheme with nodes connected by straight line segments of continuously varying dislocation character is used for all simulations. A dislocation node can have one (fixed point), two (point on line) or more connections (junctions). Figure 9 shows a pictorial representation of three dislocations discretized using the nodal method, where nodes 1, 2 and 3 are junction nodes.

Using this implementation, it is the dislocation nodes rather than the dislocation segments that are propagated, and the dislocation lines are generated according to their assigned nodal connectivity. As a result, the dislocation dynamics equations of motion are solved in terms of nodal quantities. The total nodal force can be written as

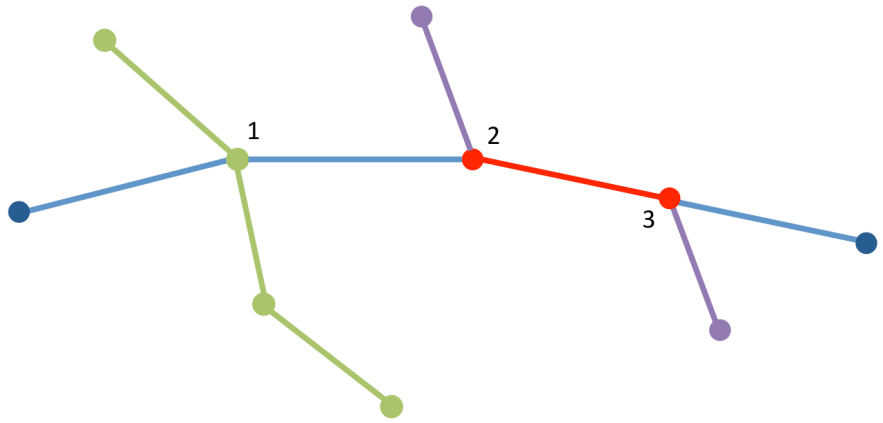

Figure 9: Nodal representation of a dislocation. The blue dislocation is interactin with the green dislocation, which is of a Burgers vector results in a pinned node at node 1. The purple dislocation has a Burgers vector that can form a junction with the blue dislocation, as highlighted between nodes 2 and 3.

$$\vec{F_i} = \sum_j \vec{f_{ij}} \tag{17}$$

where $\vec{F_i}$ is the force vector on node i, and $\vec{f_{ij}}$ is the force contribution on node i from the connected segment terminating at node j. The force contribution $\vec{f_{ij}}$ is written as

$$\vec{f_{ij}} = \int_{\vec{x}_i}^{\vec{x}_j} N_i(\vec{x}) \vec{f}(\vec{x}) |d\vec{x}|, \tag{18}$$

where $N_i(\vec{x})$ is the shape function associated with node i. As previously mentioned, closed form expressions exist for the force on the end nodes caused by dislocation-dislocation interactions of straight dislocation segments using a non-singular formulation [30], and for a straight segment, the nodal force can be expanded as

$$\vec{f_{ij}} = \vec{f}_{ij}^{\text{int}} + \frac{1}{2} L_{ij} \left(\left[\boldsymbol{\sigma} \cdot \vec{b}_{ij} \right] \times \vec{t}_{ij} \right) \tag{19}$$

Equation 19 is found using linear shape functions in Equation 18 and carrying out the integration over a line with length $|\vec{x}_i - \vec{x}_j|$. In general, the dislocation nodal force

calculations are by far the most numerically demanding step in DDD simulations and are the bottleneck for computational performance. Because every dislocation segment interacts with every other dislocation segment, this problem is $\mathcal{O}(N_{\text{seg}}^2)$ and the calculation for a single interaction requires on the order of 1500 function calls [8]. Approximations and optimizations are thus a necessity to achieve a meaningful amount of accumulated strain or dislocation density in a DDD simulation. The elastic fields of a dislocation decay as $1/R$ where R is the separation distance between the dislocation and the field point. This slow decay means that one cannont simply negate interactions at large distances; however, two approximation methods proposed in the literature provide signficant acceleration while retaining sufficient accuracy. The first method, and the method used in the present thesis, is called a box method [233]. This method optimizes long-range dislocation interactions by assuming that the stress contributions from dislocations far away from a point can be assumed to be constant over a discrete volume, taken to be a box. This is accomplished by subdividing the simulation volume into boxes, on the order of 10-20 in each dimension (for a total of 1000-8000) but the exact number of which depends on the dislocation segment density. For a dislocation segment, the direct (exact) stress field computations are performed for other segments within the same box or the neighboring 26 boxes. For segments outside these 27 boxes, the stress is calculated at the center of the box containing the dislocation segment, and is assumed to be constant in that region.
Figure 10 depicts the box method in a simple 2D case. For dislocation segments contained within the red box, elastic interactions are directly calculated for all segments within the blue box. For the segments outside the blue box, their average stress fields are computed at the center of the red box, and this value of stress is used to calculate the Peach-Koehler force on the segments inside the red box.

The stress contribution from the dislocation segments beyond the neighbouring

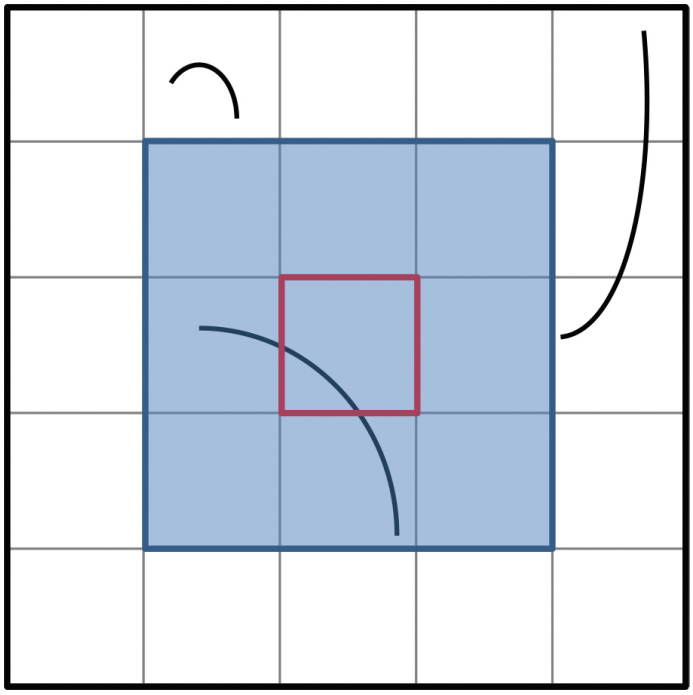

Figure 10: 2D pictorial representation of the box method optimization for long-range dislocation-dislocation interactions.

boxes is called the "box stress." Because this interaction necessarily occurs over relatively large separation distances, the box stress will vary less quickly in time than the direct contributions; consequently, the box stress can be calculated over a longer time interval than a single time-step. For instance, the box stress may be recalculated every 10 steps, resulting in an even greater degree of numerical optimization. The second long-range interaction optimization method is the Fast Multipole Method [238, 117, 5]. This method is effectively a Taylor expansion of the derivatives of the radius vector $R_{,ij}$ that appear in the expression of the Green's function. The computational complexity of this method is $\mathcal{O}(N_{\text{far}})$, albeit with a large prefactor as the calculations of the multipole expansions involve many calculations. This method was not used during the course of this thesis.

Next, the drag matrix $\mathbf{B}_i$ must be obtained. The drag coefficients for edge and screw dislocations are inputs to the DDD simulation, and are a parameter extracted from from experimental [77, 99, 33] or atomistic [61, 35, 73] studies. With the edge

and screw mobilities defined, one obtains the mobility tension $\mathbf{B}(\theta_{ij})$ by integrating over the segment length. Drag coefficients are expressed in terms of the screw drag and edge drag, and are interpolated using the following expression:

$$\mathbf{B}(\theta_{ij}) = \left(B^e_{ij}\sin^2\theta_{ij} + B^s_{ij}\cos^2\theta_{ij})\right)\mathbf{I} \tag{20}$$

where θ_{ij} is the angle made by the segment connected to nodes i and j with respect to a screw dislocation. The final equation of motion for a dislocation (Equation 9) can be written as

$$\vec{F}_i = \sum_{i\neq j}\frac{L_{ij}}{6}\mathbf{B}(\theta_{ij})\left(2\vec{\mathbf{V}}_i + \vec{\mathbf{V}}_j\right) \tag{21}$$

Equation 21 is therefore an $3N\times 3N$ system of linear equations, where N is the number of dislocation segments on one dislocation, and can be solved by using standard linear algebra methods. However, such operations are very costly and N can reach large numbers because many dislocations can connect by forming junctions to create a single dense network. An approximation which alleviates this computational burden is the local velocity method. Assuming that the discretization of the dislocation network well-represents the dislocations, the velocities of neighbouring node j should not vary greatly and for the purposes of the drag calculation, can be approximated as identical, i.e., $\vec{\mathbf{V}}_i \approx \vec{\mathbf{V}}_j$ and non-neighbouring nodes k can be assumed to have negligible influence, i.e., $\vec{\mathbf{V}}_k \approx 0$. As a result, Equation 21 (originally $3N \times 3N$) becomes decoupled, resulting in a system of N 3×3 equations:

$$\vec{\mathbf{F}}_i \approx \left[\sum_j \frac{L_{ij}}{2}\mathbf{B}(\theta_{ij}) + \sum_k \frac{L_{ij}}{3}\mathbf{B}(\theta_{ik})\right]\vec{\mathbf{V}}_i \tag{22}$$

resulting in a noteworthy reduction in computational cost, and an observed decrease in numerical instabilities such as nodal velocity vibrations.

With the nodal velocities established, the nodal positions $\vec{x}^t_i$ can be updated to

find $\vec{x}_i^{t+\Delta t}$ (where Δt is the time step for the simulation). Numerous well-established different numerical integration methods are applicable for this problem, but one must take care in selecting which method to avoid undue computational burden. Backwards Euler integration is a simple, A-stable method of integration:

$$\vec{x}_i^{t+\Delta t} = \vec{x}_i^t + \vec{\mathbf{V}}_i \left(\vec{x}_i^{t+\Delta t}\right) \Delta t. \tag{23}$$

However, the implicit nature of Equation 23 requires multiple force calculations and as previously mentioned, a single force calculation is already the most intensive calculation by a wide margin. The force calculation is so intensive (and even further scales as $\mathcal{O}(n^2)$ where n is the number of segments) that the increase in simulation time step afforded by the nature of Equation 23 often is not sufficient to achieve a faster computation than by simply reducing the time-step Δt and using explicit Forward Euler integration:

$$\vec{x}_i^{t+\Delta t} = \vec{x}_i^t + \vec{\mathbf{V}}_i \left(\vec{x}_i^t\right) \Delta t. \tag{24}$$

After the dislocation node positions have been updated, the discretization is verified to ensure that dislocation nodes are well spaced. As a dislocation glides under an applied stress and bows out between obstacles, such as other dislocations or point defects in the lattice, the line length changes and the discretization must evolve to maintain a realistic dislocation morphology. Long dislocation segments are undesirable as they tend to oversimplify the dislocation shape and fail to capture fine scale phenomena, whereas short dislocation segments tend to be numerically unstable and can cause artifical numerical oscillations. Where short dislocation segments are required (for fine scale phenomena), accordingly small time-steps are crucial to avoid numerical instability. Therefore, the dislocations are re-discretized (remeshed) at the end of every time step. Two methods of remeshing are used in this thesis: a segment

based method, and a spline based method. The segment based method is a simple length criteria: if a segment is over a threshold length, the segment is split into two equal length segments, and if a segment is too short, its terminating nodes are merged into a single node. Depending on the threshold values for bisection/merging, this method tends to maintain an approximately equal segment length across all dislocation segments but has the drawback that the simulation is sensitive to the chosen threshold value. In the simulations performed here, the criteria to merge nodes is 1/4 the bisection length. An asymmetric criterion is essential to avoid numerical artefacts. When a dislocation node is added, the change in dislocation shape may result in a net decrease in dislocation length following relaxation, and if the criteria to split/merge is symmetric, the new node will be merged. This new configuration bows out once again, creating an artificial oscillation that accumulates plastic strain, and thus causes erroneous simulations. The value of the bisection length must also be user-specified depending on the nature and the length-scales of the calculation to be performed. The second method is based on cubic spline interpolations. Each dislocation line is interpolated using cubic splines, and the nodes are repositioned along cubic spline to guarantee equal segment lengths. If the density of nodes is too low or too high along the line, the nodes can be added or removed (and a similar asymmetric criteria is essential to avoid numerical issues). Both of these methods are used in this thesis: the segment method is used for all standard DDD calculations, and the spline method is used for DDD-NEB calculations (detailed in section 2.7.2).

In a general DDD simulation, junction formations such as zipping, unzipping and annihilation are considered using a deterministic power dissipation formulation (Equation 25). The short-range numerical treatment is detailed in Figure 11. New dislocation nodes are created to avoid dislocation passing through each other when performing simulations with large time-steps.

After a junction has formed as shown in Figure 11, the dislocation configuration may

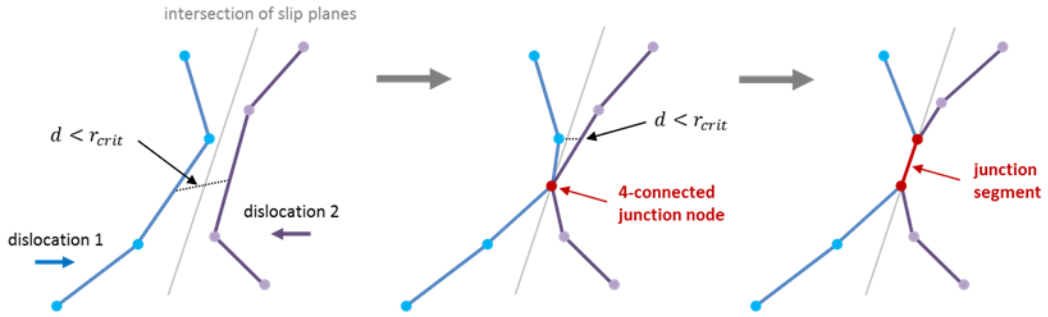

Figure 11: Pictorial representation of the junction formation. When two segments are below a threshold distance d_{crit} defined by the segment speed, a node is inserted where the glide planes intersect. As other points on the dislocation segment approach to decrease their separation distance below d_{crit}, additional nodes are added and the junction zips. [23]

change in such a way that the junction shrinks. The power dissipation of two nodes j and k is compared to the power dissipation of a single node i with connections to four other dislocation nodes. The configuration inducing the maximum dissipation is selected by the simulation for the following step:

$$\max_{jk}\left(P_{jk}^{diss}\right) = \max_{jk}\left(\vec{\mathbf{F}}_j \cdot \vec{\mathbf{V}}_j + \vec{\mathbf{F}}_k \cdot \vec{\mathbf{V}}_k\right) \tag{25}$$

where $\vec{\mathbf{F}}_j$ is the nodal force at j, $\vec{\mathbf{B}}_j$ is the nodal velocity at j, and P_{jk}^{diss} is the power dissipation induced by configuration jk.

In this thesis, the dislocation dynamics simulations are highly targeted to certain phenomena, and solely elastic interactions are responsible for junction formation. Dislocation annihilations must be treated numerically because when two gliding dislocation segments of opposite Burgers vector or line direction intersect, the dislocations annihilate to return the crystal to a perfect lattice (locally) and the numerical morphology must change significantly to reflect the changes. Annihilations are checked by examining segments separated by a threshold distance defined by the user as well as the maximum nodal velocity times the time-step (to avoid missing any crossing events). The dislocation segments will intersect, creating a node with four connections. When a second four connection node is formed the segment between them has

a Burgers vector of zero magnitude and is removed from the system.

Dislocation dynamics simulations are a cycle, starting with the discretization of continuous dislocation lines. Next, the force on each dislocation node is calculated using close form internal contributions and as well as calculating the contribution from an external stress term representing the material boundary conditions. An overdamped equation of motion is applied to determine nodal velocities, which are then updated using simple numerical integration. Finally, junction formation is considered, and the discretization verified. This process is repeated thousands to millions of times for a typical DDD simulation.

Greater details regarding the numerical developments for the simulations used herein can be found in the thesis of Nicolas Bertin [23].

2.2.3 Fundamental Applications

Before the classical DDD simulations are augmented to enable simulations of more complex microstructure associated to irradiated materials, two classical cases are explored to highlight the capabilities of the simulations and to elucidate the roles of input parameters on the material behaviour.

2.2.3.1 Frank Read Source Activation

The stress required to cause dislocation propagation for a dislocation segment pinned between two fixed points is an archetypical example in the domain of dislocation dynamics, and was proposed by Frank and Read [66] as a mechanism by which dislocation and plastic deformation can occur. Such a configuration is denoted a Frank-Read source (FRS). Figure 12 shows an FRS under an applied stress that is sufficient to activate the source. This geometry, with a varying radius of curvature at a minimum near the pinned points, is characteristic for an FRS. Dislocation multiplication is possible because the two arms of the dislocation below the pinned points with propagate towards each other, resulting in a large, growing dislocation loop. The remnants the

annihilated segments reform a straight dislocation between the pinned points, and the process repeats.

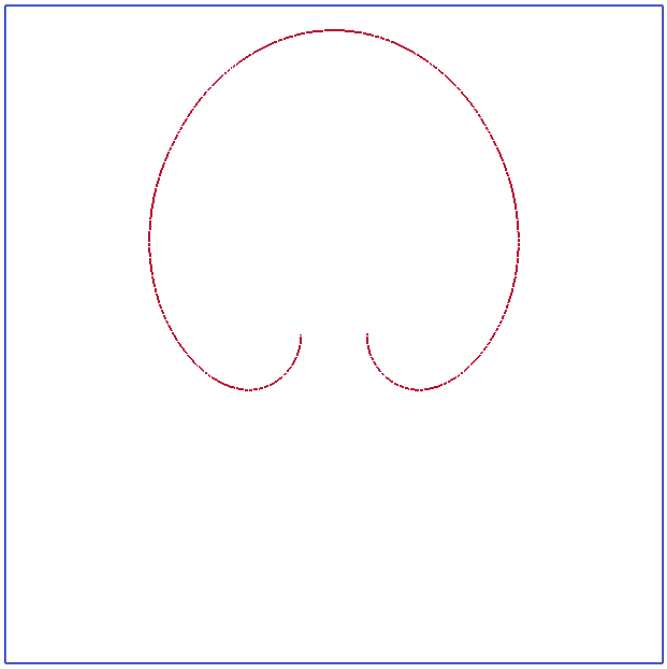

Figure 12: A Frank-Read dislocation source (red) activating under an applied stress. The blue lines represent the periodic simulation boundaries.

The stress to activate an FRS can be derived using line tension approximations to be proportional to $\mu b/L$ where μ is the shear modulus, b the magnitude of the Burgers vector, and L the distance between the pinning points. This value is plotted with the calculated values of activation stress for an edge dislocation in Figure 13.

The stress to activate the FRS is weakly dependent on the discretization. As long as a sufficient number of segments to accurately represent the dislocation geometry are used, the adaptive discretization algorithm ensures a satisfactory description of the dislocation.

Figure 14 reveals the activation stress dependence on core width parameter for an FRS with a length of 500a and a discretization of 100a. In contrast to the discretization, the core width parameter plays a fundamental role on the activation stress for an FRS as noted by the authors of this formulation [30]. The self-energy of a dislocation

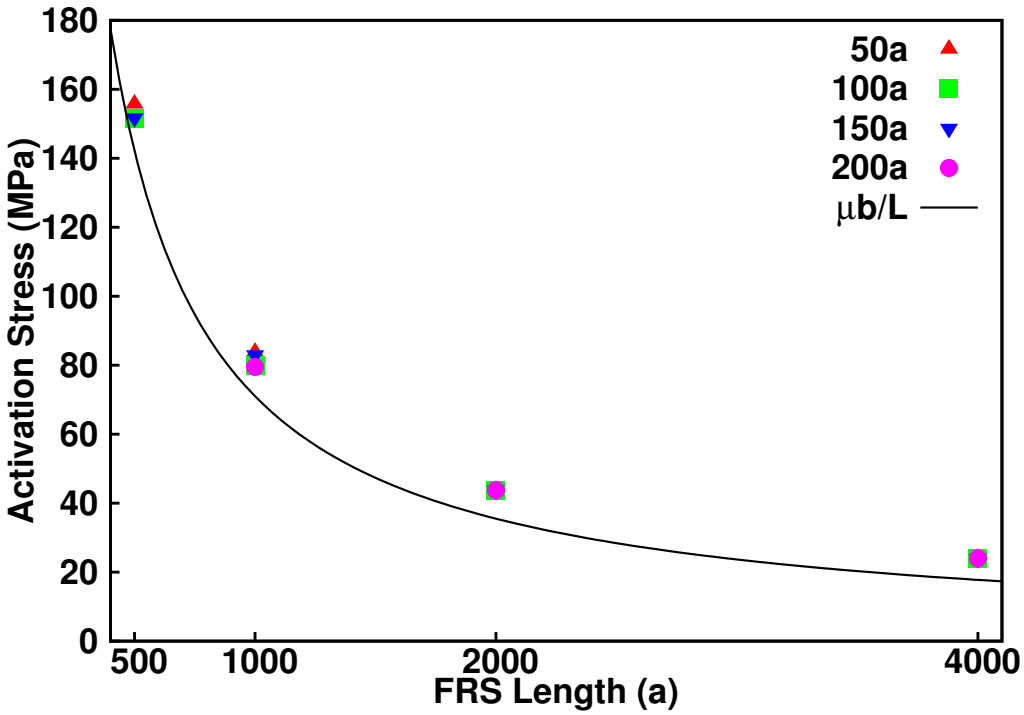

Figure 13: Stress to activation a Frank-Read source as a function of dislocation segment discretization and FRS length.

increases with decreasing core width. Therefore, a larger stress is required to bow out a dislocation with a more confined core, and this is evident in Figure 14. This parameter is necessarily an input to a DDD simulation from either experimental or atomistic simulations. In conclusion, the adaptive meshing algorithm ensures that the dislocation is described well regardless of changes in morphology if the user selects an appropriate discretization for the length scale of the problem at hand.

2.2.3.2 Dislocation Loop Stabilising Stress

As a second example, a specific dislocation configuration is chose to enable direct comparison with atomistic calculations: the stress required to equilibrate a $1/2(111)[\bar{1}01$ prismatic dislocation loop in aluminum. The goal is to calculate the required stress using strictly axial stress components to equilibrate the dislocation loop. In the absence of applied stress, the loop will collapse and self-annihilate (disappear). Using a crystal oriented with the x,y, and z axes along the [100], [010], and [001] directions

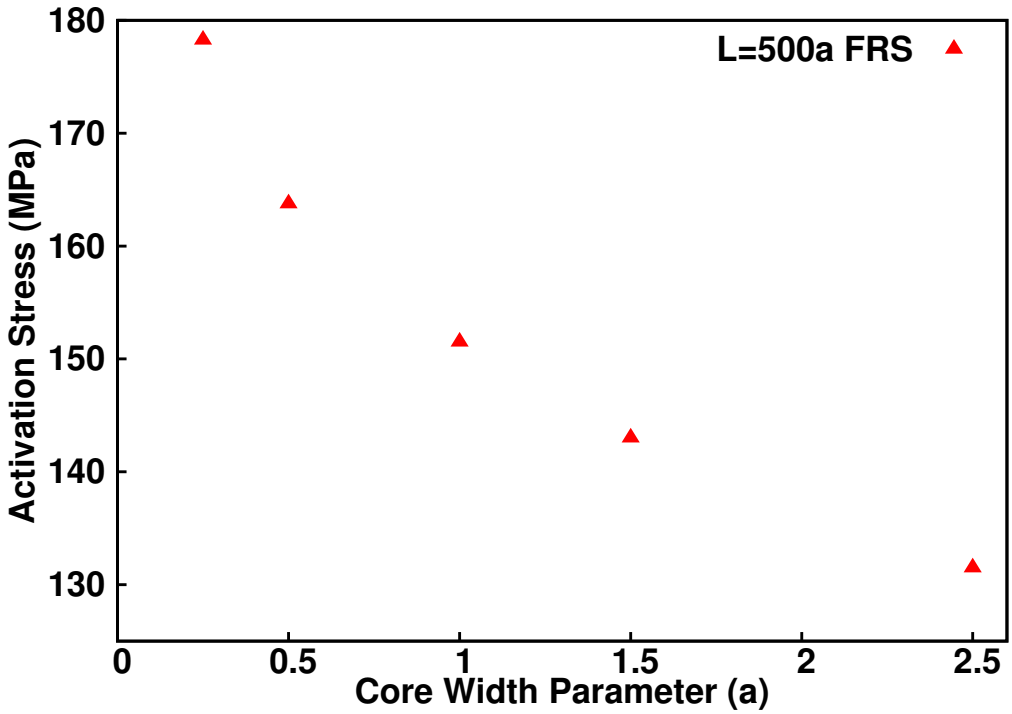

Figure 14: A Frank-Read dislocation source (red) activating under an applied stress. The blue lines represent the periodic simulation boundaries.

respectively, it can be shown by analysing the Schmid factors of each axial stress on this plane and along the Burgers vector direction that one must apply $\sigma_{xx} = -\sigma_{zz}$ and $\sigma_{yy} = 0$. The configuration in DDD is shown in Figure 15.

With the geometry and stress state fully defined, the remaining parameters in the DDD study are the average segment discretization length and the core size parameter. To elucidate the impact of these parameters, the radial force on the dislocation nodes is compared for a range of applied stresses, and the equilibrating stress is found between the stress levels with opposite radial force.

With the goal of reproducing the equibrating stresses from atomistic calculations, which are describe with the following correlation: $\sigma_{\text{eqm}} = 3322.9$ MPa $(R(\text{nm}))^{-0.811}$ [201]. A core parameter of 0.4a is taken (matching the stress level found in atomistics for a loop $R = 5.67$nm), and the equilibrating stresses are calculated for a range of stresses as shown in Figure 16.

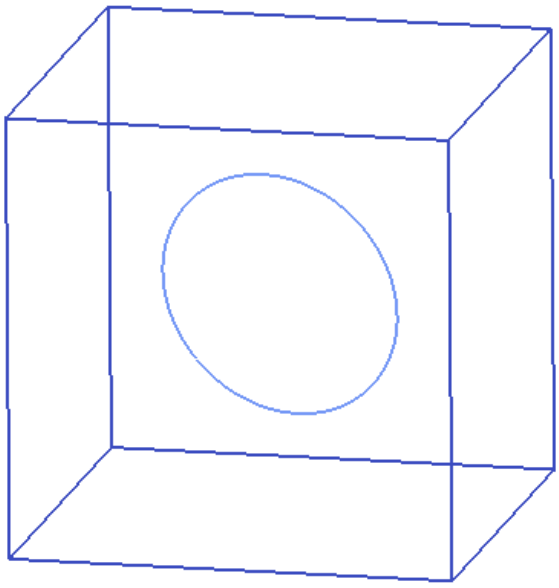

Figure 15: Dislocation loop configuration taken to compare with atomistic calculations. Periodic boundary conditions are applied to the volume.

Despite the fact that pure dislocation in aluminum split into two partial dislocations and a stacking fault, a good match is possible over a range of loop size with a maximum relative error of 3.5%. This comparison is valuable to both validate the accuracy of continuum formulations as well as provide input parameters such as the core size.

2.3 Dislocation Energy

The total potential energy of an elastic crystal containing dislocations can be derived using a methodology following that of Bowers [27] starting with the classical definition of the potential energy E of a crystal with the volume R with a zero traction boundary condition on $\partial_1 R$ and a zero displacement boundary condition on $\partial_2 R$ and with an isothermal assumption, the enthalpy can be written as

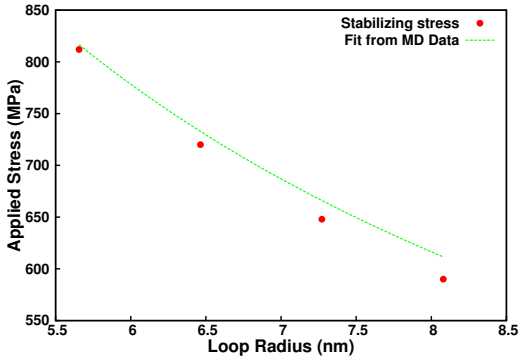

(a) The core parameter and discretization parameters to match a loop size of 5.6nm are taken, and the equilibrating stress as calculated using DDD is compared to the results from MD.

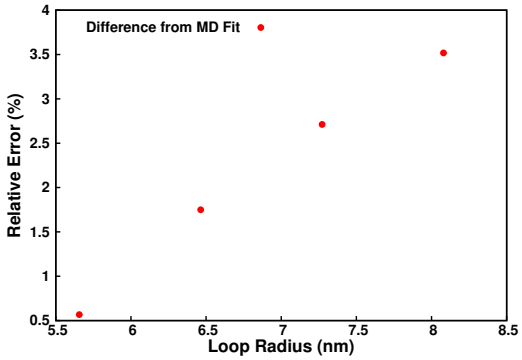

(b) Relative error compared to fit of molecular dynamics data.

Figure 16: Comparison of the applied stress required to equilibrate a dislocation loop in aluminum. [201]

$$H = \int_R \frac{1}{2}\sigma_{ij}\varepsilon_{ij}dV - \int_{\partial_1 R} t_i u_i dA, \tag{26}$$

where σ_{ij} is the stress tensor, ε_{ij} the elastic strain tensor, t_i the traction vector $\sigma^*_{ij}n_j = t_i$ and u_i the displacement field. Expanding the stress and strain into the dislocation (D) and applied ($*$) components and using the major symmetry in C_{ijkl} to simplify the expression.

$$H = \int_R \frac{1}{2}\left(\sigma^D_{ij} + \sigma^*_{ij}\right)\left(\varepsilon^D_{ij} + \varepsilon^*_{ij}\right)dV - \int_{\partial_1 R} t_i\left(u^D_i + u^*_i\right)dA. \tag{27}$$

The strain arising from the presence of the dislocation is expanded using the major symmetry in C_{ijkl} to simplify the expression:

$$E = \int_R \left(\frac{1}{2}\sigma^D_{ij}\frac{\partial u^D_i}{\partial x_j} + \sigma^*_{ij}\frac{\partial u^D_i}{\partial x_j} + \frac{1}{2}\sigma^*_{ij}\varepsilon^*_{ij}\right)dV - \int_{\partial_1 R} t_i\left(u^D_i + u^*_i\right)dA. \tag{28}$$

Using equilibrium ($\sigma_{ij,j} = 0$) and integrating by parts each term containing $\frac{\partial u^D_i}{\partial x_j}$:

$$\int_R \frac{1}{2}\,\sigma^D_{ij}\frac{\partial u^D_i}{\partial x_j}dV = \int_R \frac{1}{2}\,\frac{\partial(\sigma^D_{ij}u^D_i)}{\partial x_j}dV = \int_S \frac{1}{2}\,\sigma^D_{ij}u^D_i m_j dA. \tag{29}$$

where m_j is the normal to the surface swept by the dislocation. The surface is partitioned into three regions: the area swept above and below the dislocation S^+ and S^-, and the region at which the displacement boundary condition is applied $\partial_2 R$:

$$\int_S \frac{1}{2}\,\sigma_{ij}^D u_i^D m_j dA = \int_{S^+} \frac{1}{2}\,\sigma_{ij}^D u_i^{D+}(-m_j) dA + \int_{S^-} \frac{1}{2}\,\sigma_{ij}^D u_i^{D-}(m_j) dA + \int_{\partial_2 R} \frac{1}{2}\,\sigma_{ij}^D u_i^D n_j dA. \tag{30}$$

The displacement caused by dislocations u_i^D is zero on $\partial_2 R$, and therefore the final term is zero. The discontinuity in the displacement field across S is $u_i^- - u_i^+ = b_i$ (the Burgers vector)

$$\int_R \frac{1}{2}\,\sigma_{ij}^D \frac{\partial u_i^D}{\partial x_j}\,dV = \int_S \frac{1}{2}\,\sigma_{ij}^D b_i m_j dA. \tag{31}$$

A similar method was applied to the term containing $\sigma_{ij}^* \frac{\partial u_i^D}{\partial x_j}$

$$\int_R \sigma_{ij}^* \frac{\partial u_i^D}{\partial x_j}\,dV = \int_R \frac{\partial(\sigma_{ij}^* u_i^D)}{\partial x_j}\,dV = \int_S \sigma_{ij}^* u_i^D m_j dA + \int_{\partial_1 R} \sigma_{ij}^* u_i^D n_j \tag{32}$$

On $\partial_1 R$ where the traction boundary condition is applied, $\sigma_{ij}^* n_j = t_i$ and on $\partial_2 R$, u_i^D is zero. Therefore, the potential energy of the crystal is given as

$$H = \int_S \frac{1}{2}\,\sigma_{ij}^D b_i m_j dA + \int_S \frac{1}{2}\sigma_{ij}^* b_i m_j dA + \int_S \frac{1}{2}\sigma_{ij}^* \varepsilon_{ij}^* dA - \int_{\partial_2 R} t_i u_i^* dA. \tag{33}$$

The decrease in potential due to dislocation motion can be calculated by considering a small change in the area swept by the dislocation $\delta a(s)$ while moving in the direction $\mathbf{n}(s)$.

$$\delta H = -\int_{\delta C} \epsilon_{kjl} \left(\sigma_{ij}^D + \sigma_{ij}^*\right) b_i \tau_l n_k \delta a(s) ds. \tag{34}$$

where τ_l is the tangent to the dislocation line. It is clear that Equation 34 is simply the action of the Peach-Koehler force integrated over the distance traversed by the dislocation where the Peach-Kohler force is written as

$$F_i^{PK} = \epsilon_{ijk} \left(\sigma_{jm}^D + \sigma_{jm}^* \right) b_m \tau_k. \tag{35}$$

The energy calculation can be simplified considering that only the difference in energy values is of interest, i.e.,

$$\Delta H_{2-1} = \int_S \frac{1}{2} \sigma_{ij}^D b_i m_j dA \Big|_2 - \int_S \frac{1}{2} \sigma_{ij}^D b_i m_j dA \Big|_1 - \int_{\delta C} \epsilon_{kjl} \sigma_{ij}^* b_i \tau_l n_k \delta a(s) ds. \tag{36}$$

An identical result could also be derived starting from an approach inspired by micro-continuum constitutive modelling philosophies [83, 65]. The enthalpy of the systems can be written as the sum of three contributions associated with that of macroscale, microscale and interaction between the scales. Considering the microscopic displacement as $b_i \delta(x - x')$ and using the divergence theorem to write the external displacement in terms of stress and strain, Equation 36 is found.

2.4 Application to Confined Microstructures

Material systems with confined internal geometries arise in many metallic systems including nanocrystalline materials, nanolaminates, and irradiated materials. As the carriers of plastic deformation, the geometric confinement of dislocation glide plays a particularly important role on the yield point and plastic behaviour of these systems. From a simplistic line-tension perspective, the stress to activate a Frank-Read source (a finite dislocation segment pinned at its ends) is written as

$$\sigma_{\text{act.}} = \frac{\mu b}{L} \tag{37}$$

An inverse dependence on dislocation segment length is immediately clear, which motivates a deeper investigation into the true hardening effect of constrained slip.

Before moving to the case of irradiated materials, an example highlighting the effects of confined dislocation glide as well as many of the concepts regarding the capabilities of discrete dislocation dynamics simulations is presented here.

2.4.1 Multi-layered Metallic Laminates

Multi-layered metallic laminate (MML) materials are composed of layers of alternating metals deposited in a lamellar structure. Due to the high ratio of interfaces to bulk volume their mechanical behaviour is strongly influenced by interfacial geometry and coherency. Experiments on electrochemically deposited Cu/Ni (coherent interface) with Cu layer thickness ranging from 0.9 nm to 20 nm [135, 211] and on PVD Cu/Nb (incoherent interface) [126], among numerous other experiments, have revealed exceptional yield strengths approaching theoretical limits. Other properties such as ductility, fatigue performance, and radiation resistance are also maintained or improved in Cu/Nb MMLs in comparison to bulk properties [126, 240, 136].

The mechanical behaviour of MMLs depends on the individual microstructure of the layer, such as crystal structure, elastic properties, and thickness, as well as on the properties of the heterophase interface. The latter is a direct function of the orientational relationship between the layers, the consequence of which is the formation of an intricate network of misfit dislocations [17]. Molecular dynamics simulations have shown that the Cu/Nb interface in the $\{111\}_{\mathrm{Cu}} \parallel \{110\}_{\mathrm{Nb}}$ Kurdjumov-Sachs (KS) orientation, commonly seen in PVD prepared Cu/Nb MMLs, can act as both a dislocation source [256] and sink [93, 239]. Wang *et al.* (2009) [239] also found that the PVD Cu/Nb interface can be sheared by dislocations, generating an attractive force on dislocations and spreading the core. In contrast, while the $\{112\}_{\mathrm{Cu}} \parallel \{112\}_{\mathrm{Nb}}$ KS Cu/Nb interface generated during accumulated rolled bonding (ARB) [115] may also absorb dislocations, the interfacial shear strength has been found to be significantly higher than for the PVD interface Cu/Nb [25].

The yielding and plasticity of MMLs, and thus their mechanical performance, can be studied in simple cases with analytical models, and in more complex cases, with discrete dislocation dynamics (DDD). Existing models of the mechanical behaviour of MMLs focus primarily on the prediction of the yield point [138, 137]. As a first

approximation, one can apply the Hall-Petch relation using layer thickness as a mean grain diameter. However, this relation predicts a yield point assuming yielding is governed by dislocation pileup at grain boundaries. In thin films and multilayers, the confined nature of dislocation motion results in a behaviour governed not by dislocation pile-up but by single dislocation interactions. Nix [153] showed that the very high strengths and high strain hardening rates of thin metal films can be accounted for by confinement effects on the motion of dislocations, and TEM experiments [119] have confirmed that dislocations propagating in 30 nm thick layers are confined within their layers. Misra *et al.* [138, 137] developed the Confined Layer Slip (CLS) model predicting the microscopic yield point (stress to propagate dislocations) of MMLs. However, studying the more complex mechanisms leading to macroscopic yielding and plastic behaviour requires DDD simulations. To date, DDD simulations in MMLs have been limited to microscopic phenomena such as single dislocation interaction and interface penetration [3, 255]. Studies on thin films with or without substrates also have relevance to MML simulations as dislocations are forced to glide subject to geometric constraint without interface penetration [80, 81]. In addition to discrete dislocation dynamics, several other modelling techniques have been used to analyze plasticity in Cu/Nb MMLs. Atomistic simulations have been used to directly simulate Cu/Nb interface structure to investigate its behaviour under mechanical loading. For example, Zhang et al. [256] determined that dislocation nucleation from the interface relies on interface geometry as well as Schmid factor. In another atomistics study [82], the role of the Cu/Nb interface under spallation was investigated, and it was found that the typically observed high strength of Cu/Nb did not appear because of bulk void nucleation at the interface. At the continuum scale, crystal plasticity finite element simulations have been used to study the deformation mechanisms of Cu/Nb MMLs. In Mayeur et al. [131], the deformation texture following rolling deviated from those of pure Cu and pure Nb and the kinematic constraint imposed

by the interface was not seen to influence crystal stability. Jia et al. [101] studied shear-banding behaviour in a Cu/Nb bicrystal subject to compression, and predicted that stress concentrations at the interface trigger shear bands which could propagate through heterophase interfaces.

While the role of layer thickness on material strength has been the focus of several studies [137], key questions remain before one can understand the relationship between MML microstructure and mechanical response. Macroscopic properties such as plastic response, plastic anisotropy and the microscopic phenomena influencing these properties have yet to be investigated. The present work aims at independently quantifying the effect of (1) the ability of heterophase interfaces to act as dislocation sinks, and (2) elastic stiffness mismatch on both mechanical response and plastic anisotropy in Cu/Nb MMLs. Two models of the Cu/Nb incoherent interface, shearable and hard, are implemented and their influence on material response is quantified. Finally, the implications of elastic constant mismatch and plastic anisotropy effects on material strength and plastic behaviour are investigated by comparing the mechanical responses of multilayered Cu/Cu, Nb/Nb, and Cu/Nb.

A finite element method (FEM) is used to solve the mechanical equilibrium boundary value problem, which incorporates the plastic strain generated by dislocation motion through an elasto-viscoplastic constitutive model. Additionally, modifications are required to represent the interfaces between the layers. Dislocations in different layers may experience a stress due to elastic interactions with dislocations in other layers as well as image stresses from the presence of internal surfaces. The boundary conditions associated with an ideal interface are continuous displacement and traction. The FEM automatically enforces displacement continuity, but traction continuity requires the calculation of additional nodal forces. Traction on the interface due to dislocations in neighbouring layers is integrated on each element face to obtain nodal forces. For Cu/Nb laminates, this correction is in fact very small because of

their similar Young's and shear moduli (E =120/105, μ =45/38 GPa respectively). This is clear from the closed form expression of the stress field components of a screw dislocation at a distance a away from the interface in an infinite bimaterial **??**:

$$\sigma_{xz}(1) = \frac{-\mu_1 yb}{2\pi\left[(x-a)^2+y^2\right]} - \frac{\gamma\mu_1 yb}{2\pi\left[(x+a)^2+y^2\right]} \tag{38}$$

$$\sigma_{xz}(2) = -\frac{\beta\mu_2 yb}{2\pi\left[(x-a)^2+y^2\right]} \tag{39}$$

$$\gamma = \frac{\mu_2-\mu_1}{\mu_2+\mu_1} \tag{40}$$

$$\beta = \frac{2\mu_1}{\mu_1+\mu_2} \tag{41}$$

where a subscript 1 represents the material containing the dislocation, subscript 2 represents the half-space perfectly bonded to the material containing the dislocation, and a is the distance separating the dislocation core from the interface. The terms γ and β that correct for the presence of the interface are 0.0667 and 1.0667 respectively. Consequently, the image force corrections for this material system are negligible. Nevertheless, the coupling to a finite element analysis is necessary to account for the different macroscopic stress states in the layers arising from the mismatch and elastic properties. With different shear moduli as well as glide plane orientations (copper has an FCC structure whereas niobium has a BCC structure), dislocation glide will be favoured in one of the material systems until dislocation-dislocation interactions cause sufficient hardening to activate glide in the other system.

Longitudinal and transverse strains (with respect to the interface plane) are applied to a dislocation dynamics simulation sample of four layers measuring 2.7μm $\times$2.7μm $\times$300nm per layer with periodic boundaries enforced in the plane of the interface as shown in Figure 17. Both loading directions are examined here for two

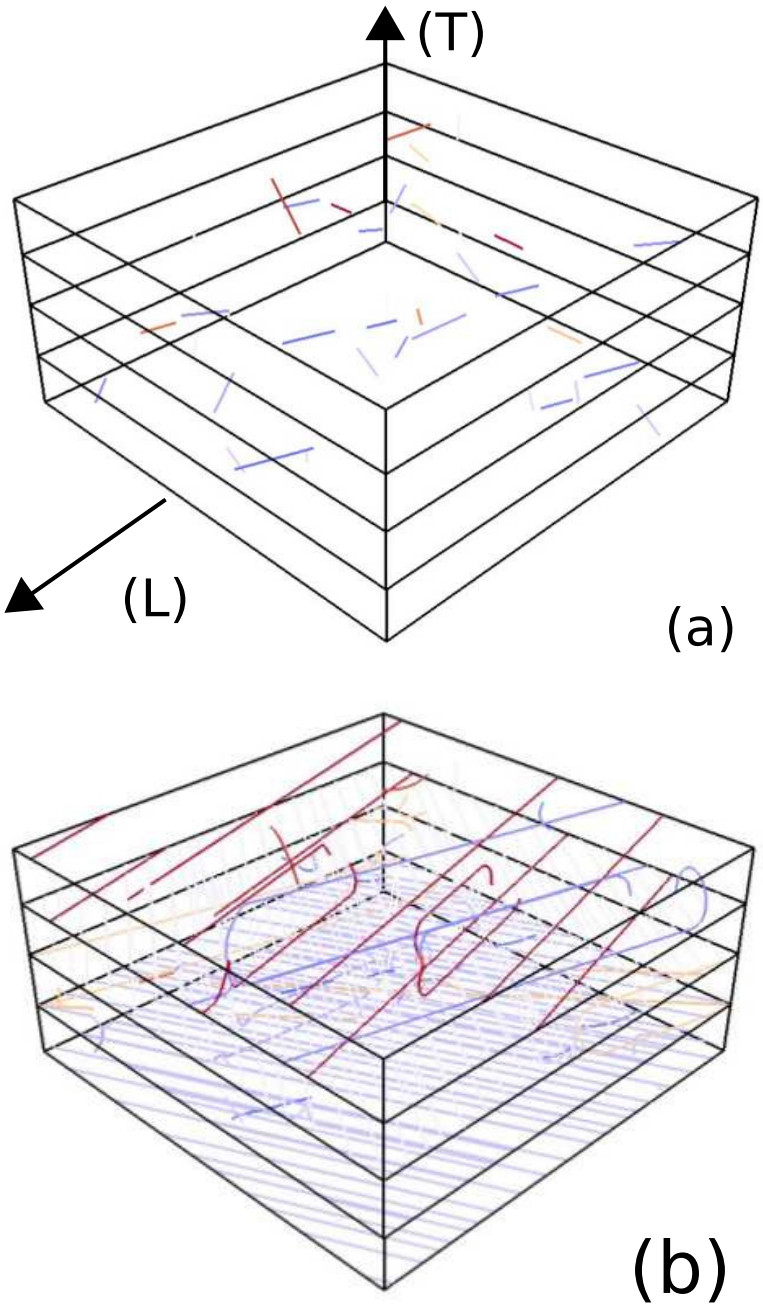

Figure 17: (a) Initial Frank-Read dislocation source configuration in a four layer Cu/Nb MML and (b) the dislocation configuration after 0.5 % strain applied. Interfacial dislocation dipoles deposited by the threading dislocations are clearly visible.

reasons. First, the layered nature of the Cu/Nb MML is inherently transversely isotropic, and the material responses along each axis of symmetry are of interest. Second, these loading directions are those commonly tested in experiments [26]. In

the FEM code, $15 \times 15 \times 5$ elements are used per layer. A strain rate of 10^3 s^{-1} is used in all simulations. Dislocations have been experimentally observed to be confined within their layers in a Cu/Nb MML with 30 nm layer thickness [119]. Therefore, the dislocations here are confined within their 300 nm thick layers. Elastic isotropy is also assumed, and the crystal structure is rotated to the KS orientation in the $\{111\}_{Cu}$ habit plane.

The confining geometry of MMLs causes layer thickness to govern initial yield unless the longest initial dislocation length is less than the layer thickness (under the same resolved shear stress). A set of Frank-Read sources with random lengths, positions, glide planes and Burgers vectors are generated such that the desired dislocation density of $\rho = 10^{12}$ m^{-2} ($\approx$ 10 dislocations per layer) is reached. Such a starting configuration is typical in discrete dislocation dynamics studies [255].

2.4.2 Interfacial Behaviour Models

When a dislocation impinges on a heterophase interface, the core structure may alter as it interacts with the interface. While molecular dynamics simulations have revealed core spreading (as previously mentioned), the practical implications on dislocations within the framework of the continuum theory of defects are not immediately clear. Lacking any experimental evidence regarding the structure of deposited interfacial dislocations, limiting cases are chosen here such that the true material behaviour must lie between the calculated bounds. Therefore, the mechanical response of a Cu/Nb MML is simulated using two interface models: the first is a hard interface that does not accommodate any deformation and preserves the core structure of contacting dislocations, and the second is a shearable interface that entirely absorbs and spreads contacting dislocation cores. A hard interface maintains the core structure of dislocations touching the interface such that stress contributions from the laid-down

interfacial dislocations are those of perfect dislocations. While a truly shearable interface would accommodate deformation associated to the Burgers vector component parallel to the interface, contributions from the normal component are also removed representing an absolute lower bound on strength for interfacial behaviour. This case will be referred to as "shearable." These two systems represent the highest and lowest possible interface strengths and thus provide the range of a real material's behaviour. A third system in which all dislocation-dislocation interactions, both short range and elastic, are removed quantifies the material response solely due to geometric constraint.

The hard interface model is more likely to apply to MMLs in which the interface structure is more compact, such as the ARB Cu/Nb interface, and in which the resistance to dislocation transmission, which, in atomistic calculations, has been seen to be low [256]. The shearable interface, on the other hand, is more likely to apply to MMLs with incoherent interface structures and high dislocation slip barriers, such as the PVD Cu/Nb interfaces. The effect of the interface type on the mechanical behaviour of the MMLs is shown in Figure 18.

Interface behaviour with respect to contacting dislocation core structure clearly and strongly influences the yield point and plastic response. Preserving the full dislocation core structure (hard interface) results in the highest yield point (point 3 in Figure 18), approximately 60% higher than all other considered cases, and the strongest hardening. Removing the stress fields of interface dislocations, as in the case of the shearable interface, produces a defined yield point followed by approximately linear hardening. The assumption of no dislocation transmission at this layer thickness can be seen to be valid because the yield stress is significantly lower than the critical stress required for transmission, which is greater than 1.5 GPa for the ARB Cu/Nb interface [25].

Initial microscopic yield (first dislocation propagation) occurs simultaneously in

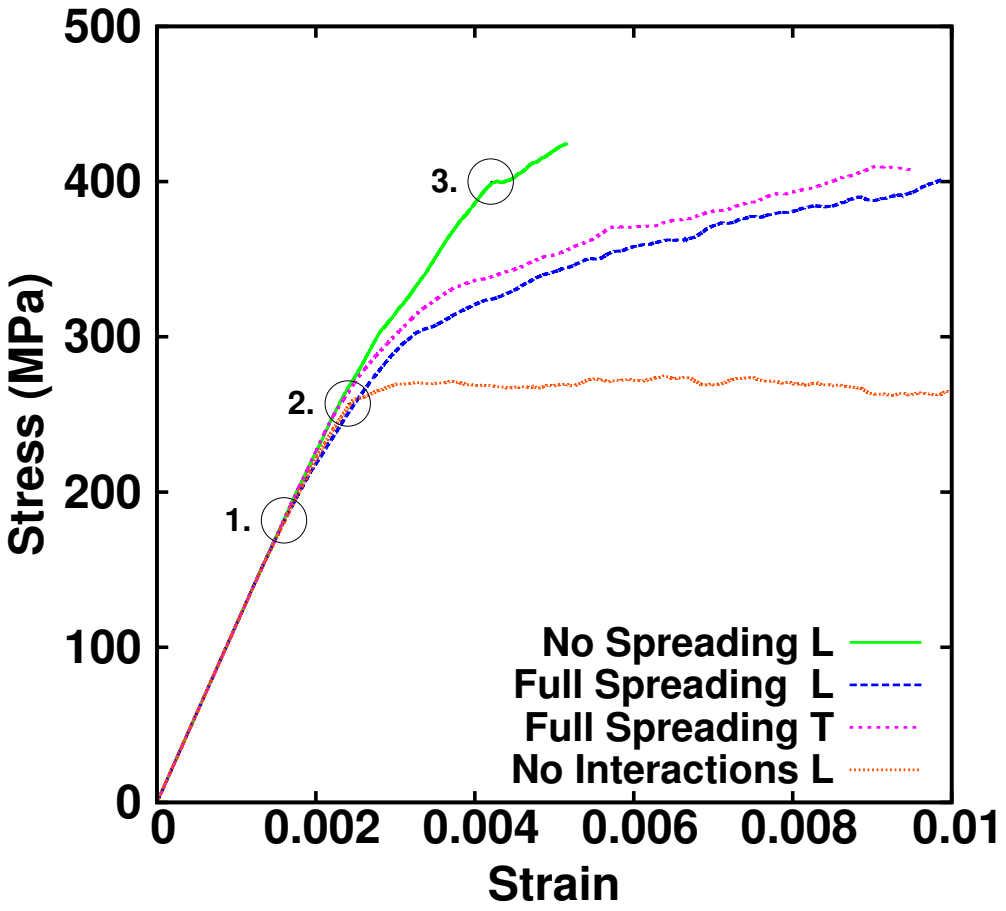

Figure 18: Effect of interface behaviour on mechanical response in longitudinal (L) or transverse (T) test configurations. Microscopic yield of all systems occurs at point 1, macroscopic (experimentally observable) yield of systems with shearable interfaces occurs at point 2 and of the system with hard interfaces at point 3.

all cases (hard, shearable, no interaction) as shown at point (1.) in Figure 18. This is expected because the initial dislocation configurations are random and no interface dislocations are present initially. The first gliding dislocations propagate unhindered until they interact with other dislocations crossing their paths, thus impeding their motion. As further strain is applied, other dislocations begin to propagate and the two systems begin to differ significantly in material response. In MMLs with hard interfaces, the gliding dislocations must deform to pass between the interfacial dislocation obstacles that have been laid down by other gliding dislocations, as seen in

Figure 17b), which can cause significant hardening as shown by Nix [153]. The interface dislocation density continues to increase to the extent that the plastic response is nearly linear with a hardening coefficient close to the Young's modulus.

When the stress fields from the interfacial dislocations are removed, the threading dislocations are not forced to squeeze through them and can propagate until they encounter an obstacle. The material response directly reflects this: it is much easier for dislocations to propagate in general, and as a result, there is a well-defined yield point at point (2.) with a lower hardening rate than the previous case. However, hardening from dislocation-dislocation interaction is not negligible, as can be seen from the third system in which all dislocation interactions are disregarded. A perfectly plastic response is recovered after all layers have yielded. At 0.5% strain, dislocation hardening results in an approximately 50% increase in strength. In all cases the material response is highly influenced by dislocations within the layers, highlighting the profound effect of the initial dislocation configuration because they can pin or form junctions with other dislocations causing hardening.

In this example of a simulation of confined dislocation motion using DDD, the contributions from confinement, dislocation-dislocation and dislocation-interface interactions have been analysed and deconvoluted. Simple dislocation confinement has been shown to result in a macroscopic yield-point, followed by perfectly plastic behaviour. The added effect of dislocation-dislocation interactions within the layers results in an increase in yield-point as well as hardening. Finally, the effect of dislocation-interface interactions were studied by considering two limiting interface models: shearable (interfacial dislocation stress fields removed) and hard (stress fields remain). The hard interfaces, which include the dislocation-interface interactions, produced a yield point 60% greater than the yield point of the shearable case, which is followed by hardening. In this instance, the layer thickness is not the sole factor in determining MML strength, and that the ability of the interfaces to maintain the structure of interfacial

dislocations play a strong role in governing the material response of MMLs and can lead to dramatic increases in the strength of the material.

An important notion from these conclusions is that the nature of the interaction between a gliding dislocation and the constraining object is a critical factor on the mechanical properties in addition to the effect of confinement itself. Whereas in this instance, two limiting cases are adopted for interfacial behaviour, irradiation defect strength has been studied from the atomistic perspective and will be used to inform the DDD simulations used here. Dislocation discretization is particularly important in such fine-scale geometries as dislocation curvature is expected to be very high and the average dislocation segment length must reflect this. Once the user has selected an appropriate length-scale, the adaptive remeshing algorithm serves to maintain an accurate spatial description of the dislocation network.

2.5 Athermal Dislocation-Irradiation Defect Interactions

The first step towards predicting how irradiation damage causes hardening is the characterization of unit dislocation-obstacle interactions. Atomistic simulations are well suited to the length-scales associated to these processes as they include all inherent complexities in a material which may not be computationally feasible at the mesoscopic scale, such as free surfaces, elastic anisotropy, and the prediction of dislocation reactions. Some phenomena must necessarily be examined from atomic scale calculations; for example, in the case of voids, small voids are non-spherical due to the crystal lattice structure, and therefore the forces on dislocations caused by complex interactions with the atomic, discretized free surface are incorporated in atomistic simulations. However, such calculations are not without significant drawbacks, which are discussed at greater length in Chapter 4.

The interactions between pure edge and pure screw dislocations with SIA loops of

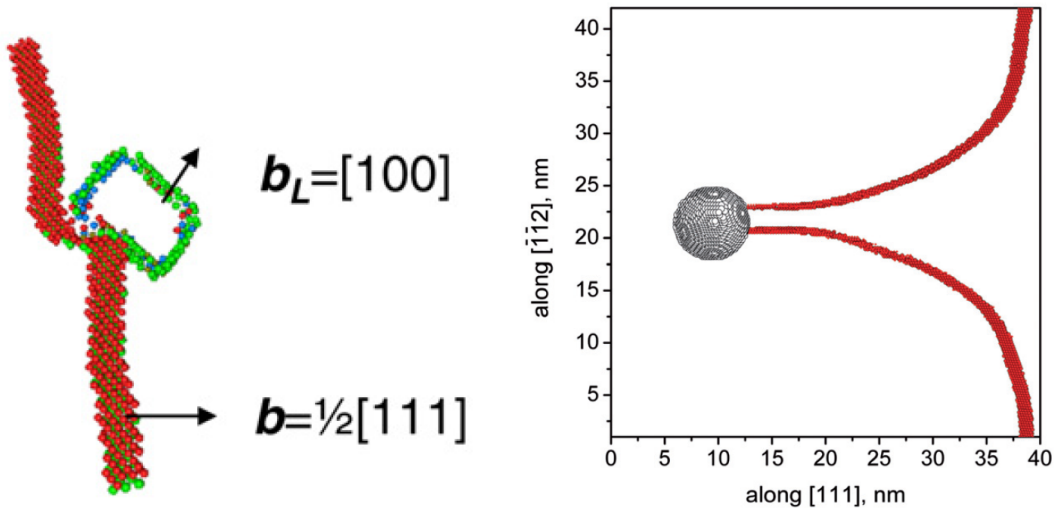

(a) Edge dislocation interacting with a [100] SIA loop in α-iron. [215]

(b) Edge dislocation interacting with a void in α-iron. [163]

Figure 19: Molecular dynamics simulations of a dislocation interacting with an irradiation induced obstacle.

character $\langle 100 \rangle$ and $1/2\langle 111 \rangle$ with different relative orientations between the glide dislocation and SIA loops ([128, 156, 11, 122, 217, 212]), and with voids ([85, 163, 218]) have been investigated to some degree. Atomistic calculations show that the obstacle strength of SIA loops is highly dependent on the relative orientations during the interaction, and have characterized the strength of voids for a range of sizes. However, studies relying on atomistic calculations are highly limited in their scope of investigation because only unit processes can be simulated and only under shock loading ($\dot{\varepsilon} \geq 10^6$) in dynamic simulations. The statistics one can extract from atomistic simulations have limited intrinsic value when considering the influence of irradiation defects on the macroscopic material response: computational demands limit atomistic simulations to rectangular arrays of defects, and a limited number of defect sizes and interaction geometries, which result in strength values which are not representative of a physical material. Mechanical strength cannot be directly derived from atomistic obstacle strength calculations because the calculated values are valid only for the simulated defect size, density and distribution. Moving towards macroscale

properties of engineering materials requires coarse graining, which is possible using mesoscale simulations such as DDD.

Dislocation dynamics studies on irradiation hardening are most often limited to dislocations interacting with defects composed of dislocations such as SIA loops [188, 95, 155, 4] or stacking fault tetrahedra [127], the details of which are discussed further in Chapter 3. Representing defects such as voids in dislocation dynamics simulations pose a much greater challenge from the standpoint of physics as well as implementation and computational burden. With the goal of multi-scale modelling irradiation damage to obtain macroscopic measures of irradiation hardening, atomistic simulations can inform higher scale models such as DDD as described in the following sections.

2.5.1 Void Implementation

Irradiation induced voids influence dislocation motion via two different mechanisms: elastic and core interaction. Elastic interactions between voids and dislocations exist because the traction vector must be zero at the void surface, giving rise to image forces acting on the dislocation. As a void tends to small sizes (<20 vacancies), the shape deviates significantly from the typical spherical approximation and surface tension effects begin to influence the stress field as well. However, in any case, the strength of interaction decreases as $1/r^3$ and at a distance equal to the void radius R from the void surface, the change in stress with respect to an infinite medium is $\approx 10\%$. Given that the voids considered in this body of work are at most 5nm in diameter, the range of interaction is highly limited and therefore explicit elastic interactions with voids are neglected. However, dislocation core reactions are treated directly. When a dislocation core contacts a void, the dislocation terminates on the surface, and begins to bow around the void as applied stress increases. If a void acts as an impenetrable defect, a dislocation would have to bow completely around the

defect and self-annihilate in order to break free from the void. However, molecular statics simulations (Figure 22 [14]) show that this is not the case - a dislocation may break free from a void before it has bowed completely around it. Two main methods have been developed to model obstacle dislocation breakaway behaviour: a breakaway angle criterion ([64],[54],[228]) and a Gibbs free energy based formulation [213]. Each of these models has its respective advantages and disadvantages. Breakaway angle formulations, which have been favoured in line tension simulations, are simple to implement and qualitatively reproduce the behaviour observed in molecular statics. In the aforementioned studies, breakaway angles were directly specified rather than extracted from atomic scale simulations, which precludes direct comparison with a realistic material or experiment. The Gibbs free energy formulation has the potential to capture thermally activated spontaneous breakaway as well as deterministic stress based breakaway (0K behaviour), but requires significant atomistic scale simulations over a range of defect types, sizes, temperatures and stresses.

Here, an atomistics informed breakaway angle criterion incorporating void size dependence is used to model core interactions between dislocations and voids. Angle breakaway criteria have only been used in line tension simulations, from which the justification of a breakaway angle is clear. Assuming a line tension $\Gamma = \mu b^2/2$, Burgers vector magnitude b, and shear modulus μ, a dislocation as shown in Figure 20 exerts a force of

$$F_{\text{void}} = 2\Gamma\cos(\theta/2) \tag{42}$$

and it is assumed that the strength of the defect can be characterised by the maximum resistive force of the defect.

The included angle θ can be written in terms of the applied shear stress on the plane τ and inter-defect spacing L because $F = \tau bL$ (a simplified version of the Peach-Koehler force for line tension simulations), i.e.,

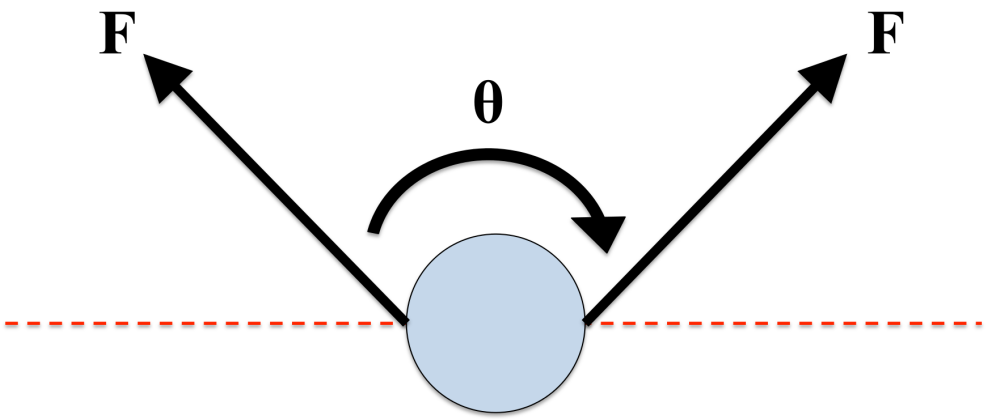

Figure 20: Dislocation-void interaction configuration for an angle based criterion for dislocation breakaway.

$$\theta = 2\,\mathrm{acos}\left(\frac{\tau b L}{2\Gamma}\right) = 2\,\mathrm{acos}\left(\frac{\tau L}{\mu b}\right). \tag{43}$$

The validity of Equation 43 for dislocations has never been verified, and is explicitly shown here to be valid. A single edge dislocation is placed in periodic simulation volume such that its end points are separated by 2.87 nm (10 a). An applied stress with a Schmidt factor of unity on the glide place is applied and the dislocation dynamics simulation is performed until equilibrium was reached. The resulting bowing angles and a fit of the data is shown in Figure 21.

The surface fit to the data in Figure 21 is identical to Equation 43 with the line tension left as a parameter. The behaviour of a dislocation described using the continuum theory of defects therefore has the same functional form as under line tension approximations; however, this fit omits one crucial behaviour observed while conducting the simulations. When the dislocation is significantly bowed, i.e. θ is on the order of $\frac{\pi}{4}$, the elastic interaction between the nearly-touching dislocation segments becomes sufficiently strong to pull the bowed segments together and spontaneously overcome the defect. This behaviour cannot be reproduced using line tension simulations and represents an important limit to a breakaway angle criterion. The exact value of the

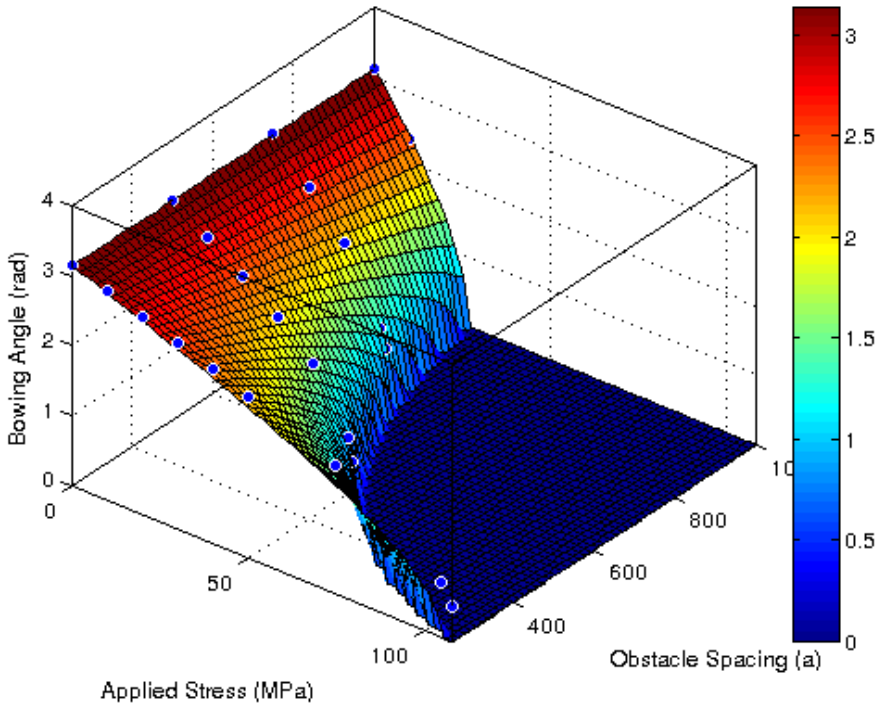

Figure 21: Bowing angle of a dislocation as a function of applied stress and obstacle spacing.

critical angle is also a function of defect size and nature, and thus must be determined on a case-by-case basis.

To determine the breakaway angles to be used to represent dislocation-void interactions, void strength data from the literature was adopted. In [14], the stress to cause dislocation breakaway is given for several defect sizes as shown in Figure 22. The dislocation configuration shown in Figure 22 was produced using atomstic calculations and therefore inherently incorporates anisotropic elasticity and the effects on the complex core structure and motion of screw dislocations in BCC α-iron. One cannot reasonably expect to match both the physical configuration and breaking strength found using atomistics with DDD calculations of dislocation-void interactions. The strength of the defect is the most important consideration when the goal is to determine the change in material strength as a result of the presence of voids, and

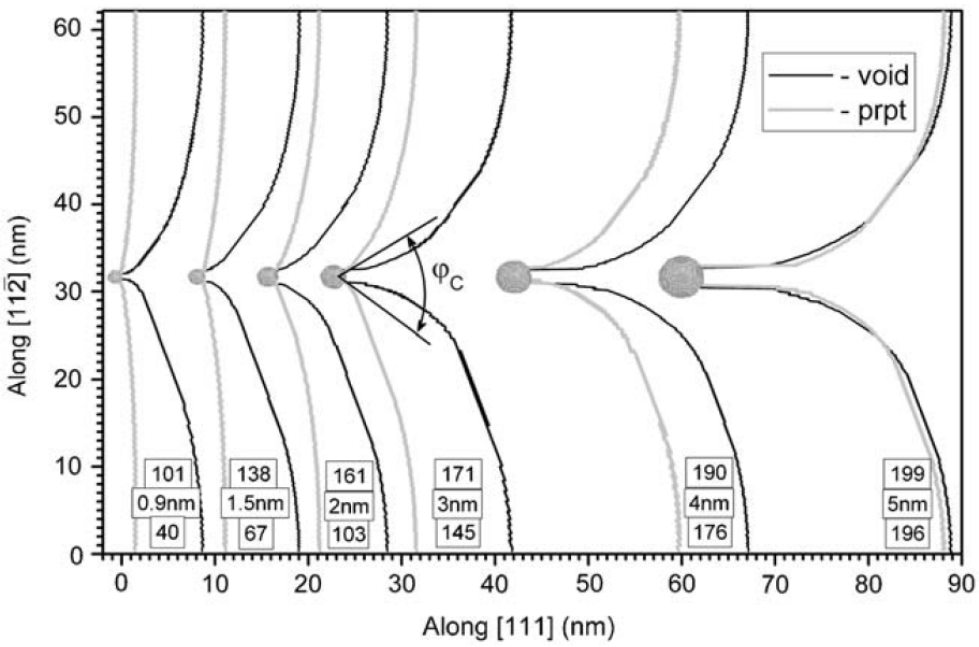

Figure 22: Void and precipitate strength for various obstacle sizes as calculated using molecular statics. [14]

therefore is the information that is used to coarse-grain the atomistic simulations to the mesoscopic scale. An identical void configuration was reproduced in the dislocation dynamics simulations, and a shear stress was applied along the glide dislocation Burgers vector direction. The stress was gradually increased during which the included angle between the dislocation arms was measured, and is displayed in Figure 23. To interpolate between void sizes, a cubic polynomial was fit using all data points with the additional condition that void strength must go to zero as size goes to zero.

Figure 23 also shows several notable phenomena. In a line tension simulation, which consider obstacles as points and neglect elastic dislocation self-interaction, each line would be identical. As one can see in a full dislocation dynamics simulation with finite defect sizes, the addition of these two effects resulted in a notably different response. A size dependence was in fact only possible with dislocation self-interaction - the effect is clearly stronger at smaller defect sizes, because the distance between the bowing dislocation arms was smaller and therefore the stress field (proportional

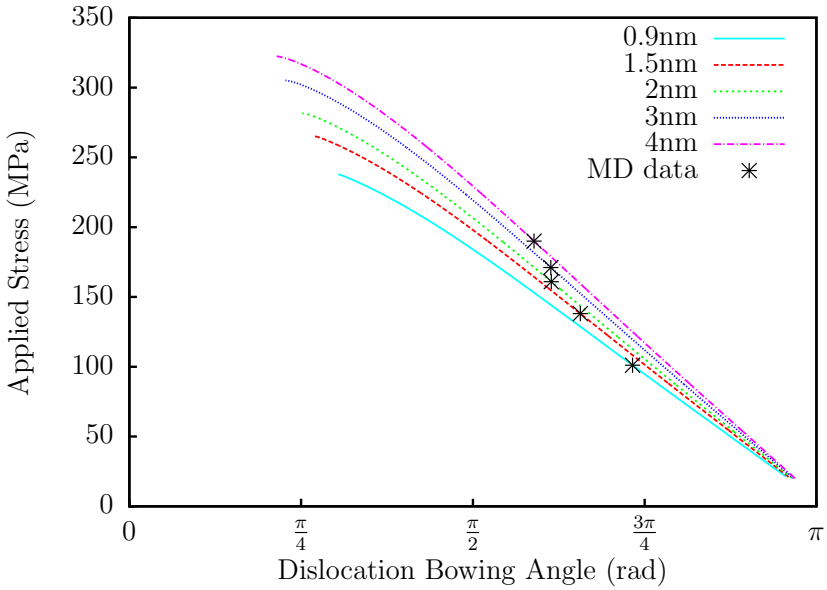

Figure 23: Dislocation bowing angle as a function of void diameter and applied shear stress. Black asterisks denote the angle extracted for the MD specified breaking strength.

to $1/r$) was stronger. The line for each void size terminated when the configuration became unstable and the dislocation self-annihilated, which corresponds to the behaviour of spontaneous bypass as described with Figure 21.

Modelling void strength in this manner is analogous treating the interaction as a dislocation-particle interaction with a non-attractive particle, whereas the true dislocation-void interaction is attractive. Using line tension models, Arzt et al. [7] showed that dominating process for dislocation bypass of an attracting obstacle is governed by the obstacle-dislocation attraction after the dislocation has passed the obstacle. The void model used here assumes that the attraction at detachment is inherently included in the atomistics void strength calculation used to generate the void strength model. For thermally activated bypass, the attractive interaction becomes crucial in determining if bypass is possible [6] and therefore the current void strength model would require further refinements to be valid in the thermally activated case.

The discrete nature of the lattice creates non-negligible distortion of the spherical void shape as expected from continuum mechanics, and at an even smaller scale,

the interaction between a dislocation and very small vacancy clusters (which occur commonly in irradiated α iron as seen in Figure 2b) is unknown. A very recent molecular statics study on voids as small as 2.5nm [50] show that at this length scale, voids strength decreases faster than predicted using the BKS model; however, only a single defect spacing was used, and a far more comprehensive study is necessary to drawn any firm conclusions. It is possible that edge dislocations may absorb vacancies resulting in dislocation climb and that these small defects with only several vacancies may have no effect on the dislocation motion (i.e. zero obstacle strength).

Another factor influencing the strength of a dislocation-void reaction is the position at which the glide plane intersects the void relative to the void center. A coupled FEM-dislocation statics study examined the force on a dislocation as a function of glide plane offset from the void center with comparison to atomistic calculations [85]. The atomistic calculations showed that the stress to propagate an edge dislocation past a void decreased as the effective radius on the glide plane decreased. However, at the void edge, the stress to bypass had decreased by only 20% relative to bypassing at the void center, and non-zero stresses were found at 1.5R away from the void. Without mapping over defect size, offset, and density, piecing together atomistics data from independent studies with different boundary conditions, potentials, and other simulation parameters would likely introduce far greater errors than simply by adopting the approximations used herein. Therefore, the approximations adopted by implementing a void strength law based on the atomistics data in Figure 23 are reasonable within the framework of this thesis.

2.5.2 SIA Loop Implementation

Irradiation induced self-interstitial atom loops have been observed in α-iron as $1/2\langle 111\rangle$ glissile loops [259], and $\langle 100\rangle$ sessile loops [91]. Experiments indicate that α-iron SIA loop populations tend to be dominated by $1/2\langle 111\rangle$ loops at lower temperatures with

⟨100⟩ loops occupying 90% of the population at 573K (300°C), though experimental data is limited. Recent simulations [251] have also shown that 1/2⟨111⟩ loops can combine to produce a ⟨100⟩ loop. In this thesis, only ⟨100⟩ loops are considered, because they are far more populous than 1/2⟨111⟩ loops, and 1/2⟨111⟩ loops are highly mobile and therefore cannot be characterised with single dislocation simulations.

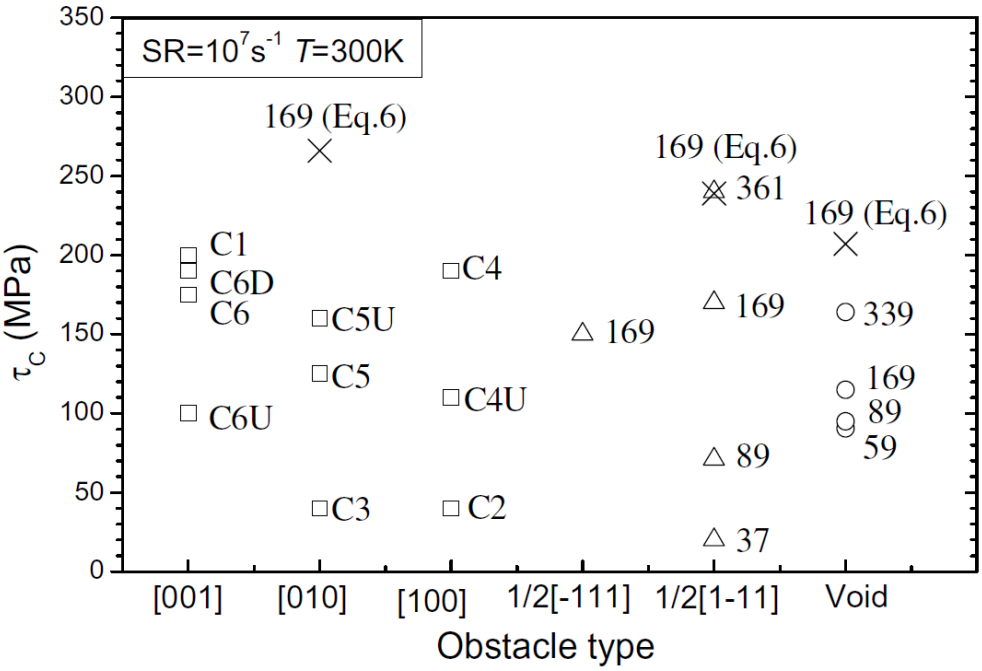

Figure 24: Stress required for stress-activated bypass of a ⟨001⟩ SIA loop as determined using molecular dynamics simulations.[217]

Each loop is represented using four straight edge segments in a square configuration [212]. Molecular dynamics simulations of edge dislocation interacting with SIA loops reveal complex behaviour such as loop absorption [217], which may explain experimentally observed channel clearing [259]. The obstacle strength of an SIA loops has also been shown to vary significantly depending on the relative loop-dislocation orientation [217]. An attempt to reproduce one of these complex reactions using atomistics-informed DDD was only able to achieve similar behaviour using a fitting parameter for certain dislocation parameters [194]. For the analysis of athermal irradiation hardening in this thesis, it is the ensemble response which is desired rather

than reproducing each individual interaction. Consequently, an ensemble of loops of all possible Burgers vectors and with a mean spacing equal to the configuration in [217] is taken and the flow stress calculated. Considering only elastic interactions between the glide dislocation and SIA loops, the stress to propagate a dislocation as calculated by dislocation dynamics is found to be the mean stress of the different $\langle 001 \rangle$ configurations in atomic scale simulations as shown in Figure 24 and is therefore adopted as the method of interaction for athermal hardening calculations. This behaviour model is a first order approximation to the highly complex, atomic scale nature of dislocation-SIA loop interactions. While atomistic simulations can provide some insight, studies have observed dependence on temperature, stress, loop size and orientation, and incoming dislocation character [128],[122], [156]. A much greater study into these reactions, particularly at loop ranging in size from 0.5-5 nm are necessary to develop a more physically accurate model of interaction.

2.6 Thermal Activation of Dislocation Motion

2.6.1 Transition State Theory

The developments leading to the field of transition state theory began from the work of van't Hoff [226], who expressed chemical equilibrium constants in the form

$$\left(\frac{\partial \ln K}{\partial T}\right)_P = \frac{\Delta E}{RT^2}, \tag{44}$$

where K is the equilibrium reaction constant, ΔE the internal energy change, P the pressure, R the universal gas constant, and T the absolute temperature. Because K is the ratio of the forward and backwards reaction rates k_1 and k_{-1}, one can also write the following:

$$\left(\frac{\partial \ln k}{\partial T}\right)_P = \frac{\Delta E}{RT^2}, \tag{45}$$

This work was inspired by the developments of Maxwell's law, which implies that

the fraction of molecues with an energy greater than E is given by $\exp\left(\frac{-E}{RT}\right)$, as well as the work of Pfaundler [172], who first posulated that only molecules with an energy greater than E could participate the chemical reaction [112]. Arrhenius then postulated that the equilibrium that is being predicted must be that which is established between the normal and activated states in the reaction process. He then followed that it is exactly this equilibrium that is predicted by van't Hoff's equation [112].

The notion of a rate being governed by a pathway passing through a saddle point on a potential energy surface was first introduced by Pelzer and Wigner [170] before being generalized to transition state theory with the work of Eyring *et. al.* [60]. The basic components of transition state theory are as follows:

1. Reaction rates can be calculated by characterising the saddle point of the potential energy surface. The details of the pathway between the minima and the saddle point are irrelevant to the reaction rate.

2. The initial reactants are in equlibrium with the activated complexes (as stated by Arrhenius). Such is to say that the reaction rate is independent of the concentration of products or the state following the saddle point.

3. The motion of the system at the saddle point may be considered as pure translational motion described using kinetic theory.

Vineyard extended transition state theory to solid state problems by considering the rate of many-body interactions [234]. For a crystal containing $N/3$ atoms and N degrees of freedom, the potential energy for the entire crystal is denoted by $\Phi(y_1, y_2, ..., y_N)$. Minima of Φ are found at A and B with the saddle point between them at P in the N dimensional hyperspace, as shown in Figure 25. S is a hypersurface passes through P and is normal to all contours everywhere else. Therefore, any point moving from A to B with non-zero velocity at S will transition to B.

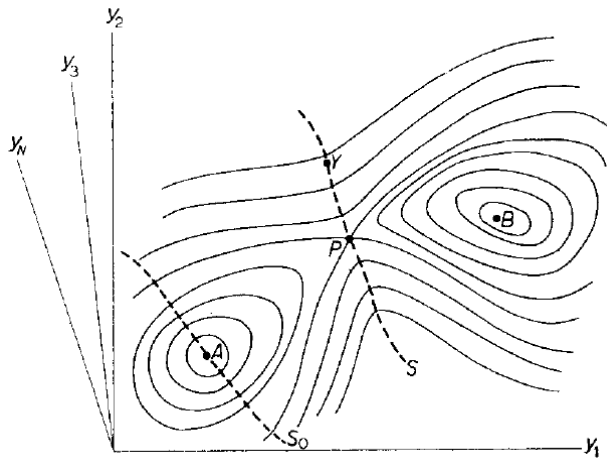

Figure 25: The energy contours for an N dimensional space with solid contours of constant potential energy and dash lines, constraining hyperplanes. [234]

The average jump rate of from A to B is determined by the number of points Q_A to the left of S, and the rate I at which points cross S:

$$\Gamma = \frac{1}{\tau} = \frac{I}{Q_A} \tag{46}$$

The first principle assumption in this work is to adopt the principle that for classical systems in equilibrium, the probability distribution of position and velocity in configurational space can be written as

$$\rho = \rho_0 \exp(-\Phi/k_B T) \tag{47}$$

where ρ_0 is a normalizing factor. The number of points to the left of S is then

$$Q_A = \rho_0 \int_A \exp(-\Phi/k_B T) dv \tag{48}$$

where the integration occurs over the configurational space left of S. Quantifying the number of points crossing from left to right I begins with the probability density at any point Y in S having a hyper-velocity $\mathbf{V} = \dot{y_1}...\dot{y_N}$ within range $d\mathbf{V} = d\dot{y_1}...d\dot{y_N}$

$$\rho(Y,\mathbf{V})d\mathbf{V} = \rho_1 \exp(-\Phi/k_BT)\exp(-V^2/2k_BT)\,dy_1...dy_N \tag{49}$$

where $\rho_1 = \rho_0(2\pi k_BT)^{-N/2}$. The total current of phase points crossing an element $d\mathbf{S} = dS_1...dS_N$ of S is found by integrating over all possible velocities:

$$d\mathbf{I} = d\mathbf{S}\cdot\int \mathbf{V}\rho(Y,\mathbf{V})d\mathbf{V} \tag{50}$$

To ensure that $d\mathbf{S}\cdot\int\mathbf{V} > 0$, the axes are rotated such that one direction is parallel to $d\mathbf{S}$ at Y

$$\begin{aligned} dI &= \rho_0(2\pi k_BT)^{-N/2}\exp(-\Phi(Y)/k_BT)dS_1\int_0^\infty \dot{y}_1\exp(-y_1^2/2k_BT)d\dot{y}_1 \\ &\prod_{j=2}^{N}\int_{-\infty}^{\infty}\exp -y_j^2/2k_BTd\dot{y}_j \\ &= \rho_0\sqrt{k_BT/2\pi}\exp(-\Phi(Y)/k_BT)dS_1 \end{aligned} \tag{51}$$

where thanks to the rotation, $dS = d\mathbf{S} = dS_1$. Integrating dI over S is the final step to obtain the rate of points crossing S from left to right:

$$I = \rho_0\sqrt{k_BT/2\pi}\int_S \exp(-\Phi(Y)/k_BT)dS \tag{52}$$

Substituting Equations 48 and 52 into Equation 46 yields the rate of crossing for an arbitrary system between two minima:

$$\Gamma = \sqrt{\frac{kT}{2\pi}}\frac{\int_S e^{-\Phi/kT}dS}{\int_A e^{-\Phi/kT}dv}. \tag{53}$$

Expanding the energy Φ at point A to second order yields $\Phi \cong \Phi(A)+\sum_{j=1}^{N}\frac{1}{2}(2\pi v_j)^2q_j^2$ and $\Phi \cong \Phi(P)+\sum_{j=1}^{N}\frac{1}{2}(2\pi v_j)^2q_j'^2$.

$$\Gamma = \left(\frac{\prod_{j=1}^{N}\nu_j}{\prod_{j=1}^{N-1}\nu_j'}\right)e^{-[\Phi(P)-\Phi(A)]/kT} \tag{54}$$

$$\nu_a = \frac{\prod_{j=1}^{N} \nu_j}{\prod_{j=1}^{N-1} \nu'_j} \tag{55}$$

$$\Delta S = \frac{\prod_{j=1}^{N-1} \nu_j^0}{\prod_{j=1}^{N-1} \nu'_j} \tag{56}$$

Therefore, the effective attempt frequency is given by the ratio of the product of the normal frequencies of the initial (relaxed) configuration and the saddle point (activated) configuration. Finally, the Arrhenius equation can be rewritten in terms of the fundamental frequency ν_1, the change in entropy and the change in enthalpy for the process:

$$k = \nu_a e^{-\Delta G/k_B T} = \nu_1 e^{\Delta S/k_B} e^{-\Delta H/k_B T}. \tag{57}$$

The problem is therefore determining ν_1, ΔS, and ΔH so that the reaction rate (or mean waiting time) can be used to simulate the time evolution of thermally activated processes.

2.6.2 Thermally Activated Dislocation Glide

2.6.2.1 Activation Energy

Thermally driven material behaviour such as creep deformation or strain rate sensitivity has long been described using a modified Arrhenius equation, motivated from a experimental observations:

$$\dot{\varepsilon} = B_0 \exp\left(-\frac{\Delta G}{k_B T}\right) \tag{58}$$

where B_0 is a frequency factor incorporating the average plastic strain increment with each thermally activated event (assumed to be constant). With greater theoretical developments in the continuum theory of defects came several attempts to determine the parameters of the Arrhenius equation, in particular for the activation energy ΔG

and its contributing terms, in closed form. The change in Gibbs free energy is defined as

$$\Delta G = \Delta U - \tau \Delta V - T\Delta S \tag{59}$$

where ΔU is the change in internal energy, and ΔV is defined by the $\tau\Delta V$ as the total work done by the externally applied stress τ (and is not related to physical volume change of the system). Experimental measures of activation energy for creep are found from the temperature dependence of the creep strain rate, found using [94] and Equation 58

$$\begin{aligned} Q_c &= k_b T^2 \left(\frac{\delta \ln \dot{\varepsilon}}{\partial T} \right)_\tau \\ &= \Delta H - T \left(\frac{\partial \Delta H}{\partial T} \right)_\tau + T^2 \left(\frac{\partial \Delta S}{\partial T} \right)_\tau \end{aligned} \tag{60}$$

A correct application of Equation 60 requires a careful examination of the Second Law of Thermodynamics. A crystal in its ground state described by T, S, and V will not necessarily be the lowest possible free energy state of the crystal due to an internal defect structure, but will correspond to the lowest free energy for the specific configuration.

Gibbs then examined the specific contributions to the activation energy for dislocation movement. The plastic strain rate in a simplified two dimensional case can be written as

$$\dot{\varepsilon} = \rho b v \tag{61}$$

where ρ is the dislocation density, b the magnitude of the Burgers vector, and the glide velocity v is determined by the rate of unpinning from local obstacles for thermally activated dislocation glide. Gibbs acknowledged the complexity arising from the distribution of segment lengths between pinning points, but treated the simpler case

with equal connected lengths in closed form. A key notion of the analysis is that the free energy is considered for the entire defective crystal rather than the local region around the pinned dislocation segment. The reasons are twofold:

- It is the entire crystal that adopts a minimum free energy configuration, not the local region.
- The concepts of thermodynamics are only applicable to a large ensemble of atoms.

Gibbs formalized a problem consisting of a finite dislocation segment of length $2l$, Burgers vector b pinned at its ends and at its midpoint by local obstacles. A "long-range" stress $\tau_\mu < \tau$ acts in a direction opposite to the applied stress τ. Assuming the glide dislocation remains straight, at a position x, the Helmholtz free energy (incorporating contributions from the internal stress τ_μ) $F = U - TS$ will vary as a function of x. As the dislocation moves, the an applied stress performs work τlbx, resulting in a change in Gibbs free energy of $\Delta G = \Delta F - \tau blx$ for a thermally activated event. Gibbs was mistaken in this derivation if one considers the derivation of the attempt frequency by Vineyard, detailed in the above section. The entropic contributions arise as a result of the ratio of states between the normal and activated complexes, and are not inherently included in the free energy, which Gibbs makes note of in reference to the work of Vineyard [234] and Granato *et.al.* [78]. In this thesis, Gibbs' analysis of Helmholtz free energy and Gibbs free energy are referred to as the internal energy and the enthalpy. The analysis of Gibbs does addresses many complex points for the first time, including the notion of activation volume for a dislocation process. The Gibbs free energy barrier to be overcome as shown in Figure 26 is written as $\Delta G = \Delta F - \tau bld$. The activation volume is defined as

$$\Delta V = -\left(\frac{\partial \Delta G}{\partial \tau}\right)\Bigg|_T \tag{62}$$

which one can immediately recognize as the quantity *lbd* for this scenario. This is a thermodynamic quantity rather than a change in volume for this specific process, as dislocation motion changes the crystal shape without changing its volume (to first order).

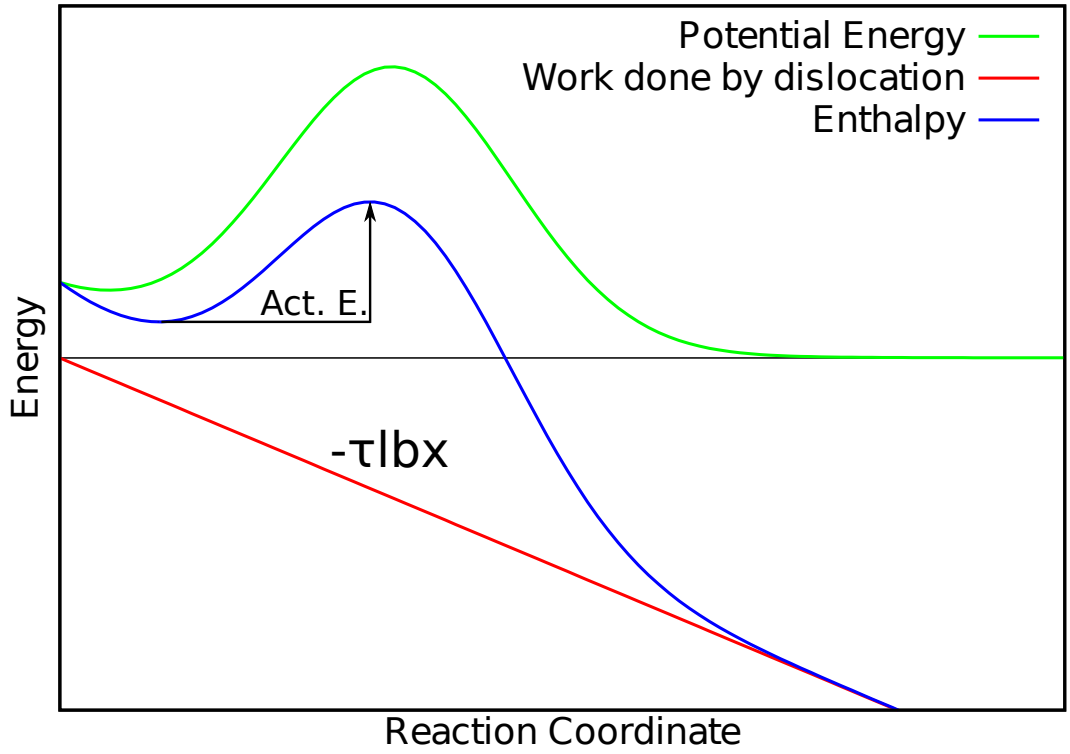

Figure 26: The free energy evolution as a function of distance for the configuration described by Gibbs.

Gibbs also discussed the concept of rigid and deformable energy profiles with regards to Figure 26, recognizing that for deformation occurring during thermal activation, there is no unique ΔG vs. x curve than can be written down, but an high dimensional hypersurface encompassing all possible bypass events. In the case that one can determine the minimum energy pathway (MEP) for a reaction, a similar one-dimensional ΔG vs. x diagram can be written down.

While the analysis of Gibbs cannot be applied to calculate physically realistic activation energies for thermally activated dislocation glide because of its assumption of a rigid dislocation segment pinned by a specific geometry, the insight gained is

valuable with regards to better understanding thermally driven dislocation processes. First, the notion that the entire crystal must be the subject of the energetic analysis is key. Second, the work done by the dislocation gliding under the influence of an externally applied stress strongly influences the activation energy barrier for bypass. Finally, the activation volume for a dislocation processes is not a volume of visually identifiable atoms, but a thermodynamic measure of the stress sensitivity of the Gibbs free energy.

2.6.2.2 Attempt Frequency

The Arrhenius equation was generalized to many-body processes in the work of Vineyard [234] in order to extend it to solid state processes. By considering the ratio of configurational partition functions for the normal and activated states for an M-dimensional system and assuming each degree of freedom can be approximated a harmonic oscillator, the rate of phase points crossing the saddle point can be written as

$$k = \nu_a e^{-\Delta G/k_B T} = \nu_1 e^{\Delta S/k_B} e^{-\Delta H/k_B T} \tag{57}$$

where

$$\nu_a = \nu_1 \prod_{i=2}^{M} (\nu_i/\nu_i'), \tag{63}$$

ν_1 is the fundamental attempt frequency, ν_i is the frequency of the i^{th} mode of the normal state, and ν_i' is the frequency of the i^{th} mode of the activated state. The factor $\prod_{i=2}^{M}(\nu_i/\nu_i')$ is called the entropic factor as it explicitly accounts for the entropy change during the process.

In the context of dislocation-obstacle bypass processes, Equation 63 can be applied if the normal modes of the dislocation configuration in the relaxed and activated configurations can be described, either in closed form or numerically. The first study,

and principle work to this day, was performed using a line-tension dislocation model such that closed form expressions are attainable. Granato *et. al.* [78] described a dislocation line using the following partial differential equation:

$$\mu y'' + \rho(x)F(y) + b\sigma = \mu\ddot{y}/c^2 \tag{64}$$

where y is the displacement of the dislocation at x, μ is the line tension, b is the Burgers vector magnitude, σ is the applied stress, $\rho(x)$ the pinning point density, the mass per unit length is assumed to be μ/c^2 and c is the speed of sound in an isotropic medium. At equilibrium but allowing for small perturbations, $z(x)$ must satisfy

$$y(x) = Y(x) + z(x)\cos(\omega t), \tag{65}$$

where $Y(x)$ is the mean equilibrium configuration, ω is an eigenfrequency of the system and $z(x)$ represents the small oscillations about the mean configuration. With this substitution and assumption of equilibrium, Equation 64 becomes an ordinary differential equation:

$$z'' + (\omega^2/c^2 - [\rho(x)/\mu]\, f)z = 0 \tag{66}$$

where $f = -(dF/dy_0)_{y_0=Y_0}$ and the fixed boundary conditions $z(-l,t) = z(l,t) = 0$. Granato *et. al.* [78] considered a point defect $\rho(x) = \delta(x)$ and continuously distributed ρ constant. Focussing on the case of a single point defect, the perturbation of the dislocation $z(x)$ is described by

$$z = A\sin\left((\omega/c)(l+x)\right) \text{for} - l < x < 0, \tag{67}$$

$$z = \pm A\sin\left((\omega/c)(l-x)\right) \text{for } 0 < x < l. \tag{68}$$

The two solutions are joined with the added conditions

$$\lim_{\epsilon \to 0} z(-\epsilon, t) = z(\epsilon, t) \tag{69}$$

$$\lim_{\epsilon \to 0} z'(-\epsilon, t) - z'(\epsilon, t) = z_0 f/\mu \tag{70}$$

For even modes $z(0) = 0$ and are therefore unaffected by the pinning point and with $\theta_i = \omega_i l/c$, the frequencies for even modes is given by $\theta_{2r} = r\pi$. For arbitrary f, the odd frequencies must obey the equation

$$\tan\theta = -(2\mu/fl)\theta, \tag{71}$$

which provides the values for θ_{2r-1}. Assuming that for the pinned state $f = \gamma$ and $f = \gamma' = -s\gamma$ at the saddle point with $s, \gamma > 0$. Using these two expressions with Equation 63, one can provides estimates of attempt frequency for several strength bounds. For large f, $\tan\theta \ll 1$, θ_{2r-1} approaches θ'_{2r+1}, resulting in all θ' being cancelled in so that Equation 63 the attempt frequency is governed by $\theta_{N-1} \approx N\pi/2$ and ν_{eff} is on the order of the Debye frequency. A more complex analysis is required for the minimum value of γ resulting in a saddle point (detailed in [78]), with the final value for the attempt frequency being $\nu_{\text{eff}} = 3.2\nu_0$ with an associated entropic factor of 1.8. Their work remains at the forefront of dislocation vibration characterization, yet relies on line tension approximations in which dislocations are modelled as a line with an associated energy per unit length. Dislocations have complex elastic self-interactions which cannot be captured by a line tension model, and therefore further investigation is required to determine if line tension approximations are appropriate within the context of this phenomenon. In this chapter, the effect of approximations are explicitly investigated within the context of dislocation vibrations by comparing to calculations without such approximations.

2.7 Minimum Energy Pathway Finding Methods

The most direct access to the minimum energy pathway is by assuming a harmonic potential and calculating the Hessian matrix (matrix of second derivatives for each degree of freedom) [178] about the minimum in question. The system state is advanced in the direction of the minimum eigenvalue of the Hessian, which will trace the minimum energy pathway. However, the size of the Hessian is $N \times N$ where N is the number of degrees of freedom, which is three times the number of atoms in the case of an atomistic calculation. This brute force method is too computationally expensive to be of practical use, particularly with atomistic methods because the Hessian matrix becomes unmanageably large at even small simulation volumes. Consequently, several efficient saddle point energy calculation methods have been developed to enable activation energy calculations.

Two commonly used classes of MEP finding methods exist: those where the final state following the reaction is known, and those where it is not. The first class are well adapted to calculating the activation energy for a single targeted process, such as a chemical process, or a specific change in morphology in a material system (e.g. diffusion, clustering). These methods are often referred to as "chain-of-state" methods as they used a series of system duplicates (called images) to evolve a pathway linking the initial and final states to the minimum energy pathway. Numerous numerical techniques proposing different methods of evolving the images exist in the literature, including string methods [243, 171] and the nudged elastic band method [102]. String methods determine the MEP by assuming a pathway described by continuous interpolation functions such as cubic splines, creating a new series of images at each step in the convergence, evolving the image positions according to the force on the images normal to the interpolation function tangents, and then updating the interpolations to reflect the new positions. The nudged elastic band method differs by describing the pathway with a fixed number of images that are created at the start of

the simulation and maintained throughout the convergence to the MEP. The tangent to the pathway is calculated using a discrete difference method, and a spring force acts parallel to the image to keep the images sufficiently spaced along the pathway. Chain-of-states method have been used to calculate activation energies for processes such as dislocation mobility [174], dislocation cross slip [182], and screw dislocation kink-pairs [244]. In contrast, the second class of methods, in which the final state is unknown, can be used to find all possible reactions for a phenomenon. These include the activation relaxation technique [147] and the dimer method [88]. Each method starts with a small random perturbation from the initial equilibrium. The activation relaxation technique inverts the component of the force along the direction between the current position and the local minimum and drives the system according to this modified force. From the saddle point, the system is relaxed using the physical force. The dimer method creates a pair of system duplicates that are used to evaluate the curvature of the energy surface to drive the system to the saddle point. These methods such as helium migration near an edge dislocation [87] and possible transition states of point defects in α-iron [70]. Each class of methods has strengths and weaknesses, and must be selected according to the problem at hand. These MEP finding methods allow atomistic methods to calculate activation energies for reactions; however, the limited simulation volume, dependence on selected interatomic potential, and further challenges associated with atomistic simulation techniques motivate further development of these techniques, particularly with regards to continuum methods.

In this chapter, the implementation and numerical methods of the dimer and NEB methods are analyzed in greater detail for their applicability regarding their augmentation to a DDD code to calculate the minimum energy pathway for dislocation processes.

2.7.1 Dimer Method

The dimer method [88] is a numerical method used to find saddle points on energy surfaces without inverting the Hessian matrix. The method has been used in materials science for applications such as improving activation energy mapping of crack tip dislocation nucleation citeZhu2004 and investigating the structure of irradiation induced defects in MgO [222]. While developed with the goal of accelerating atomistic simulations, the dimer method formulation can be applied to discrete dislocation dynamics systems. First, classical dislocation dynamics is used to relax the dislocation to what will become the initial dimer position. Then, the dimer is created by splitting the relaxed configuration by a small distance ΔR (eg. 0.01a in atomistics) along a random direction $\hat{\mathbf{N}}$.

$$\mathbf{R_1} = \mathbf{R} + \Delta R\hat{\mathbf{N}} \tag{72}$$

$$\mathbf{R_2} = \mathbf{R} - \Delta R\hat{\mathbf{N}} \tag{73}$$

The vectors here are of size $3N$ where $3N$ is the number of degrees of freedom in the system (here, N dislocation nodes result in $3N$ degrees of freedom). Using a finite difference formula for the curvature of the potential surface C,

$$C = \frac{(\mathbf{F_1} + \mathbf{F_2}) \cdot \hat{\mathbf{N}}}{2\Delta R} \tag{74}$$

and the energy at the midpoint of the dimer can be written as

$$E_0 = \frac{E}{2} + \frac{\Delta R}{4}(\mathbf{F_1} + \mathbf{F_2}) \cdot \hat{\mathbf{N}} \tag{75}$$

and the force on the dimer is simply the average of dimer image forces:

$$\mathbf{F}_R = (\mathbf{F}_1 + \mathbf{F}_2)/2 \tag{76}$$

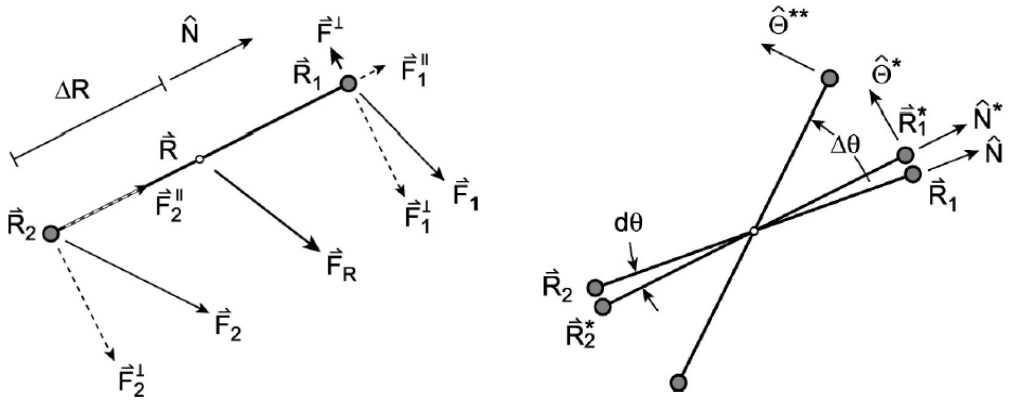

(a) (b)

Figure 27: Definitions for dimer rotation and translation variables. [88]

The dimer is rotated once after each displacement towards the minimum energy configuration, which is possible using a conjugate gradient method [88] incorporating a Newton method approximation. The dimer is rotated in the direction of the rotational force $\mathbf{F}^{\perp} = \mathbf{F}_1^{\perp} + \mathbf{F}_2^{\perp}$, where $\mathbf{F}_i^{\perp} = \mathbf{F}_i - (\mathbf{F}_i \cdot \hat{\mathbf{N}})\hat{\mathbf{N}}$. The unit vector in the direction of $\mathbf{F}^{\perp}$ is defined as $\boldsymbol{\Theta}$.

First, image 1 is rotate by some angle of rotation $d\theta$:

$$\mathbf{R}_1^* = \mathbf{R} + (\hat{\mathbf{N}}\cos\, d\theta + \hat{\boldsymbol{\Theta}}\sin\, d\theta)\Delta R \tag{77}$$

Next, the new $\mathbf{N}^*$ is calculated, and then the second image is repositioned at $\mathbf{R}_2^*$ using eqn. 73. Next, the forces $\mathbf{F}_1^*$, $\mathbf{F}_2^*$, and $\mathbf{F}^* = \mathbf{F}_1^* - \mathbf{F}_2^*$ are recalculated. The scalar rotation force is defined as $F = \mathbf{F}^{\perp} \cdot \hat{\boldsymbol{\Theta}}/\Delta R$, and the derivative of the scalar rotation force is defined as (using a finite difference method):

$$F' = \frac{dF}{d\theta} \approx \left| \frac{\mathbf{F}^* \cdot \hat{\boldsymbol{\Theta}}^* - \mathbf{F} \cdot \hat{\boldsymbol{\Theta}}}{d\theta} \right|_{\theta = d\theta/2} \tag{78}$$

The estimate of the rotation is obtained using a Taylor expansion of the potential surface to obtain the desired rotation angle:

$$\Delta\theta = -\frac{1}{2}\arctan\left(\frac{2F_0}{F_0'}\right). \tag{79}$$

With the new rotation, the updated image position

$$\mathbf{R}_1^{**} = \mathbf{R} + (\hat{\mathbf{N}}\cos\,\Delta\theta + \hat{\mathbf{\Theta}}\sin\,\Delta\theta)\Delta R \tag{80}$$

is used to find an updated position $\mathbf{R}_1^{**}$. dimer orientation $\hat{\mathbf{N}}^{**}$, and dimer rotation direction $\hat{\mathbf{\Theta}}^{**}$. Next, a conjugate gradient method is used to obtain a faster convergence:

$$\mathbf{G}_i^{\perp} = \mathbf{F}_i^{\perp} + \gamma_i \left|\mathbf{G}_{i-1}^{\perp}\right| \hat{\mathbf{\Theta}}_{i-1}^{**} \tag{81}$$

$$\gamma_i = \frac{(\mathbf{F}_i^{\perp} + \mathbf{F}_{i-1}^{\perp})}{\mathbf{F}_i^{\perp} \cdot \mathbf{F}_i^{\perp}} \tag{82}$$

The process is iterated until $\mathbf{G}_i^{\perp} = \mathbf{0}$.

The dimer translation is straightforward in comparison to the rotation. A modified force $\mathbf{F}^{\dagger} = \mathbf{F}_R - 2\mathbf{F}^{||}$. The position is updated according to the desired method such as Verlet integration, with a modification to leave convex regions rapidly:

$$\mathbf{F}^{\dagger} = \begin{cases} -\mathbf{F}^{||} & \text{if} \quad C > 0 \\ \mathbf{F}_R - 2\mathbf{F}^{||} & \text{if} \quad C < 0 \end{cases} \tag{83}$$

The dimer method was implemented and tested with the DDD code developed for this thesis. In performing basic simulations to examine the efficacy of the dimer method for dislocation based processes, it became apparent that while the method is an effective method for both determining the possible saddle points for a reaction as well as the activation energy for each associated transition, the method is ill-suited to the desired applications in this thesis.

Without some additional constraint, the dislocation line can deform in a kink as shown in Figure 28, thereby creating an energy barrier to a process which is effectively

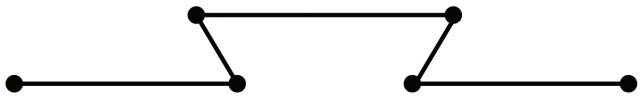

Figure 28: Using a random perturbation vector may lead to non-physical phenomena such as a dislocation forming a kink as shown here. The nodes that have deviated out of the dislocation line create an energy barrier, and the segments forming acute angles with the dislocation line will rotate to self-annihilate with the dislocation. A large number of such meaningless saddle points will be found, and therefore greater constraint is necessary to apply the dimer method to with this technique.

non-physical. It is possible that by picking a non-random perturbation vector $\hat{\mathbf{N}}$ one could target a certain reaction; however, another method to characterise energy methods was selected for this thesis as detailed in the following section.

2.7.2 Nudged Elastic Band Method

The nudged elastic band (NEB) method [102] is a generalized numerical method that seeks the minimum energy pathway following steepest descent between transition states [193].The NEB method used in this thesis closely follows the original method detailed in [102], and applying the formulation to a system described using the continuum theory of defects rather than an atomistic calculation simply requires changing the computation required for certain vectors. A typical NEB calculation begins with two known local minima between which the minimum energy pathway is desired. Such is the strength and the weakness of this method: whereas the dimer method can find all barriers to escape from a minimum energy state, the NEB method will only find the activation energy for a single, minimum pathway. Therefore the NEB is better suited to studies targeting a single process, whereas the dimer method provides a more global perspective of possible reactions.

An NEB calculation begins with the definition of a set of images, which are duplicates of the system. After convergence to the MEP, the images will represent the different steps through which the system passes as the reaction occurs. Images are

typically initialized as a linear interpolation between the initial and final state. Each image is described using a vector R_i that contains the degrees of freedom. The minimum energy pathway is found by evolving the entire system of images simultaneously according to a modified force. The tangent between these images is an imporant parameter in the evolution of the system, which will become clear in the formulation. Applying a straightforward centered difference scheme gives the following:

$$\boldsymbol{\tau}_i = \frac{\mathbf{R}_i - \mathbf{R}_{i-1}}{|\mathbf{R}_i - \mathbf{R}_{i-1}|} + \frac{\mathbf{R}_{i+1} - \mathbf{R}_i}{|\mathbf{R}_{i+1} - \mathbf{R}_i|} \tag{84}$$

This formulation is effective in some cases, but can lead to kinking in the path formed by the images when the force parallel to the path is large. Kinks result in an inaccurate characterization of the MEP, or possibly numerical instability during the convergence calculation. In the implementation used for this thesis, an improved tangent method based on the energy of the relative images is used as defined in [89]. The tangent modified in such a way to smooth the transition between images at minima and maxima. This tangent scheme is often referred to as the "upwind" scheme, because the tangent vector is taken from a lower energy image to a higher energy image. First, the simplest cases are treated is defined as:

$$\boldsymbol{\tau}_i^+ = \mathbf{R}_{i+1} - \mathbf{R}_i \tag{85}$$

$$\boldsymbol{\tau}_i^- = \mathbf{R}_i - \mathbf{R}_{i-1} \tag{86}$$

$$\boldsymbol{\tau}_i = \begin{cases} \boldsymbol{\tau}_i^+ & \text{if } \; V_{i+1} > V_i > V_{i-1} \\ \boldsymbol{\tau}_i^- & \text{if } \; V_{i+1} < V_i < V_{i-1} \end{cases} \tag{87}$$

Equations 85, 86, and 87 are used when image i is not an extrema. In the case that i is an extrema, the tangent is described using the following equations:

$$\boldsymbol{\tau}_i = \begin{cases} \boldsymbol{\tau}_i^+ \Delta V_i^{\max} + \boldsymbol{\tau}_i^- \Delta V_i^{\min} & \text{if } V_{i+1} > V_{i-1} \\ \boldsymbol{\tau}_i^+ \Delta V_i^{\min} + \boldsymbol{\tau}_i^- \Delta V_i^{\max} & \text{if } V_{i+1} < V_{i-1} \end{cases} \tag{88}$$

$$\Delta V_i^{\max} = \max\left(|V_{i+1} - V_i|, |V_i - V_{i-1}|\right) \tag{89}$$

$$\Delta V_i^{\min} = \min\left(|V_{i+1} - V_i|, |V_i - V_{i-1}|\right) \tag{90}$$

Using the improved tangent scheme with a DDD-NEB calculation showed good numerical stability with no observed kinking along the MEP.

The total force depends explicitly on the tangent between images, which for each image is written as [102]:

$$\mathbf{F}_i = \mathbf{F}_i^s|_{\parallel} + \mathbf{F}_i^R|_{\perp}. \tag{91}$$

where F_i is the force vector, $F_i^s|_{\parallel}$ is the component of the so-called "spring force" parellel to the tangent vector, and $F_i^R|_{\perp}$ is the component of the real force (as defined by the physical problem) that is normal to the tangent vector. The true force is written as

$$\mathbf{F}_i^R = -\nabla V(R_i) = \mathbf{F}_i^{PK}, \tag{92}$$

Equation 92 is exact; however, obtaining $\mathbf{F}_i^{PK}$ in analytically is only possible for specific dislocation configurations or by using the closed form non-singular solutions of Cai *et. al* [30]. The component normal to the tangent is extracted using a typical projection as follows:

$$\mathbf{F}_i^R|_{\perp} = \mathbf{F}^{PK}(\mathbf{R}_i) - \mathbf{F}^{PK}(R_i) \cdot \hat{\boldsymbol{\tau}}_i \tag{93}$$

where $\hat{\tau}_i$ is the unit tangent to the energy surface. Along with the improved tangent, the authors in [89] also introduced the following formulation for the spring force:

$$\mathbf{F}_i^s|_{\|} = k\left[|\mathbf{R}_{i+1} - \mathbf{R}_i| - |\mathbf{R}_i - \mathbf{R}_{i-1}|\right]\hat{\boldsymbol{\tau}}_i. \tag{94}$$

From Equation 94, one can see that the spring force acts to keep the mean of the image separation vectors equal along the MEP tangent. With the forces fully defined, the system of iamges can be evolved to the MEP using a Verlet integration method, i.e.,

$$\mathbf{R}_i^{t+\Delta t} = 2\mathbf{R}_i^t - \mathbf{R}_i^{t-\Delta t} + \mathbf{F}(\mathbf{R}_i^t)\Delta t^2, \tag{95}$$

The system does not evolve in time but rather is a convergence to the minimum energy pathway, and thus the time-step parameter Δt is set to the largest value to perform the relaxation in the minimum number of steps while retaining numerical stability. The convergence can be accelerated by using a Velocity Verlet integration [102]:

$$\mathbf{R}_i^{t+\Delta t} = \mathbf{R}_i^t + \mathbf{V}_i^t\Delta t + 1/2\, F(\mathbf{R}_i^t)\Delta t^2 \tag{96}$$

$$\mathbf{V}_i^{t+\Delta t} = \begin{cases} (\mathbf{V}_i^t \cdot \mathbf{F}(\mathbf{R}_i^t))\,\mathbf{F}(\mathbf{R}_i^t) & \text{if } V_i^t \cdot F(\mathbf{R}_i^t) > 0 \\ 0 & \text{otherwise} \end{cases} \tag{97}$$

The velocity component in Equation 97 increases the rate of convergence by increasing the velocity until the dot product of the velocity and force is negative, or in physical terms, when the force is driving the system in a direction opposite to its motion.

Figure 29 provides a visual representation of an NEB calculation in a simple case using a 2D potential. The images are first initalized as a straight connecting the first and the last states, which are fixed. The force on each node is calculated according to Equations 92,93 and 94 and the image configurations are advanced according the Verlet method in Equations 96 and 97. This process is repeated until convergence is achieved, which can be defined using a variety of conditions. One often-used criteria

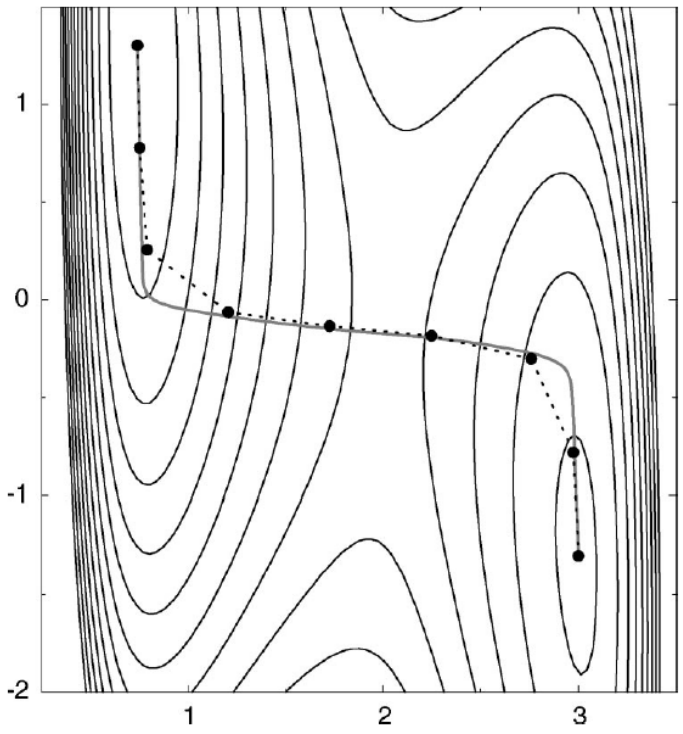

Figure 29: The MEP for a 2D potential as found using the nudged elastic band method (dashed line) and analytically (solid grey). Each image is denoted with a solid black circle. [89]

for atomistic simulations is a force threshold [89]: the simulations is deemed to have converged when the normal component of the real force is below a defined value.

The NEB method is formulated in a general way such that if one can defined a degree of freedom vector R for the system and calculate the physical force F^R, then the method can be applied. Using the NEB method also requires some knowledge of the initial and final states of the system to calculate the activation energy for a specific barrier. These requirements are naturally fulfilled by discrete dislocation dynamics simulations, in particular for the processes examined in this thesis. The system is already discretized into dislocation nodes, so the degree of freedom vector R can be readily generated as a $3N$ length vector, where N is the number of dislocation nodes in the system. The physical force is known in closed form as the Peach-Koehler force (Equation 7) using a non-singular formulation, unlike in atomistic simulations

where Equation 92 must be applied in a discretized form. These two simple properties result in dramatically faster simulations, and the capability to simulate volumes far beyond the reach of atomistic simulations. The NEB calculations in this thesis are performed uniquely to calculate the bypass energies for a dislocation bypassing a sessile, undeformable self-interstital atom loop and the following details are elaborated in the context of this particular process.

The procedure to calculate an activation energy using the DDD-NEB method begins with a traditional DDD simulation. With the desired applied stress and interaction geometry initialized, the DDD simulation runs until equilibrium is established using a criteria on the velocity of all dislocation nodes. If a certain amount of plastic strain is accumulated, the value of which is chosen such that the glide dislocation has necessarily bypassed all obstacles, the simulation is terminated and a zero activation energy is recorded. If the simulation reaches equilibrium, this configuration serves as the first image in the NEB calculation. The final image is an assumed state: once the glide dislocation has bypassed all obstacles and is beyond range of elastic interactions with any dislocation segments except for those of the glide dislocation, the glide dislocation is assumed to return to a straight dislocation because of self-interaction acting to minimize the energy of the system. The intermediary images are generated using linear interpolation.

Figures 30 and 31 depict the evolution of image positions during an NEB relaxation, and the energy profiles corresponding to each of these steps.

The physical force and spring force are calculated according to Equations 92, 93 and 94 using the Peach-Koehler force as the real force. For the spring force, values of k ranging over several orders of magnitude were tested and the activation energy values were seen to be independent of k as shown in the energy profiles in Figure 32. If the tangent calculation is exact, the NEB calculation is independent spring force; however, the tangent is calculated using a discrete difference approach and therefore

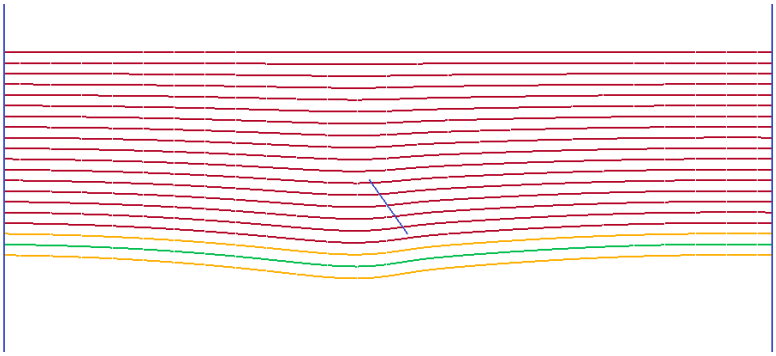

(a) Step 1. The first three images are used to depict the tangent calculation. The tangent at the green image relies only on the neighbouring orange images.

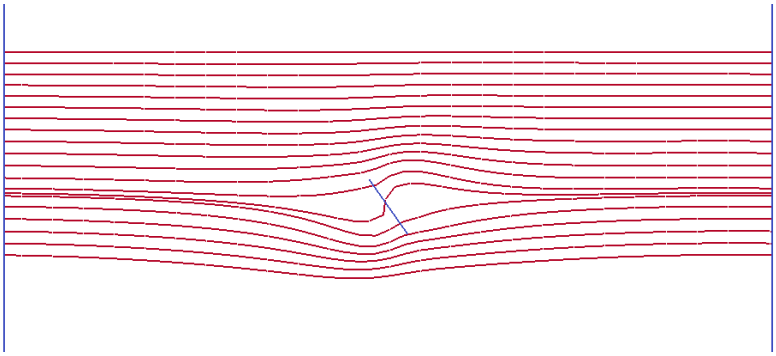

(b) Step 2.

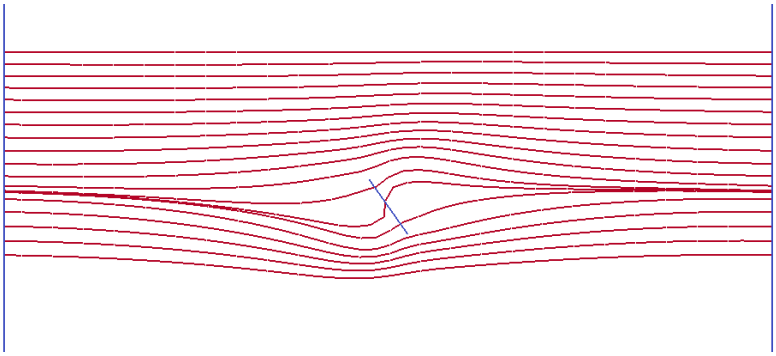

(c) Step 3.

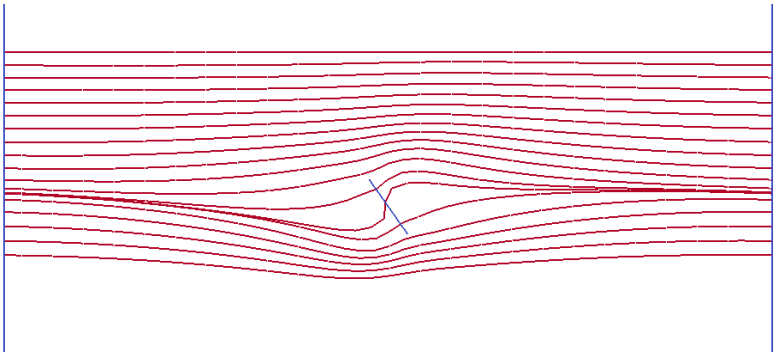

(d) Step 4.

Figure 30: NEB configuration at varying stages of relaxation.

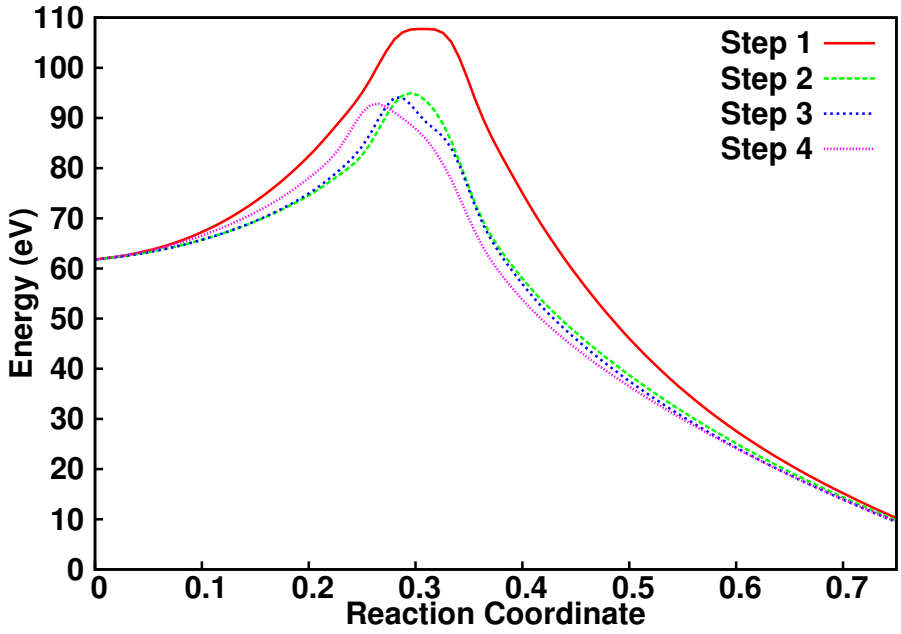

Figure 31: The activation energy profile converges towards the minimum energy pathway for a $1/2\,[111]\,(1\bar{1}0)$ glide dislocation bypassing a [001] self-interstitial atom loop under an applied shear stress on the glide plane of 10 MPa. The profiles correspond to the plots in Figure 30.

independence of this factor must be explicitly verified.

A large number of images are used with this method compared to atomistic simulations. Whereas atomistic simulations often use 5-20 images [90], the NEB calculations performed for this thesis used 40-200 images, depending on the number of defects present. Such a large number of images enables a high resolution characterization of the energy landscape. The large number of images allows one to obtain a smooth activation energy map without curve fitting or cubic interpolation, and with the low computational requirements, there are no associated drawbacks to having a large number of images.

In contrast to intrinsically discretized atomistic NEB simulations, the discretization of continuous dislocation lines must be specified. A range of discretization lengths were tested to ensure convergence, detailed in Chapter 4. As described previously,

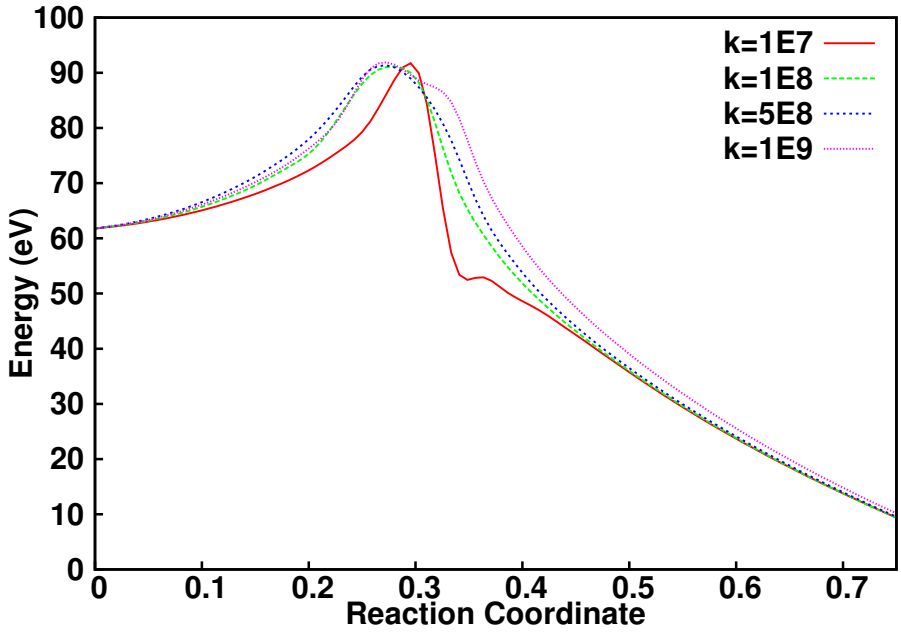

Figure 32: The activation energy is observed to be independent of spring constant. A weaker spring combined with small errors in the tangent result in the images shifting near the loop, causing a different profile as a function of reaction coordinate. However, accuracy is maintained in every case.

the dislocation line is re-discretized at every step during a typical dislocation dynamics simulation and dislocation nodes are moved, added, or removed as a function of spacing along the dislocation line to maintain numerical stability and a physically realistic configuration. However, in an NEB calculation involving discretized dislocations, maintaining the number of degrees of freedom constant and equal across all images is highly desirable to avoid interpolations between degrees of freedom of different images. Further, the tangent equation depends directly on the position of the nodes in the neighbouring images and consequently the nodes cannot be moved significantly. Figure 33 shows an example case where a remeshing method is essential.

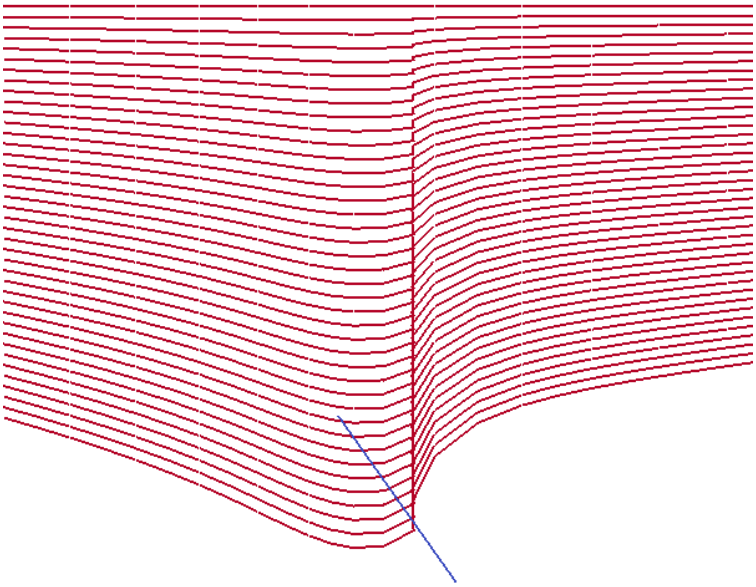

(a) Initial NEB image configuration created from relaxed DDD configuration and assumed final state of a straight dislocation line beyond the SIA loop.

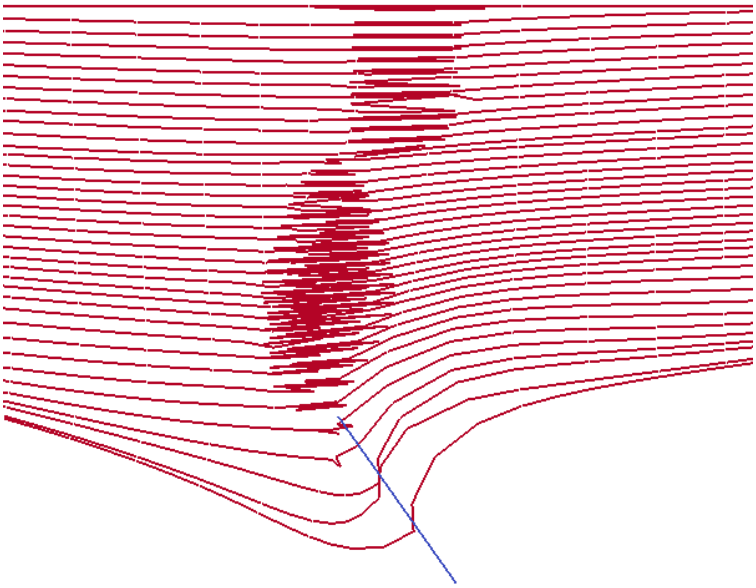

(b) Without remeshing, numerical artifacts are observed because of insufficient distance between nodes. The line becomes kinked and diverges from the MEP.

Figure 33

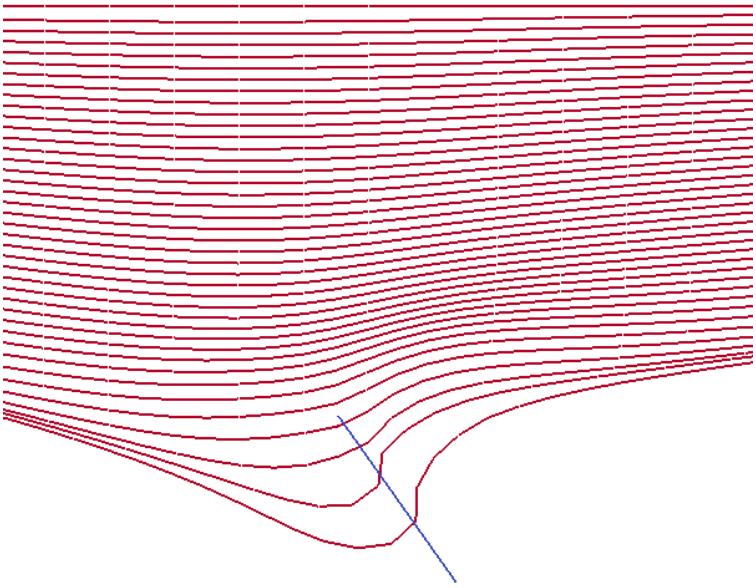

(c) With a cubic remeshing method, the dislocation line keeps a more realistic shape and numerical artifacts are not observed. This figure is of the same simulation time-step as Figure 33b.

Figure 33: A cubic interpolation re-discretization method maintains tangent continuity and ensures a good description of the dislocation line. These images are extracts from a large periodic simulation volume, and the boundaries are not shown.

Within these limitations, a re-meshing method was developed that maintains numerical stability as shown in Figure 33c. The dislocation line was recreated using a cubic spline interpolation through all dislocation points, and the dislocation nodes were repositioned along this line relative to a point fixed on the simulation boundary volume to maintain constant spacing. No points were added or removed. As a result, the point positions did not vary significantly between steps and therefore the re-meshing did not perturb the tangent calculation, while preventing the introduction of numerical artifacts such as kinking into the dislocation line shape.

In practice, the NEB method can be coupled to an existing dislocation dynamics implementation without an onerous numerical implementation. The DDD code naturally calculates the true force in Equation 91. Once the starting and ending

configurations are chosen, the images are created by making complete duplicates of the initial configuration and repositioning the glide dislocation to an interpolated position. Each image is evolved similarly to a dislocation dynamics simulation, except that the dislocation force is the NEB force in Equation 91. The vector R_i in Equations (91-94) is simply a $3N$ length vector containing the coordinates of each moving dislocation node. The numerical procedure to converge to the MEP is nearly identical to simulating the time evolution of several DDD simulations simultaneously - each image influences its neighbours via the tangent and spring force, but otherwise evolves independently. Consequently, the method can be readily parallelised with little communication overhead.

2.8 Summary

The numerical foundations upon which the studies in this thesis are performed rely on the description of dislocations within the framework of the continuum theory of defects. For an isotropic, infinite material, a non-singular solution exists [30] which greatly accelerates calculation times and also improves physical fidelity. With the theory underpinning the elastic fields, interactions and motion of dislocations established, a significant numerical framework is required to ensure realistic discretization and boundary conditions with a strong focus on computational efficiency. A brief study of dislocation motion in a Cu/Nb laminate material highlights the need to consider both geometric constrains to dislocation motion as well as the local interactions when predicting mechanical properties. In such confined geometries, the discretization is particularly important and a carefully chosen adaptative re-discretization technique is necessary to maintain physical fidelity. Atomistics-informed behaviour for dislocations intersecting SIA loops and voids is implented to enable athermal irradiation hardening calculations in α-iron. Moving beyond the athermal regime requires a more complex analysis including the calculation of activation energies. The dimer

and nudged elastic band methods are considered, and the nudged elastic band method is selected to perform activation energy calculations for dislocation-SIA loop bypass processes.

CHAPTER III

ATHERMAL IRRADIATION HARDENING

Constitutive models for irradiation hardening in metals such as dispersed barrier hardening [191], Friedel Kroupa Hirsch [107], and Bacon Kocks Scattergood [13] models have been proposed and applied in experimental studies, but the limits of their applicability has never been investigated for varying defect types, sizes, and densities. In this chapter, dislocation dynamics calculations of irradiation induced obstacle hardening in the athermal case are compared to these models for voids, self-interstitial atom (SIA) loops, and a combination of the two types. The Bacon Kocks Scattergood model is found to accurately predict hardening due to voids, whereas the Friedel Kroupa Hirsch is superior for SIA loops. For both loops and voids, the hardening from a normal distribution of defects is compared to that from the mean size, and is shown to have no statistically significant dependence on the distribution. A mean size approach is also shown to be valid for an asymmetric distribution of voids. A nonlinear superposition principle is shown to predict the hardening from the simultaneous presence of voids and self-interstitial atom loops.

3.1 Introduction

Predicting the mechanical behaviour of an irradiated material in the athermal regime is a key component in nuclear reactor pressure vessel lifetime estimation. Thermally activated events can be characterized by a mean waiting time (inverse of reaction rate) and therefore require a finite amount of time to occur for a specific set of loading conditions. Under shock loading, such as an external impact or internal spike in pressure, the material behaviour of nuclear pressure vessel will be strictly athermal as the loading occurs too quickly to allow for thermally processes to play a role. The

nature of the reaction between dislocations and irradiation induced cascade damage strongly influences the mechanical response of the material, because lattice defects act as obstacles to dislocation motion. The atomic scale interaction between a dislocation core and an irradiation induced defect strongly influences dislocation motion, as the strength of this interaction, along with longer range elastic interactions, will have a significant impact on the yield strength of the material. However, this interaction is also highly complex and must be investigated using molecular statics and dynamics simulations.

As the steel reactor pressure vessel is typically of the highest concern regarding irradiation hardening, the majority of atomic scale studies focus on interactions between dislocations and irradiation induced defects in α-iron [128, 156, 11, 122, 217, 212, 85, 163, 218]. From an experimental perspective, SIA loops have been observed with a large range of diameters from the TEM resolution threshold ($\approx$ 2 nm) to 25nm or larger at densities on the order of 10^{22} m^{-3} [91], whereas voids typically exist with diameters of 0.5-10 nm at densities of 10^{24} m^{-3} ([59, 259, 91]). These values were observed for fast neutron irradiated α-iron, and are strongly dependent on irradiation dose and dose rate. The interactions between pure edge and pure screw dislocations with SIA loops of character $\langle 100 \rangle$ and $1/2\langle 111 \rangle$ with different relative orientations between the glide dislocation and SIA loops ([128, 156, 11, 122, 217, 212]), and with voids ([85, 163, 218]) have been investigated to some degree. Atomistic calculations show that the obstacle strength of SIA loops is highly dependent on the relative orientations during the interaction, and have found the strength of voids over a range of sizes. However, further investigations are required to fully understand dislocation-irradiation defect interactions. In particular, dislocation interactions with very small (<1 nm) defects need much greater attention. Defect composed of a few vacanies or interstitial atoms cannot be assumed to behave according to continuum approximations, i.e. as a spherical void or self-interstitial atom loop. Given that a high density

(10^{24} m^{-3}) of voids are observed at irradiation levels seen by fission power reactors, very small defects may govern dislocation motion in a material. Conversely, if small defects can simply be absorbed by an edge dislocation (causing dislocation climb), these defects may play no role whatsoever. Only atomistics simulations are able to capture such behaviour, and provide valuable insight that can be coarse-grained to higher scale simulations and models, such as DDD.

Characterizing dislocation-irradiation defect interactions is the first step towards predicting the mechanical response of an irradiated material. Before this information can be used, a scale transition to a macroscopic constitutive equation is necessary to account for the effect of an ensemble of defects in a bulk material, which can be performed using discrete dislocation dynamics simulations. Computational line tension simulations have been used extensively to investigate obstacle hardening under several regimes [64, 108, 54, 228, 46]. Line tension simulations treat a dislocation as a line defect with an associated energy per unit length corresponding to its strain energy; however, the elastic interactions between different parts of the dislocation line and the differences between edge and screw dislocations are omitted. In simulations considering obstacles, dislocation breakaway occurs when the included angle ϕ between bowing dislocation arms descends past a specified threshold angle ϕ_c. While simpler in implementation and lower in computational requirements than dislocation dynamics simulations, line tension simulations are highly simplified by omitting effects such as thermal activation, dislocation self-interaction, and variable line tension as well as the consideration of defects as having infinitesimal size. Despite their simplicity, line tension simulations can serve as a starting point from which basic trends can be extracted before continuing to more representative simulations. Foreman [64] calculated single dislocation hardening due to a square lattice and random spatial distribution of a single defect type (strength), and showed that for weak point defects

($\phi_c > 140°$), the yield strength can be predicted exactly using Friedel's approximations for obstacle spacing on a dislocation. Modern studies have provided insight into more complex and realistic cases using line tension simulations. Kulkarni [108] investigated precipitate hardening using a distribution of particle sizes and a breakaway angle dependent on particle size. Hardening due to the particles with a size distribution was compared to the hardening resulting from all particles having the distribution mean size, and showed that for the chosen size distribution a mean radius approach systematically overestimates the change in yield strength. The yield point difference between the mean radius and full distribution approaches decreases with increasing particle size (increasing obstacle strength) which was attributable to asymmetry in the size distribution. Dong [54] simulated dislocation-obstacle interaction with two obstacle types present simultaneously: a square lattice of strong obstacles, and a random distribution of weak obstacles. For varying strong obstacle strengths, the authors compared the calculated hardening to an commonly used superposition principle [111]:

$$\tau_T^n = \tau_1^n + \tau_2^n \tag{98}$$

where τ_T^n is the increase in yield strength due to obstacles 1 and 2, τ_1^n the hardening due to obstacles of type 1, τ_2^n the hardening due to obstacles of type 2, and n is some constant and found that the coefficient varies continuously depending on the defect strengths and, in the case that both obstacles are weak, n=2 is seen to be exact. Vaucorbeil proposed a superposition principle for simulations containing three different obstacle types of different strengths [228], and also showed that clustering/spatial correlation of defects has a strong effect on hardening [46].

Dislocation dynamics simulations have also been used to a limited extent in the analysis of irradiation hardening. Scattergood and Bacon [188] studied the strengthening effect of void hardening by modelling voids using the solution for a dislocation

terminating on a free surface in a half-space. The authors found voids to act as strong dislocation obstacles approaching the limit of impenetrable obstacles. Huang et al. [95] studied Frank Read source activation in an atmosphere of out of plane SIA loops and showed that the stress to unlock the dislocation from the atmosphere decreases by up to a factor of two compared to earlier estimates due to rigid dislocation assumptions in the models. Highly fine-scale dislocation structure was investigated by Nogaret et. al. [155], who theorized that helical twists in glide dislocations are instrumental in the formation of clear bands. Arsenlis et al. [4] investigated localized deformation (channel clearing) in irradiated materials by simulating infinite screw dislocation motion in α-iron moving in an atmosphere of 25nm $1/2\langle 111\rangle$ SIA loops and found that channel size and initiation depends on loop coalescence initiated by the elastic fields of moving dislocations. The interaction between an ensemble of SIA loops of both glissile and sessile types in thin α-iron films have been studied using DDD with a spectral method representation of free surfaces in order to reproduce the mechanical loading and boundary conditions experienced by the material during in-site TEM experiments as well as elucidate the relative influence of different forces on SIA loop motion[62]. Particle induced hardening has also been the subject of extensive DDD investigation, which can potentially be used analogously with radiation induced defects with certain approximations. Mohles et. al. [141] simulated the glide of an infinite dislocation through a medium containing incoherent spherical particles and showed that a refined BKS model [151] including particle properties can accurately predict. These results were extended successfully predict hardening caused by shearable or coherent particles [140] as well as hardening caused by particle distributions over a range of spatial correlation [139]. More recently, three dimensional DDD simulation including multiple interacting dislocation and impenetrable particles were used to study the Bauschinger effect in dispersed-particle strengthened materials [180] and superposition models incorporating dislocation friction and dislocation

forest hardening [181].

Material properties at length scale relevant to irradiated materials in engineering applications can be predicted using higher scale methods such as constitutive modelling. Such models exist principally on two different scales: the dislocation scale, which will be the focus of the current chapter, and crystal plasticity. Crystal plasticity is a widely-accepted and highly used modelling methodology linking material response to dislocation motion using a relatively high number of internal state variables to describe the kinetics of dislocation glide [189, 210]. With these methods, one can model the evolution of the material state in a polycrystalline materials using techniques such as the finite element method. Dislocation dynamics simulations play a fundamental role in ensuring that these models accurately describe the physics governing dislocation motion and interactions. Latent hardening, the hardening observed on one slip system due to dislocation interaction with other slip systems, is described using a matrix of coefficients describing the strength of interactions between all glide systems for a specific crystal structure. These coefficients have been characterised using dislocation dynamics simulations of these specific interactions for the common lattice structures in metals (FCC, BCC, HCP) [124, 180, 22]. Crystals plasticity models have been further extended to include irradiation damage [167, 18, 118, 248]. Analogously to latent hardening between dislocations, dislocation-defect interactions can be incorporated using a model describing this specific interaction. However, this local interaction model must first be validated and the hardening coefficients determined. This finer scale model is the focus of this chapter, which begins with a derivation of the most commonly used dislocation-defect hardening models.

3.1.1 Hardening Models

Given that all classical models for irradiation hardening rely on a line tension model of dislocations, a brief introduction is detailed here. The basis of a line tension model

is that a dislocation has an associated energy per unit length that can be derived as follows. For a screw dislocation, the displacement field is defined as $u_z = \frac{b\theta}{2\pi}$ where b is the magnitude of the Burgers vector. Assuming small strain, elastic isotropy, and using cylindrical coordinates, the elastic strain tensor is zero everywhere except

$$\varepsilon_{\theta z} = \varepsilon_{z\theta} = \frac{1}{2r}\frac{d}{d\theta}(u_z) = \frac{b}{4\pi r}. \tag{99}$$

Applying Hooke's law in shear, the stress field is obtained:

$$\sigma_{\theta z} = \sigma_{z\theta} = \frac{\mu b}{2\pi r} \tag{100}$$

Line tension Γ is taken as the associated elastic energy per unit length, defined as

$$\Gamma = \int_{r_c}^{R} U^{el} d\Omega = \int_{r_c}^{R} \sigma_{ij}\varepsilon_{ij} d\Omega \tag{101}$$

Substituting in ε_{ij} and σ_{ij} as found in equations 99 and 100, line tension can be written as

$$\Gamma = \int_{r_c}^{R} \frac{\mu b}{8\pi^2 r^2} d\Omega = \int_{r_c}^{R} \frac{\mu b}{8\pi^2 r^2} 2\pi r dr = \frac{\mu b^2}{4\pi} ln\left(\frac{R}{r_c}\right) \tag{102}$$

where R is the size of the crystal, and r_c is the core radius. Typically r_c is taken as one Burgers vector length, and R is somewhat arbitrary. Given this arbitrary nature, the line tension can be written as

$$\Gamma = \alpha \mu b^2 \tag{103}$$

No core energy is included explicitly in this formulation, and is thus taken into account through the parameter α. Taking $\alpha = 1$ and equating line tension to applied force, one recovers the classical expression for dislocation source activation:

$$\tau = \frac{\mu b}{L} \tag{104}$$

Importantly, the dislocation does not interact with itself, that is to say the stress field associated with the dislocation does not influence the dislocation itself.

The first proposed model of irradiation hardening was proposed by Seeger. If N obstacles with equal radius R are distributed uniformly in space, then the areal density of obstacles can be written as Nd, and the mean distance between them as $1/\sqrt{Nd}$. If line tension is assumed to be $\Gamma = \mu b^2$, balance of forces between Peach-Kohler force and line tension (assuming a parameter α) can be written as:

$$\tau = \alpha \mu b \sqrt{Nd} \tag{105}$$

This model assumes that every defect intersecting the glide plane interacts with the glide dislocation with the same strength, which defies physical intuition. One would naturally assume that the defect size or interaction geometry must be a factor influencing the strength of the dislocation-defect interaction, which is discussed in greater detail in the coming sections.

The first numerical dislocation dynamics study on irradiation hardening was undertaken by Foreman and Makin (1966) [64]. Using a line tension model with $\Gamma = \mu b/2$, the authors calculated the flow stress for a single dislocation. From a basic sum of forces in the direction of dislocation propagation while pinned to a defect,

$$F = 2\Gamma cos\left(\frac{\phi}{2}\right) \tag{106}$$

Combining this the Peach-Kohler force over the dislocation segment between obstacles, the stress to propagate a dislocation past a uniformly spaced array can be written as

$$\tau = \frac{\mu b}{L} cos(\phi/2) \tag{107}$$

The equilibrium radius of curvature in this case is given as

$$R = \frac{\Gamma}{\tau b} \tag{108}$$

To compare to theoretical predictions of hardening, the authors substituted an expression from Friedel (1963) [68] for the mean spacing of defects on a dislocation. The derivation for this mean spacing expression is as follows.

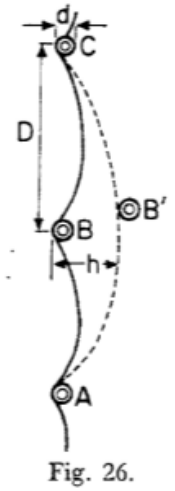

Fig. 26.

Figure 34: Dislocation bowing between non-attracting obstacles. [68]

First, three approximate quantities must be derived using Figure 34. First, Friedel states that each time a dislocation overcomes an obstacle, it sweeps out an area AB′CB $\approx l^2$. This can related to the quanities D and h by

$$Dh \approx l^2 \tag{109}$$

Next, the approximation

$$D^2 \approx 2\rho h \tag{110}$$

which can be shown by expressing each of these quantities in terms of its geometric formula approximating each segment as an arc of a circle:

$$D = 2\rho sin(\theta/2) \tag{111}$$

$$h = 2\rho'(1 - cos(\theta/2)) \tag{112}$$

where ρ is the radius of AB or CD, and ρ' is the radius of AB′C, and it can be shown that $\rho' = 2\rho$. Rewriting equation (110) using (111) and (112):

$$4\rho^2 sin^2(\theta/2) = 4\rho^2(1 - cos(\theta/2)) \tag{113}$$

$$sin^2(\theta/2) = (1 - cos(\theta/2)) \tag{114}$$

Taylor expanding both sides:

$$1-\frac{1}{4}(x-\pi)^2+\frac{1}{48}(x-\pi)^4+O((x-\pi)^6) = 1+\frac{1}{2}x-\pi-\frac{1}{48}(x-\pi)^3+O((x-\pi)^5) \tag{115}$$

Clearly, the approximation is only accurate in the constant term, which is rather poor. Combining equations (108), (109) and (110):

$$\frac{l^2}{h} \approx \sqrt{2\rho h} \tag{116}$$

$$D \approx \frac{l^2}{h} \approx \sqrt{\frac{2\Gamma h}{\tau b}} \approx \sqrt{\frac{2\Gamma \frac{l^2}{D}}{\tau b}} \tag{117}$$

$$D \approx \left(\frac{2\Gamma l^2}{\tau b}\right)^{\frac{1}{3}} \tag{118}$$

For a square lattice, the mean spacing between nearest neighbor defects is $L^2 = 1/N$ where N is the number density of defects. Substituting in equation (101):

$$D \approx \left(\frac{\mu b}{\tau N}\right)^{\frac{1}{3}} \tag{119}$$

Finally, this expression can be substituted into 106 as L to obtain the Friedel estimate of critical shear stress for a square array of defects:

$$\tau = \frac{\mu b}{\left(\frac{\mu b L^2}{\tau}\right)^{\frac{1}{3}}} cos(\phi/2) \tag{120}$$

$$\tau = \frac{\mu b}{L} cos(\phi/2)^{\frac{3}{2}} \tag{121}$$

In the work of Kroupa and Hirsch [107], the authors studied the elastic interactions between a straight edge dislocation migrating past a circular prismatic dislocation loop in an FCC material. The authors calculated the interaction energy between loops on $\{111\}$ planes with $\frac{1}{2}[110]$ Burgers vectors and pure screw dislocations with $\frac{1}{2}[110]$ Burgers vectors moving on $\{111\}$ planes. Considering 14 different relative orientations and averaging over all relative positions in which the maximum possible interaction occurs, the maximum interaction energy $E_{\max}$ and the maximum interaction force $P_{\max}$ were found as

$$E_{\max} \approx \frac{\mu b^0 b^1 R}{4} \tag{122}$$

$$P_{\max} \approx \frac{\mu b^0 b^1}{4} \tag{123}$$

where b^0 and b^1 are the Burgers vectors of the loop and glide dislocation, respectively. Given the $1/r^2$ nature of the force outside the loop and the constant nature inside, the authors only consider the contributions from loops with a center within R of the glide plane. The average force from these loops is approximated as $\frac{1}{2}P_{max}$. The separation distance of loops on the dislocation is given using the work of Friedel [68] and Mott [145]. First, Mott derived the average spacial coordinates of a dislocation locked at impurity atoms.

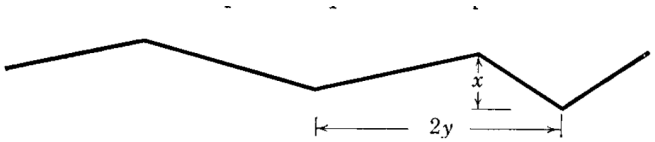

Figure 35: Dislocation locked at impurity atoms. [145]

First, a locking potential due to impurity atoms of V_0 and a uniform distribution was assumed. If $N\frac{atoms}{m^3}$ are distributed, and there are $Na\frac{atoms}{m^2}$ per unit area, then number of impurities in a region $< x$ is thus $Nax\frac{atoms}{m}$. The mean separation of these atoms is therefore $y = 1/Nax\frac{m}{atom}$. The resulting energy per unit is then $-V_0/y$, or $-V_0Nax$. The increase in line length compared to a straight line can be written as (assuming straight segments):

$$\Delta L = 2(\sqrt{x^2 + y^2} - y) \tag{124}$$

and the relative change in energy per unit length can be written as

$$\Delta\frac{2\Gamma}{y}(\sqrt{x^2 + y^2} - y) \approx \frac{\Gamma x^2}{y^2}, \tag{125}$$

where the approximation is obtained by Taylor expansion in x of order $O(x^4)$. Substituting the expression for $y = 1/Nax$, the change in energy can be written as

$$\frac{\Gamma x^2}{y^2} = \Gamma N^2 a^2 x^4. \tag{126}$$

To find the configuration of energy, the total change in energy (combining the decrease due to solute atoms and the increase due to line tension) to be minimized is given by

$$\Delta E = Na(-V_0 x + Na\Gamma x^4), \tag{127}$$

which results in a minimum at

$$x = \left(\frac{V_0}{4\Gamma Na}\right)^{\frac{1}{3}}, \frac{1}{y} = Na\left(\frac{V_0}{4\Gamma Na}\right)^{\frac{1}{3}} \tag{128}$$

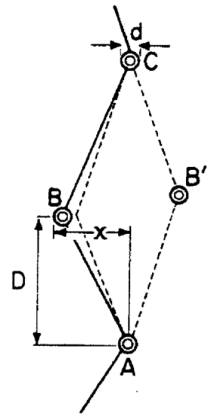

Figure 36: Dislocation pinned at attractive obstacles. [68]

Friedel then took Mott's final result in equation (128), and applied it to the configuration in Figure (36). Here, Friedel approximates l, the distance between obstacles on the line, as

$$Dx \approx l^2 \tag{129}$$

which differs from the true expression by a factor of two. Solving for D and substituting in $Na = 1/l^2$ in Mott's expression for x, one obtains:

$$D \approx \frac{l^2}{x} = \left(\frac{4\Gamma l^4}{\Delta U}\right)^{\frac{1}{3}}. \tag{130}$$

Friedel's equation (39) in [68] differs by a factor of $2^{1/3}$:

$$D \approx \frac{l^2}{x} \approx \left(\frac{2\Gamma l^4}{\Delta U}\right)^{\frac{1}{3}}. \tag{131}$$

However, Kroupa-Hirsch apply the Mott version (eqn. 130) and thus this factor of $2^{1/3}$ error is not present. With equation (133), we can return to the derivation of the Kroupa-Hirsch irradiation hardening equation. Substituting the energy as $E_{avg} = E_{max}/2$ from equation 122 and $\Gamma = \mu b^2/2$, the mean distance between obstacles on the dislocation line can be rewritten as

$$D \approx l\left(\frac{4\Gamma l}{\Delta U}\right)^{\frac{1}{3}} = l\left(\frac{4l}{R}\right)^{\frac{1}{3}} \tag{132}$$

The average distance between loops in the plate region under consideration can be written as $1/\sqrt{2Rn}$.

$$D \approx l\left(\frac{4l}{R}\right)^{\frac{1}{3}} = \frac{1}{\sqrt{2Rn}}\left(\frac{4\frac{1}{\sqrt{2Rn}}}{R}\right)^{\frac{1}{3}} = \frac{1}{Rn^{\frac{2}{3}}} \tag{133}$$

The force to propagate a dislocation must overcome the force of these loops. The average force from loops is assumed to be $\frac{1}{2}P_{max}$ where P_{max} is given in equation (123), and the Peach-Kohler force must overcome this force, resulting in the following criteria:

$$\Delta\tau = \frac{\mu b^0 R n^{\frac{2}{3}}}{8} \tag{134}$$

The Bacon Kocks Scattergood (BKS) model [13] (eqn. 135) advances dislocation-obstacle hardening models considerably by foregoing a line tension approximation and directly including dislocation self-interaction as well as explicitly including the finite size of defects in its formulation. The authors directly calculated, in closed form, the stress required to propagate a dislocation past a collinear infinite array of impenetrable spherical obstacles. Using the insight gained from this model, the authors incorporated the essential features into a line tension model for a random spatial distribution of obstacles, which is presented in equation 135. For a dislocation with a Burgers vector magnitude b, obstacle strength α, number density N, obstacle spacing $L = 1/\sqrt{ND}$ and effective obstacle diameter $D' = \frac{DL}{D+L}$, the BKS model predicts the change in yield stress as

$$\tau^{\mathrm{c}}_{\mathrm{BKS}} = \frac{\mu b}{2\pi L}\left[\ln\left(\frac{L}{b}\right)\right]^{-\frac{1}{2}}\left[\ln\left(\frac{D'}{b}\right) + 0.7\right]^{\frac{3}{2}}. \tag{135}$$

The classical value of Orowan bowing is $\propto \mu b/L$ (where L is the mean spacing between

obstacles), which is the foundation of equation 135 with the addition of several factors. A factor of $\frac{\ln(L/b)}{2\pi}$ accounts for interactions over one bowing loop, and a factor of $\left(\frac{\ln(D'/b)}{\ln(L/b)}\right)^{3/2}$ accounts for mutual loop interactions and the randomness of the obstacle array [13].

Each of these models aiming to predict hardening in metals due to irradiation make significant assumptions regarding the type, distribution or interaction behaviour of defects. The Seeger model assumes a single type and size of uniformly distributed obstacles with an associated parameter α, representing its strength relative to an impenetrable obstacle. The Kroupa-Hirsch model attempts a much high level of complexity by considering the elastic interaction between dislocation loops and a glide dislocation. In doing so, however, the authors also only capture a small portion of the true interaction, and the law is only valid for interactions between dislocations and SIA loops. First, the approximation of interaction energy and force on the glide dislocation were calculated for 14 unspecified orientations in FCC metals on a pure screw dislocation. Interactions were assumed to only ever be elastic, even if the loop intersected the glide path of the dislocation. Furthermore, the calculation of these quantities only considered contributions from loops within a distance R (radius of dislocation loops) of the glide plane, and yet DD studies have shown that loops outside this region can significantly influence motion [95]. Furthermore, the assumptions made by Friedel to obtain equation (133) are quite extreme, and are only valid for breakaway angles very close to π. Friedel found this approximation starting from an analysis by Mott [145], which also makes significant assumptions on the form of the potential energy locking the dislocation, and the distribution of defects.

Obstacle hardening models have also been the subject of experimental investigation. The superposition in Eqn. 98 was applied with a BKS model modified for particle distribution, and found an exponent n =1.8 (eqn. 98) for solid solution and dispersed oxide hardening in a Cu-Au alloy [111]. In a more complex case with a

greater number of obstacle types, Bergner et. al. [21] examined the capabilities of the DBH and BKS models in combination with several superposition principles in an Fe-Cr model alloy. The hardening parameter α was calculated for α' phase particles, dislocation loops, and NiSiPCr-rich clusters in an Fe-Cr model alloy. Three parameters were fit to four data points using linear regression, and regardless of the chosen hardening model and superposition principle, a good fit to the data was possible. This is unsurprising given the low degree of overdetermination, and requires further experimental data to reveal if the proposed models and hardening parameters are predictive.

In this thesis, a multi-scale modelling approach is adopted to scrutinize and to quantify the uncertainty regarding the predictive capabilities of the proposed obstacle hardening models for irradiation induced defects. Discrete dislocation dynamics simulations are informed using atomistic calculations, which can then be used to inform constitutive models. First, the hardening due to a single defect size and type is studied for voids and SIA loops over a range of densities. The change in yield strength from each obstacle hardening model is compared to the calculated hardening using dislocation dynamics simulations, and the capabilities of each model is analyzed. Then, the hardening caused by a distribution of defect sizes for a single defect type is studied, and the validity of a mean defect size approach is considered for SIA loops and voids. In a culmination of the preceding studies, the material behaviour is simulated for most physically realistic case of a material containing both SIA loops and voids and a superposition principle using single defect hardening data to predict simultaneous hardening is proposed.

3.2 Investigation of Single Dislocation Irradiation Hardening

Using the DDD code development and atomistics-informed defect strength law developed in Chapter 2, a series of DDD simulations and the following analysis is detailed in

this section. The mechanical behaviour of irradiated α-iron following yielding is governed by dislocation interactions with voids, SIA loops, as well as other dislocations. The hardening coefficients in α-iron have been calculated using dislocation dynamics [180] and thus the goal of this thesis is to determine the individual hardening contributions of voids and SIA loops so that one can predict the strength of a material simply from the defect content, regardless of the relative populations of defects. To achieve this goal, single dislocation are ideal as they target a single phenomena while minimizing computation time.

3.2.1 Method

The details of the implementation that are unique to this chapter are as follows. Whereas dislocation-SIA loop interactions are treated using elastic interactions that are typical calculations for the DDD code, the void implementation requires an additional numerical framework to support the dislocation-void interaction as detailed in Chapter 2. Voids are represented numerically using the center of the void and its radius. Following the dynamics portion of the code, in which the nodal forces are calculated, the velocities found using an overdamped equation of motion, and the integration of the velocity to update the nodal positions, a new algorithm is used to find void intersections.

For each dislocation segment, the void radii of all voids in the vicinity of the segment are projected onto the glide plane. The minimum distance between the projected void center and the dislocation is calculated. An interaction occurs if and only if:

- The separation distance is below a critical distance threshold defined by the velocity of the dislocation segment and the simulation time step.
- The dislocation segment motion must be such that it is moving to intersect the void, i.e. $\vec{v} \cdot \vec{r} > 0$ where $\vec{v}$ is the segment velocity and $\vec{r}$ is the separation vector

from the segment to the void center.

To optimize the search for voids, the simulation volume is subdivided into boxes and each box has an associated list containing the information regarding every void within it. The minimum box side length is prescribed to at least the average dislocation length (also prescribed at the start of the simulation). To search for void intersections with a specific dislocation segment, the box containing the dislocation segment center is searched as well as the 26 surrounding boxes. The condition on box size guarantees that no voids are erroneously ignored due to the optimization method. Each void is uniquely identified by its box, and an assigned number.

Dislocation unpinning is performed according to the atomistics informed void strength model, which calculates a breakaway angle as a function of void size. At each step, a subroutine scans over every dislocation node. The numerical structure of a dislocation node is such that it includes whether it is pinned on a void, the radius of the void projected on the glide plane, and the box containing the void. All dislocation nodes connected to voids are tabulated, and the list of nodes is sorted by box, then void number. Two pinned node are expected for each void to which a dislocation node is pinned, which acts as a method of error checking. Each pair of dislocation nodes pinned to the same void are used to calculate the bowing angle. The velocities of the nearest-neighbour points of the pinned dislocation nodes is also evaluated to ensure that the dislocation is moving in the same direction as the bowing angle. When the angle and velocity criteria are satisfied, the two pinned dislocation nodes are merged, placed at the average position of their nearest neighbors, and all defect information is removed from the new pinned node's numerical structure.

Depending on the parameters of the simulation (specified in each subsection), a number of voids and/or SIA loops are placed in the simulation volume. Voids are either placed on the glide plane or randomly distributed in a plate centered on the glide plane. The plate thickness is governed by the largest void size to avoid placing

an excessive number of voids that will never interact with the dislocation. Omitting voids that are far away the glide plane serves to accelerate simulations while having no influence on the calculated mechanical strength (under the dislocation-void model used in this thesis).

The studies detailed in the following sections of this chapter are performed under strain controlled conditions. A single infinite edge dislocation is placed in the volume at zero stress, and the strain is incremented. The dislocation glides until it reaches an equilibrium configuration in contact with defects. The material behaviour is elastic until the applied stress is sufficient to break the dislocation free, as shown in Figure 37.

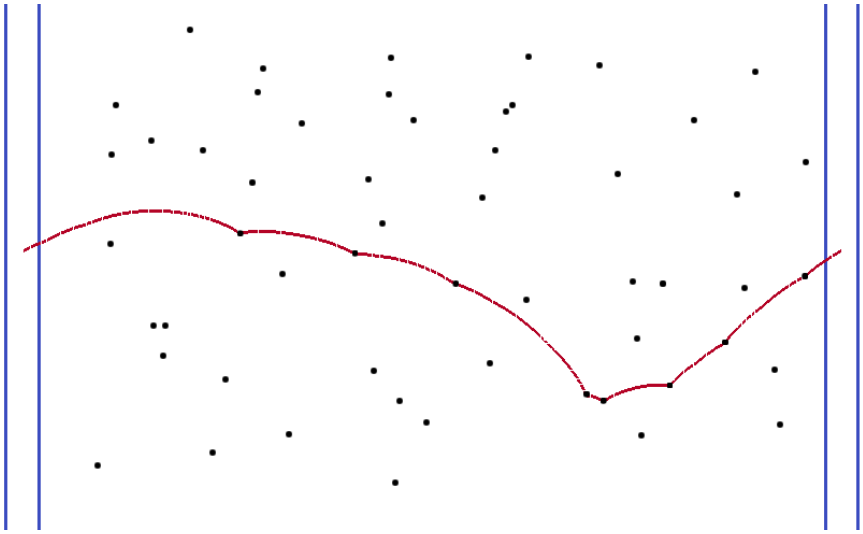

Figure 37: Single dislocation migrating under an applied shear stress through a field of voids. Individual voids are not visualized to avoid cluttering, as they are ¡0.1% of the simulation volume width and number in the thousands. The blue vertical lines represent the periodic boundaries of the simulation of the volume, and the void positions are denoted with black dots (the dot size does not represent void size).

Following initial yielding, the material exhibits an approximately perfectly-plastic behaviour as shown in Figure 38, as one would anticipate with a single dislocation (and therefore no increase in dislocation density following yielding). For each hardening value that is presented here, five simulations are performed and the average stress following yielding is used to define the change in hardness.

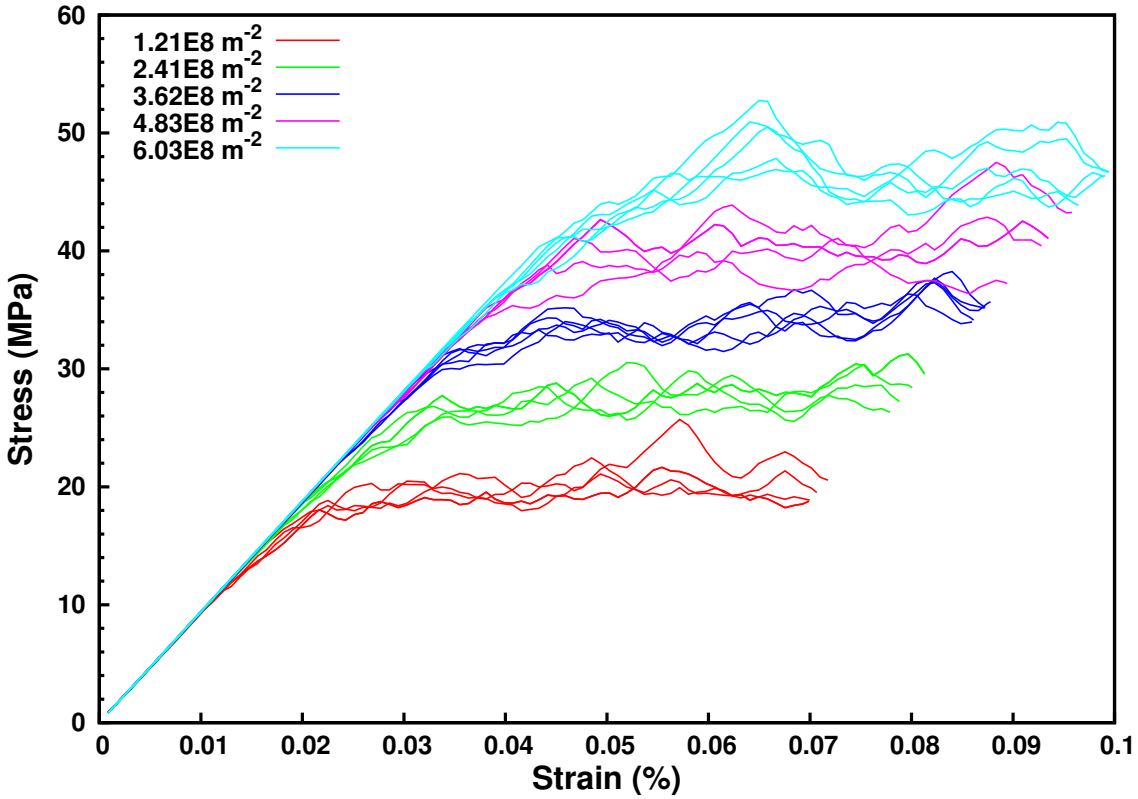

Figure 38: Example stress/strain curves for five areal densities of R=2.87nm voids with five repetitions of each configuration.

Zero friction stress is used, so that the dislocation glides under any non-zero applied shear stress (resolved in the correct direction). The increasing in hardening is thus exactly the average stress after yielding.

3.2.2 Void Hardening

Line tensions simulations have been widely used to study generic obstacle hardening. However, these simulations consider defects as infinitesimal points causing dislocation pinning, and omit important phenomena such as dislocation elastic self-interaction. Dislocation dynamics simulations are used here to calculate the increase in yield point due to a range of sizes and densities of voids, which are then compared to the predictions of the applicable irradiation hardening models. The four cases examined here are depicted in Figure 39 and are named (for clarity) as following:

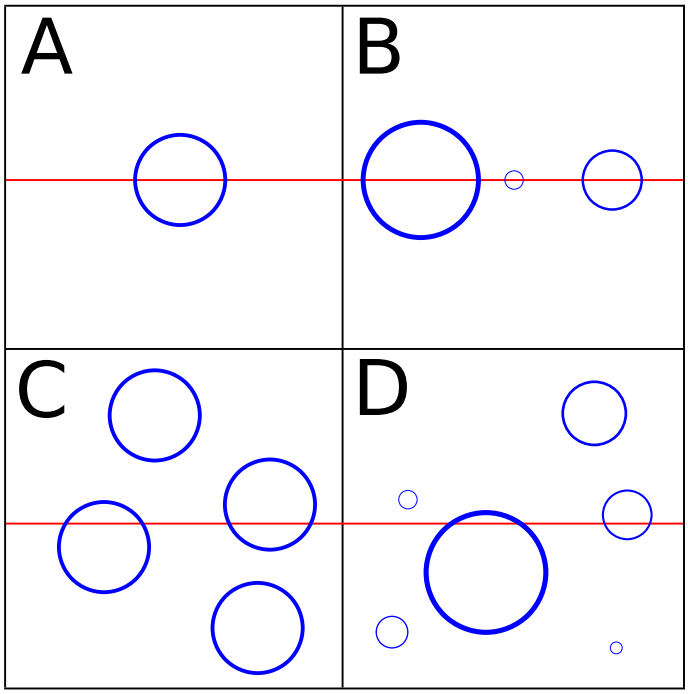

Figure 39: The four cases of size and space distributions examined here.

- Case A: Single size of voids centered on glide plane.
- Case B: Distribution of void sizes centered on glide plane.
- Case C: Single size of voids distributed in space.
- Case D: Size distribution of voids distributed in space.

This investigation is accomplished in two stages: first, a Case A configuration is used so that the glide dislocation encounters only one effective size of obstacle and thereby enabling direct comparison with the DBH and BKS models. Next, a Case B configuration is used to investigate the validity of a mean size approach. A mean size approach is defined as using the mean defect size in a given hardening model rather than treating the whole distribution directly. Given that in reality voids exist in a distribution of sizes, the ability to apply a mean size approach to predict hardening would greatly simplify the analysis. The hardening due to Case B is calculated for a constant mean and several standard deviations, and compared to the hardening due

Case A scenario using the mean size. In Case C, a dislocation encounters voids of different effective sizes: voids intersecting but not centered on the glide plane have a reduced radius on the glide plane of the dislocation.

3.2.2.1 Equal Sized Voids Centered on Glide Plane

A single dislocation gliding in a random distribution of defects is studied using voids centered on the glide plane (Case A), replicating the assumed configuration in which the DBH and BKS models were derived. The stress to propagate an infinite edge dislocation through an atmosphere of voids is calculated and analyzed using the DBH and BKS models as shown in Figures 40 and 41. Hardening is plotted against the functional form of each law, such that if the laws are predictive, all data points would lie on a line defined by $\tau^{c}_{\mathrm{DDD}} = \alpha\tau^{c}_{\mathrm{Model}}$. A range of void diameters between 0.57 nm and 4.59 nm, and a range of densities of resulting in a range of mean free paths over $[126 - 274]$b are considered. For these hardening models to serve in practical applications, the hardening parameter must be a material property and independent of irradiation dose. Otherwise, the functional form is fundamentally incorrect.

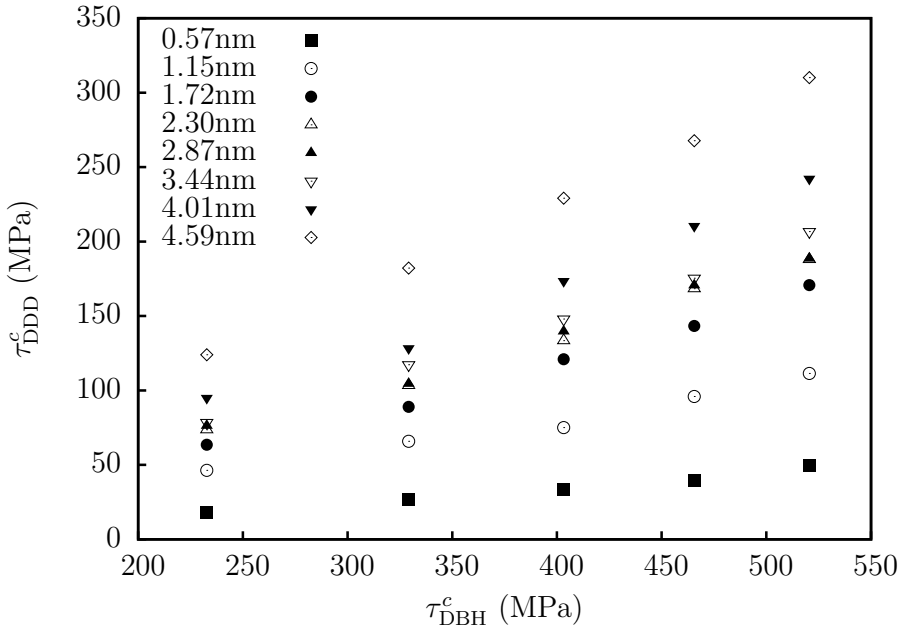

Figure 40: DBH hardening model.

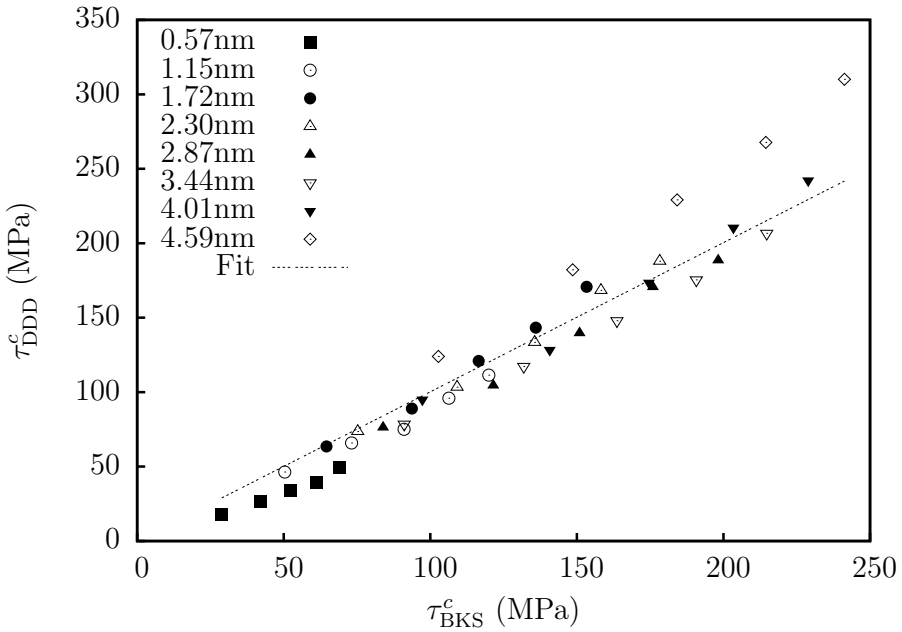

Figure 41: BKS hardening model.

From Figure 40, it was immediately clear that under these conditions, the DBH model cannot accurately predict hardening. For each void size, the DBH model could fit the calculated values; however, a single value of α cannot be used for all sizes. The reason for this is clear from the derivation of the model: line tension approximations aside, the model assumes that any defect in the thin plate region of thickness d interacts with equal strength with the dislocation. Given that void strength had an explicit size dependence, this was not the case here. The DBH model is markedly improved by adopting a size dependent strength as seen in Figure 42. For each size in Figure 40, a proportional fit with a coefficient $\alpha(d)$ was obtained, and each of these values is plotted in Figure 42a as a function of defect size. The measured values of α were also compared to the assigned defect strengths (given that α is often supposed as a defect strength) but the functional relationship was unclear. The points are tightly clustered around the 1:1 proportional line, showing that for a single defect strength, the DBH model accurately predicted hardening. This indicates that the DBH model could possibly be applicable for materials containing voids if a size dependent strength

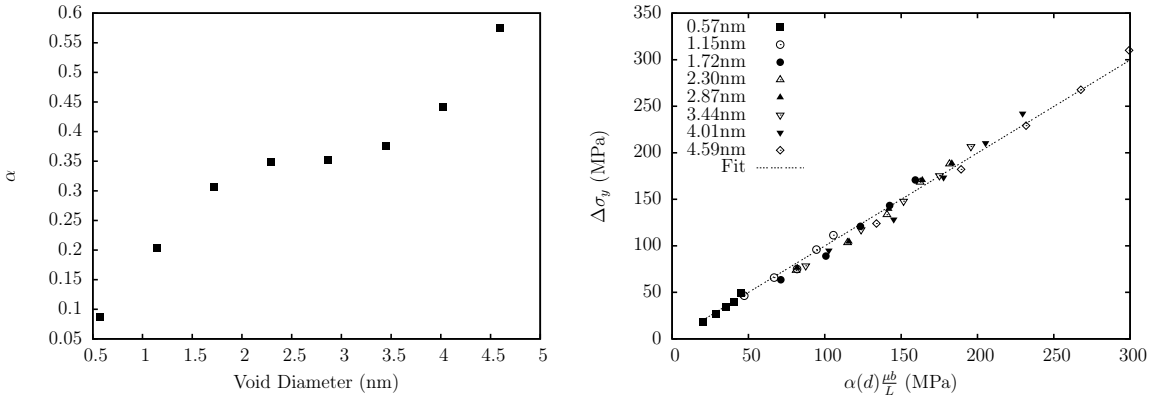

(a) α as a function of void diameter. (b) DBH model using a size dependent α.

Figure 42: The DBH model can be refined using a size dependent α, which dramatically improves the fit (Case A).

formulation can be determined.

The shortfalls of the original DBH model were largely remedied in the BKS model. The functional dependence on defect size is clearly important as the BKS model provides a much better overall fit for hardening caused by a single size of voids. In this case, a single value of α=1.003 provides a reasonable estimate of hardening over a range of void sizes and densities. Given that the strength of the smallest and largest void sizes were an extrapolation of atomistics data, the fit improved dramatically if the largest and smallest void sizes are omitted. If the BKS model was truly predictive here, it would suggest that the atomistic derived strength law adopted here underestimated small defect strength and that further atomistic simulations are required for very small (≈0.5nm) defects. In conclusion, the BKS model is shown here to predict void hardening over a range of defect sizes and densities for a single value of α, and it is therefore applicable for irradiation hardening predictions in the athermal case shown here.

3.2.2.2 Size and spatial distribution of voids.

Experimental studies [114, 21] have used mean defect size as an input to hardening models such as DBH and BKS; however, the validity of such an approach has

never been shown. Any significant change in hardening as a function of distribution standard deviation would invalidate such an approach for a symmetric distribution of defects. Several studies ([108, 54, 46]) have investigated hardening caused by obstacles with a distribution of different strengths from a modelling perspective using line tension simulations. Dong and Vaucorbeil ([54, 46]) focussed on determining a combination law using a modified DBH model, whereas Kulkarni [108] investigated the hardening due to a given distribution of defects and compared it to the hardening due to the same number of defects with a size equal to the mean defect size. These studies have the same limitations cited in the previous section - line tension simulations neglect defect size effects arising from elastic interactions, which are significant and non-linear. However, the notion of comparing calculated hardening from a defect strength distribution with the mean strength is highly relevant to both modelling and experimental studies. If a mean size approach predicts hardening correctly, one can straightforwardly extract α values from experiments without treating complex defect size distributions, and from a modelling perspective, the hardening can be calculated directly from the defect state of the material rather than using a dislocation dynamics simulation.

Introducing a distribution of defect sizes also introduces many additional parameters such as distribution type, mean, and variance. Void sizes must also lie within the size range as simulated by atomistics resulting in the truncation of continuous distributions. Understanding the role of each parameter on the change of material behaviour becomes increasingly challenging with such a high number of degrees of freedom. Therefore, a single specific case was considered here: hardening due to a normal size distribution of voids (Case B). The distribution mean was held constant while the size standard deviation was increased. This case reveals the relative influence of small and large defects compared to the mean. If an increased standard deviation increases/decreases the relative strength, one can infer that presence of

larger/smaller defects are more influential on material strength. Here, a mean size of 2.30nm and a standard deviation s ranging on [0.3-1.5]nm was used. The relative change in strength $\Delta\tau^c$ and corresponding error bars were calculated as follows:

$$\Delta\tau^c = \frac{\tau^c_{\text{Dist}} - \tau^c_{\text{Mean}}}{\tau^c_{\text{Mean}}} = \frac{\tau^c_{\text{Dist}}}{\tau^c_{\text{Mean}}} - 1 \pm \sqrt{\left(\frac{\delta\tau^c_{\text{Dist}}}{\tau^c_{\text{Dist}}}\right)^2 + \left(\frac{\delta\tau^c_{\text{Mean}}}{\tau^c_{\text{Mean}}}\right)^2}. \tag{136}$$

where $\tau^c_{\text{Dist/Mean}}$ is the average of five simulations, and $\delta\tau^c_{\text{Dist/Mean}}$ is the corresponding standard deviation.

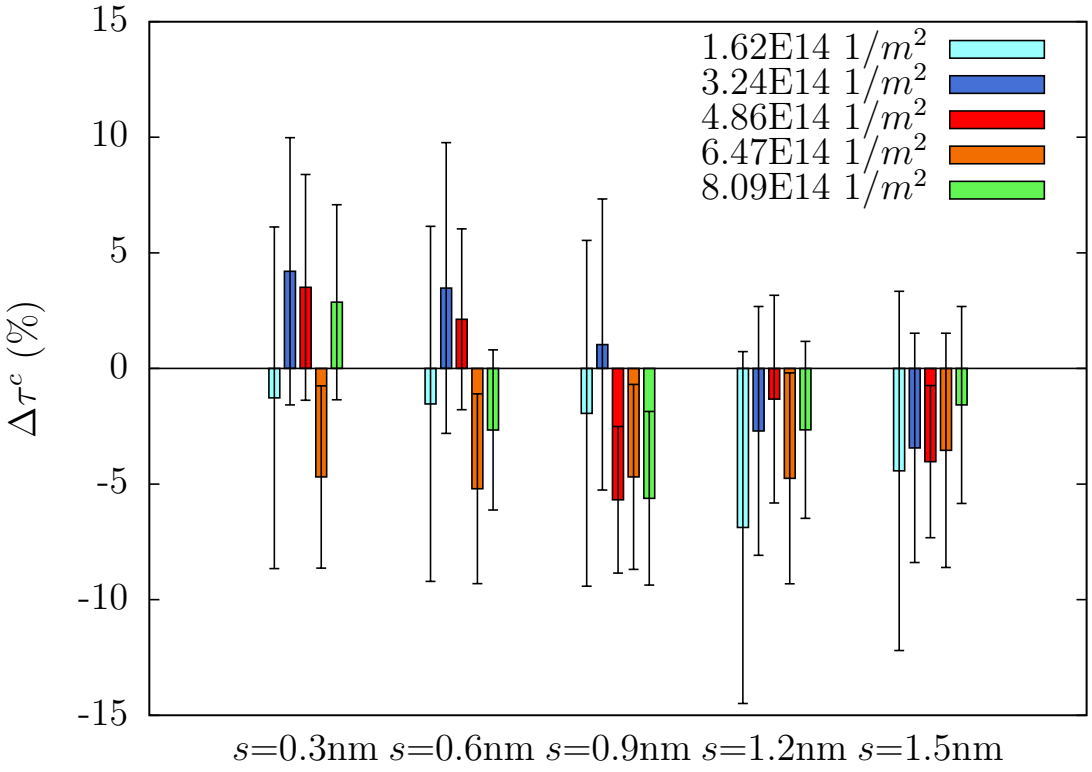

Figure 43: Hardening caused by a Gaussian distribution of void sizes relative to the hardening for the mean size. Bars are coloured by defect density.

Several trends between hardening and distribution width can be observed in Figure 43. First, $\Delta\tau_c$ largely decreased as a function of size standard deviation. However, most points lay within one standard deviation of the mean defect size hardening. Second, the relative difference in hardening compared to a mean size approach showed that the change is typically on the order of a few percent, and almost all cases lay

within one standard deviation of zero strength difference. In cases where the void distribution in a material can be approximated as Gaussian, the material hardening caused by the distribution can be approximated using the mean size and therefore, the mean size approach typical to experimental studies was shown to be valid here.

3.2.2.3 Effective versus distribution mean size.

To validate and to extend the prior result beyond a symmetric distribution, one further case is studied: the hardening caused by a single size of voids distributed in 3D space (Case C). This case also evokes the notion of effective defect size. An arbitrary size and spatial distribution of defects can be described using the radii of the defects. However, given that voids intersecting but not centered on the glide plane would have a reduced radius on the glide plane of the dislocation, the effective mean defect radii encountered by the dislocation could differ from this significantly. One can analytically describe the effective size distribution using a function of random variables. The void radius as seen by the glide dislocation R_{eff} can be written as

$$R_{eff} = R\sqrt{1 - X^2} \tag{137}$$

For a function f of a single random variable x and $Y = g(X)$, the probability density can be written as

$$f_Y(x) = f_X(g^{-1}(x)) \left| \frac{dg^{-1}(x)}{x} \right| \tag{138}$$

Here, the distribution of the random variable x is simply

$$f_X(x) = \begin{cases} \frac{1}{R} & 0 \leq x \leq R \\ 0 & \text{otherwise} \end{cases}$$

Therefore $f_Y(x)$ can be written as

$$f_Y(x) = \frac{1}{R}\left|\frac{-x}{\sqrt{R^2 - x^2}}\right|, \tag{139}$$

where R is the void radius, and X is a uniformly distributed random variable on the interval $[0, 1]$. The probability distribution function of R_{eff} can be straightforwardly calculated as

$$f_R(x) = \frac{1}{R}\frac{x}{\sqrt{1 - x^2}}, \tag{140}$$

which is plotted in the inset of Figure 44 and is clearly asymmetric about the mean size (vertical dashed line).

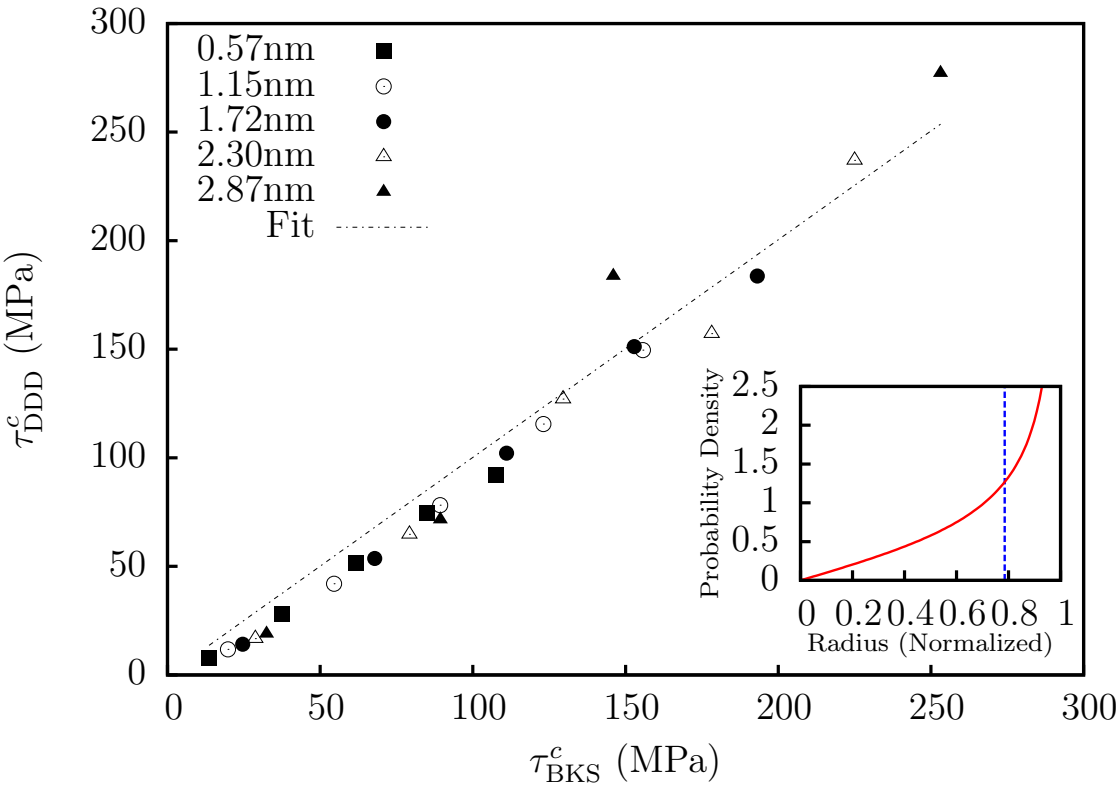

Figure 44: Hardening caused by a single size of voids distributed randomly in space (Case C) plotted against the BKS model using effective D' and L. Inset shows void radius (normalized to R) as seen by glide dislocation. Mean size denoted with blue dashed vertical line.

The hardening is predicted using the BKS model with the previously calculated

value of α=1.003 and effective mean void size and plotted against the calculated values of hardening using dislocation dynamics. An effective mean size analysis influences the degree of hardening predicted using the BKS model through both effective length $L_{eff} = 1/\sqrt{ND_{eff}}$ and effective diameter $D'_{eff} = \frac{D_{eff}L_{eff}}{D_{eff}+L_{eff}}$. Figure 44 strongly suggests that over a wide range of void sizes and densities, a full defect size distribution analysis can be captured using an effective mean size approach not only for a symmetric distribution, but for asymmetric distributions as well. Furthermore, it shows that an effective mean radius approach must be used to accurately predict hardening. While this result differs from that of Kulkarni, it is also not contradictory because the details of the size distribution are fundamentally different. In this work, the mean size was held constant, whereas in Kulkarni's work, the mean was also varied and the distribution became increasingly biased to large obstacles with increasing mean size. The results obtained here simply represent a different material state and show that for the distributions of defects studied here, a mean size approach was in fact applicable.

In addition to the hardening calculations performed for the previous distributions of defects, the statistics pertaining to other distributions were also of interest from a qualitative standpoint. The configuration used to produce Figure 43 featured defects centered on the glide plane (Case B), so that the true size distribution and the effective size distribution were the same. However, when the voids were randomly distributed in space (Case C and D), two additional factors influenced the size distribution. First, the probability that a void intersected the glide plane was a function of defect size. Second, if a defect was assumed to intersect the glide plane, the glide plane was assumed to intersect the void at a position uniformly distributed on $[-R, R]$ away from the center. The distribution of defect radii on the glide plane can be described using a function of random variables; however, even with simple distributions, a closed form expression is often impossible. Therefore, three distributions were numerically

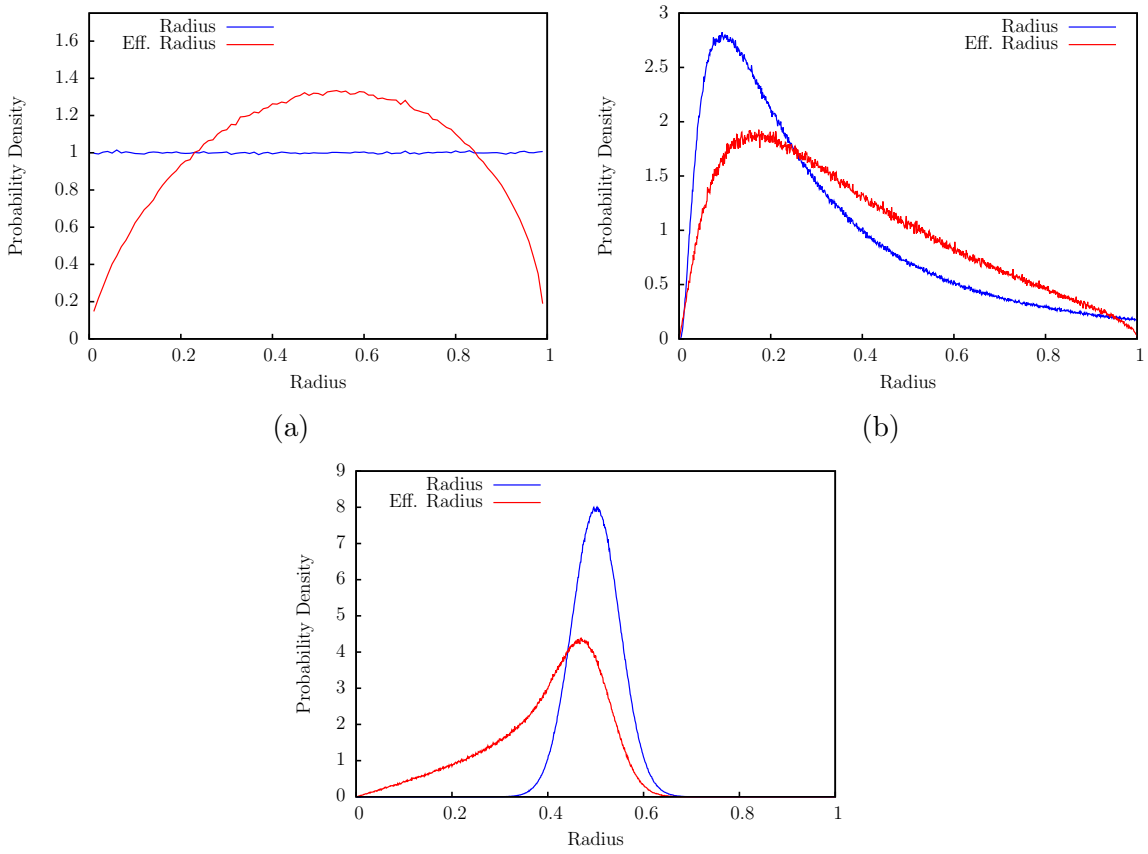

Figure 45: The size distribution PDF of voids (blue) and effective radii on the glide plane (red) for uniform (a), lognormal (b), and normal (c) distributions.

computed after validation using a closed form expression for a single size of voids.

It is clear from Figure 45 that the trends in effective radii are markedly different depending on the governing size distribution. In the uniform case, the distribution is nearly symmetric resulting in almost no difference between the effective mean radius and distribution mean radius. A lognormal distribution, however, results in an increased effective mean because the probability that a small defect intersects the glide plane was low, and the extended tail of the distribution increased the average effective size. A normal distribution results in a decreased effective mean size particularly in the example case where the distribution was confined. The purpose of Figure 45 is not to provide a definitive investigation into the effective defect radii on the

glide plane, but to highlight the need to analyze each experimentally obtained size distribution and calculate the effective mean radius rather than the observed mean radius. Such an analysis is applicable not only for voids, but for all obstacles that can be approximated as spherical, such as inclusions or oxides. Topuz *et. al.* [220] acknowledge the added complexity due to the notion of effective defect size, particularly as their study was limited to two-dimensional dislocation dynamics and required an initial coarse-graining of dislocation defect interactions before ever performing dynamics studies. Further atomistic scale studies are required before using the effective radius distribution, because it is unclear if a dislocation intersecting an obstacle with radius R_1 off-center with an effective radius $R' < R_1$ is equivalent to a dislocation intersecting an obstacle through its center with radius (and therefore effective radius) $R_2 = R'$. Hafez et al [85] used atomistic scale simulations of an edge dislocation intersecting a void at varying off-center positions, which revealed decreasing strength with decreasing effective radius but a much more comprehensive study is required to draw any conclusions.

3.2.3 SIA Loop Hardening

Dislocation loop hardening has been the subject of some investigation using dislocation dynamics, typically to study purely elastic interactions or to reproduce experimentally observed dislocation channel clearing. Here, the macroscopic changes in mechanical response are of interest, specifically within the framework of proposed hardening models such as the DBH, FKH and BKS models. These models have seen some usage in DDD literature such as in [4] where a value of α for a modified DBH model was calculated for varying densities of 25nm $1/2\langle 111\rangle$ loops. However, the validity of such a law over a range of both SIA loop sizes and densities has never been shown. Here, the DBH, FKH, and BKS models are compared against the hardening as predicted by dislocation dynamics over a range of both SIA loop sizes and densities.

A case by case analysis as performed for void hardening is not required here because of the extended nature of dislocation-SIA loop interaction. Whereas voids away from the glide plane did not influence dislocation motion, the stress field of an SIA loop influenced the dislocation and could not simply be placed on the glide plane. Therefore, SIA loops are uniformly distributed in space for the studies performed here.

3.2.3.1 Equal Sized SIA Loops

The hardening caused by the presence of SIA loops is analyzed by calculating the flow stress of a single dislocation in an atmosphere of $\langle 100 \rangle$ dislocation loops. While the elastic stress field of an SIA loop is short range ($\propto 1/r^3$), the influence of both in plane and out of plane loops must be considered. A plate of thickness 20R centered on the glide plane was populated with SIA loops of a single size and a Burgers vector chosen randomly from the permissible SIA loop Burgers vectors. The hardening τ^c was plotted against the functional form of the DBH, FKH, and BKS models as shown in Figure 46. Although the BKS model was formulated for impenetrable spherical defects without an elastic stress field, the model was nevertheless included for the sake of comparison.

Each model was fit with a proportional line $\tau^{\mathrm{c}}_{\mathrm{DDD}} = \alpha \tau^{\mathrm{c}}_{\mathrm{Model}}$, and while a general proportional trend exists in each case, it is unclear if any of the models are truly predictive here. It is therefore difficult to infer which model is more physically realistic than the others, or if any truly capture the behaviour of the dislocation-SIA loop interaction. However, for the purposes of predicting irradiation hardening, the constant of proportionality α and its associated R^2 correlation for the fit were extracted and are shown in table 1. Qualitatively, the DBH model has a wide scatter but a size-dependent obstacle strength α could significantly improve the fit. The FKH model is the most tightly grouped, and any significant deviations occur at the maximum and minimum sizes. While the BKS model does correlate with the data, it is more

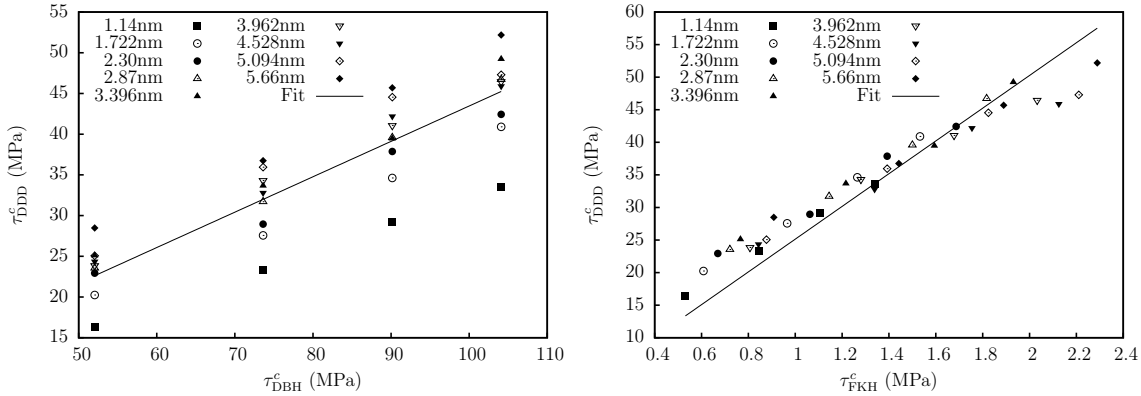

(a) DBH hardening model.

(b) FKH hardening model.

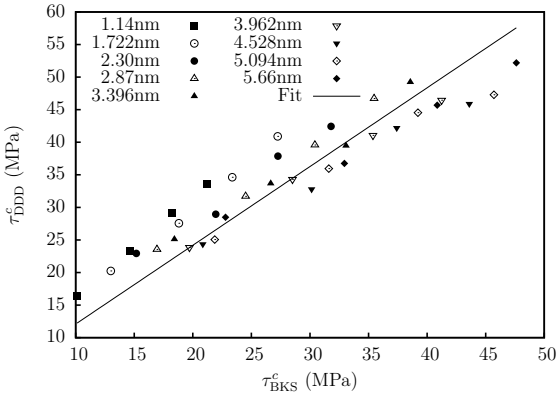

(c) BKS hardening model.

Figure 46: Hardening caused by a random array of equal size SIA loops.

Model	α	R^2
DBH	0.435	0.776
FKH	25.12	0.864
BKS	1.209	0.807

Table 1: Size dependence of α: fit parameters of for each model.

spread than in the FKH case. In quantitative terms, the FKH model provided the most accurate proportional fit as determined by the R-squared value. As a result, for irradiated materials containing SIA loops, the FKH model is shown here to provide the best estimation of material hardening.

3.2.3.2 Size Distribution of SIA Loops

As in the case of voids, studying the hardening effect of a size distribution of SIA loops presents a large number of variables, so the specific case of a normal distribution with a constant mean size of 4.592nm and a range of standard deviations s on [0.5-2.5]nm is used, which models an irradiation of 0.051 DPA well [91]. A single edge dislocation is propagated through the defects, the hardening is determined and the results are shown in Figure 47.

It is immediately clear that the distribution width has no discernible effect on hardening. In nearly every case, zero strength change is within one measurement standard deviation. Such an outcome cannot be reasoned intuitively from the similar void strengthening case, because the mechanisms of defect-dislocation interaction differ greatly. Voids are placed with their centers on the glide plane, ensuring a Gaussian distribution of sizes and not the effective distribution as shown in Figure 45c. In contrast, SIA loops are distributed over a plate of thickness 20R. An effective size distribution on the plane is also difficult to define for SIA loops because of the extended nature of their associated stress fields - out-of-plane loops influence dislocation motion via their stress field. In conclusion, the mean size of SIA loops can be used to predict the hardening in a material containing a size distribution of loops using the

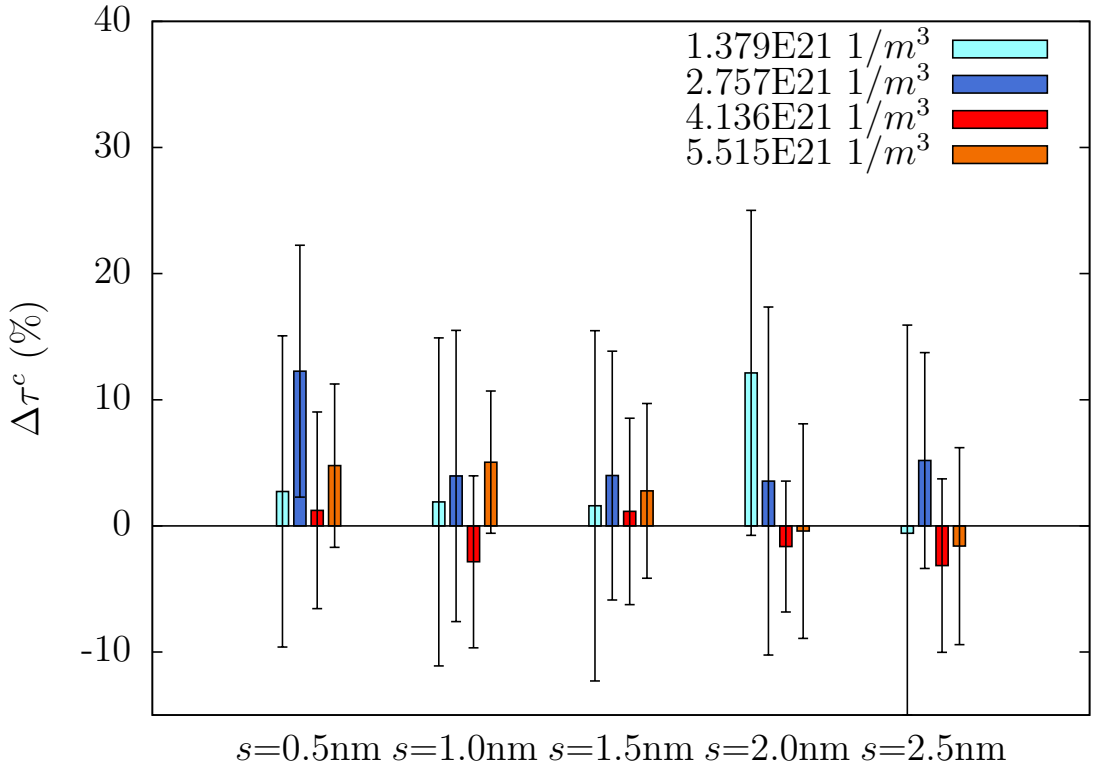

Figure 47: Hardening caused by a Gaussian distribution of SIA loop sizes relative to the hardening for the mean size. Bars are coloured by defect density. Experimental values of s are typically 1.5 or greater [91]. The error bars are calculated using eqn. 136.

FKH approach.

3.2.4 Multiple Defect Types

The previous studies in this work provide insight into the hardening caused by SIA loops and voids, and the applicability of different hardening models under several different regimes for a single defect type. In an irradiated material, SIA loops and voids exist simultaneously and their combined effect has never before been studied with dislocation dynamics with regards to hardening models, and only once with regards to mechanical response [213]. As in the investigation of the influence of a size distribution of defects on hardening, the number of variables when considering multiple defect types of multiple sizes quickly becomes overwhelming. Therefore, one

specific case yielding the greatest insight for a limited number of simulations is chosen. A range of sizes of void and SIA loops were used investigate possible superposition principles. In α-iron irradiated by fast neutrons, the sizes and densities of SIA loops and voids have been experimentally observed to differ significantly, with void number density typically an order of $10^2 - 10^3$ times greater than SIA loop number density [59]. This material state is modelled using densities as found in experiment ($\approx 10^{22}$ m^{-3} for SIA loops, $\approx 10^{24}$ m^{-3} for voids) [59] and a mean size approach, which provides insight into the simultaneous applicability of the FKH and BKS hardening models on a realistic irradiation state.

A simultaneous combination of a single size of voids centered on the glide plane and a single size of SIA loops distributed in a plate of thickness 20R are used to investigate hardening with the presence of multiple defect types. As a result, the defect density varies accordingly with the size. The method of superposition was taken to be the same as equation 98. The hardening contributions from voids and SIA loops are calculated individually using the BKS and FKH models and the values of α calculated in this work. Then, the exponent n in equation 98 is taken as a fitting parameter. A value of α must be independent of defect sizes and densities to be predictive and useful in practice.

Figure 48 shows the material hardening from the presence of both voids and SIA loops over a range of sizes and densities. The best fit of equation 98 in terms of least squares is accomplished with an exponent of n=2.22. Using this exponent, a superposition of the BKS model and the FKH model provides an excellent fit to the calculated hardening results. Therefore, in a material containing void and SIA loops such as irradiated $\alpha-$iron, a superposition principle can be applied to combine the independent defect hardening contributions to predict a real yield strength.

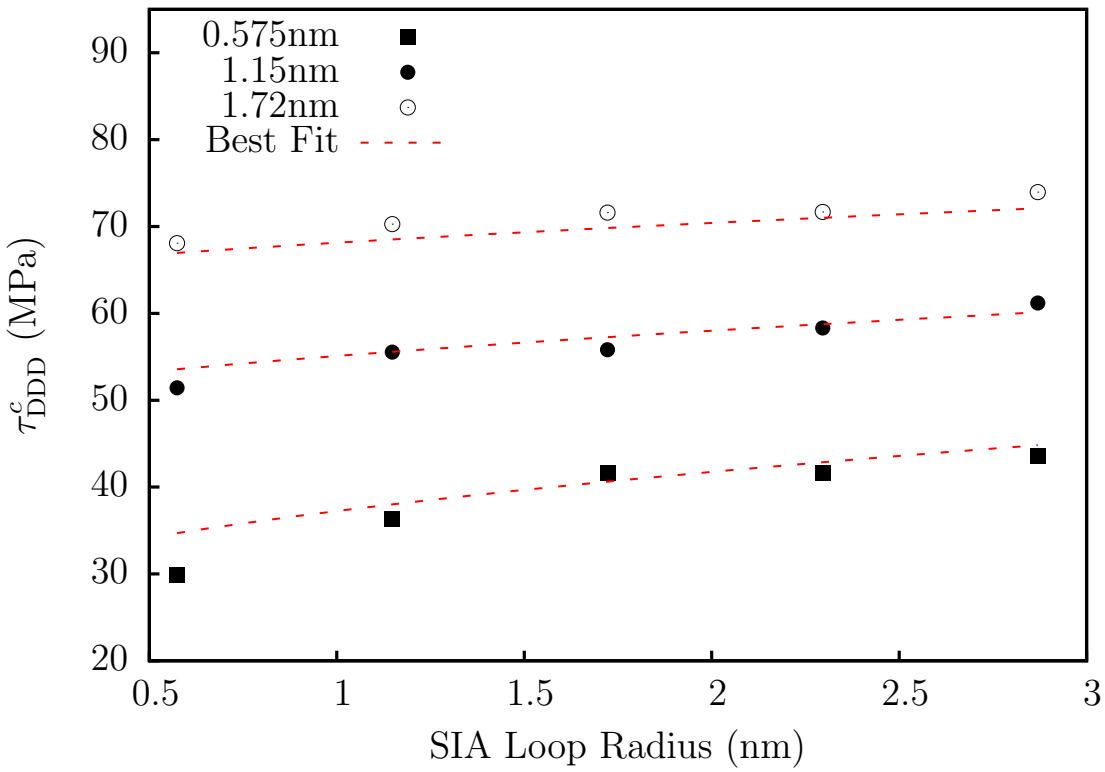

Figure 48: Hardening caused by a combination of SIA loops and voids (radii given in legend). A best fit superposition principle is shown using a superposition of FKH (loops) and BKS (voids) using the previously calculated values of α and a principle of the form of equation 98 and n=2.22.

3.3 Conclusion

This portion of the thesis represents an important advancement in coarse-graining techniques from two different perspectives. First, the complexities of atomistics scale dislocation-void interactions are reduced to a breakaway angle criteria using a DDD simulation to measure the angles at which dislocation breakaway occurs for the same configuration as in the atomistics calculation. The interactions between SIA loops and dislocation are seen to be accurately reproduced (in the mean response) through elastic interactions, already accounted for in DDD simulations, and therefore do not require additional rules for their inclusion. Second, these DDD simulations enable one to gain insight into the accuracy and predictive capabilities of macroscopic scale

models. For the first time, the predictive capabilities of the DBH, FKH, and BKS models are analyzed for voids, SIA loops and a combination of both defect types using this atomistics informed dislocation dynamics simulation. For a single defect size, the BKS and FKH models are shown to accurately predict hardening for voids and SIA loops, respectively. If a size dependent defect strength parameter is allowed for, the DBH model is also valid for hardening predictions. A mean size approach, in which hardening is calculated assuming all defects have the mean size of a distribution rather than treating the full distribution, is shown to well-predict hardening for both void and SIA loops using a normal size distribution of defects. Even further, a mean size approach also accurately predicts hardening for an asymmetric size distribution of defects, strongly indicating that not only does a mean size approach capture the hardening caused by a full distribution but that an effective mean size analysis is necessary as well. The effective defect size distribution versus physical defect size distribution was shown for several common distributions, which reveals that the mean effective size can potentially increase, decrease or remain unchanged compared to the distribution mean. Finally, a previously proposed superposition principle is shown to be valid in predicting the hardening due to the simultaneous presence of SIA loops and voids over a range of defect sizes and densities. These simulations provide insight into the individual contributions to hardening from each species as well as into the synergistic effect between different defect types and sizes. Predicting the mechanical properties of materials demands a full 3D dislocation dynamics simulations because dislocation-dislocation interactions act as yet another hardening contribution and must be considered in conjunction with irradiation obstacle hardening to develop an extended superposition principle validated in 3D.

CHAPTER IV

THERMALLY ACTIVATED DISLOCATION MOTION

Obstacles such as precipitates or irradiation-induced defects impede dislocation motion and directly influence macroscopic mechanical properties such as yield point and ductility. Dislocation-defect interactions involve atomic scale interactions as well as long range elastic interactions, therefore constituting a complex multi-scale modelling problem. Thermally assisted dislocation bypass of obstacles occurs when lattice vibrations contribute sufficient energy in combination with the energy from driving stresses that the dislocation can overcome the energy barrier. Characterization of the thermally activated barrier combined with harmonic transition state theory is a cornerstone of coarse-graining, facilitating scale transition with a simple Arrhenius type expression. Accurate activation energy calculations based on the NEB method are typically performed with calculations and reaction pathways identified using atomistic simulations, but these become infeasible with increasing complexity of state transition processes and increasing activation volumes of the phenomena in question. In this chapter, the NEB method is generalized to coarse-grain continuum representations of evolving microstructure states beyond the discrete particle descriptions of first principles and atomistics. The novel method proposed in Chapter 2 using continuum discrete dislocation dynamics is analyzed with regards to applications in coarse-graining and scale transition of unit dislocation-SIA loop bypass activation energies, and direct comparison with atomistic calculations provides insight into the physical fidelity of this continuum method with respect to widely accepted atomistic methods.

4.1 Overview

Thermally activated phenomena underlie numerous processes of material microstructure evolution such as diffusion, defect clustering, and dislocation migration. Energy provided by thermal fluctuations can assist the applied stress in driving a system to overcome energy barriers for each characteristic process, with the wait time for thermally activated barrier bypass defining the rate limiting step for evolution. The rate of these processes is experimentally observed [159] to exhibit an inverse exponential dependence on 1/T, where T is absolute temperature. Accordingly, rates of relevant evolution processes can vary by orders of magnitude. Transition state theory focuses on the minimum energy pathway (MEP) between two adjacent states for such processes and assumes that the rate of a reaction is controlled by the saddle point energy between two the states on the associated potential energy surface. This technique is a fundamental component of time-scale extension because the rate of barrier bypass informs longer time scale relations using Eq. (57), and simulation techniques exploiting this method have been experimentally validated for numerous physical phenomena [53, 129]. In addition, activation energy calculations are valuable in spatially coarse graining by encapsulating details of the size and spatial distribution of obstacles.

Energy methods have also been successfully applied in analytical studies such as Orowan looping of dislocations past obstacles. For more complex cases, molecular dynamics simulations are often used to calculate activation energies as they are well-suited to address the length scales involved in atomic scale structure rearrangement processes with limited volumes, such as dislocation bypass of nm-scale obstacles, or point defect migration. First principles (e.g., DFT) and molecular statics/dynamics simulations have been the only methods employed to rigorously compute activation energy barriers for such microscopic state transitions. Their computational complexity (high degrees of freedom) has motivated the development of several efficient saddle point energy calculation methods. The dimer method [88] (as detailed in Chapter 2)

uses a pair of images of the system, slightly offset in space, to drive the system towards a saddle point according to the local curvature of the system. The activation relaxation technique [147] first perturbs a degree of freedom in the system, from which the system is driven up the potential energy surface towards the saddle point. From the saddle point, the system is relaxed to find the final configuration of the system. Another commonly used technique is the nudged elastic band (NEB) method [102] (also detailed in Chapter 2), which determines the minimum energy pathway between two known local energy minima. A series of system images are created (typically linear interpolations between the initial and final states), which are relaxed under the combination of a physical force and a fictitious spring force. In combination with atomistic simulations, these methods have been used to investigate numerous phenomena such as point defect formation and migration as well as dislocation migration and cross-slip [15, 76, 182].

Although atomistic methods provide valuable insight into atomic-scale processes, significant computational requirements limit simulations to processes involving small activation volumes and therefore restrict the possible range of phenomena that can be considered. Furthermore, spatial and temporal coarse-graining atomistic simulation methods that link directly to constitutive models have yet to be firmly established. Recent studies have demonstrated success in several cases such as dislocation nucleation at boundaries [32] and shear-coupled grain boundary migration [177], but the use of NEB based on atomistic simulations to inform continuum descriptions of thermally activated processes has been primarily limited to unit processes with activation volumes comprising of up to tens of atoms. A mesocale continuum phase field modelling approach combined with NEB was used to find the critical nucleus configuration and activation energy in a cubic to tetragonal transformation using a free-end NEB method [192]. However, larger scale cooperative processes of microstructure rearrangement characteristic of dislocation-obstacle interactions that have both short

and long range character have eluded treatment via such methods.

For dislocation-obstacle interactions, this problem can rendered computationally tractable by employing discrete dislocation dynamics (DDD) to represent the energy landscape based on the continuum elastic theory of defects. When the necessary approximations are valid, simulations described using a continuum theory are desirable in terms of low computational requirements and offer a more direct connection to constitutive models. With such significant reductions in computation time, it is possible to compute the MEP and saddle point energies for transition not only for a single reaction, but for more complex many-body dislocation-obstacle field interactions to map a more comprehensive energy landscape for obstacle interactions; this potentially represents a significant advancement in coarse-graining techniques to achieve what one of the authors had referred to as activation volume averaging of collective evolving microstructure events [132, 133] as an alternative to classical homogenization approaches for effective properties of stationary (non-evolving) microstructures in micromechanics. This chapter demonstrates the capabilities of a novel DDD-NEB method to investigate the size and stress dependence of dislocation bypass activation energy with self-interstial atom (SIA) loops induced by irradiation for activation volumes comprised of several hundreds of atoms. Results are used to inform a constitutive transition state theory model [104] as well as to create a complete activation energy map for different interaction geometries.

4.2 Perspectives on Coarse-Graining via Activation Energies

Higher order complexities in the dislocation morphology which may be captured by atomistic simulations are inherently omitted using the continuum theory of defects. Such phenomena include highly localized core deformations and structures formed

when dislocation cores are overlapped. However, atomistic simulations are not without significant drawbacks, particularly in relation to inter-atomic potentials and simulation boundary conditions. Hafez *et al.* [84] showed that the critical stress to cause a dislocation to bypass a void in α-iron can varies significantly between three potentials with differences, in some cases by over 50%. High computational demands of atomistic calculations limit simulations to highly confined spatial volumes and as a result the choice of boundary conditions have profound consequences. Fixed boundary conditions have been established to cause spurious results [208] and fully periodic boundary conditions require closed dislocation loops and propagate the long-range elastic fields characteristic to dislocations. Comparison of continuum methods to atomistic simulations would not necessarily provide a quantification of the accuracy of the proposed method because of the aforementioned challenges of atomistic simulations. Such effects may have a greater impact on activation energy barriers than the approximations associated to the continuum description of defects used here.

The influence of dislocation core width (and thus core energy) on activation energy barriers is detailed after the method and primary studies are presented. Any possible omission of physical effects otherwise captured in atomistic simulations is tempered by the fact that the simulations detailed in this thesis are far beyond feasible computation times for atomistic simulations. The minimum simulation volume in this chapter contains 25×10^9 atoms - three orders of magnitude greater than any atomistic simulation to date. The proposed method provides direct and computationally efficient access to activation energies for mesoscopic dislocation processes and such processes inherently require a mesoscopic simulation method such as DDD.

4.3 Prismatic Loop Bypass

Irradiation induced voids and prismatic self-interstitial atom (SIA) loops are significant obstacles that contribute to irradiation hardening in bcc alloys and, to a lesser

extent, in fcc alloys [59, 91]. Accounting for thermally activated bypass of obstacles requires characterizing the activation energies associated with the dislocation-obstacle bypass events.

Here, all calculations are performed for α-iron under the assumption of elastic isotropy. The linear elastic material constants are taken as E=211GPa, μ=82GPa, and ν=0.29. Dislocation mobilities do not influence the simulations as the simulations are performed at equilibrium. The interaction configuration for all simulations is a pure edge $1/2\,[111]\,(1\bar{1}0)$ dislocation impinging on an obstacle under a shear stress oriented such that the resolved shear stress on the system of the glide dislocation is equal to the applied shear stress. A dislocation core width parameter of $1a$ is used. The obstacle considered here is a $\langle 001 \rangle$ prismatic dislocation loop, as observed in irradiated α-iron at 300°C [91], which has been shown with atomistic simulations to have a square geometry [217]. Periodic boundary conditions are applied so that the glide dislocation is infinite in extent, and the simulation represents a periodic linear array of SIA loops. The starting configurations for the NEB calculation are created by relaxing a configuration using dislocation dynamics and the final state is assumed as the glide dislocation returning to a straight configuration at a large distance beyond the obstacle. The size of dislocation loops is small relative to the overall simulation volume ($<$ 10% of the simulation volume width) such that the curvature due to Orowan bowing is approximately constant between loop sizes. Dislocation climb is not permitted in this study, as discussed in Chapter 2.

In contrast to intrinsically discretized atomistic NEB simulations, the discretization of continuous dislocation lines must be specified. Several methods are commonly used; for example, an edge-screw discretization approximates a smooth line as a series of straight segments of pure edge or pure screw dislocation character, or a nodal discretization interpolating a series of points (nodes) along the line with a chosen function. Here, a nodal method using linear interpolation (of continuously varying

dislocation character) is used. A range of discretization lengths are tested to ensure convergence. During a typical dislocation dynamics simulation, the dislocation line is re-discretized at every step and dislocation nodes are moved, added, or removed as a function of spacing along the dislocation line to maintain numerical stability and a physically realistic configuration. However, in an NEB calculation involving discretized dislocations, maintaining the number of degrees of freedom constant and equal across all images is highly desirable to avoid interpolations between degrees of freedom of different images. Further, the tangent equation depends directly on the position of the nodes in the neighbouring images and consequently the nodes cannot be moved significantly. Within these limitations, a re-meshing method is developed that maintains numerical stability. The dislocation line is recreated using a cubic spline interpolation through all dislocation points, and the dislocation nodes are repositioned along this line relative to a point fixed on the simulation boundary volume to maintain constant spacing. No points are added or removed. As a result, the point positions did not vary significantly between steps and therefore the re-meshing did not perturb the tangent calculation, while preventing the introduction of numerical artifacts such as kinking into the dislocation line shape.

Activation energy dependence on dislocation discretization is shown in Figure 49. The activation energy barrier is seen to be relatively insensitive to dislocation discretization. The maximum normalized segment length used here is 0.8.

The limitations of this study concern the capabilities of DDD with regard to the complex motion of dislocations in BCC α-iron. Screw dislocation migration occurs via a kink-jog mechanism, often approximated in DDD simulations with a much lower screw dislocation mobility [154] as an approximation of the complex screw dislocation motion in BCC materials [55]. Other effects such as temperature dependent lattice friction or friction stresses caused by impurities are also not considered here.

Molecular dynamics simulations have studied dislocation-SIA loop stress-driven

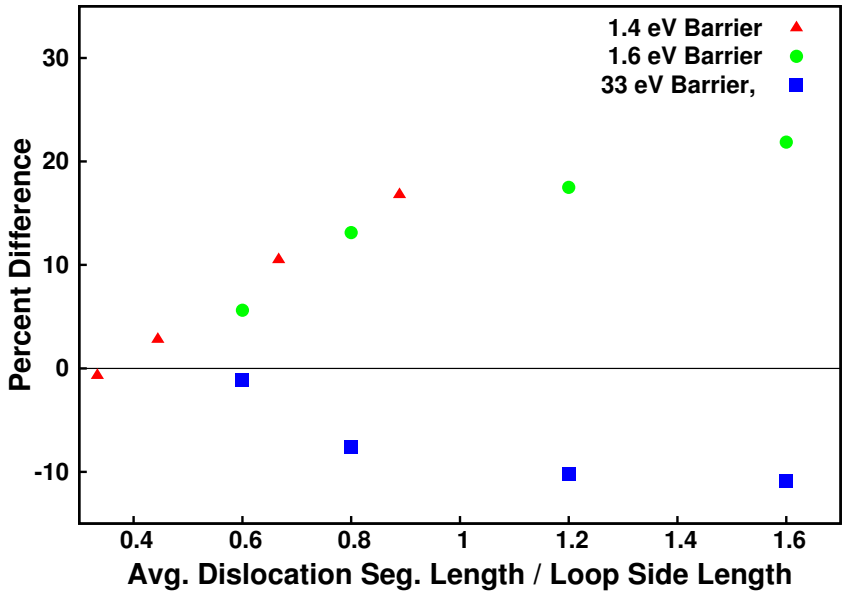

Figure 49: Effect of dislocation discretization on activation energy barrier. The percent change in activation energy relative to the lowest discretization is plotted against the average dislocation segment length normalized to the SIA loop side length.

bypassing for a select number of loop sizes, interaction geometries, and applied loads [217, 128, 156, 11, 122, 212]. A functional form of dislocation-SIA loop bypass activation energy has been calculated in one case [213] for dislocations crossing the center of $1/2\langle\bar{1}1\bar{1}\rangle$ glissile dislocation loops and voids. Atomistic calculations [217] have been performed for stress activated bypass of a $1/2\,[111]\,(1\bar{1}0)$ glide dislocation moving past a $\langle 001\rangle$ self-interstitial prismatic dislocation loop over all possible Burgers vectors and a selection of interaction geometries. During this process, the loop is often absorbed, highly deformed, or altered in Burgers vector. Predicting such processes requires either atomistic simulations or dislocation dynamics-based simulations with additional atomistically-informed rules for dislocation migration and loop reconstruction. Dislocation dynamics simulations of this processes have also been performed [194] and reproduce the stress for bypass in [217] within 18%. The authors used a molecular-dynamics informed dislocation mobility, but were required to use a trial-and-error simulations to find a different value of mobility to reproduce the reactions seen in [217]. The SIA loop deformation in these MD works is stress driven (and

therefore overdriven, potentially far from equilibrium), and would not necessarily be observed for thermally activated bypass. Here, the SIA loop structure is assumed to be preserved throughout the reaction, and the configuration studied in this chapter corresponds to the SIA loop Burgers vector in [217] where the SIA loop structure was deformed the least to enable the most direct comparison.

4.3.1 Elementary Case

The following sections rely on variations of the simulation case presented here. NEB calculations are typically performed between two known states which represent energy minima; however, as previously stated, the NEB method effectively finds the minimum energy pathway which represents the steepest descent [193] between two given states regardless of their energy relative to each other or the surrounding phase space. Simulating dislocation-SIA loop bypass using periodic atomistic calculations represents an infinite dislocation moving through a rectangular array of defects. Hence, the dislocation and obstacle densities are typically quite high, as are interaction stresses. While periodic boundary conditions are also used here, the volume is arbitrarily long in the glide direction with no increase in computational cost and thus representing a periodic linear array of obstacles in the slip plane is possible. The spacing of obstacles can also be made as large as desired in the present case. A periodic rectangular array of obstacles can also be simulated by performing the NEB calculation with two or more SIA loops arranged along the dislocation line in the direction of dislocation migration. From a physical perspective, simulating a periodic linear array provides a more accurate representation for the unit process of a single obstacle bypass event. In addition to the fundamental difference in the physical phenomena simulated using one or more loops, there are significant computational drawbacks associated with using two or more loops.

The simulations are performed with a single glide dislocation subject to a given

applied stress and relaxed to an equilibrium position using dislocation dynamics, serving as the initial NEB image position. The final image, the leftmost dislocation line in Figures 50 and 51, is a straight dislocation far from the loop for a single SIA loop, and is a duplicate of the first image for the two loop setup. Images are interpolated between the initial position and chosen final position, as shown in Figures 50a and 51a. The images are then evolved according to the force in Equation 91 until equilibrium is reached (Figures 50b and 51b).

The energy of each image is calculated as described in the Chapter 2 and is plotted in Figures 50c and 51c. The high number of images results in a smooth and well-sampled characterisation of the bypass process. The activation energy is defined as the largest energy difference considering all minima and the maxima after the given minima.

The differences between using a periodic linear or rectangular array of SIA loop obstacles are clear from Figures 50c and 51c. For zero applied stress, the second loop decreases the activation energy by from 91.5 eV to 87.2 eV, while increasing computation time. The difference could be reduced further with a greater separation distance and more images, but this would only increase computation time further by requiring more images to maintain the density of images. With an applied stress of 5 MPa, the difference is smaller with bypass activation energies of 60.8 eV (one loop) to 60.2 eV (two loops). In the following sections, a single SIA loop configuration is used resulting in faster computations as well as a process more representative of the unit bypass process.

4.3.2 Loop Size Effects

In this section, the dependence of bypass activation energy on SIA loop size is studied over a range of applied shear stresses, and from zero applied stress to the yield stress. A single square [001] SIA loop is used in a configuration identical to that in Figure

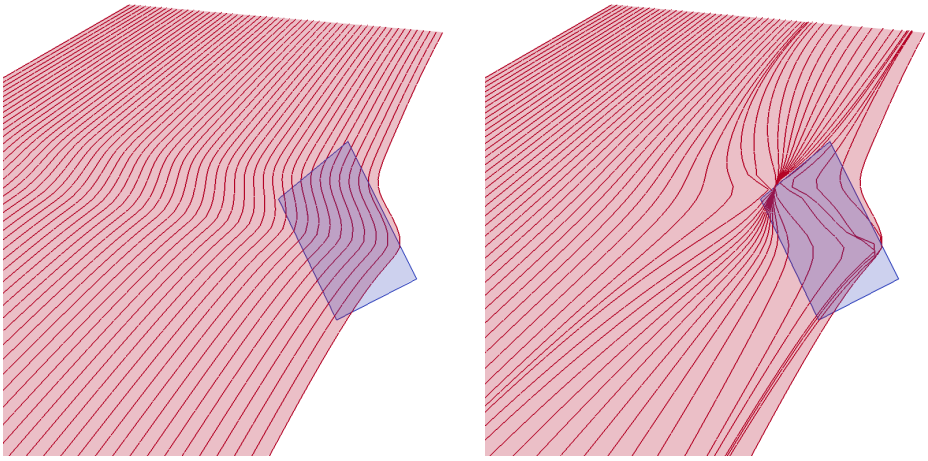

(a) NEB images before relaxation. (b) NEB images after relaxation.

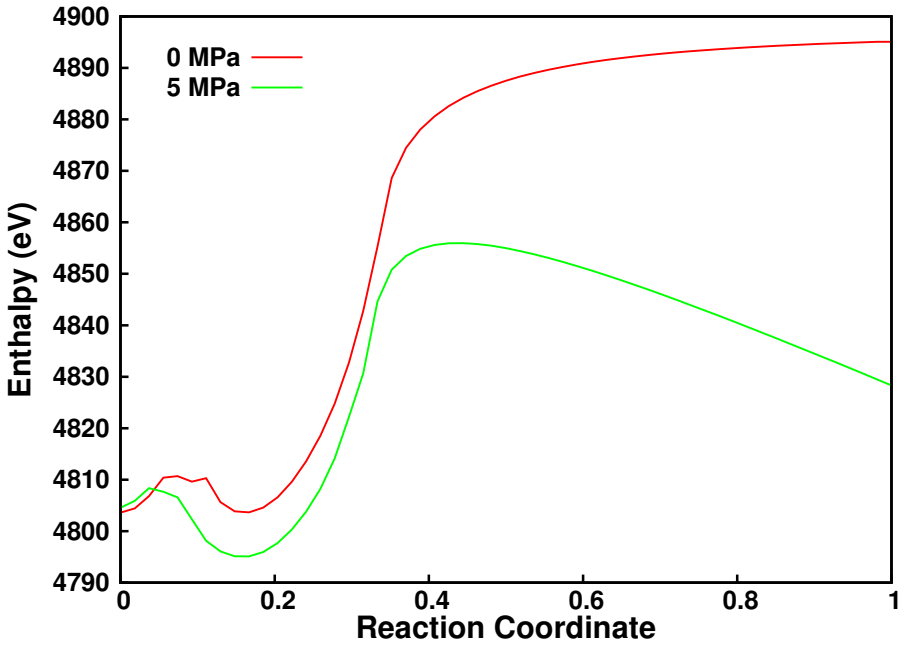

(c) Reaction energy profile.

Figure 50: NEB energy calculation for a $1/2\,[111]\,(1\bar{1}0)$ glide dislocation bypassing a [001] loop in a periodic linear array with a side length of 15.3nm under an applied stresses of 0 and 5 MPa. Planes of glide dislocation (red) and SIA loop (blue) are shaded accordingly.

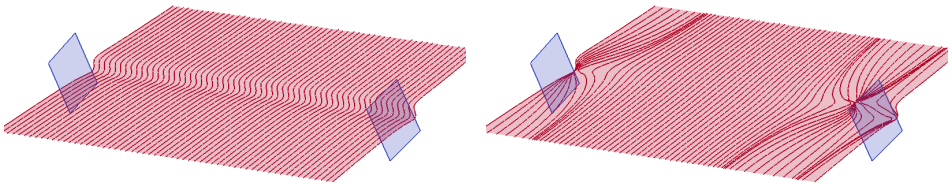

(a) NEB images before relaxation. (b) NEB images after relaxation.

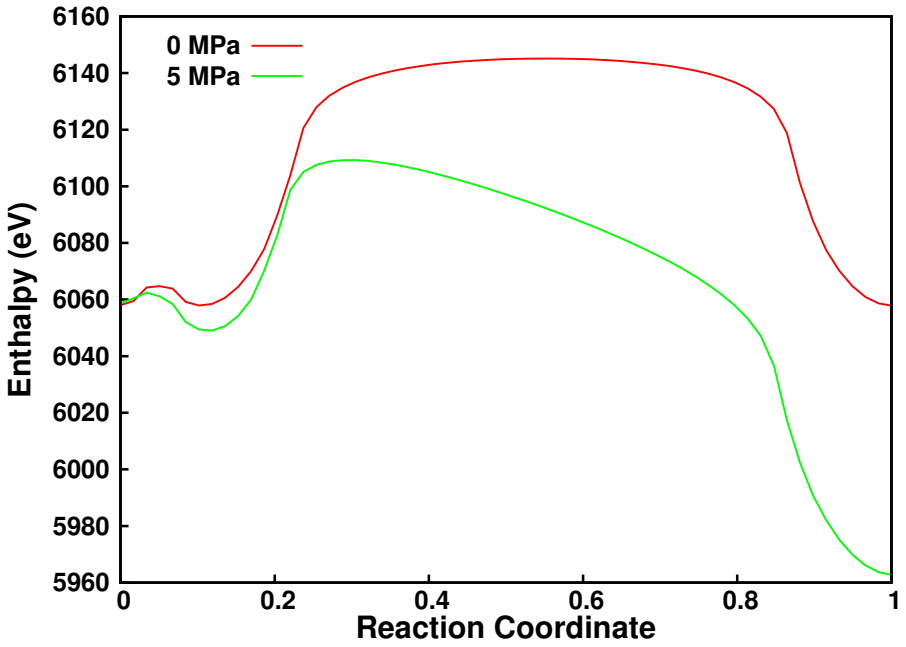

(c) Reaction energy profile.

Figure 51: NEB energy calculation for a $1/2\,[111]\,(1\bar{1}0)$ glide dislocation bypassing a [001] loop in a periodic rectangular array with a side length of 15.3nm under an applied stresses of 0 and 5 MPa. Planes of glide dislocation (red) and SIA loop (blue) are shaded accordingly.

50, and the activation energies are presented in Figure 52.

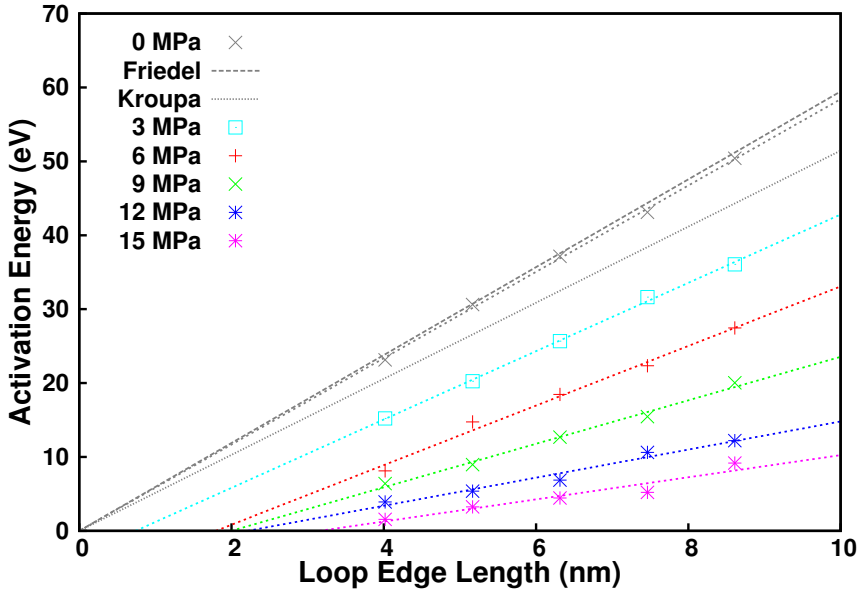

Figure 52: Activation energy for a $1/2\,[111]\,(1\bar{1}0)$ edge dislocation bypassing a [001] SIA loop with an offset of -0.3R and 172.2nm spacing as a function of size and applied stress. Each set of points for a given applied stress is fit with a linear equation.

A linear loop size-activation energy dependence is clear from Figure 52, with a decreasing slope with increasing stress. With increasing applied stress, a greater amount of work is performed by the dislocation migration resulting in a decrease in activation energy. The dependence of activation energy on applied stress is discussed in the following section. The x-intercept of each line also increases with applied stress, which represents the maximum loop size that can be bypassed spontaneously (without thermal activation) at the given stress level.

From a theoretical standpoint, Kroupa and Hirsch [107] developed an expression for the average maximum interaction energy between an infinite straight edge dislocation and a circular prismatic dislocation loop, i.e.,

$$E_{\max} \approx Gb^0b^1R/4, \tag{141}$$

where G is the shear modulus, b^0 the prismatic loop Burgers vector, b^1 the edge dislocation Burgers vector, and R the prismatic loop radius. Friedel [68] also estimated the interaction energy as

$$E_{\max} \approx Gb^2R/3. \tag{142}$$

Both of these equations predict a linear relationship between interaction energy and SIA loop size. Equations 141 and 142 assume a straight glide dislocation but in the simulations performed here, as the applied stress is increased the curvature of the dislocation increased; despite the significant deviation from the assumption of a straight dislocation, the linear fit model remained accurate. Both models, however, omit the work performed by the stress field acting on the migrating dislocation, and are therefore only valid in the absence of applied stress.

Equations 141 and 142 are valid for a circular loop, whereas [001] loops are square. To compare the calculations in this section to these two models, the radius R is selected that would result in a loop of equal area as a square loop of with length L. Doing so results in the same number of atoms in the SIA loop. A close fit with these estimates corroborates the orders of magnitude of the calculations performed here; however, Equations 141 and 142 are estimates themselves and only serve as an approximate validation.

4.3.3 Connection with Transition State Theory

Kocks, Argon and Ashby [104] developed a phenomenological viscoplastic flow rule for thermally activated dislocation bypass of barriers that employed the functional dependence of activation energy on applied stress, which is written as

$$\Delta G = F_0 \left(1 - \left(\frac{\sigma}{\sigma_0}\right)^p\right)^q, \tag{143}$$

where ΔG is the activation energy, F_0 the activation energy at zero stress, σ the

applied stress, σ_0 the yield stress, and the exponents p and q, which are functions of the shape of the activation energy barriers as well as the physical barrier distribution. Exponents p and q were found in [104] to be $\frac{1}{2}$ and 2 after fitting across many materials. Equation 143 enables an even higher degree of coarse-graining: the stress dependence, which is calculated explicitly for Figure 52, could be predicted without calculation if it can be shown to be valid. For three loop sizes, Equation 143 is fit using a calculated yield point and zero stress activation energy, and a fitted p and q. The result is shown in Figure 53.

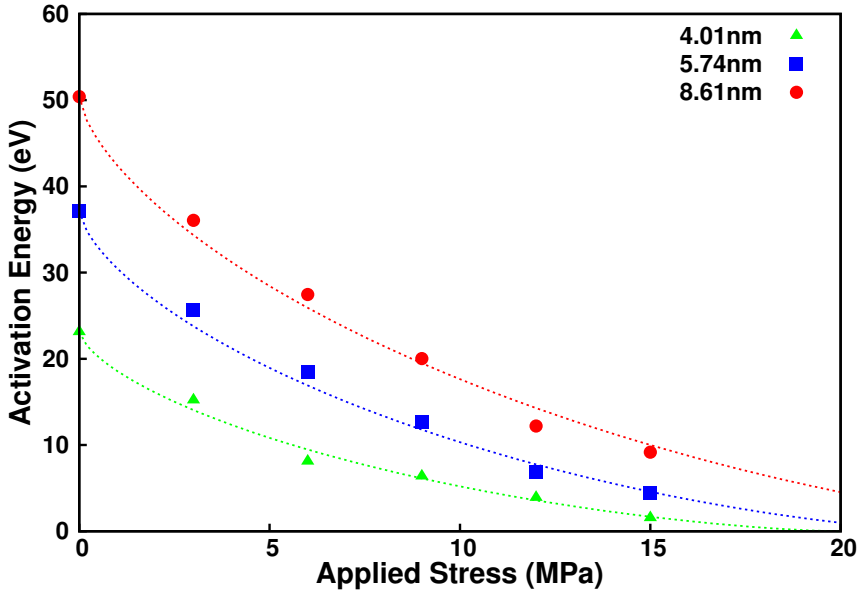

Figure 53: Equation 143 with fitted exponents $p = 1/q = \frac{2}{3}$ for a $1/2\,[1\bar{1}1]\,(011)$ edge dislocation bypassing a [001] SIA loop with an offset of -0.3R. SIA loop size given in legend.

The exponents found here are an exact match to that of the Mott-Nabaro-Seeger model [146, 72], which models an energy barrier with a sinusoidal form. The exponent differs from that of Kocks, Argon and Ashby, which may attributed to a variety of factors; Kocks, Argon and Ashby calculated the exponents for various bulk metals without irradiation whereas here the exponents are valid for a specific SIA loop configuration in α-iron. Fitting the exponents phenomenologically relies on an ensemble average of all interactions inside the material, whereas only a single dislocation

character, Burgers vector, and interaction geometry is simulated for results shown in Figure 53. The quality of the fit of Equation 143 in Figure 53 is promising but the same must be repeated for an ensemble of defects before the results can be applied to higher scale models, following our discussion of activation volume averaging of thermally assisted processes in the Introduction.

4.3.4 Interaction Geometry

This study is restricted to the interaction between a $1/2\,[111]\,(1\bar{1}0)$ edge dislocation with [001] SIA loops such the only free parameter with regards to geometry is the relative offset between the dislocation glide plane and loop center. The offset is defined as zero when the glide dislocation crosses the center of the loop, and increased positively with increasing vertical offset of the glide plane. The stress field of an SIA loop is proportional to r^{-3}, and therefore has a limited interaction volume. Here, the distance at which the elastic interaction becomes negligible is investigated by varying the off-axis separation distance. A total of 1058 activation energy data points are calculated and are plotted in Figure 54 as a contour plot. A minimum applied stress of 5 MPa is applied such that the dislocation reached an equilibrium position inside the simulation volume on the desired side of the loop in the case of a repulsive dislocation-SIA loop interaction.

Several qualitative properties of the activation energy map in Figure 54 are apparent; there are two peaks roughly centered about a zero offset, but the map is asymmetric and each peak as also asymmetric in its own right. Such asymmetry is anticipated because of the orientation of the SIA loop and the asymmetry of the edge dislocation stress field. The activation energy is non-zero for small distances away from the loop, but is negligible more than two times the loop side length away from the loop. The ability to map an energy landscape as in Figure 54 is a significant

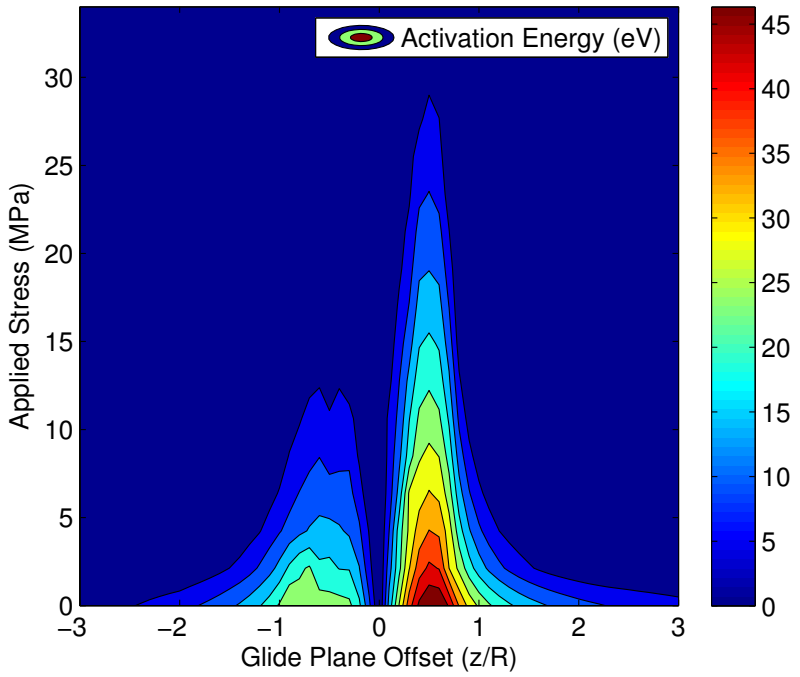

Figure 54: Activation energy for a $1/2\,[111]\,(1\bar{1}0)$ edge dislocation bypassing a 4.3nm [001] SIA loop with a spacing of 172 nm.

advancement given that such a calculation out of reach of atomistics due to computational resource requirements. From Figure 54, it is immediately clear that a full activation energy mapping of these defects is necessary because of the complexity of the energy landscape. A typical atomistic calculation may contain a single point or at most a single line on the landscape, which is clearly insufficient to describe the range of interactions seen in Figure 54. With the application of the NEB methods to DDD continuum calculations, such activation energy maps are now accessible and feasible to produce.

Considering the phase space covered by Figure 54, several key properties of the activation energy distribution are of interest. First, 76.9% of the stress/glide plane offset combinations are spontaneous. For the events with a non-zero activation energy barrier and assuming a limit of 2.0 eV as the upper threshold for thermal activation, 26.0% events may occur via thermal activation, and 74.0% of events will not. A

cumulative distribution of activation energies is shown in Figure 55.

The possible influences of continuum inaccuracies regarding the dislocation core description can be quantified by examining Figure 54. For any glide plane offset $\left|\frac{z}{R}\right| > \frac{1}{\sqrt{2}}$, the glide and SIA loop dislocation cores do not intersect and therefore any fine-scale effects from dislocation core structure and interaction are negligible. These interaction events account for 45.1% of events less than or equal to 2.0 eV. For $\left|\frac{z}{R}\right| \leq \frac{1}{\sqrt{2}}$, core interaction for the normal and activated states is dependent on the applied stress and glide plane offset. For $\frac{-1}{\sqrt{(2)}} < \frac{z}{R} < 0$, the nature of the reaction is such that the dislocation cores are significantly separated (> 5 core widths) normal and activated states and these events account for a further 36.4% of events with an activation less than or equal to 2.0 eV. Therefore, a total of 81.5% of events likely to occur via thermal activation are dominated by long-range elastic interaction and are robust against any possible omissions in the continuum theory of defects.

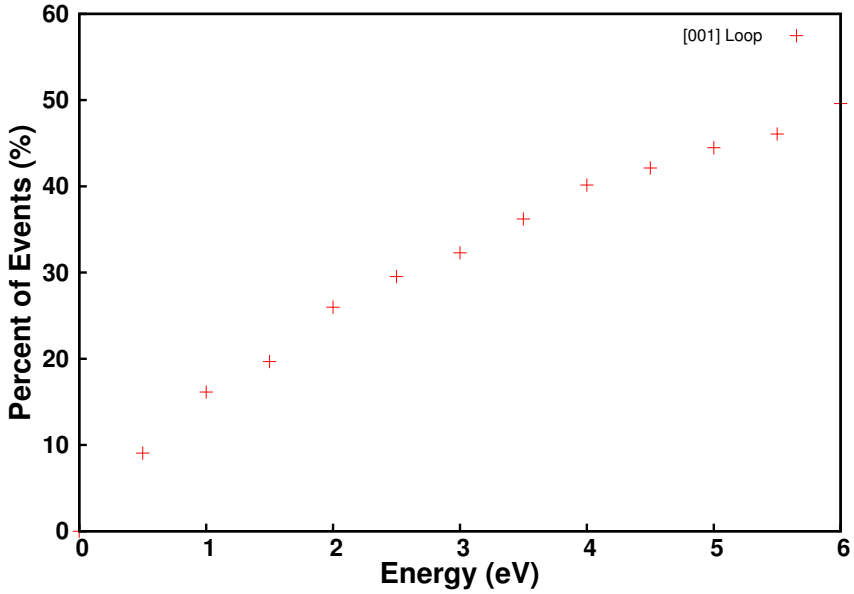

Figure 55: Activation energy cumulative distribution for events with non-zero activation energy for a $1/2\,[111]\,(1\bar{1}0)$ edge dislocation bypassing a 4.3nm [001] SIA loop with a spacing of 172 nm.

4.4 Obstacle Spacing

Dislocation obstacle density has a strong effect on athermal stress activated bypass, as dense obstacles force a dislocation to bow with high curvature, incurring a large penalty of self-energy. For regularly spaced defects, a $1/L$ dependence on obstacle spacing L is expected from a simple line-tension estimate of the activation stress of Orowan bowing. An SIA loop interacts with a glide dislocation in a more complex manner than a pinning point as assumed in the Orowan estimate, and a $y \propto -a\log(x) + b$ trend is clear in Figure 56.

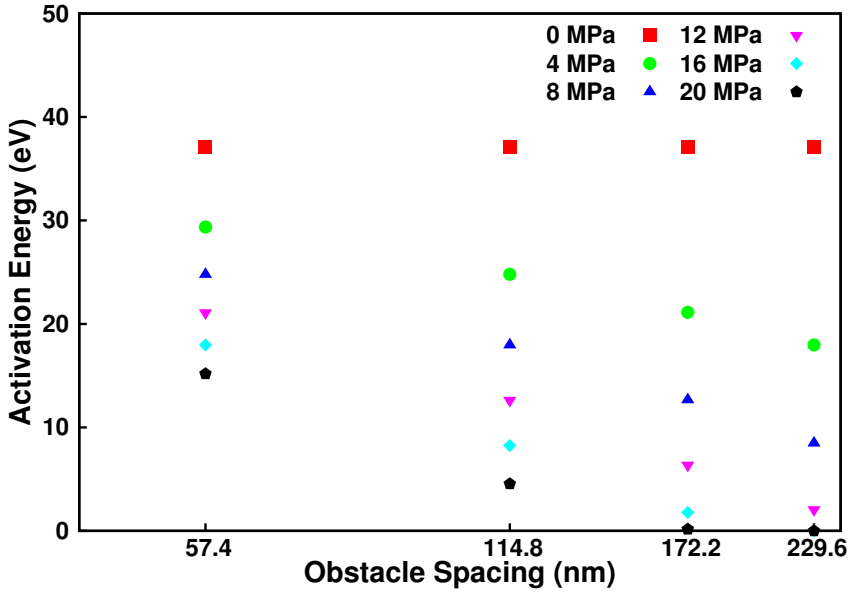

Figure 56: Semi-log plot of effect of obstacle spacing (simulation volume width) on activation energy for a $1/2\,[111]\,(1\bar{1}0)$ edge dislocation bypassing a 4.3nm [001] SIA loop with an offset of 0.8R.

The activation energy for bypass as a function of obstacle spacing and applied stress for a constant loop size and offset is shown in Figure 56. The trend of decreasing activation energy with increasing stress is explained by two factors: the increased self-energy of the glide dislocation due to the greater degree of bowing, and the increased energy dissipated by performing work under a greater applied stress. Consequently, the stress dependence of the process must be inherently dependent on dislocation

bowing, therefore factoring into the activation volume.

The role of obstacle spacing on bypass barrier energy is of particular importance regarding thermal activation because a single bypass event can cause a cascade of unpinning events. An unpinning event increases the obstacle spacing of the two neighbouring defects on the dislocation line and the energy barriers for some dislocation-SIA loop interactions, which are otherwise strictly stress-activated, may become feasible for thermal bypass. Events with a low energy barrier may also occur spontaneously in this case as well. In Figure 54, 26.0% of the events with non-zero energy are under 2.0 eV. Assuming a doubling of obstacle spacing with an unpinning event results in an activation barrier decrease by a factor of two, a total of 40.2% events are accessible via thermal activation.

4.5 Activation Volume

Activation volume, which describes the stress dependence of the activation energy, is defined rigorously by the relation:

$$\Delta V = -\left(\frac{\partial \Delta G}{\partial \tau}\right)\Bigg|_T. \qquad \text{(62 repeated)}$$

The activation volume for a simple dislocation reaction is defined from a statement of the Gibbs free energy [72], i.e.,

$$\Delta G = \Delta F - \tau \Delta V, \qquad (144)$$

where τ is the local stress, ΔV the activation volume and ΔF the Helmholtz free energy. For a straight dislocation, ΔV was expressed as bld [72], where b is the magnitude of the Burgers vector, l is the dislocation length, and d is the distance between the equilibrium position and the saddle point [190]. Equation 144 was derived assuming a constant ΔF; if it is a function of stress, the activation volume must derived using its definition because the work performed to create the activated state

must also be taken into account. In general, the physical meaning of the activation volume is process dependent because of these two contributions. During processes such as phase transformation, the activation volume corresponds to a physical volume change of the activated complex [176], whereas for dislocation unit processes, Gibbs [72] states that "dislocation movement changes the shape of a crystal without changing its volume, to first order." Therefore, in this case the activation volume is a thermodynamic quantity without a unique correspondence to a specific set of visually identified atoms.

For the reaction plotted in Figure 53, the activation volume calculated according to Equation 62 is on the order of 500 nm^3. For a point of comparison, the size of the simulation volume is 11.8×10^6 nm^3. Computationally expensive simulations often do not directly investigate stress dependence, but apply Equation 144 using an estimate of the activation volume. For example, the activation volume of a unit process such as a dislocation bypassing an array of impenetrable obstacles with spacing λ was assumed as λb^2 [45] and for an edge dislocation bypassing a $1/2\,[111]$ loop, the activation volume was taken as the length of the junction Burgers vector, approximately the loop diameter, multiplied by the square of the Burgers vector [213]. These approximations span orders of magnitude for a similar process and in comparison to the previous direct calculation of activation volume using Equation 62, are coarse approximations severely underestimating the activation volume. The activation volume for dislocation processes is a result of Eq. 62 rather than a simply identified collection of atoms comprising a physical volume [72]. This is increasingly problematic with increase of activation volume and the corresponding cooperative large scale atomic restructuring involved.

4.6 Prospects and Limitations of DDD-NEB

Augmenting mesoscopic simulations of dislocation migration, such as discrete dislocation dynamics, with an NEB calculation provides a computationally efficient method to investigate the energy barriers associated with thermally activated dislocation glide at a representative length scale. Atomistic calculations have been highly favoured for dislocation-SIA loop interaction simulations in the literature, and thus an analysis and comparison of these two methods is natural in this context.

4.6.1 Dislocation Core Parameter

The non-singular dislocation formulation of Cai *et. al.* [30] contains a parameter a representing the core width in Equation 5. The value of a is an input to DDD simulations that must be provided from atomistic calculations or experiments. Lacking a definitive value of the core width, a value of one lattice spacing was taken for the studies performed herein. The sensitivity of the activation energy values to this parameter is therefore very important such that one can gauge the necessary accuracy in estimating this parameter. Activation energy sensitivity to dislocation core spreading is analyzed by repeating the calculations shown in Figure 52 with core spreading radii of 0.1a, 0.5a, and 1.5a. Greater core spreading influences the energy landscape by decreasing the core energy as well as reducing the self-force and allowing the dislocation to curve more easily (lower energetic penalty).

As seen in Figure 57, the core width was varied over a range of [0.1-1.5]a, and the activation energy for the reaction was seen to increase with decreasing core width. Core width (and thus core energy) has a much stronger influence for bypass processes with direct core reaction (Fig. 57a) than without (Fig. 57b). Importantly, this effect scales with the total energy of the reaction such that for low energy barriers which are accessible in terms of thermal activation, the possible effect is minimized. Even further, it will be shown that the majority of low energy events are as in Fig. 57b

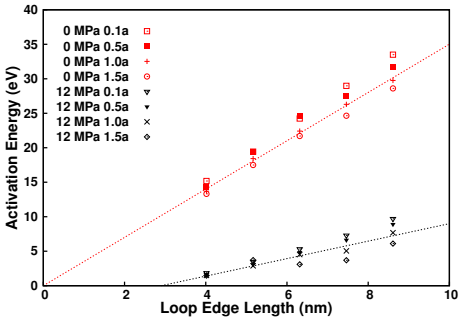

(a) Direct dislocation-SIA loop core interaction.

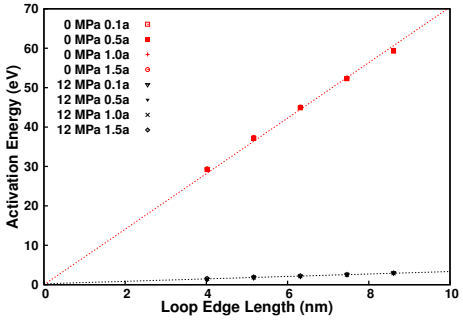

(b) Dislocation-SIA loop interaction without direct intersection. Points are overlapping for each loop size/applied stress combination.

Figure 57: Effect of core width parameter on activation energy for a $1/2\,[111]\,(1\bar{1}0)$ edge dislocation bypassing a [001] SIA loop. A linear fit is provide for a core width of $1a$. The configurations were specifically chosen as one with a high degree of close-range dislocation-SIA loop core interaction, and one without direct intersection (i.e. strictly elastic field interactions.)

and have negligible dependence on core energy.

For an edge dislocation in α-iron, the elastic energy per atom plane (assuming elastic isotropy) is approximately 6 eV and the core energy not captured by continuum theory is estimated to be on the order of 1 eV [96]. Such an additional contribution to the dislocation self-energy causes a greater resistance to bowing (and the associated increase in dislocation line length); however, the influence on the energy barrier is likely significantly less than the 18.3% difference in dislocation energy. Figure 57 shows that that the energy barrier dependence on dislocation core width, and therefore core energy, is weak. Varying the core width from 0.1a to 1.5a decreases the system energy by 50%, yet changes the energy barrier in the worst case by less than 20% for large energy barriers and far less for events accessible by thermal activation. Therefore, the process of a dislocation-SIA loop bypass is dominated by elastic interactions and relatively insensitive to details of the dislocation core.

4.6.2 Comparison to Molecular Dynamics

Atomistic studies of dislocation-SIA loop interactions have been heavily favoured the stress driven regime in past works. A novel atomistics NEB calculation, for which all calculations and figures are generously provided by Enrique Martinez, provides a point for a direct comparison with the DDD-NEB method to provide valuable insight into the physical fidelity of the DDD-NEB method, and even further, whay could be gained from studying processes of this nature using mesoscopic methods. The following molecular dynamics and NEB calculations were run to provide such a point for direct comparison. A sample with a $1/2\,[111]\,(1\bar{1}0)$ edge dislocation and a square [001] SIA loop of approximately 3.3 nm in side was built with the dislocation glide plane cutting the SIA loop close to one of its corners (offset of approx. $z/R = 0.6$. The sample has free surfaces in the direction normal to the dislocation glide plane. The width of the simulation volume in the direction of the dislocation line is 28.8 nm and the number of atoms is 1,287,851. Such a large number of atoms was chosen to minimize the effect of the image forces on the dislocation. The sample was relaxed using a conjugate gradient algorithm, with the Ackland 2004 interatomic potential for Fe [1] using the MD code LAMMPS. The simulation configuration is shown in Fig. 58c. Subsequently, strain has been applied on the free surfaces in the direction of the dislocation Burgers vector in the sample at 10K at a strain rate of 10^7 s^{-1}. The resulting stress-strain curve is shown in Fig. 59b, along with the evolution of the energy in the system.

As seen in Figures 58b and 58c, the equilibrium configurations near the yield point are similar but not identical between MD and DDD and such is to be expected given the complex nature of dislocation motion at low temperatures in BCC metals. Screw dislocations dislocations have a non-planar core structure resulting in a significantly higher Peierls energy than an edge dislocation [207]. A strong difference in dislocation mobility as a function of temperature and dislocation character results, which can be

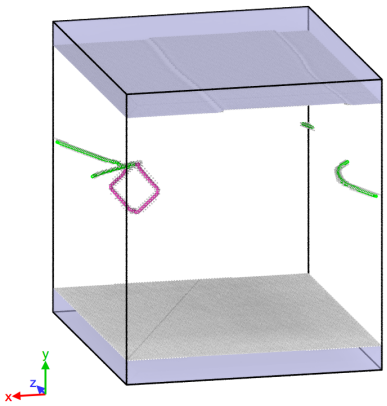

(a) NEB images before relaxation.

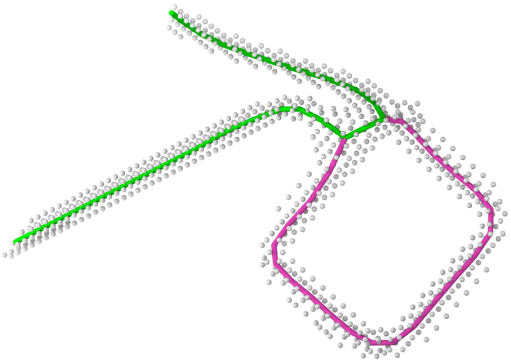

(b) NEB images after relaxation.

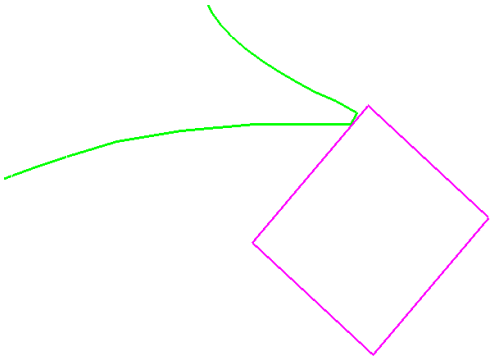

(c) Configuration found using DDD simulation.

Figure 58: Atomic configuration of an edge dislocation interacting close to a corner of a [001] self-interstitial atom loop. The green line denotes a $1/2\,[111]\,(1\bar{1}0)$ dislocation whereas the pink line refers to a [001] dislocation.

Temperature	DDD (MPa)	MD (MPa)	Percent Diff.
10K	520	566.6	-8.2 %
300K	170	190 [217]	-10.2 %

Table 2: Comparison of stress values to cause spontaneous dislocation-SIA loop bypass as calculated by DDD and MD.

modelled using the appropriate mobilities in a DDD simulation [154]. The DDD simulation does, however, capture the essential behaviour in the process and similar elastic interactions between the two cases are evident.

The first point of comparison between atomistic and DDD calculations is the stress to cause athermal bypass (yield stress). This represents the point at which the activation barrier disappears, and is a parameter in the model for activation energy stress dependence in Section 4.3.3. Using molecular dynamics, the stress to cause spontaneous loop bypass (yield point) is seen to be 566.6 MPa in Figure 59a. Before a corresponding value can be directly computed using DDD, the nature of the temperature effects on dislocation motion, which includes non-linearities for difference dislocation characters, for each must be included. These effects can have highly complex manifestations on the dislocation morphology as the Peierl's energy for edge and screw segments differs significantly [207]. In DDD, a common method of coarse-graining these effects is through an isotropic friction stress [175] . The data point calculated here at 10K and an athermal bypass stress calculation at 300K in the work of Terentyev *et.al.* [217] act as the points of comparison for DDD. The friction stresses used in to compare to these points are necessarily inputs from experiments or atomistic calculation. Here, they are taken as experimental value for flow stress at 10K of 350 MPa [203, 202, 109], and a value of 25 MPa at 300K corresponding to the observed Peierls' stress in MD [162]. The dislocation-loop orientation was reproduced in DDD (with the appropriate simulation dimensions for each comparison) with a low strain rate applied to find the yield stress. The values and relative differences are shown in Table 2.

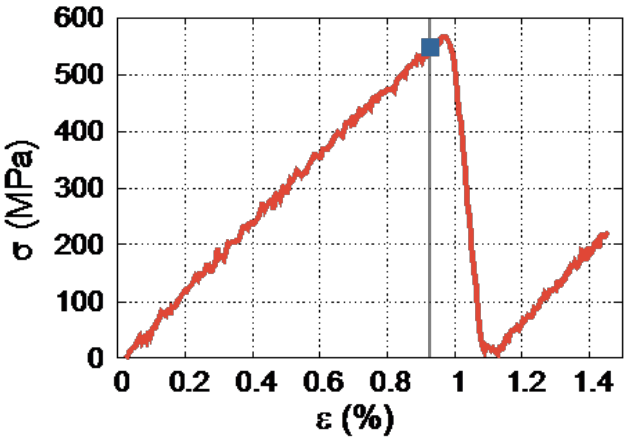

(a) Stress-strain curve for a edge glide dislocation bypassing an SIA loop.

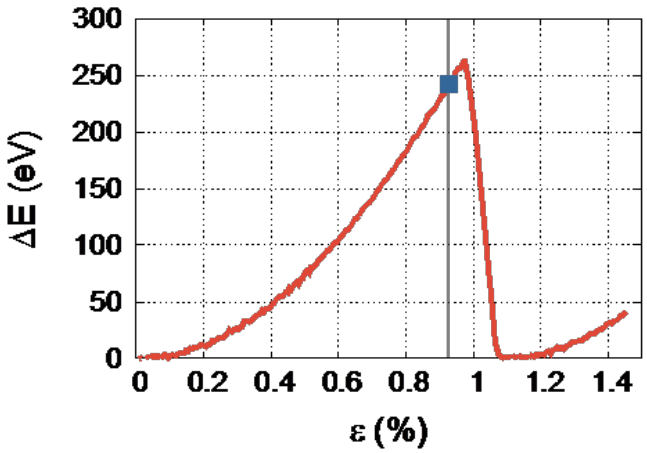

(b) Energy-strain curve corresponding to (a).

Figure 59: Figure 2. (a) Stress-strain and (b) energy-strain curves for the process of the dislocation overcoming a square [001] SIA loop with a side length of 3.3nm. The vertical line and square point show the configuration picked to calculate the energy barrier.

Without any fitting parameters and using a dislocation core parameter equal to 1a as used elsewhere in this chapter, a close match between the yield points for a specific reaction involving direct glide dislocation-SIA loop core contact is seen with at most 10% difference in value. Reducing this difference may be possible by changing the discretization and core parameter with larger simulation volumes and SIA loop sizes, but for the current configuration the an exact match is not possible.

The second point of comparison is between a value of activation energy calculated at a stress near the yield point. The atomistic NEB calculation was performed at constant strain, in contrast to the constant stress DDD-NEB calculations. The reason for this is because the stress to drive the dislocation is created by displacing atoms and maintaining a constant average stress would require an iterative procedure to determine these displacements for each image, consequently greatly increasing the computational time. In contrast, a constant stress calculation was performed using DDD-NEB as this is more physically relevant: in a bulk material, the slip of a single dislocation will have negligible effect on the macroscopic stress state and the activation energy barrier should be calculated under these conditions. For a constant strain calculation, the applied stress decreases as the dislocation glides to accommodate the applied deformation and therefore from a qualitative standpoint, one can expect a larger activation energy barrier under constant strain because the work done by the dislocation decreases as the applied stress decreases.

For the NEB calculation, the dislocation configuration at 0.93% strain was chosen (corresponding to 547.4 MPa) and relaxed using a conjugate gradient algorithm. The resulting configuration shows the dislocation pinned at the loop (Fig. 58b). From that energy minimum, the sample was slowly heated up for the system to escape from the minimum. At a given number of steps the configuration is minimized. We obtained an intermediate minimum and the final ground state as the dislocation overcomes the obstacle. An NEB calculation was performed between each of those configurations,

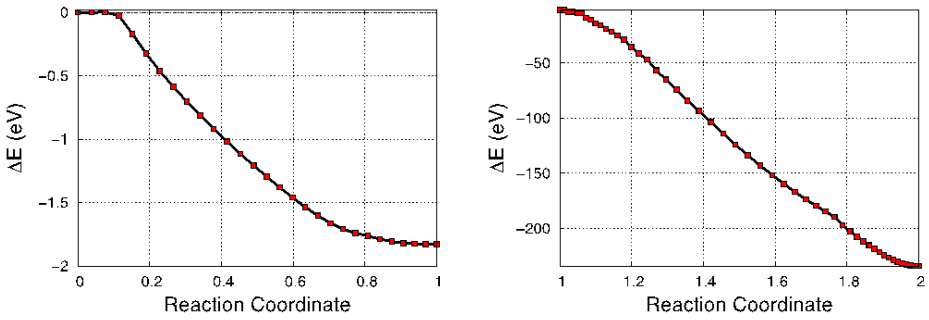

(a) (b)

Figure 60: The minimum energy paths calculated through NEB between different configurations escaping from a minimum close to the critical point.

i.e., the initial minimized configuration at the 0.93% strain level and the intermediate minimum (Fig. 60a) and between the intermediate minimum and the final ground state (Fig. 60b). The landscape is particularly rough and a large number of images are required to obtain meaningful activation energy barriers. The first barrier is 0.002 eV, while the second is approximately 0.007 eV. The barrier in both cases was close (in reaction coordinate space) to the initial configurations, and therefore a large number of equally spaced images were needed to capture the barrier.

The spatially confined simulation configuration that is necessary in order to be able to perform an atomistics calculation of bypass activation energy presents several challenges for the DDD-NEB method. Segment discretization must be taken on the order of a few lattice spacings, which requires very fine discretization in time to maintain numerical stability. Particularly severe numerical instability was observed with dislocation segment length approaching the core size parameter in the non-singular formulation, which establishes a lower bound on the length scales that one can access with confidence. Furthermore, the earlier approximations made to apply the closed form energy calculation enabled with the non-singular formulation are unlikely to be valid at such high stresses. Specifically, a cross term between the micro and macro stress states that is on the order of a few percent in the tens of MPa increases with applied stress to become too significant to neglect at these stress levels. To avoid

inaccuracies from this approximation, the functional form of the stress dependence of the activation energy shown previously to be valid for dislocation-SIA loop bypass is used to estimate the activation energy for bypass at 96.6% of the yield point (as calculated using in the atomistics). The activation energy at zero applied stress was calculated using a zero friction stress, modelling a sample under 350 MPa applied stress and a 350 MPa friction stress. The two instances are not identical, but this is a minor approximation under these simulation conditions with the vast majority of dislocation glide in the direction of the applied stress. The value obtained was 238.9 eV resulting in an activation energy of 0.8 eV at 96.6% of the yield point. The friction stress increases the activation energy in the absence of applied stress by over 200 eV compared to the case in the absence of friction stress. The difference between the activation energy values in both relative and absolute terms is notable, but it is important to remember that these are the least favourable simulation conditions under which one can perform a DDD-NEB calculation. In terms of the total energy barrier, the DDD-NEB predicts an activation energy barrier 0.3% whereas atomistic NEB predicts an activation energy barrier of 0.002%. For a smaller activation barrier such as those calculated in this chapter, such a difference is negligible because both events would have a mean waiting time for thermal activation lower than a typical time-step for a dislocation dynamics simulation.

The energy-strain curve in Figure 59b is not equivalent to activation energy for thermal processes as the system is significantly out of equilibrium; however, the magnitude of the energy values is nevertheless noteworthy in that dislocation-SIA loop bypass activation energies can easily reach hundreds of eV in the unit case, yet thermally activated bypass is possible following changes in the friction stress, the driving stress or long range dislocation morphology (e.g. dislocation-obstacle bypass elsewhere on the dislocation line). Here, we have selected a configuration very close to the yield point to perform the NEB calculation because we must find the final state

for the process. An additional challenge for an atomistics NEB calculation is that the final state following bypass must be found before performing the calculation; this was performed by heating the sample until thermally activated bypass occurs and recording the state following bypass.

Regarding the atomistic NEB calculations, the large number of images with the large number of atoms makes such simulations computationally expensive. Exploring the whole phase space in terms of the offset between the dislocation and obstacle, dislocation length or SIA loop size is infeasible if not impossible. Large energy barriers cannot be probed as the final state cannot be reached via thermal activation, and the boundary conditions and choice of interatomic potential introduce a degree of uncertainty, as mentioned in a previous section. Moreover, a statistically representative minimum energy path for a dislocation to overcome a distribution of obstacles with defect densities comparable to experiments is far beyond the reach of contemporary MD capabilities. A coarser mesoscopic model is necessary to obtain statistically meaningful deformation pathways for dislocation motion in the presence of obstacles. A DDD-NEB approach is therefore a computationally efficient method to obtain good estimates (if not extremely precise values) of activation energy for thermally activated reactions involving dislocation rearrangement. The approximations involved with a continuum dislocation formulation such as isotropy, a simplified core structure, and dislocation segment discretization are trade-offs between physical fidelity and computational burden. We show here that for a decrease in accuracy (that remains to be formally and comprehensively quantified), the entire domain of thermally activated dislocation motion of realistic defect configurations is opened to investigation.

4.7 Attempt Frequency Calculation

The adopted methodology applies transition state theory (TST) to describe complex, fine-scale processes using the Arrhenius equation. The challenge in applying this

approach is in its reliance on an accurate characterisation of the activation energy and attempt frequency for the thermally activated processes - the attempt frequency for processes involving dislocation rearrangement must be established before one can apply the Arrhenius equation. Friedel [67] first derived the fundamental frequency of vibration for a dislocation described using a line tension model (approximating a dislocation as a string with tension Γ). Granato *et. al.* [78] developed a significantly more advanced analysis for attempt frequencies for dislocation-obstacle bypass events, deriving bounds and estimates for attempt frequency, which were summarized at the beginning of this section. However, direct numerical calculations using a more accurate dislocation description have yet to be performed.

This study aims to determine the attempt frequency for a dislocation bypassing a self-interstitial atom (SIA) loop as described using the continuum theory of defects. To this end, the study is divided into three sections. First, the fundamental modes of a finite dislocation segment with pinned ends are characterized and compared to line tension predictions for the fundamental frequency as well as the functional form of the spectrum. Next, the attempt frequency for a finite dislocation segment bowed against an SIA loop is determined and compared to theoretical estimates where possible. A more realistic configuration of an infinite dislocation bowed against an array of SIA loops is then considered and the attempt frequency determined. The study concludes with discussion on the sensitivity the numerical calculation of attempt frequency and the possible implications on predictions of the reaction rate.

4.7.1 Numerical Approach

As stated previously, the Arrhenius equation was generalized to many-body processes in the work of Vineyard [234] in order to extend it to solid state processes. By considering the ratio modes of of configurational partition functions for the normal and activated states for an M-dimensional system and assuming each degree of freedom

can be approximated a harmonic oscillator, the rate of phase points crossing the saddle point can be written as

$$k = \nu_a e^{-\Delta G/k_B T} = \nu_1 e^{\Delta S/k_B} e^{-\Delta H/k_B T} \tag{57}$$

where

$$\nu_a = \nu_1 \prod_{i=2}^{M} (\nu_i/\nu_i'). \tag{63}$$

and ν_1 is the fundamental attempt frequency. The factor $\prod_{i=2}^{M}(\nu_i/\nu_i')$ is called the entropic factor as it explicitly accounts for the entropy change during the process. Further work in the field of the continuum theory of defects resulted in dislocation attempt frequency estimates, particularly by Granato *et. al.* [78] who characterized the vibrations of a dislocation pinned to a single defect and continuously pinned dislocations. Their work remains at the forefront of dislocation vibration characterization, yet relies on line tension approximations in which dislocations are modelled as a line with an associated energy per unit length. Dislocations have complex elastic self-interactions which cannot be captured using a line tension model, and therefore further investigation is required to determine if line tension approximations are appropriate within the context of this phenomenon and thus whether or not the close form calculations in [78] can be applied to estimate the attempt frequency of a more physically realistic system.

Assuming a harmonic potential and negligible damping for small excursion from equilibrium, the vibrational characteristics of dislocations can be analysed by constructing the Hessian matrix and solving for its eigenvalues and vectors. To calculate vibrational frequencies, the Hessian must be mass-weighted; Granato *et. al.* estimated dislocation mass per unit length as $\frac{\mu b^2}{c^2}$ with an assumed line tension of μb^2 [78], which is also used here. The effective nodal mass can then be approximated as the average length of the connected segments multiplied by the mass per unit length.

The potential energy of the system with degrees of freedom x_i can be written as a Taylor expansion about the origin as

$$E(x_i) = E(0) + \frac{\partial E}{\partial x_i} x_i + \frac{1}{2} \frac{\partial^2 E}{\partial x_i \partial x_j} x_i x_j + ... \tag{145}$$

Assuming a harmonic potential, all terms above second order are negligible which was confirmed to be valid for small dislocation line perturbations. For an equilibrium configuration, the gradient terms are exactly zero. If the kinetic energy of the system can be written as

$$T = \frac{1}{2} M_i \dot{x_i}^2, \tag{146}$$

where m_i is the mass for degree of freedom i, then applying the conservation of energy while assuming that damping is negligible for small excursions from equilibrium requires that

$$M_i \ddot{x_i} = -\frac{\partial^2 E}{\partial x_i \partial x_j} x_i \tag{147}$$

The vibration frequencies and modes of the system are then defined by the eigenvalues and eigenvectors of the Hessian matrix of the system. A Hessian matrix is defined in general as a matrix of second order partial derivatives of a scalar function. Here, the scalar function is the energy of the system and can thus be defined as

$$H_{i,j} = \frac{\partial E}{\partial x_i \partial x_j} \tag{148}$$

where E is the system energy, and x_i is one of the degrees of freedom of system. For dislocations described using the continuum theory of defects, the closed form Peach-Koehler force provides access to the analytic first derivatives of energy with respect to the dislocation node position resulting high precision with low computational requirements. Such an optimization reduces the number of energy calculations by a

factor of two, and has the advantage of a closed form first derivative. Using a centered derivative only two force evaluations are required per entry in the Hessian and no further approximations beyond derivative discretization are required. To calculate vibrational frequencies, the Hessian must be mass-weighted:

$$H^m_{i,j} = \frac{H_{i,j}}{\sqrt{M_i M_j}} \tag{149}$$

Granato *et. al.* estimated dislocation mass per unit length as $\frac{\mu b^2}{c^2}$ with an assumed line tension of μb^2 [78]. The effective nodal mass can then be approximated as the average length of the connected segments multiplied by the mass per unit length.

Performing these calculations in conjunction with the DDD-NEB approach provides a clear path for spatially and temporally coarse-graining dislocation bypass events. First, a dislocation dynamics simulation is performed to equilibrium, which is referred to as the normal state. An NEB calculation [102, 89] is performed assuming a final state of a bowed dislocation segment pinned at its ends for calculations using a finite dislocation segment or a straight dislocation beyond the obstacle in the case of an infinite glide dislocation. The NEB method determines the minimum energy pathway for the transition, and therefore the dislocation configuration at any point during the reaction including the activated state. The Hessian is calculated using a curvilinear coordinate system along the dislocation line taking the degrees of freedom as the directions normal to the dislocation line at the dislocation nodes. Tangential dislocation node movement corresponds to a change in line discretization and incurs no energetic penalty so such motion is excluded from the vibration analysis.

4.8 Perfectly Pinned Dislocation Segment

To elucidate the nature of dislocation vibrations, the frequencies and modes of a pinned finite straight dislocation segment are calculated in the absence of applied stress. A line tension dislocation is analogous to a vibrating string with fixed end

conditions with a Debye frequency cut-off (equal to the dislocation length divided by the Burgers vector magnitude). Consequently, modal frequencies are discretized and scale linearly with the mode and inversely with the dislocation length. Figures 61 and 62 reveal the differences of this simplified model in comparison to dislocation oscillations.

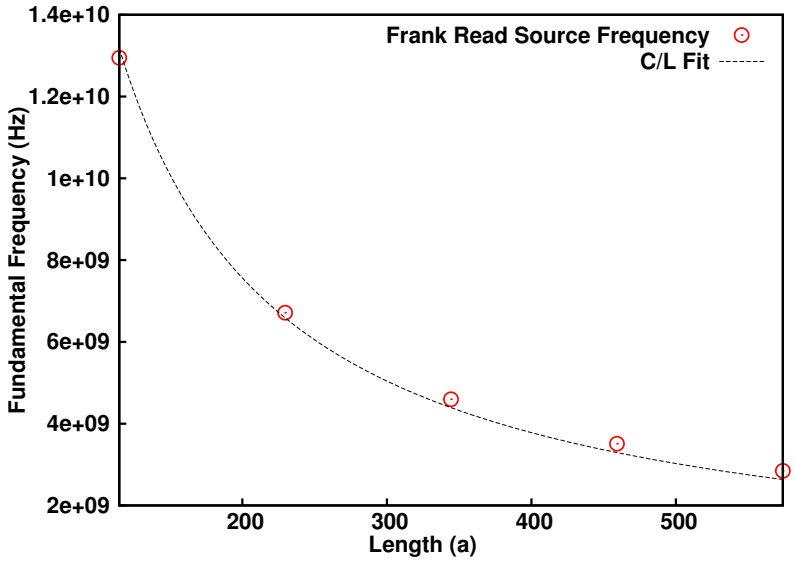

Figure 61: Fundamental frequency length dependence is well fit as $f \propto 1/L$.

Figure 61 shows that fundamental frequency of dislocations exhibit a $1/L$ dependence in agreement with the prediction using a line tension model by Friedel [67]. However, contrary to the linear increase predicted by line tension approximations, the dislocation vibration frequency spectrum exhibits a power law dependence as seen in Figure 62a. The exponent of the power law is dislocation length dependent and converges to an asymptotic value by a length of 2000a as seen in Figures 62a and 62b. At this length, the frequency spectrum of an edge dislocation with is well described using a functional form $\nu(m) = Am^n$ where m is the mode number, and taking A equal to the fundamental frequency and n =0.867. Pure screw character dislocation modal frequencies have a spectrum functionally similar to an edge dislocation, as shown in Figure 62a. As such, a screw dislocation could be modelled as an

edge dislocation using a shorter effective length.

Deviations from a linear mode-frequency relation are likely due to dislocation self-interaction; elastic self-interactions become significant with a short wavelength, which line tension models inherently omit. The change in dislocation character in the perturbed configuration undoubtedly influences the vibrational properties as well. Figure 62b shows the deviation of the modal frequency from a linear spectrum on a semi-log axis and reveals the power law nature of a dislocation's vibrational spectrum approaching an asymptotic value with increasing line length. The derivation of Equation 63 by Vineyard [234] did not require assumptions on the modal frequency distribution and therefore remains a valid approach by which to analyze the attempt frequency of dislocation processes. Models applying line tension approximations may remain relevant as well if the ratio of the frequencies ν and ν' accurately represent the true dislocation behaviour but otherwise do not describe dislocation oscillations well, particularly at higher order modes.

4.9 Application to SIA-loop bypass

Under nuclear irradiation, high energy particles cause SIA loops and voids to form in α-iron, which causes a significant increase in yield strength as seen in experimental [59, 259, 91, 114, 21] and simulation studies [155, 4, 197]. Such defects induce material hardening by acting as obstacles to dislocation motion, and the fine-scale interactions between dislocation and defects in the material determine the degree of hardening. Few studies have examined the activation energies of such processes; atomistic studies have only examined stress-activated bypass of pure edge/screw dislocation with SIA loops α-iron [217, 128, 156, 11, 122, 215, 217, 14, 85, 163, 212, 218].

Reaction attempt frequencies used in the Arrhenius equation are often far less rigorous, resorting to heuristic arguments. Rigorous derivations of this parameter include that of Granato *et. al.* [78] elucidated the nature of dislocation vibrations

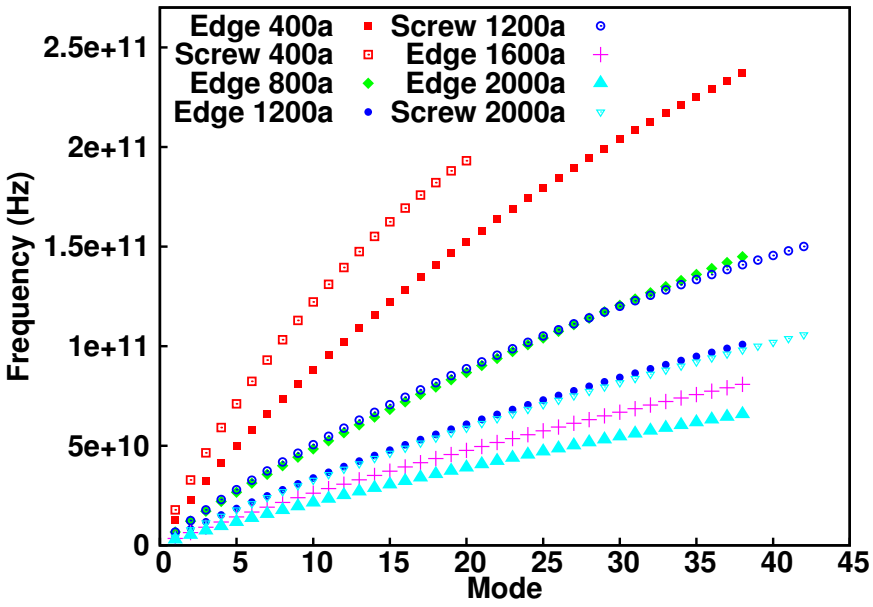

(a) Length dependence of the modal frequencies of a perfectly pinned dislocation segment (pure edge or pure screw type).

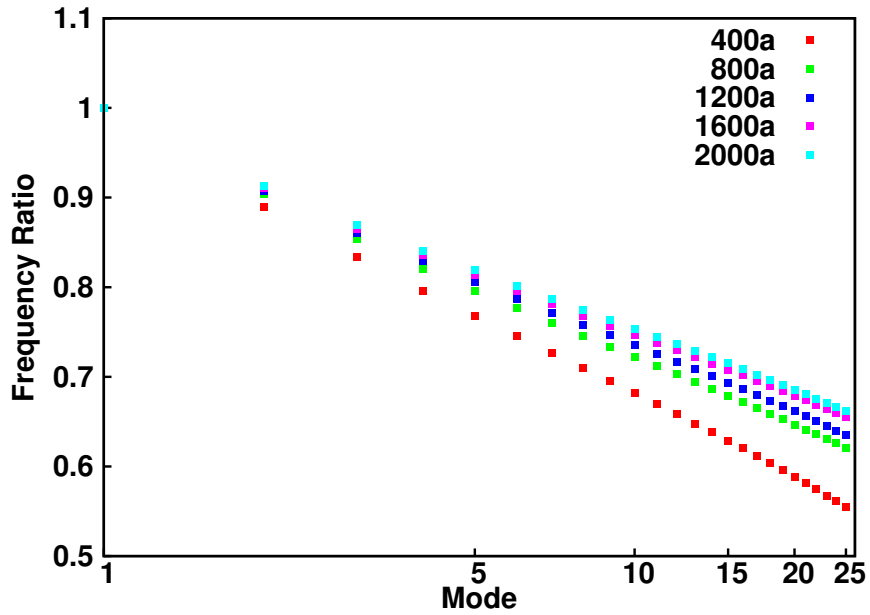

(b) Deviation of modal frequencies from a linear spectrum for a pure edge dislocation.

Figure 62: Vibrational characteristics of a dislocation perfectly pinned at its ends.

with a single infinitesimal pinning points using a line tension dislocation model. In this case, an SIA loop acts as the obstacle, constituting a much more complex obstacle than an infinitesimal pinning point. First, a bowed dislocation segment pinned to an SIA loop is studied to facilitate comparison to the work of Granato *et. al.*, followed by the more physically realistic case of an infinite dislocation pinned to a regular linear array of SIA loops.

4.9.1 Perfectly Pinned Dislocation Segment Bypass

To best replicated the work of Granato *et. al.*, a single SIA loop is placed at the center of a finite dislocation segment pinned at its ends and an applied stress is necessary to create a saddle point for obstacle bypass. The resulting normal and activated configurations are shown in Figure 63.

Figure 63: Dislocation configuration for a finite dislocation segment (red) in the normal (lower line) and activated (upper line) states while bypassing an SIA loop (blue). The loop is viewed on edge so it appears as a line, and is a repulsive obstacle in this configuration.

In this configuration, the even modes of the normal and activated states are expected to cancel in Equation 63 and contribute very little to the entropic effect as the middle of the dislocation is a node for even frequencies. The influence of the odd modes is more challenging to predict from the results of Granato *et. al.*, because of the interaction between the defect and the dislocation is not confined to a point of infinitesimal size. The calculated entropic factors are presented in Figure 64 as a function of the number of modes included in Equation 63.

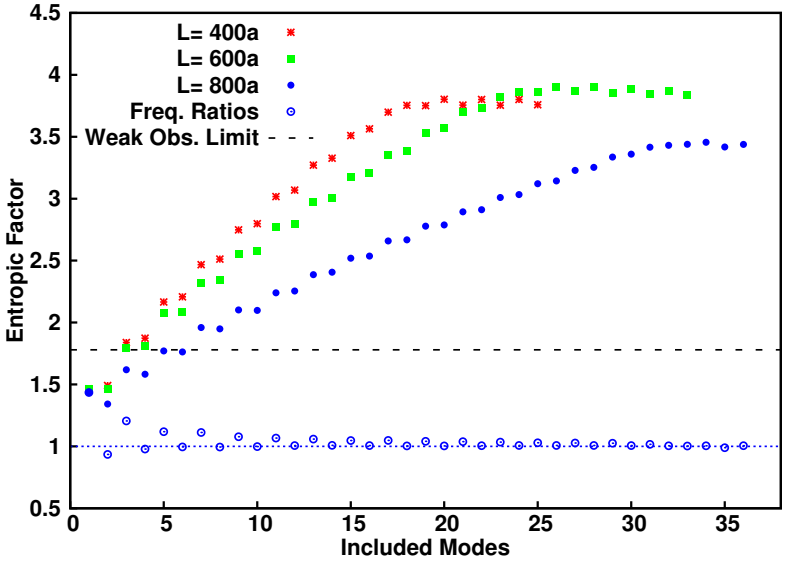

Figure 64: Entropic factor for three dislocation segment lengths bypassing a 20a side length SIA loop. Included modes refers to M in equation 63.

Figure 64 reveals convergence to an entropic factor is independent of segment length resulting in an attempt frequency scaling with $1/L$. A length-independent entropic factor case corresponds closely to that of a weak strength obstacle as described by Granato *et. al.*, who approximated the entropic factor in the limit of weak pinning as 1.78 (denoted as "Weak Obs. Limit" in Figure 64). The factor found here is higher indicating that an SIA loop is a stronger defect than the limiting case but weaker than an intermediate strength defects as defined in [78]; however, such bounds are unlikely to apply to defects with a spatial extent. The mode ratios calculated here reflect similar tendencies as those predicted for a line tension model. Even modes cancel to contribute very little to the entropic factor, and the odd modes are dominant.

4.9.2 Infinite Dislocation Bypass

An infinite dislocation bypassing a regular linear array of defects more accurately represents dislocation glide in an SIA loop atmosphere than the previous configuration, because the gliding dislocation is pinned between loops rather than rigid pinning points. However, the applicability of the work of Granato *et. al.* to this case is

unclear. The formulation in [78] cannot capture the physical behaviour without extension to include free end conditions, which requires a reformulation of the solution. With terms containing both $\cos(x)$ and $\sin(x)$, all modes are likely to contribute to the entropic factor. Figure 66 shows a typical configuration for the normal and activated configurations used to characterize the entropic factor for bypass.

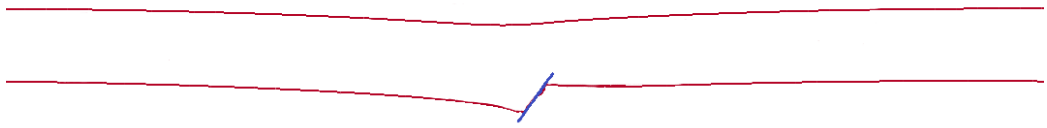

Figure 65: Dislocation configuration for an infinite dislocation (red) in the normal (lower line) and activated (upper line) states while bypassing an SIA loop (blue). The loop is viewed on edge so it appears as a line, and is an attractive obstacle in this configuration.

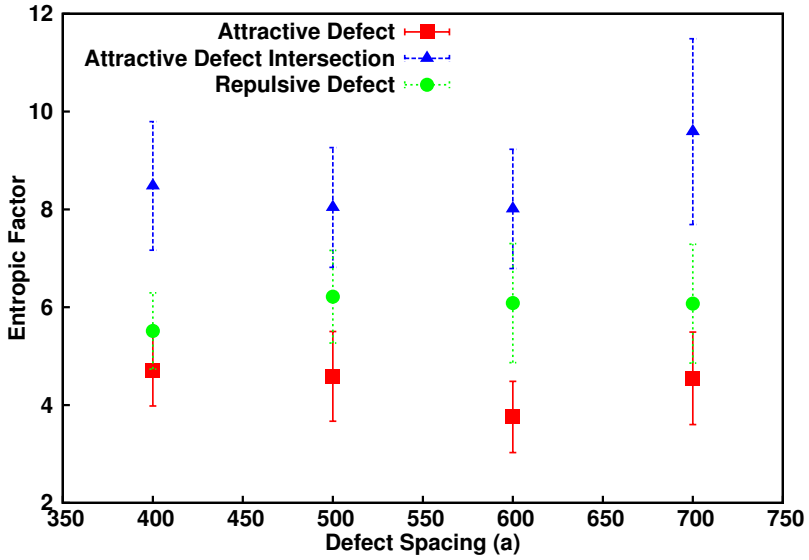

Figure 66: Entropic factor for an infinite dislocation bypassing an attractive and repulsive 20a side length SIA loop for a range of obstacle spacing.

Figure 66 shows the entropic factors for attractive and repulsive interactions for a range of SIA loop spacings. As in the case of the perfectly pinned dislocation, the

entropic factors for an infinite dislocation interactions are also independent of obstacle spacing. Attractive defects result in a lower entropic factor on average compared to repulsive defects, and both are on the order of the pinned segment case. Comparing the entropic factor for a dislocation bypass involved direct core interaction (blue triangle) and strictly elastic interaction (red square), stronger core interactions act to increase the entropic factor. Granato *et al.* [78] predicted increasing entropic factor with obstacle hardness. Two of the most advanced estimates of dislocation attempt frequency have no explicit length dependence [78, 104] because of cancellations between the entropic factor (scaling as L) and the fundamental frequency (scaling as $1/L$) for intermediate strength defects. Here, this is not seen to be the case, which can be explained directly from the frequency spectrum. The only significant deviations from unity of $\frac{\nu_i}{\nu_i'}$ occur at for the first several frequencies, which suggests that the SIA loops act as weak obstacles as defined by Granato *et. al.*.

4.9.3 Discussion of Numerical Characteristics

Analysing dislocation vibration is challenging from the standpoint of the functional form of Equation 63 and determining the saddle-point configuration with sufficient precision. When ν and ν' are computed numerically, any error in the calculation results in the rapid accumulation and amplification of error when computing the entropic factor; such is clear in Figure 64, which presents the individual and cumulative modal contribution for a Frank Read source bypass event.

It is clear from Figure 64 that only the first several modes are truly contributing to the entropic factor, yet its value continues to increase significantly at high order frequencies. One may expect small numerical fluctuations to average to zero, which is often not the case. A bias arises due to the unequal dislocation lengths of the normal and activated states: the activated state has a shorter total line length in every configuration used here, resulting in lower frequencies for the same modes. The

SIA loop often acts as a double pinning point thereby resulting in one very short dislocation segment, and a correspondingly shorter main segment. For low obstacle spacing this effect is particularly problematic, and convergence of Equation 63 is not reached with the modes captured in the analysis.

Equation 63 is also particularly sensitive to uncertainty in the modal frequency calculations because of the large number of terms involved. The total relative error for the attempt frequency can be written as $\sqrt{2N}(Re)$ where N is the number of included modes (approx. 40) and Re is the relative error per mode. It is clear that minor uncertainty of each modal frequency results in significant total uncertainty in the entropic factor.

As a result, precisely characterizing the saddle point is essential in predicting the attempt frequency of the process, once again due to the sensitivity of Equation 63. Very fine discretization on the order of several atoms is required to describe the saddle point, particularly in portions of the glide dislocation in close proximity to the SIA loop. Consequently, directly calculating the attempt frequency for a unit or ensemble dislocation process is impractical in general, and existing approximations provide sufficient characterisations of attempt frequency. The entropic factors calculated here provide valuable insight into attempt frequency predictions: the factor is independent of length, and on the order of 5 for a range of typical defect spacings. The attempt frequency is then on the order of 10^{10}-10^{11} Hz, which is significantly less than the Debye frequency on the order of 10^{13} Hz.

Figure 67 shows reaction rates for several applied stresses and SIA loop spacings, revealing that order of magnitude accuracy is sufficient accuracy for attempt frequency characterization because of the exponential dependence of reaction rate on activation energy. Increasing the dislocation length from 500a to 600a decreases the attempt frequency by 16.7%, but the reaction rate increases by several orders of magnitude because of the change in activation energy.

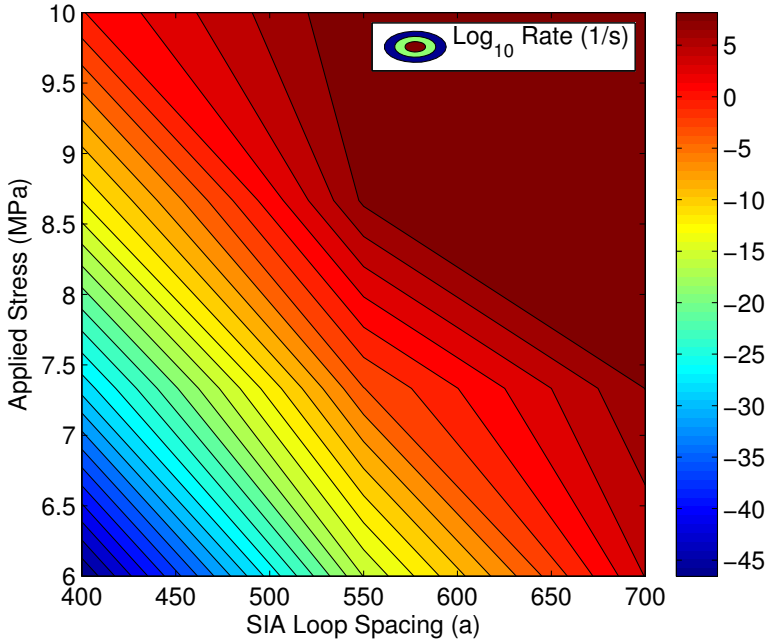

Figure 67: Reaction rates for an attractive defect (red squares in Figure 66).

Applying an error propagation analysis to the Arrhenius reveals the sensitivity to error in the attempt frequency and activation energy. Using $E_a = 2$ eV, $\nu = 10^{11}$ Hz, and $T = 600$ K, the total reaction rate relative error can be written as

$$\frac{\delta k}{k} = \sqrt{\left(\frac{\delta \nu}{\nu}\right)^2 + 1496.4\left(\frac{\delta E_a}{E_a}\right)^2}. \tag{150}$$

Any inaccuracy in the attempt frequency characterisation is drowned out by any minute inaccuracy in the activation energy, which is ≈ 40 times more influential for these parameters. The attempt frequency accuracy bounds found here, which are more precise than one order of magnitude, are sufficient when an error of 0.5% in activation energy causes a perturbation in the reaction rate of the same size.

4.10 Conclusion

Localized dislocation-obstacle interactions strongly influence the macroscopic properties of numerous material systems. Thermal lattice vibrations can provide sufficient

energy for bypass reactions to occur spontaneously and the rates of such reactions can be predicted from the magnitude of the activation energy barrier to be overcome and rate at which the system attempts the process. For the first time, the NEB method is applied to a continuum based discrete dislocation formulation to determine activation energies for dislocation bypass of obstacles, which paves the way for a significant advancement in coarse-graining techniques. The low computational demands of continuum calculations enable far broader and more detailed energetic mapping than possible with atomistic calculations, which is applied here to the interactions between an edge dislocation and a [001] SIA loop. A constitutive state transition theory model for thermally activated barrier bypass developed by Kocks, Argon and Ashby [104] is then applied to single dislocation-obstacle activation energies based on DDD simulations. This studies in this chapter reveal that this phenomenological model can correlate activation energy stress dependence using the Mott-Nabaro-Seeger model exponents, but with different exponents than found experimentally, which implies that more representative, larger scale energetic calculations are necessary to compare with the experimental results. An activation energy map characterizing bypass energy as a function applied stress and interaction geometry is created, revealing a complex energy landscape for the reaction. The feasibility of thermal activation is analyzed and it is shown a significant fraction of interaction events with non-zero activation energy can occur via thermal activation, and a study examining the effect of obstacle spacing on activation energy revealed complex stress dependence, motivating a discussion on the physical meaning of activation volume for dislocation-mediated processes.

The work in this chapter also develops more advanced predictions of attempt frequency for dislocation-obstacle bypass events, one of the two necessary factors that allow higher scale constitutive models such as in [236] to predict the rate of thermally activation dislocation migration. In doing so, the present chapter shows

that:

- The fundamental frequency of a dislocation is scales with $1/L$ as predicted from line tension modes.
- Higher modes do not scale linearly but with a power law, contrary to line tension predictions.
- The entropic factor for SIA loop bypass is independent of dislocation length, resulting in an attempt frequency scaling with $1/L$.

With activation energy calculations made possible using first principles or continuum methods, and the characterization of dislocation attempt frequencies presented here, a direct path to predicting the thermal activation of unit dislocation processes is clear. The reaction attempt frequencies directly calculated in this thesis show that one can adopt an entropic factor independent of obstacle spacing and therefore an attempt frequency on the order of the fundamental frequency, which is sufficiently accurate for scale transition of unit dislocation processes via the Arrhenius equation.

CHAPTER V

REDUCED ORDER MODELLING

The developments of this thesis have enabled a dislocation dynamics simulation to predict hardening caused by dislocation-irradiation defect interactions in the athermal case. Incorporating the role of thermal energy on these interactions is possible with a framework provided by transition state theory (TST) enabling direct access to thermally activated reaction rates, including rates of dislocation-obstacle bypass processes as shown in the previous chapter. Unit dislocation-defect reaction processes may be within reach of atomistic calculations, but the scale transition of information from the nano-scale to representative volumes is unclear. Moving beyond unit dislocation-defect reactions to an environment containing a large number of defects requires coarse-graining the activation energy barriers of each obstacle into an effective energy barrier that accurately represents the large scale collective process. This chapter investigates the relationship between unit dislocation-defect bypass processes and the distribution of activation energy barriers calculated for ensemble bypass processes. A significant difference between these cases observed, which is attributed to the inherent cooperative nature of dislocation bypass processes. In addition to the dislocation-defect interaction, the morphology of the dislocation segments pinned to the defects play an important role on the activation energies for bypass. A phenomenological model for activation energy stress dependence is shown to well-describe the mean of a distribution of activation energies, and a probabilistic activation energy model incorporating the stress distribution in a material is presented.

5.1 Introduction

The activation energy for macroscopic dislocation migration has been studied from the perspective of line tension simulations. Such simulations approximate dislocations as a line with an associated energy per unit length resulting in a tension Γ. This simplified dislocation model omits important phenomena such as dislocation self interaction, and the representation of defects is limited to infinitesimal pinning points. In the works of Xu and Picu [252, 173], the authors consider that the activation energy was a function of the bowing angle θ of a dislocation segment pinned by an obstacle, which is a measure that inherently captures the effect of stress and obstacle spacing on the force of the dislocation on the defect; however, it has been shown that for the activation energy for bypass of a $\langle 001 \rangle$ self-interstitial atom (SIA) loop [198], the applied stress and obstacle spacing have dramatically different effects and functional forms than for the force on the defect. Xu and Picu [252] also show that rate sensitivity and bypass kinetics for a distributed random field of obstacles is governed by correlated motion of dislocations rather than the unit processes. Therefore, a more complex analysis using dislocations is necessary to gain insight into coarse-graining unit process activation energies to representative environments. It is important to note the distinction between athermal hardening calculations using atomistics-informed defect strength and ensemble thermally activated bypass activation energy calculations using unit bypass energies. In the athermal (stress driven, deterministic) case, a dislocation overcomes an obstacle impeding its motion when a certain force on the dislocation is exceeded. This force can correspond to the force necessary to shear the defect or to break away from the elastic interaction and, most importantly, only depends on highly localized interactions between the gliding dislocation and the defect. As a result, an angle-based breakaway criteria is justified. The case of thermally activated bypass is far more complex because an unpinning event can involve changes in dislocation morphology far away from the defect that

also alters the Gibbs free energy of the system. The energy of the entire crystal is minimized [72] and thus coarse-graining defect activation energy is therefore far more complex than defect strength because as the dislocation interacts with multiple defects, it engenders a cooperative process that does not correspond to the unit bypass activation energies.

The high computational cost of atomistic simulations has limited studies to simulations of a dislocation interacting with a single obstacle, often at a single stress level and interaction geometry. These studies provide valuable insight into the complex, atomic scale interactions between the dislocation and obstacle; however, such information must be coarse-grained to higher scale simulations in order to simulate realistic materials, rather than idealized configurations. Describing the system using the continuum theory of defects with a discrete dislocation dynamics (DDD) simulation significantly reduces the degrees of freedom of the system and simplifies simulation boundary conditions compared to atomistic calculations. With the added advantage of significantly reduced computational requirements, DDD simulations can determine the minimum energy pathway for both unit and ensemble bypass processes using the nudged elastic band method [102] at the expense of a reduction in accuracy at the atomic scale where the continuum formulation of dislocations is no longer valid. Even if details of dislocation core interactions with obstacles are approximately described, the ability to compare and normalize activation energies for unit processes with collective bypass of randomly distributed obstacles from such a DDD approach is of high potential utility.

The principal goal of this chapter is to investigate the possibility of coarse-graining unit dislocation-defect bypass activation energies to more realistic obstacle configurations. Dislocation migration through a field of defects inherently captures the effects of varying obstacle spacing and interaction geometry on effective activation energy, but the influence of these parameters on activation energy distributions has never

before been studied. In this work, such activation energy distributions are directly calculated with DDD-NEB and are compared to the activation energies calculated using unit bypass simulations for the same defects and planar defect spacing. In Section 5.3, these distributions are compared for two configurations to examine if unit bypass events can accurately describe material behaviour for application in higher scale models. In Section 5.4, the functional form of the activation energy distribution is analyzed and the evolution of effective activation activation energy as a function of applied stress is compared to the Kocks transition state theory model. In Section 5.5, a probabilistic description for thermally activated dislocation migration is developed by considering the joint probability distribution of activation energy and stress in the material. In the final section, the plastic strain increment distribution is investigated as a function of applied stress and the distribution mean is compared to conventional predictions assuming a square lattice.

Any discrepancies in the non-singular core description compared to atomistic simulations are rendered largely irrelevant for the purposes of this study, because it is the relative statistics between the unit and ensemble bypass processes from DDD that are of interest rather than accuracy of the numerical value of the unit bypass activation energy. Whether the local dislocation-SIA loop bypass event is realistically described or not, it is described identically between these two scenarios and therefore any differences arise are strictly those associated to the distributions of the obstacles in space and in energy barrier.

5.2 Method

The numerical method underpinning the DDD-NEB simulations in this chapter is identical to that in Chapter 4. The only fundamental differences are that the simulation volume is significantly larger and multiple SIA loops are present. This simple

act of increasing the number of SIA loops does, however, have important implications regarding the numerical stability of the simulations that do not exist for unit dislocation-defect interactions. The difficulties with numerical stability arise because of how the images interact, and the nature of the dislocation-loop interaction. Recalling the definitions of the NEB force and tangent:

$$\mathbf{F}_i = \mathbf{F}_i^s|_{\parallel} + \mathbf{F}_i^R|_{\perp}. \tag{91 repeated}$$

$$\boldsymbol{\tau}_i^+ = \mathbf{R}_{i+1} - \mathbf{R}_i \tag{85 repeated}$$

$$\boldsymbol{\tau}_i^- = \mathbf{R}_i - \mathbf{R}_{i-1} \tag{86 repeated}$$

$$\boldsymbol{\tau}_i = \begin{cases} \boldsymbol{\tau}_i^+ & \text{if } V_{i+1} > V_i > V_{i-1} \\ \boldsymbol{\tau}_i^- & \text{if } V_{i+1} < V_i < V_{i-1} \end{cases} \tag{87 repeated}$$

$$\mathbf{F}_i^s|_{\parallel} = k\left[|\mathbf{R}_{i+1} - \mathbf{R}_i| - |\mathbf{R}_i - \mathbf{R}_{i-1}|\right]\hat{\boldsymbol{\tau}}_i. \tag{94 repeated}$$

The tangent plays an important role for the spring force as seen in Equation 94 because it determines how the real and spring forces are projected to drive the system into the MEP. Any inaccuracy in the approximation of the tangent to the energy hypersurface results the real force driving the image along the reaction pathway. Movement of dislocation nodes directly influences the spring force because the magnitude of the spring force is a function of the norm of the difference of the degree of freedom vectors. As a result, the spring force on each node is changed by otherwise confined changes in dislocation morphology, such as deformations near an SIA loop. Numerical instability was observed for glide dislocations interacting with many loops for this reason - inaccuracy in the tangent caused images to be driven in the glide direction for one or more loops, causing a change in spring force everywhere along the line. For

the purposes of this study, a large number of simulation repetitions with a restricted simulation volume with six SIA loops. The width results in a realistic loop density and the dislocation is often interacting with several SIA loops simultaneous, but remains more numerically stable than simulations with very large volumes and a glide dislocation interacting with with tens of loops simultaneously. Figure 68 depicts a typical configuration used to produce activation energy distributions in this chapter.

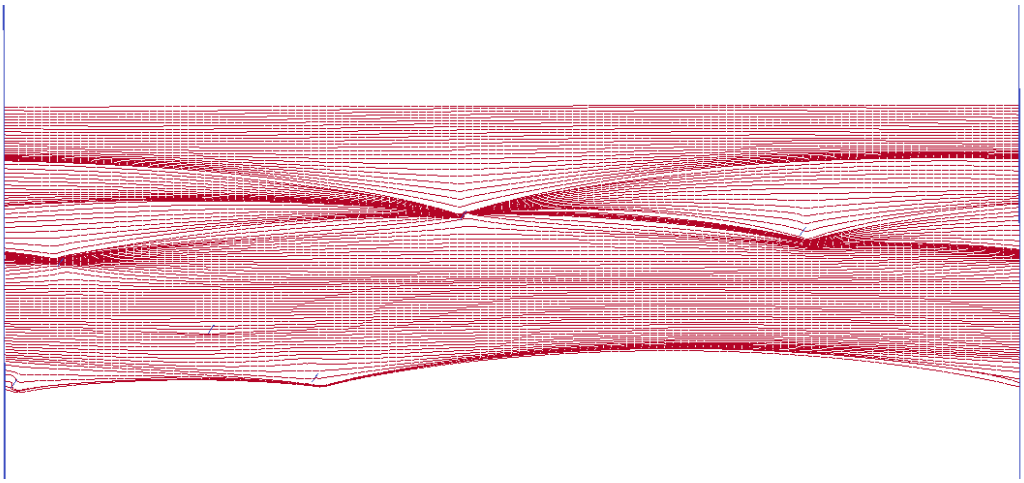

Figure 68: Converged dislocation image configuration for a glide dislocation bypassing an ensemble of SIA loops.

5.3 Activation Energy Distribution

5.3.1 Geometric Considerations

Atomistic simulations are favoured for studying dislocation-obstacle interactions. Stress-driven dislocation bypass reactions have been studied extensively with these techniques for obstacles composed of dislocation segments such as stacking fault tetrahedra [185, 164, 184, 127] and self-interstitial atom loops [156, 217, 14, 212, 194] and well as voids [215, 85, 163, 218, 50, 249] and precipitates [105, 86, 214, 216, 209]. These simulations reveal details of nano-scale dislocation reactions and obstacle deformation caused by the dislocation but extending the results to predict material properties is challenging. The studies that investigate only the the effect of stress aim to determine the critical stress for bypass, and only a single study has reported the system

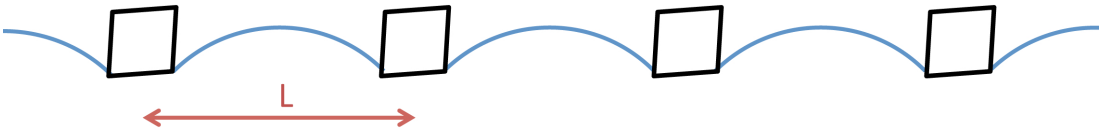

(a) Dislocation bowing against a regular linear array of SIA loops.

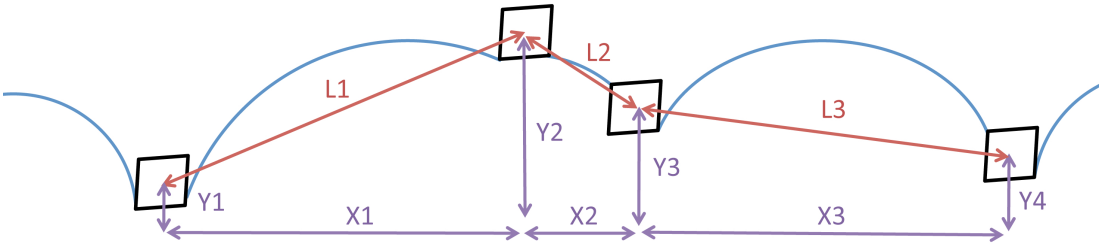

(b) Dislocation bowing against SIA loops with a random spatial distribution.

Figure 69: Many interaction geometries result in energies far beyond the range of thermal activation, a significant number to exist.

energy evolution during the bypass process [142]. The effect of interaction geometry, dislocation character, or interactions with more than a single defect have seen little investigation.

A major barrier to scale transition of unit bypass activation energy results to consider realistic distributions of obstacles is the dramatic departure in geometry from a square planar array. Figures 69a and 69b illustrate the different possible geometric factors influencing the activation energy barriers for two configurations with an identical defect density.

The linear (or square) regular array in Figure 69a represents the configuration that is accessible using atomistic calculations with periodic boundary conditions or when performing a unit process calculation with DDD-NEB. It is clear from Figure 69b that a dislocation passing through a non-uniform distribution of defects is a cooperative process in which many statistics influence the individual activation energy barriers. Moreover, the effective activation energy barrier, related to the strongest obstacle configuration, can differ substantially from the uniform case. The obstacle spacing

normal to glide (X1,X2,X3) and parallel to glide (Y1,Y2,Y3,Y4) will change activation barriers in addition to the center-to-center loop spacings (L1,L2,L3). Moreover, it is clear that a single defect does not entirely characterize the bypass process but that the neighbouring defects also play a fundamental role, the degree of which remains to be determined. Another nuance is that the dislocation configuration at the critical point for a regular linear array of obstacles is relatively independent of applied stress. The glide dislocation will bypass an obstacle via Orowan bowing before it can contact another obstacle. In the case of randomly distributed obstacles, however, increasing the stress driving the dislocation may cause the dislocation to bow into additional obstacles. As a result, new barriers are introduced and the statistics characterising the lengths of dislocation segments are changed. The effect of defect density is therefore likely a nonlinear function of applied stress. In comparison to a more realistic (but nevertheless simplified) configuration in Figure 69b, the activation energies obtained from a linear array are evidently insufficient to describe the process, which will be shown quantitatively in the following sections.

A tempting means to coarse-grain unit bypass activation energy is to characterize the unit process activation energies over a range of variables, such as applied stress and inter-obstacle spacing to nearest neighbors (parallel and normal to the glide direction). This direct approach falls short as the synergistic effects results in complex dependencies. To highlight these challenges, the simplified case of a linear array of loops is taken, as shown in Figure 70. In this configuration, two loops are evenly spaced to create a regular linear array when periodic boundary conditions are applied. Next, one of the loops is displaced in the glide direction by up to 15% of the inter-obstacle spacing (i.e. $x/L = 0.15$). The minimum energy pathway and activation energy are calculated as a function of x/L to reveal the complex evolution of activation energy for subtle changes in the defect geometry.

A small offset of every second loop (or an arbitrary obstacle) in the glide direction

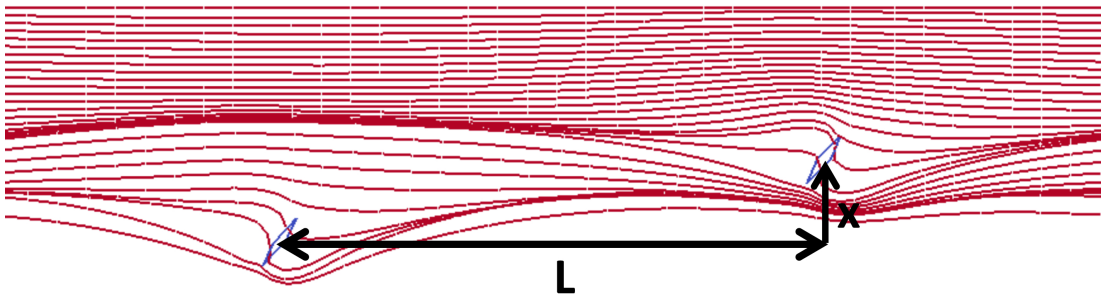

Figure 70: Dislocation bypass process of two ⟨001⟩ SIA loops slightly offset in the glide direction (7.5% of the loop spacing).

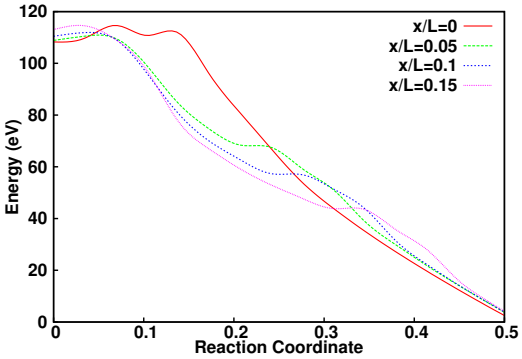

(a) System energy along the minimum energy pathway for a $1/2\langle 111\rangle(1\bar{1}0)$ glide dislocation bypassing two 4.3nm side length ⟨001⟩ SIA loops with 10 MPa applied stress.

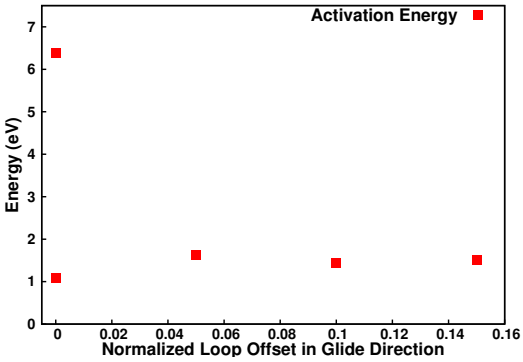

(b) Activation energy for bypass decreases by a factor of ≈ 3.5 as the slight offset causes the loops to be bypassed independently.

Figure 71: The activation energy for a regular array with a small offset x/L in the glide direction results in a dramatic change in activation energy.

results in two separate bypass events as seen in Figure 70 and confirmed by the minimum energy pathways for several values of x/L shown in Figure 71b.

Displacing the second loop in the glide direction 5% of the loop spacing reduces the activation energy from 6.37 eV to 1.63 eV. Increasing the displacement in the glide direction has negligible effect, as the process has already transformed to two separate bypass events, which is clear from Figure 71a. Furthermore, this process is dependent on the magnitude of the activation energy barrier, the applied stress, and the obstacle

spacing. This simple, symmetric configuration reveals significant challenges to coarse-graining unit bypass activation energies, and is greatly complicated if one considers asymmetric loop spacing and obstacles of different activation energies. To access the distributions in activation energy arising from the interplay between these numerous variables that solicit non-linearity, simulations with a non-uniform defect population are necessary.

5.3.2 Ensemble Bypass - Multiple Defect Activation Energies

Direct comparison of the energy distributions obtained for all possible unit bypass reactions with an ensemble of defects with the same possible interactions at the same planar density is a direct and explicit method to reveal the possibility of coarse-graining using the effective energy as a function of defect spacing. In principle, atomistic calculations are capable of performing such simulations; however, the computational requirements put such large simulations far beyond reach of feasible computation times. The volumes required for the studies in this work constitute on the order of billions of atoms, and simulating dislocation motion at these length scales is only currently possible with mesoscale methods such as discrete dislocation dynamics. To elucidate the effect of distributing defects in space and creating a cooperative bypass reaction for the dislocation, three series of calculations are performed at a constant stress level and mean defect spacing:

- Unit bypass energy of an SIA loop as a function of interaction geometry.
- Minimum energy pathway through an ensemble of SIA loops as obstacles randomly distributed in space.
- Minimum energy pathway through an ensemble of SIA loops with a single interaction geometry.

A two dimensional representation of the gliding edge dislocation and SIA loop configuration are shown in Figure 72.

The DDD-NEB method enables a direct comparison of activation energies for unit and ensemble bypass events calculated with the same methodology to reveal the effect of the collective process created by a dislocation in contact with multiple obstacles.

First, the activation energy for unit bypass is calculated for a single SIA loop with a linear spacing of 117 nm as a function of interaction geometry (z/L) (i.e., the relative position of the glide plane with respect to the loop center) and an applied shear stress of 10 MPa as shown in Figure 73a. The calculated activation energies are shown in Figure 73. The activation energies are calculated with a fine discretization in offset, then interpolated with cubic splines. Ten points equally space points are taken for each per interval interpolated using the cubic spline, which are enumerated to create a probability distribution of activation energies. From the distribution shown in Figure 73b, 8.75% of events are found to be less than or equal to 2 eV.

A simple approach to coarse-graining such unit process activation energies would be done by using these energies directly for an ensemble of defects with the same mean spacing. However, the observed activation energy dependence on SIA loop spacing in a linear array is logarithmic [198] and the relative position in the glide plane also plays a significant role on the activation energy barrier for glide. A volume containing six SIA loops with a mean separation distance equal to the linear spacing of the previous calculation, 117 nm, and with all other parameters identical was taken and the activation energy barriers for glide were calculated for 800 simulation repetitions.

The activation energy probability distribution for an ensemble of loops has fewer defined features than the distribution for unit bypass. The variation in the connected segment lengths and relative defect geometry acts to spread the two well-defined peaks seen for the unit bypass process. Furthermore, the mean activation energy is

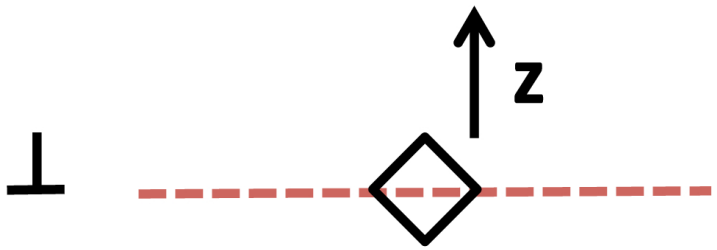

(a) Configuration for unit bypass as a function of interaction geometry (z/L, where L is the loop side length) used in Figure 73.

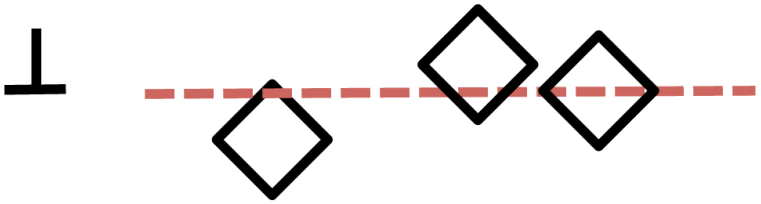

(b) Configuration for ensemble bypass to compare to the distribution obtained from Figure 72a.

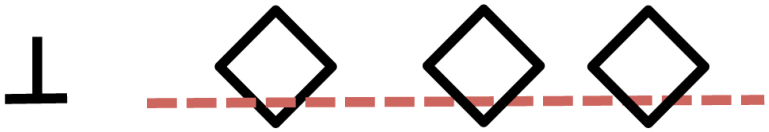

(c) Configuration for ensemble bypass to compare to a single activation energy value for the same interaction geometry in Figure 72a.

Figure 72: Pictorial representation of the simulation configurations used to investigate the possibility of coarse-graining unit SIA loop bypass events. The dislocation tangent is into the page and the volume is not periodic.

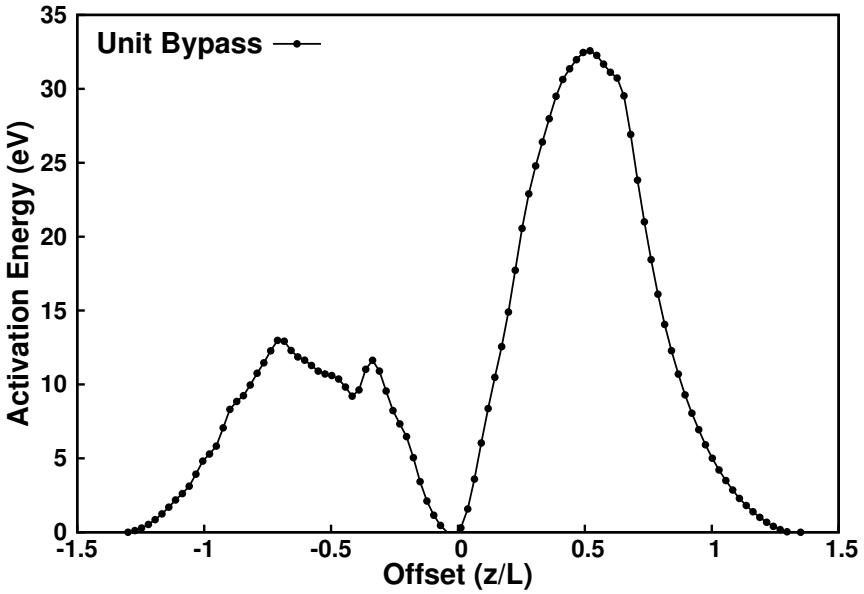

(a) Activation energy for a $1/2\langle 111\rangle(1\bar{1}0)$ glide dislocation bypassing a 4.3nm side length $\langle 001\rangle$ SIA loop with 10 MPa applied stress.

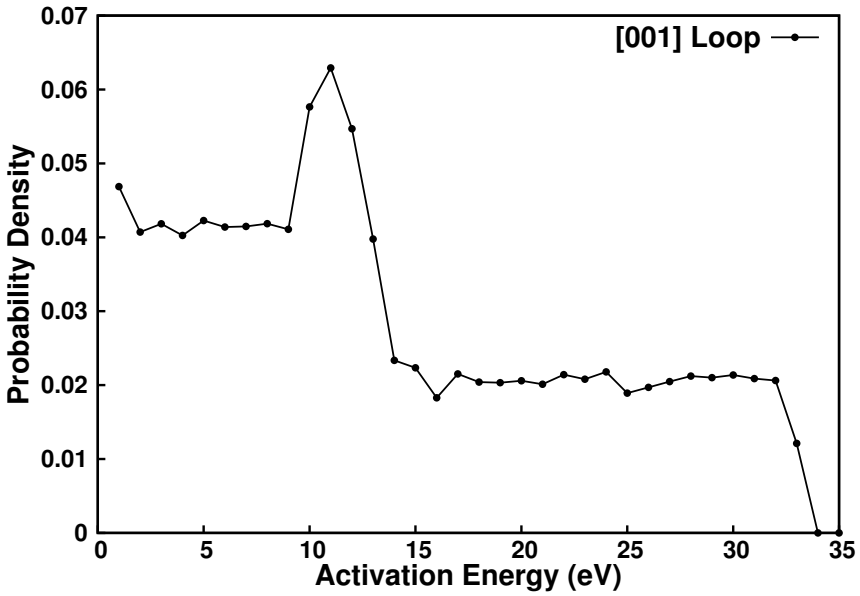

(b) Probability distribution for Figure 73a.

Figure 73: The activation energy distribution for the unit process as a function of normalized glide plane offset reveals many events with high activation energy by also a non-negligible fraction which are accessible with thermal activation.

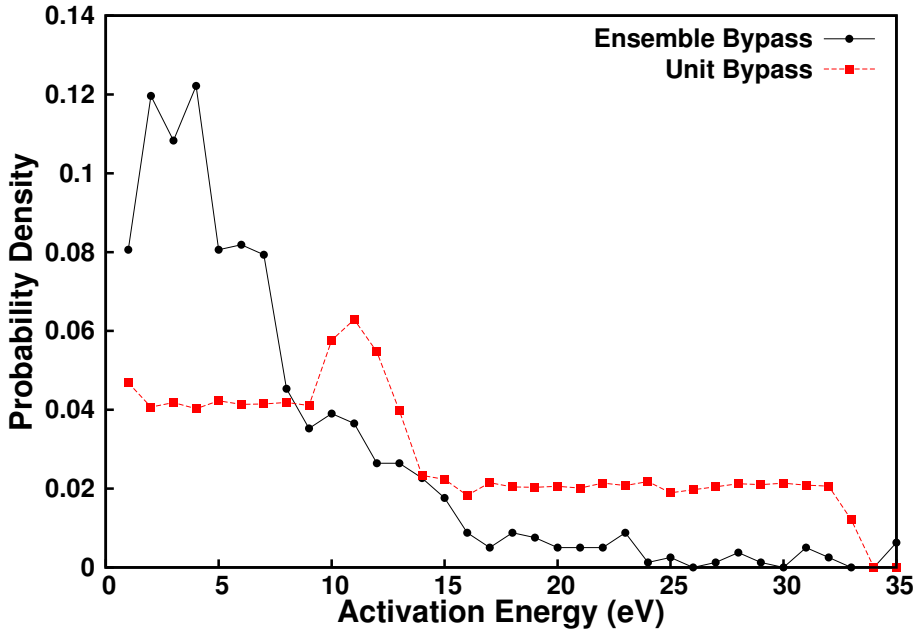

Figure 74: Probability distribution of activation energy for a edge dislocation bypassing a obstacles with a distribution of energies, compared to the probability distribution in Figure 73b.

43.4% lower for an ensemble of defects (6.56 eV vs. 11.6 eV). It is clear that the highly localized interaction between the defect and the dislocation does not entirely characterise the energetics of the process. The change in morphology of the extended dislocation segments neighbouring the bypassed defect induces important changes in the activation energy that cannot be captured in unit bypass simulations.

5.3.3 Ensemble Bypass - Single Defect Activation Energies

To investigate the effect of the extended cooperative bypass process in more detail, a simpler configuration depicted in Figure 72c is taken to remove the distribution of unit bypass activation energies and to isolate the influence of the random defect morphology on coarse-graining unit processes. Using a single loop offset, the activation energy for the unit bypass process is calculated (11.6 eV). Next, 400 simulations with six loops at the same offset are performed, and the probability distribution of the resulting activation energies is plotted in Figure 74.

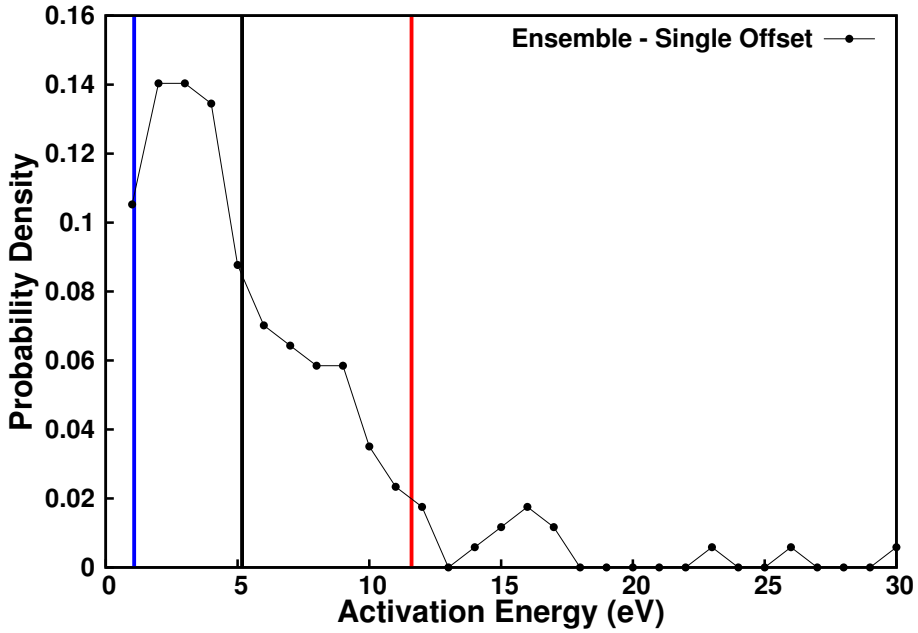

Figure 75: Probability distribution of activation energy for a dislocation migration in a distribution of defects with equal unit bypass energy.The mean activation energy for the distribution is shown with the vertical black line, the unit bypass activation energy (of the same defect density) is shown with the vertical red line, and the unit bypass activation energy using the density predicted using Friedel's approximation (Equation 151) is shown with the vertical blue line.

The vertical red line in Figure 75 denotes the activation energy for a single SIA loop with the same interaction geometry and a linear spacing equal to the mean free path of the distribution of SIA loops. As is clear from the figure, the vast majority (>90%) of the energy barriers fall below the unit activation energy (11.6 eV) and thus in this simplified configuration with defects having identical isolated activation energy barriers, the activation energy distribution for an ensemble of defects differs dramatically. Moreover, it is clear from the value of unit activation energy that thermal activation will never occur, yet in the ensemble case, a significant number (24%) of events have $\leq$2 eV. Such a dramatic shift is impossible to elucidate from unit bypass simulations using the mean defect spacing.

The mean defect spacing does not sufficiently describe the defect configuration to provide sufficient accuracy during the scale transition. Instead of the mean spacing

between defects with respect to their distribution in space, the mean spacing of defects on the dislocation line may be the more relevant parameter to coarse-grain unit bypass processes. Friedel [68] developed an approximation for inter-obstacle spacing of defects on a dislocation line pinned in a distribution of randomly distributed obstacles:

$$D \approx \left(\frac{2\tau l^2}{\sigma_a b} \right)^{1/3}, \tag{151}$$

where D is the defect spacing on the dislocation line, τ is the line tension, l^2 the average area swept by the dislocation as it moves from its initial to final pinned positions, and σ_a the applied stress. To apply Equation 151, l^2 is assumed to be equal to the square of the mean SIA loop spacing (117^2 nm^2). Applying Equation 151 and assuming a value of line tension as $\tau = \mu b^2/2$ results in a defect spacing on the dislocation line of $D = 303$ nm, an increase of nearly a factor of three.

As seen in Figure 75, predicting the mean activation energy using the defect spacing on the dislocation line predicted using Equation 151 significantly underestimates the mean energy. The line tension in Equation 151 can be take as a parameter to match the mean of the distribution; however, such a value is not general and is not necessarily valid for other applied stresses or densities given that a line tension model of a dislocation is highly simplified. A parameter related to the defect mean free path simply does not describe the necessary depth of the physics to characterise the coarse-grained activation energy distribution for dislocation glide, even when the inter-obstacle spacing of randomly distributed obstacles on a dislocation line is taken into account. Full scale calculations with a distribution of defects are necessary to capture the numerous factors influencing the activation energy distribution. This implies that thermally activated dislocation migration is highly dependent on the dislocation segments between obstacles in addition to the fine scale dislocation-obstacle interaction. The coarse-graining process can only begin when all the principal components of the process are captured, which requires ensemble bypass simulations.

5.4 Distribution Homogenization and Stress Dependence

Determining how an activation barrier depends on applied stress is critical for predicting thermally activated processes. If the activation energy for a process is sensitive to changes in stress for small normalized stresses σ/σ_0, thermally activated dislocation glide may play a fundamental role on material behaviour, whereas if thermal activation only changes dramatically with large σ/σ_0, then thermal activation only occurs near yielding and may not play a significant role in engineering applications of the material. To describe this activation energy dependence on stress, Kocks, Argon and Ashby [104] proposed a phenomenological model relating the activation energy at various stresses to the zero stress activation energy:

$$\Delta G = F_0 \left(1 - \left(\frac{\sigma}{\sigma_0}\right)^p\right)^q \tag{152}$$

where F_0 is the activation energy in the absence of applied stress, σ the applied stress, σ_0 the yield stress, and p and q are parameters to be determined. Equation 152 has also been analyzed from the theoretical perspective with the Mott-Nabaro-Seeger model and it was shown that for energy barriers with a sinusoidal form, the exponents are $p = 1/q = 2/3$. A DDD-NEB analysis of the unit dislocation-SIA loop bypass process showed that these exponents describe the stress dependence for the unit dislocation-SIA loop bypass process [198]. However, as shown in the previous section, the transition between unit bypass process and SIA loop ensemble activation energy distributions is highly non-trivial. The applicability of Equation 152 is investigated here using the expectation value of the activation energy for ΔG and F_0.

To create Figure 76, one must determine the average yield strength σ_0 and zero stress activation energy distribution. The mean yield stress σ_0 is found using a series of traditional DDD simulations using the same defect parameters as the DDD-NEB study. The value for F_0 is calculated using the same method as for any other stress value using 400 simulation repetitions to create an activation energy distribution

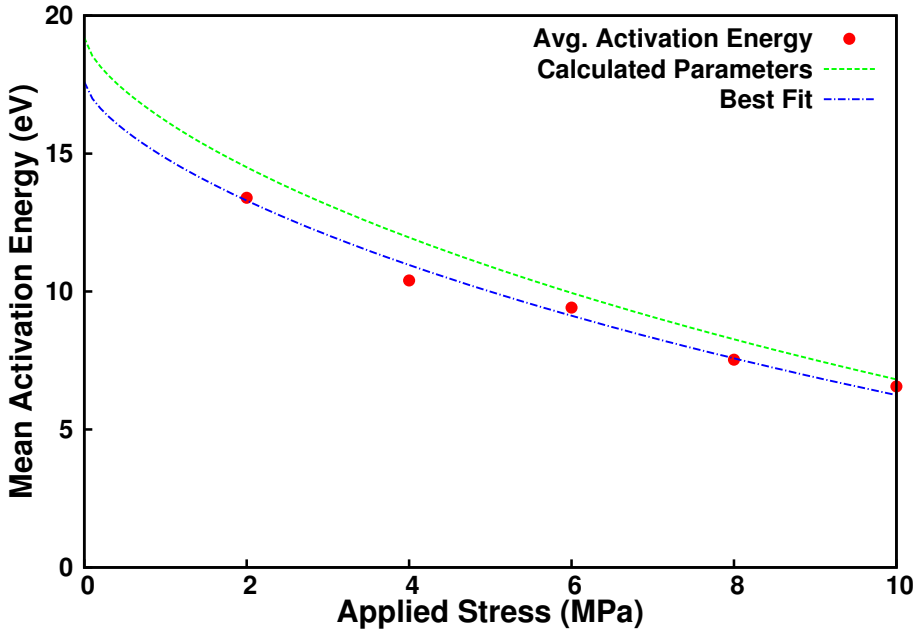

Figure 76: Using calculated values of $F_0 = 19.2$ eV and $\sigma_0 = 28.4$ MPa, Equation 152 overestimates the activation energy. The data can be well fit using a lower value of F_0 =17.6 eV.

Model	Calculated	Fit
F_0 (eV)	19.2	17.6
σ_0 (MPa)	28.4	28.4

Table 3: Parameters for each line appearing in Figure 76. The stress to spontaneously bypass σ_0 is provided by DDD calculations for both the "Calculated" and "Fit" cases.

from which the mean activation energy is calculated. The activation energy in the absence of applied stress is independent of obstacle spacing, but with an ensemble of obstacles, it is possible that multiple obstacles are aligned such that the dislocation must overcome them simultaneously, which would result in an activation barrier that cannot be produced in the unit case.

Figure 76 shows that using calculated values of F_0 and σ_0, the Kocks TST model slightly overestimates the activation energy with the greatest deviation in the absence of applied stress and monotonically decreasing to the same solution at the yield stress. If one allows the zero-stress activation energy to be a parameter, a good fit can be achieved, and this discrepancy raises questions on the meaning of the activation in

the absence of applied stress for a distribution of defects.

In the case of a single obstacle of fixed size and interaction geometry, i.e. unit bypass, the inter-obstacle spacing is the only parameter affecting zero-stress activation energy. If a second loop is introduced, the relative spacing normal to the glide direction (along the dislocation line) between each loop becomes a parameter. Figure 77 shows a simple example with two identical loops aligned in the glide direction. In the absence of applied stress, the activation energy for bypass is independent of asymmetry in the inter-obstacle spacing. With an applied stress the bypass reaction is markedly different: asymmetry in the loop spacing reduced the activation from a regular linear array and while the evolution of activation energy is not as dramatic as in the configuration of Figure 70, the activation energy can nevertheless be reduced by 50% or more depending on the configuration. In the case of unit bypass, a single parameter F_0 can capture all the parameters determining the activation energy of the reaction, whereas the higher dimensionality with multiple loops and their relative geometry can greatly influence the stress evolution of the reaction activation energy in ways that are impossible to elucidate in the absence of applied stress.

The zero-stress activation energy is therefore better left as a fitting parameter than as a calculated value for a dislocation bypassing an ensemble of defects. This finding reinforces the notion that the morphology of the dislocation segments are instrumental in calculating the activation energy barrier in addition to the dislocation-obstacle reaction. Coarse-graining must thus inherently include the effect of high order dislocation morphology effects. The exponents for the Kocks TST model found for a unit bypass process in [198] are, however, seen to accurately describe the stress evolution for an ensemble of the same type of defect if the F_0 is left as a parameter.

The probability distributions for the activation energy barriers seen by a dislocation migrating through a distribution of SIA loops are shown at two stress levels in Figure 78.

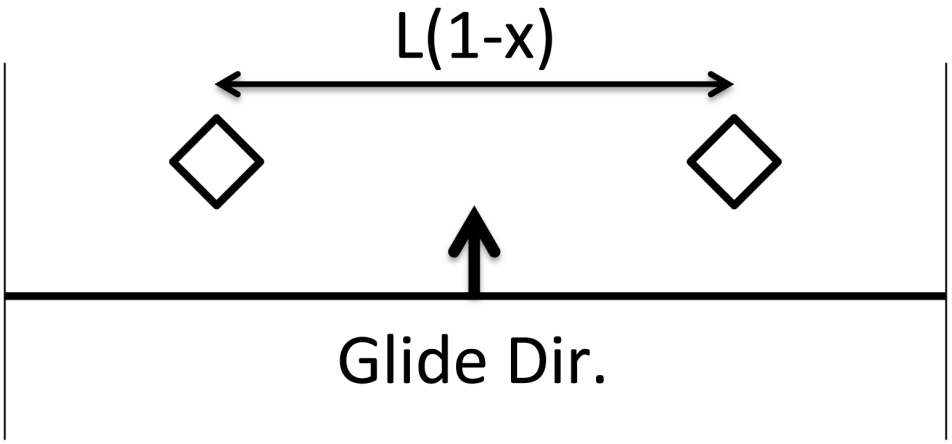

(a) Diagram of simulation configuration for Figure 77b. The vertical lines represent periodic boundaries, so that the loop spacing is $L(1+x)$ and $L(1-x)$.

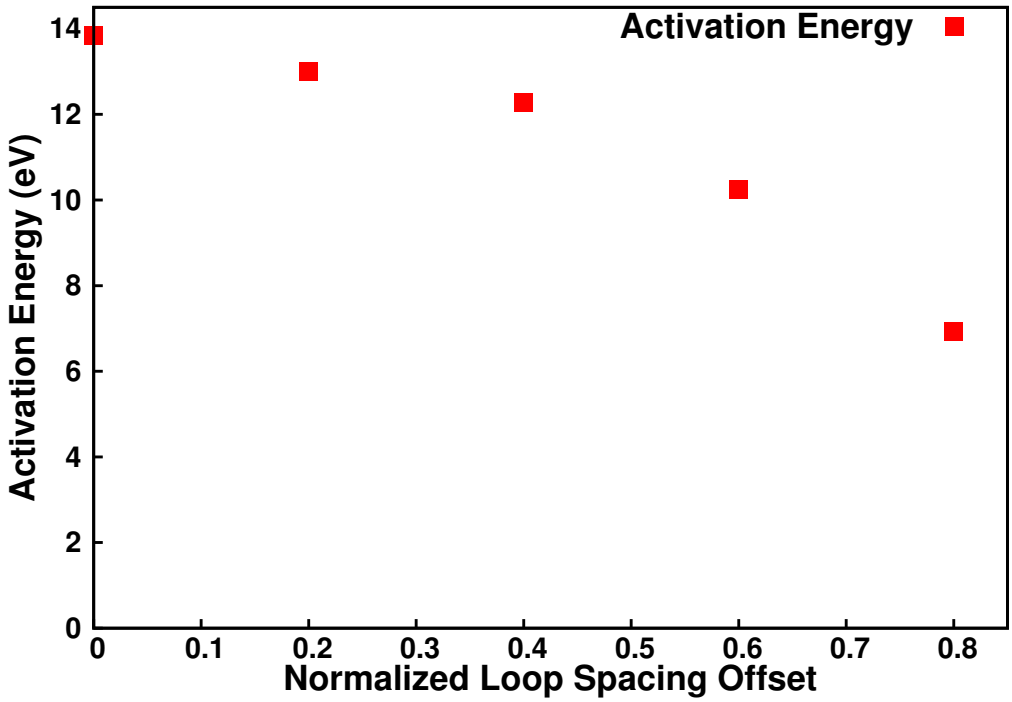

(b) Evolution of activation energy as a function of normalized loop spacing offset x.

Figure 77: The activation energy for a regular array as a function of normalized loop offset x/L normal to the glide direction is significantly altered with increasing normalized loop offset, highlighting the shortfalls of a characterisation via mean loop spacing.

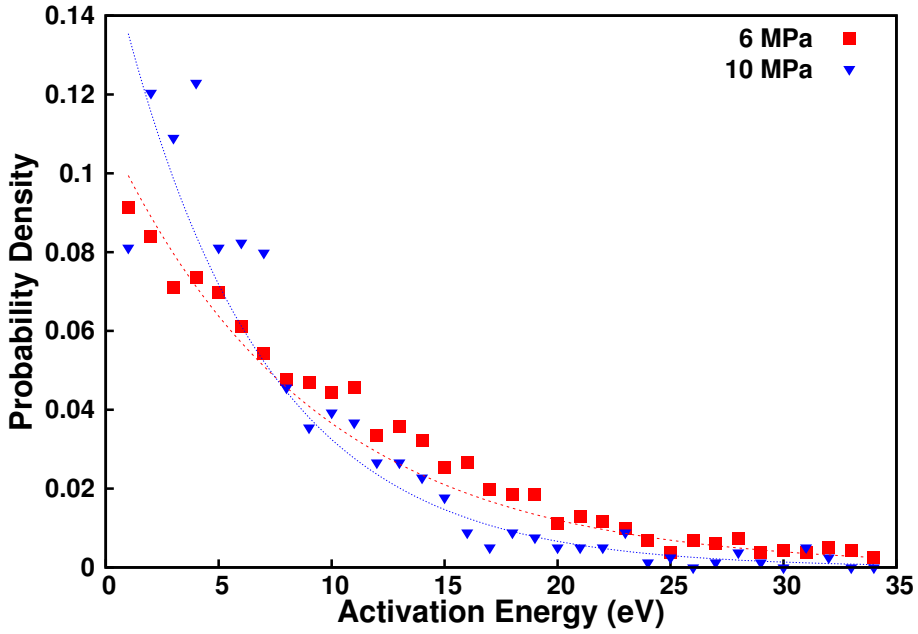

Figure 78: Probability distributions of activation energy at two levels of stress. Each stress level is well described using an exponential distribution. At 6 MPa, the mean is 9.0 eV and at 10 MPa, the mean is 6.3 eV

The statistics of the data reveal a distribution well-described by an exponential probability distribution, i.e.,

$$P(x) = \lambda e^{-\lambda x}, \tag{153}$$

where λ^{-1} is the expectation value of activation energy. This fit is purely phenomenological, and is not necessarily valid in the case of other defects or densities. Obtaining a closed-form functional form is particularly valuable for the coarse-graining process. A distribution well-described in this manner can be directly integrated into constitutive equations in closed form. The stress dependence of the expectation value of energy λ^{-1} can be expressed in closed form using the Kocks TST model and the fitted parameters found in this work, and therefore distribution of energies is fully characterized with the mean energy as the only parameter. This closed form representation is a significant step forwards in coarse-graining, as the functional form can be easily transitioned to higher scales and combined with other relevant distributions, such as

the distribution of stress in the material. While the values F_0 and σ_0 are parameters from simulation or experimental studies, the activation energy distribution can be written in closed form as a function of stress.

5.5 Effective Activation Energy

The rate of thermally activated dislocation glide, which is manifested as creep at the macroscopic scale, depends not only on the distribution of activation energies but the stress distribution as well. The mean activation energy for glide of the chosen configuration decreases from 10.4 eV to 6.56 eV with a change from 4 MPa to 10 MPa, and therefore barriers can rapidly enter the domain of thermal activation as a result of evolving stress fields in the material. Furthermore, the stress state in a material is not equal to the macroscopic applied stress but is rather a distribution with a mean equal to the applied stress, because other defects such as dislocations, grain boundaries, and lattice defects act to broaden the stress distribution. Therefore, even obstacles with very high activation energy barriers for bypass may be overcome with the evolution of the dislocation morphology elsewhere in the material. Combining these two distributions allows one to generate a comprehensive prediction of the activation energy barriers in a material, which can be directly implemented in a constitutive equation such as in [236].

With a fixed defect density and defect type, the activation energy distribution is itself a function of only a single random variable, the local stress. The probability distribution for the shear stress distribution caused by a relaxed configuration of edge dislocation dipoles has been derived analytically in [43]. The distribution is sharply peaked and decays as τ^{-3}, but cannot be written is closed form without containing an integral. For the sake of demonstration, a Gaussian stress distribution with a variable mean μ and a fixed standard deviation of $s = 10$ MPa is assumed here. The resulting probabilistic description of the activation energy is written as a function of

two random variables that are described with a Gaussian and exponential probability distributions:

$$G(x) = F_0 \left(1 - \left(\frac{\sigma(x)}{\sigma_0} \right)^{(2/3)} \right)^{(3/2)} \qquad \text{(152 repeated)}$$

where the stress $\sigma(x)$ defined as a normal distribution with variate X. The value of $G(x)$ is used as the expectation value of activation energy λ^{-1} to generate an exponentially distributed random number, which is the activation energy barrier. One condition is added from physical reasoning that the activation energy is zero when the applied stress is greater than the yield stress. This model could be further advanced by considering a distribution of F_0 and σ_0, which are likely to be correlated given that a defect simply requires a certain amount of energy to be bypassed, thermally or otherwise, and a higher deterministic bypass stress then necessarily means that a defect has a higher activation energy for bypass. The resulting distribution corresponding to E_A is calculated numerically using 10^6 samples and is presented as a cumulative distribution function in Figure 79. The accompanying probability distribution is highly biased to small activation energy values and decays rapidly, faster than an exponential probability distribution.

For an expectation value of the zero stress energy barrier of 30 eV and a yield stress of 30 MPa, 10.8% of depinning events have an activation energy ≤ 2 eV which increases to 24.3% at a stress level equal to half of the yield stress. Despite a zero stress energy expectation value that is above the level of thermal activation, the distributions of stress and activation energy enable a significant percentage of dislocation-obstacle bypass reactions to occur via thermal activation.

Even further, this analysis is simplified in that it does not include the local time-varying nature of the internal stress field. As dislocations bypass obstacles via thermal activation, their resulting displacement induces a dramatic shift in the local stress fields. The restructuring of the dislocation network in the material changes the stress

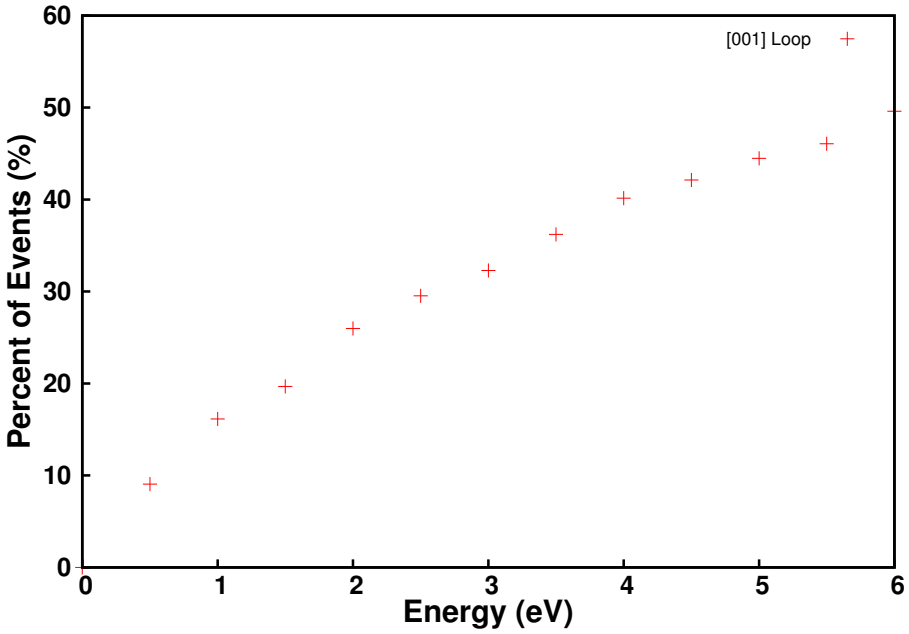

Figure 79: Cumulative distributions of activation energy at varying levels of stress for $F_0 = 30$ eV and $\sigma_0 = 30$ MPa.

field on the other defects and as a result, some bypass events having high activation energies initially may become possible with energy provided from thermal lattice vibrations. This mechanism allows for thermally activated dislocation motion in the presence of obstacles having high activation energies.

5.6 Conclusion

Transition state theory and the Arrhenius equation provide a methodology to coarse-grain general thermally activation reactions including dislocation-obstacle bypass events enabling scale transition across orders of magnitude of length and time. The necessary parameters to apply this method for unit processes are accessible using atomistic calculations and DDD-NEB; however, coarse-graining this information to predict an effective activation energy for dislocation migration in a realistic defect environment is highly complex. Geometric factors of the dislocation segments pinned to the nearest-neighbour obstacles have a strong influence on the activation energy,

which creates a high-dimensional dependency on numerous factors including the individual defects, their geometric configuration, and the applied stress. Calculating the activation energy for a unit process and directly applying this value to a configuration with the same the mean defect spacing overestimates the activation energy for the process in every case investigated. The activation energy distributions found here are seen to be well-described using an exponential probability distribution requiring only the distribution mean as a parameter. The Kocks TST model is shown to accurately describe the mean activation energy evolution using a fitting parameter. These two parametrizations, in combination with an assumed distribution of stress, are used to create a cumulative probability distribution of activation energy, revealing that thermally activated bypass can be significant even with large activation energies.

Earlier theoretical works on thermally activated dislocation glide, notably that of Gibbs [72], emphasize the importance of correctly selecting the thermodynamic system as that of the entire crystal, because "it is the entire crystal and not simply a local region which adopts the minimum free energy configuration consistent with any imposed structure." Consequently, characterising the minimum energy pathway for unit dislocation-obstacle bypass events has limited value with respect to predicting macroscopic thermally activated behaviour. The relative "strength" of defects can be elucidated from such limited bypass events, but insight into macroscopic material behaviour is not possible. Meso-scale simulation methods such as the one proposed in this thesis are thus essential to simulate thermally activated dislocation motion to serve as an input to higher scale models, particularly with the current computational limitations on atomistic simulations.

CHAPTER VI

CONCLUSION

This thesis is dedicated to advancing the forefront of irradiation hardening predictions using discrete dislocation dynamics simulations to simulate more realistic dislocation-defect interactions at the mesoscopic level than ever before, in both the thermal and athermal regimes. Nuclear pressure vessel ductility is the paramount concern for reaction lifetime extension programmes and new reactor design lifetime estimates, and yet this subject area has been the subject of relatively little study until recently as reactors approach their design lifetimes. At the atomic scale, atomistic calculations are a common method to determine the necessary stress to cause a dislocation to bypass an obstacle, but such calculations are restricted to a limited parameter set, periodic boundary conditions with highly confined volumes, and shock loading ($\dot{\varepsilon} > 10^6$). Deriving estimates of macroscopic material strength from such unrepresentative simulations is impossible without significant coarse-graining efforts. Mesoscopic simulations such as dislocation dynamics simulations are ideally suited for this role because they can capture the influence of an ensemble of defects on dislocation motion. Before the work performed in the present thesis, the most advanced simulations of dislocation-defect interactions (for obstacles not composed of dislocation segments, such as voids or precipitates) were limited to line tension simulations. Modelling a dislocation as a simple line under tension may provide insight into certain trends but the oversimplified model is incapable of providing useful parameters to higher scale models with the goal of predicting material properties for physical applications. The DDD simulations in this thesis show that that the Bacon Kocks Scattergood model and the Friedel Kroupa Hirsch model for hardening accurately predict the increase

in yield strength for a single dislocation migrating through a random array of voids and SIA loops respectively (using an atomistics-informed breakaway strength). A mean-size approach is validated for defects with a Gaussian size distribution, and a superposition principle to calculate the hardening from both voids and SIA loops simultaneously is presented.

The analysis of athermal irradiation hardening in the present thesis could be further refined and advanced with a more thorough mapping of dislocation-void breakaway strengths from atomistic calculations. The role of parameters such as interaction geometry, dislocation character, and the effect of defect spacing for random arrays have only been investigated briefly, and a full parametric mapping would undoubtedly provide a more accurate representation of the defects in DDD simulations. For defects composed of dislocations such as SFT or SIA loops, DDD simulations are capable of reproducing complex phenomena observed in atomistics [127, 194] but reproducing a single reaction is often the focus of an entire study. Including such complex reactions may be unnecessary if the most important details of the reaction can be coarse-grained using the same technique as for other defects, i.e. extract the defect strength with an additional possibility of altering the defect strength following dislocation bypass events to reproduce the effect of dislocation loop rearrangement or defect shearing.

Thermal lattice vibrations are a key driving force to enable non-spontaneous reactions to occur, including dislocation unpinning from obstacles. Drawing on numerous independent developments in the field of transition state theory, this thesis develops new methods to improve the prediction of thermally assisted dislocation migration that are able to calculate activation energies and attempt frequencies for dislocation configurations described using the continuum theory of defects. The most advanced estimate to date for the attempt frequency of dislocation-obstacle bypass relies on line tension approximations, and while this allows for closed form solutions, the dislocation line tension model is overly simple. In this thesis, it is shown that applying

a vibration analysis to a complete description of dislocations using continuum theory reveals that the fundamental frequency scales as $1/L$ as in the case of line tension, but the modal frequencies scale with a power law rather than linearly. Estimates of the entropic factor (which is multiplied to the fundamental frequency to obtain the attempt frequency) for a dislocation bypassing an SIA loop revealed an entropic factor independent of length, with accuracy better than one order of magnitude. Given that the reaction rate predicted by the Arrhenius equation is much more sensitive to activation energy, such accuracy is acceptable for these applications.

Applying the NEB method to dislocations described using the continuum theory of defects provides a new method to calculate activation energies for dislocation migration processes. Atomistic calculations are ill-suited to such configurations because of their dependence on chosen atomistic potential, restriction to highly confined simulation volumes (resulting in large image forces from the boundaries), and prohibitively high computational costs. Applying the DDD-NEB method to a unit dislocation-SIA loop bypass reaction reveals a complex energy landscape as a function of interaction geometry, a stress dependence well-described by the Kocks TST model, and a logarithmic dependence on SIA loop spacing. The methodology to transition this knowledge to more representative defect configurations of a dislocation gliding through a representative numbers of SIA loops has never been delineated. Whereas the stress necessary to cause a dislocation to bypass a defect can be effectively encapsulated by a breakaway angle for athermal irradiation hardening calculations, the activation energy for bypass is influenced by changes in dislocation morphology far away from the defect and cannot be captured with a similar method. Simulations of a dislocation bypassing SIA loops distributed randomly in space show that the activation energy distribution for an ensemble of loops is not well-described by unit simulations with the same mean defect spacing with unit process simulations systematically overestimate the mean activation energy. However, the calculated distributions are given by

an exponential probability distribution that allow the distribution to be characterized by a single parameter, its mean value.

As the DDD-NEB approach is a novel method, there are many possibilities to expand upon and develop the approach more deeply. From the standpoint of numerical methods, other formulations beyond the NEB for determining minimum energy pathways have been proposed including various string methods [171, 183]. The simplified string method uses an interpolation function to parametrize the path between images. A series of evenly distributed images are created at each iteration, evolved according to the force acting normal to the tangent, and used to update the interpolation function. The images are created at each step such that they are always evenly spaced in energy space, and the tangent calculation does not involve finite difference calculations. A simplified string method is possibly a more numerically stable method to calculate the MEP to apply to DDD calculations for several reasons. Instability arises due to the $1/r$ elastic fields of dislocations - even in the nonsingular case, the stresses are intense at the dislocation core (on the order of 10^9 Pa or greater). Any error in the tangent results in a strong force on the dislocation driving the dislocation along the tangent. Consequently, the spring force must be sufficient to counteract this force. Replacing the spring force with re-interpolation may alleviate such numerical issues if the interpolation can accurately describe the energy surface. From a physical standpoint, NEB calculations for dislocation reactions involving junction formation or SIA loop deformation can be simulated with a DDD-NEB calculation with added complexities in the numerical implementation and assuming one can determine the final deformed state (as the NEB requires knowledge of the final state). Moving beyond obstacles composed of dislocations is possible with a more complex DDD formulation and implementation. Using the discrete-continuous method [116, 227] with an FFT method [24], anisotropic dislocation dynamics simulations in inhomogeneous materials are possible, which can be readily coupled to an MEP finding method.

The research performed in this thesis has produced new numerical methods and tools providing insight into irradiation hardening and thermally activated processes, and revealing complexities that have never before been considered. Continued advancements in simulating dislocation-obstacle interactions at the atomic and meso-scales are vital to improve predictions of irradiation, precipitation, and work hardening in engineering materials and to design new materials from the bottom up to better suit their applications.

REFERENCES

[1] Ackland, G., Mendelev, M., Srolovitz, D., Han, S., and Barashev, A., "Development of an interatomic potential for phosphorus impurities in α-iron," *Journal of Physics: Condensed Matter*, vol. 16, no. 27, p. S2629, 2004.

[2] Agency, I. A. E., "Power reactor information system." Web page, 2015. Accessed: 2015-10-27.

[3] Akasheh, F., Zbib, H., Hirth, J., Hoagland, R., and Misra, A., "Dislocation dynamics analysis of dislocation intersections in nanoscale metallic multilayered composites," *J. Appl. Phys.*, vol. 101, no. 8, p. 084314, 2007.

[4] Arsenlis, A., Rhee, M., Hommes, G., Cook, R., and Marian, J., "A dislocation dynamics study of the transition from homogeneous to heterogeneous deformation in irradiated body-centered cubic iron," *Acta Materialia*, vol. 60, no. 9, pp. 3748–3757, 2012.

[5] Arsenlis, A., Cai, W., Tang, M., Rhee, M., Oppelstrup, T., Hommes, G., Pierce, T. G., and Bulatov, V. V., "Enabling strain hardening simulations with dislocation dynamics," *Modelling and Simulation in Materials Science and Engineering*, vol. 15, no. 6, p. 553, 2007.

[6] Arzt, E. and Rösler, J., "The kinetics of dislocation climb over hard particlesii. effects of an attractive particle-dislocation interaction," *Acta Metallurgica*, vol. 36, no. 4, pp. 1053–1060, 1988.

[7] Arzt, E. and Wilkinson, D., "Threshold stresses for dislocation climb over hard particles: the effect of an attractive interaction," *Acta Metallurgica*, vol. 34, no. 10, pp. 1893–1898, 1986.

[8] Aubry, S. and Arsenlis, A., "Use of spherical harmonics for dislocation dynamics in anisotropic elastic media," *Modelling and Simulation in Materials Science and Engineering*, vol. 21, no. 6, p. 065013, 2013.

[9] Averback, R. and Diaz de la Rubia, T., "Displacement damage in irradiated metals and semiconductors," *Solid State Physics*, vol. 51, pp. 281–402, 1997.

[10] Bacon, D. J., Osetsky, Y. N., Stoller, R., and Voskoboinikov, R. E., "Md description of damage production in displacement cascades in copper and α-iron," *Journal of nuclear materials*, vol. 323, no. 2, pp. 152–162, 2003.

[11] Bacon, D. J., Osetsky, Y. N., and Rong, Z., "Computer simulation of reactions between an edge dislocation and glissile self-interstitial clusters in iron," *Philosophical Magazine*, vol. 86, no. 25-26, pp. 3921–3936, 2006.

[12] Bacon, D., Gao, F., and Osetsky, Y. N., "The primary damage state in fcc, bcc and hcp metals as seen in molecular dynamics simulations," *Journal of Nuclear Materials*, vol. 276, no. 1, pp. 1–12, 2000.

[13] Bacon, D., Kocks, U., and Scattergood, R., "The effect of dislocation self-interaction on the orowan stress," *Philosophical Magazine*, vol. 28, no. 6, pp. 1241–1263, 1973.

[14] Bacon, D., Osetsky, Y., and Rodney, D., "Dislocation–obstacle interactions at the atomic level," *Dislocations in solids*, vol. 15, pp. 1–90, 2009.

[15] Bai, X.-M., Voter, A. F., Hoagland, R. G., Nastasi, M., and Uberuaga, B. P., "Efficient annealing of radiation damage near grain boundaries via interstitial emission," *Science*, vol. 327, no. 5973, pp. 1631–1634, 2010.

[16] Balogh, L., Capolungo, L., and Tomé, C., "On the measure of dislocation densities from diffraction line profiles: A comparison with discrete dislocation methods," *Acta Materialia*, vol. 60, no. 4, pp. 1467–1477, 2012.

[17] Barnett, S. and Shinn, M., "Plastic and elastic properties of compositionally modulated thin-films," *Annu. Rev. Mater. Sci.*, vol. 24, pp. 481–511, 1994.

[18] Barton, N. R., Arsenlis, A., and Marian, J., "A polycrystal plasticity model of strain localization in irradiated iron," *Journal of the Mechanics and Physics of Solids*, vol. 61, no. 2, pp. 341–351, 2013.

[19] Becquart, C. S., Barbu, A., Bocquet, J., Caturla, M., Domain, C., Fu, C.-C., Golubov, S., Hou, M., Malerba, L., Ortiz, C., and others, "Modeling the long-term evolution of the primary damage in ferritic alloys using coarse-grained methods," *Journal of nuclear materials*, vol. 406, no. 1, pp. 39–54, 2010.

[20] Becquart, C. S., Souidi, A., Domain, C., Hou, M., Malerba, L., and Stoller, R., "Effect of displacement cascade structure and defect mobility on the growth of point defect clusters under irradiation," *Journal of nuclear materials*, vol. 351, no. 1, pp. 39–46, 2006.

[21] Bergner, F., Pareige, C., Hernández-Mayoral, M., Malerba, L., and Heintze, C., "Application of a three-feature dispersed-barrier hardening model to neutron-irradiated fe-cr model alloys," *Journal of Nuclear Materials*, vol. 448, no. 1, pp. 96–102, 2014.

[22] Bertin, N., Tomé, C., Beyerlein, I., Barnett, M., and Capolungo, L., "On the strength of dislocation interactions and their effect on latent hardening

in pure magnesium," *International Journal of Plasticity*, vol. 62, pp. 72–92, 2014.

[23] Bertin, N., *On the Role of Lattice Defect Interactions on Strain Hardening: A Study from Discrete Dislocation Dynamics to Crystal Plasticity Modelling*. PhD thesis, Georgia Institute of Technology, 2015.

[24] Bertin, N., Upadhyay, M., Pradalier, C., and Capolungo, L., "A fft-based formulation for efficient mechanical fields computation in isotropic and anisotropic periodic discrete dislocation dynamics," *Modelling and Simulation in Materials Science and Engineering*, vol. 23, no. 6, p. 065009, 2015.

[25] Beyerlein, I., Mara, N., Wang, J., Carpenter, J., Zheng, S., Han, W., Zhang, R., Kang, K., Nizolek, T., and Pollock, T. *JOM*, vol. 64, p. 1192, 2012.

[26] Beyerlein, I. J., Mara, N. A., Carpenter, J. S., Nizolek, T., Mook, W. M., Wynn, T. A., McCabe, R. J., Mayeur, J. R., Kang, K., Zheng, S., Wang, J., and Pollock, T. M., "Interface-driven microstructure development and ultra high strength of bulk nanostructured Cu-Nb multilayers fabricated by severe plastic deformation," *JOURNAL OF MATERIALS RESEARCH*, vol. 28, no. 13, SI, pp. 1799–1812, 2013.

[27] Bower, A. F., *Applied mechanics of solids*. CRC press, 2009.

[28] Brimbal, D., Décamps, B., Barbu, A., Meslin, E., and Henry, J., "Dual-beam irradiation of α-iron: Heterogeneous bubble formation on dislocation loops," *Journal of Nuclear Materials*, vol. 418, no. 1, pp. 313–315, 2011.

[29] Bulatov, V., Cai, W., Fier, J., Hiratani, M., Hommes, G., Pierce, T., Tang, M., Rhee, M., Yates, K., and Arsenlis, T., "Scalable line dynamics in paradis," in *Proceedings of the 2004 ACM/IEEE conference on Supercomputing*, p. 19, IEEE Computer Society, 2004.

[30] Cai, W., Arsenlis, A., Weinberger, C. R., and Bulatov, V. V., "A non-singular continuum theory of dislocations," *Journal of the Mechanics and Physics of Solids*, vol. 54, no. 3, pp. 561–587, 2006.

[31] Cai, W. and Bulatov, V. V., "Mobility laws in dislocation dynamics simulations," *Materials Science and Engineering: A*, vol. 387, pp. 277–281, 2004.

[32] Capolungo, L., Spearot, D., Cherkaoui, M., McDowell, D., Qu, J., and Jacob, K., "Dislocation nucleation from bicrystal interfaces and grain boundary ledges: relationship to nanocrystalline deformation," *Journal of the Mechanics and Physics of Solids*, vol. 55, no. 11, pp. 2300–2327, 2007.

[33] Castany, P., Pettinari-Sturmel, F., Crestou, J., Douin, J., and Coujou, A., "Experimental study of dislocation mobility in a ti-6al-4v alloy," *Acta Materialia*, vol. 55, no. 18, pp. 6284–6291, 2007.

[34] Chang, H.-J., Segurado, J., and LLorca, J., "Three-dimensional dislocation dynamics analysis of size effects on void growth," *Scripta Materialia*, vol. 95, pp. 11–14, 2015.

[35] Chang, J., Cai, W., Bulatov, V. V., and Yip, S., "Dislocation motion in bcc metals by molecular dynamics," *Materials Science and Engineering: A*, vol. 309, pp. 160–163, 2001.

[36] Chen, Z., Chu, K. T., Srolovitz, D. J., Rickman, J. M., and Haataja, M. P., "Dislocation climb strengthening in systems with immobile obstacles: Three-dimensional level-set simulation study," *Physical Review B*, vol. 81, no. 5, p. 054104, 2010.

[37] Cheverton, R. and Sims, T., "Hfir core nuclear design.," tech. rep., Oak Ridge National Lab., Tenn., 1971.

[38] Chou, T.-W. and Pan, Y.-C., "Elastic energies of disclinations in hexagonal crystals," *Journal of Applied Physics*, vol. 44, no. 1, pp. 63–65, 1973.

[39] Cockeram, B. V., Smith, R. W., Leonard, K. J., Byun, T. S., and Snead, L. L., "Development of microstructure and irradiation hardening of zircaloy during low dose neutron irradiation at nominally 358 c," *Journal of Nuclear Materials*, vol. 418, no. 1, pp. 46–61, 2011.

[40] Cottrell, A., "Effects of neutron irradiation on metals and alloys," *Metallurgical Reviews*, vol. 1, no. 1, pp. 479–522, 1956.

[41] Cottrell, A. H., "Theory of dislocations," *Progress in Metal Physics*, vol. 4, pp. 205–264, 1953.

[42] Cottrell, A. H. and Bilby, B., "Dislocation theory of yielding and strain ageing of iron," *Proceedings of the Physical Society. Section A*, vol. 62, no. 1, p. 49, 1949.

[43] Csikor, F. F. and Groma, I., "Probability distribution of internal stress in relaxed dislocation systems," *Physical Review B*, vol. 70, pp. 064106–064106, 2004.

[44] Daulton, T., Kirk, M., and Rehn, L., "In-situ transmission electron microscopy study of ion-irradiated copper: temperature dependence of defect yield and cascade collapse," *Philosophical Magazine A*, vol. 80, no. 4, pp. 809–842, 2000.

[45] De Hosson, J. T. M., in't Veld, A. H., Tamler, H., and Kanert, O., "Dislocation dynamics in al-li alloys. mean jump distance and activation length of moving dislocations," *Acta Metallurgica*, vol. 32, no. 8, pp. 1205–1215, 1984.

[46] de Vaucorbeil, A., Poole, W., and Sinclair, C., "The superposition of strengthening contributions in engineering alloys," *Materials science & engineering. A, Structural materials: properties, microstructure and processing*, vol. 582, pp. 147–154, 2013.

[47] de Wit', R., "The continuum theory of stationary dislocations," *Solid State Physics*, vol. 10, pp. 249–292, 1960.

[48] Demkowicz, M., Hoagland, R., and Hirth, J., "Interface structure and radiation damage resistance in cu-nb multilayer nanocomposites," *Physical review letters*, vol. 100, no. 13, p. 136102, 2008.

[49] Deo, C. S., Okuniewski, M. A., Srivilliputhur, S. G., Maloy, S. A., Baskes, M. I., James, M. R., and Stubbins, J. F., "Helium bubble nucleation in bcc iron studied by kinetic monte carlo simulations," *Journal of nuclear materials*, vol. 361, no. 2, pp. 141–148, 2007.

[50] Dérès, J., Proville, L., and Marinica, M.-C., "Dislocation depinning from nano-sized irradiation defects in a bcc iron model," *Acta Materialia*, vol. 99, pp. 99–105, 2015.

[51] Devincre, B., Kubin, L., Lemarchand, C., and Madec, R., "Mesoscopic simulations of plastic deformation," *Materials Science and Engineering: A*, vol. 309, pp. 211–219, 2001.

[52] deWit, R., "Thermodynamic force on a dislocation," *Journal of Applied Physics*, vol. 39, pp. 137–141, 1968.

[53] Domain, C., Becquart, C., and Malerba, L., "Simulation of radiation damage in fe alloys: an object kinetic monte carlo approach," *Journal of Nuclear Materials*, vol. 335, no. 1, pp. 121–145, 2004.

[54] Dong, Y., Nogaret, T., and Curtin, W., "Scaling of dislocation strengthening by multiple obstacle types," *Metallurgical and Materials Transactions A*, vol. 41, no. 8, pp. 1954–1960, 2010.

[55] Duesbery, M., "On kinked screw dislocations in the bcc latticei. the structure and peierls stress of isolated kinks," *Acta Metallurgica*, vol. 31, no. 10, pp. 1747–1758, 1983.

[56] Dunn, A. and Capolungo, L., "Simulating radiation damage accumulation in α-fe: A spatially resolved stochastic cluster dynamics approach," *Computational Materials Science*, vol. 102, pp. 314–326, 2015.

[57] Dunn, A., McPhie, M., Capolungo, L., Martinez, E., and Cherkaoui, M., "A rate theory study of helium bubble formation and retention in cu-nb nanocomposites," *Journal of Nuclear Materials*, vol. 435, no. 1, pp. 141–152, 2013.

[58] Eldrup, M. and Singh, B., "Studies of defects and defect agglomerates by positron annihilation spectroscopy," *Journal of nuclear materials*, vol. 251, pp. 132–138, 1997.

[59] Eldrup, M., Singh, B., Zinkle, S., Byun, T., and Farrell, K., "Dose dependence of defect accumulation in neutron irradiated copper and iron," *Journal of nuclear materials*, vol. 307, pp. 912–917, 2002.

[60] Eyring, H., Gershinowitz, H., and Sun, C. E., "The absolute rate of homogeneous atomic reactions," *The Journal of Chemical Physics*, vol. 3, no. 12, pp. 786–796, 1935.

[61] Farkas, D., Schon, C., De Lima, M., and Goldenstein, H., "Embedded atom computer simulation of lattice distortion and dislocation core structure and mobility in fe-cr alloys," *Acta materialia*, vol. 44, no. 1, pp. 409–419, 1996.

[62] Ferroni, F., Tarleton, E., and Fitzgerald, S., "Dislocation dynamics modelling of radiation damage in thin films," *Modelling and Simulation in Materials Science and Engineering*, vol. 22, no. 4, p. 045009, 2014.

[63] Fivel, M. and Canova, G., "Developing rigorous boundary conditions to simulations of discrete dislocation dynamics," *Modelling and Simulation in Materials Science and Engineering*, vol. 7, no. 5, p. 753, 1999.

[64] Foreman, A. and Makin, M., "Dislocation movement through random arrays of obstacles," *Phil. Mag.*, vol. 14, no. 131, pp. 911 – 924, 1966.

[65] Forest, S., "Micromorphic approach for gradient elasticity, viscoplasticity, and damage," *Journal of Engineering Mechanics*, vol. 135, no. 3, pp. 117–131, 2009.

[66] Frank, F. and Read Jr, W., "Multiplication processes for slow moving dislocations," *Physical Review*, vol. 79, no. 4, p. 722, 1950.

[67] Friedel, J., "Dislocations, 1964," *Oxford*, vol. 70, pp. 15–24.

[68] Friedel, J., "Dislocation movement through random arrays of obstacles," *Electron Microsc. and Strength of Crystals*, pp. 605 – 651, 1963.

[69] Fukui, M., Sakamoto, R., Araki, K., Fujiwara, T., Muroga, T., and Yoshida, N., "In situ observation of low energy hydrogen ion irradiation damage in copper," *Journal of nuclear materials*, vol. 220, pp. 810–814, 1995.

[70] Gao, F., Henkelman, G., Weber, W. J., Corrales, L. R., and Jónsson, H., "Finding possible transition states of defects in silicon-carbide and alpha-iron using the dimer method," *Nuclear Instruments and Methods in Physics Research Section B: Beam Interactions with Materials and Atoms*, vol. 202, pp. 1–7, 2003.

[71] Ghoniem, N., M, Tong, S.-H., and Sun, L., "Parametric dislocation dynamics: a thermodynamics-based approach to investigations of mesoscopic plastic deformation," *Physical Review B*, vol. 61, no. 2, p. 913, 2000.

[72] Gibbs, G., "Thermodynamic analysis of dislocation glide controlled by dispersed local obstacles," *Materials Science and Engineering*, vol. 4, no. 6, pp. 313–328, 1969.

[73] Gilbert, M., Queyreau, S., and Marian, J., "Stress and temperature dependence of screw dislocation mobility in α-fe by molecular dynamics," *Physical Review B*, vol. 84, no. 17, p. 174103, 2011.

[74] Gold, R. and McElroy, W., "The light water reactor pressure vessel surveillance dosimetry improvement program (lwr-pv-sdip): Past accomplishments, recent developments, and future directions," in *Proc. 6th ASTM-EURATOM Symposium on Reactor Dosimetry, Jackson Hole, WY*, pp. 44–61, 1989.

[75] Gordillo, N., Panizo-Laiz, M., Tejado, E., Fernandez-Martinez, I., Rivera, A., Pastor, J., de Castro, C. G., del Rio, J., Perlado, J., and Gonzalez-Arrabal, R., "Morphological and microstructural characterization of nanostructured pure α-phase w coatings on a wide thickness range," *Applied Surface Science*, vol. 316, pp. 1–8, 2014.

[76] Gordon, P., Neeraj, T., and Mendelev, M., "Screw dislocation mobility in bcc metals: A refined potential description for α-fe," *Philosophical Magazine*, vol. 91, no. 30, pp. 3931–3945, 2011.

[77] Gorman, J. A., *The mobility of dislocations in high purity aluminum.* PhD thesis, California Institute of Technology, 1968.

[78] Granato, A., Lücke, K., Schlipf, J., and Teutonico, L., "Entropy factors for thermally activated unpinning of dislocations," *Journal of Applied Physics*, vol. 35, no. 9, pp. 2732–2745, 1964.

[79] Greer, J. R., Weinberger, C. R., and Cai, W., "Comparing the strength of fcc and bcc sub-micrometer pillars: Compression experiments and dislocation dynamics simulations," *Materials Science and Engineering: A*, vol. 493, no. 1, pp. 21–25, 2008.

[80] Groh, S., Devincre, B., Kubin, L., Roos, A., Feyel, F., and Chaboche, J., "Dislocations and elastic anisotropy in heteroepitaxial metallic thin films.," *Philos. Mag. Lett.*, vol. 83, no. 5, pp. 303 – 313, 2003.

[81] Grydlik, M., Boioli, F., Groiss, H., Gatti, R., Brehm, M., Montalenti, F., Devincre, B., Schaffler, F., and Miglio, L., "Misfit dislocation gettering by substrate pit-patterning in sige films on si(001).," *Appl. Phys. Lett.*, vol. 101, no. 1, 2012.

[82] Gupta, N., Baskes, M. I., and Srinivasan, S. G., "The Role of Interface Structure in Spallation of a Layered Nanocomposite," *JOM*, vol. 63, no. 9, pp. 74–77, 2011.

[83] Gurtin, M. E., "On a framework for small-deformation viscoplasticity: free energy, microforces, strain gradients," *International Journal of Plasticity*, vol. 19, no. 1, pp. 47–90, 2003.

[84] Hafez Haghighat, S., Fikar, J., and Schäublin, R., "Effect of interatomic potential on the behavior of dislocation-defect interaction simulation in α-fe," *Journal of Nuclear Materials*, vol. 382, no. 2, pp. 147–153, 2008.

[85] Hafez Haghighat, S., Fivel, M., Fikar, J., and Schaeublin, R., "Dislocation-void interaction in fe: A comparison between molecular dynamics and dislocation dynamics," *Journal of Nuclear Materials*, vol. 386, pp. 102–105, 2009.

[86] Hatano, T., "Dynamics of a dislocation bypassing an impenetrable precipitate: the hirsch mechanism revisited," *Physical Review B*, vol. 74, no. 2, p. 020102, 2006.

[87] Heinisch, H. L., Gao, F., Kurtz, R. J., and Le, E., "Interaction of helium atoms with edge dislocations in α-fe," *Journal of nuclear materials*, vol. 351, no. 1, pp. 141–148, 2006.

[88] Henkelman, G. and Jónsson, H., "A dimer method for finding saddle points on high dimensional potential surfaces using only first derivatives," *The Journal of chemical physics*, vol. 111, no. 15, pp. 7010–7022, 1999.

[89] Henkelman, G. and Jónsson, H., "Improved tangent estimate in the nudged elastic band method for finding minimum energy paths and saddle points," *The Journal of chemical physics*, vol. 113, no. 22, pp. 9978–9985, 2000.

[90] Henkelman, G. and Jonsson, H., "Improved tangent estimate in the nudged elastic band method for finding minimum energy paths and saddle points," *The Journal of chemical physics*, vol. 113, no. 22, pp. 9978–9985, 2000.

[91] Hernández-Mayoral, M. and Gómez-Briceño, D., "Transmission electron microscopy study on neutron irradiated pure iron and rpv model alloys," *Journal of Nuclear Materials*, vol. 399, no. 2, pp. 146–153, 2010.

[92] Hirth, J. P. and Lothe, J., "Theory of dislocations," 1982.

[93] Hoagland, R., Kurtz, R., and Henager, C., "Slip resistance of interfaces and the strength of metallic multilayer composites.," *Scr. Mater.*, vol. 50, no. 6, pp. 775 – 779.

[94] Huang, H., Sherby, O. D., and Dorn, J., "ACTIVATION ENERGY FOR HIGH TEMPERATURE CREEP OF HIGH PURITY ALUMINUM," *TRANSACTIONS OF THE AMERICAN INSTITUTE OF MINING AND METALLURGICAL ENGINEERS*, vol. 206, no. 10, pp. 1385–1388, 1956.

[95] Huang, J. and Ghoniem, N. M., "The dynamics of dislocation interaction with sessile self-interstitial atom (sia) defect cluster atmospheres," *Computational materials science*, vol. 23, no. 1, pp. 225–234, 2002.

[96] Hull, D. and Bacon, D. J., *Introduction to dislocations*, vol. 257. Pergamon Press Oxford, 1984.

[97] Hunter, A., Saied, F., Le, C., and Koslowski, M., "Large-scale 3d phase field dislocation dynamics simulations on high-performance architectures," *International Journal of High Performance Computing Applications*, vol. 25, no. 2, pp. 223–235, 2010.

[98] Inc., C. O. G., "Candu reactors," 2015. Accessed: 2015-10-27.

[99] Jassby, K. M. and Vreeland Jr, T., "An experimental study of the mobility of edge dislocations in pure copper single crystals," *Philosophical Magazine*, vol. 21, no. 174, pp. 1147–1168, 1970.

[100] Jenkins, M., English, C., and Eyre, B., "Heavy-ion irradiation of α-iron," *Philosophical Magazine A*, vol. 38, no. 1, pp. 97–114, 1978.

[101] Jia, N., Roters, F., Eisenlohr, P., Raabe, D., and Zhao, X., "Simulation of shear banding in heterophase co-deformation: Example of plane strain compressed Cu-Ag and Cu-Nb metal matrix composites," *ACTA MATERIALIA*, vol. 61, no. 12, pp. 4591–4606, 2013.

[102] Jonsson, H., Mills, G., and Jacobsen, K. W., *Nudged elastic band method for finding minimum energy paths of transitions*, ch. 16, pp. 385–404.

[103] Klueh, R., Shingledecker, J., Swindeman, R., and Hoelzer, D., "Oxide dispersion-strengthened steels: A comparison of some commercial and experimental alloys," *Journal of Nuclear Materials*, vol. 341, no. 2, pp. 103–114, 2005.

[104] Kocks, U., Argon, A., and Ashby, M., "Progress in materials science," *Thermodynamics and Kinetics of Slip*, vol. 19, pp. 110–170, 1975.

[105] Kohler, C., Kizler, P., and Schmauder, S., "Atomistic simulation of precipitation hardening in α-iron: influence of precipitate shape and chemical composition," *Modelling and Simulation in Materials Science and Engineering*, vol. 13, no. 1, p. 35, 2005.

[106] Krivit, S. B., Lehr, J. H., and Kingery, T. B., *Nuclear energy encyclopedia: science, technology, and applications*, vol. 5. John Wiley & Sons, 2011.

[107] Kroupa, F. and Hirsch, P., "Elastic interaction between prismatic dislocation loops and straight dislocations," *Discussions of the Faraday Society*, vol. 38, pp. 49–55, 1964.

[108] Kulkarni, A., Krishnamurthy, K., Deshmukh, S., and Mishra, R., "Effect of particle size distribution on strength of precipitation-hardened alloys," *Journal of materials research*, vol. 19, no. 9, pp. 2765–2773, 2004.

[109] Kuramoto, E., Aono, Y., and Kitajima, K., "Thermally activated slip deformation of high purity iron single crystals between 4.2 k and 300 k," *Scripta Metallurgica*, vol. 13, no. 11, pp. 1039–1042, 1979.

[110] Laboratory, N. P., "Nuclear fission and fusion, and neutron interactions." Web page, 2015. Accessed: 2015-10-27.

[111] Lagerpusch, U., Mohles, V., Baither, D., Anczykowski, B., and Nembach, E., "Double strengthening of copper by dissolved gold-atoms and by incoherent sio¡ sub¿ 2¡/sub¿-particles: how do the two strengthening contributions superimpose?," *Acta materialia*, vol. 48, no. 14, pp. 3647–3656, 2000.

[112] Laidler, K. J., "The development of the arrhenius equation," *Journal of Chemical Education*, vol. 61, no. 6, p. 494, 1984.

[113] Laidler, K. J. and King, M. C., "Development of transition-state theory," *The Journal of physical chemistry*, vol. 87, no. 15, pp. 2657–2664, 1983.

[114] Lambrecht, M., Meslin, E., Malerba, L., Hernández-Mayoral, M., Bergner, F., Pareige, P., Radiguet, B., and Almazouzi, A., "On the correlation between irradiation-induced microstructural features and the hardening of reactor pressure vessel steels," *Journal of Nuclear Materials*, vol. 406, no. 1, pp. 84–89, 2010.

[115] Lee, S. B., LeDonne, J. E., Lim, S. C. V., Beyerlein, I. J., and Rollett, A. D., "The heterophase interface character distribution of physical vapor-deposited and accumulative roll-bonded Cu-Nb multilayer composites," *ACTA MATERIALIA*, vol. 60, no. 4, pp. 1747–1761, 2012.

[116] Lemarchand, C., Devincre, B., and Kubin, L., "Homogenization method for a discrete-continuum simulation of dislocation dynamics," *Journal of the Mechanics and Physics of Solids*, vol. 49, no. 9, pp. 1969–1982, 2001.

[117] LeSar, R. and Rickman, J., "Multipole expansion of dislocation interactions: Application to discrete dislocations," *Physical Review B*, vol. 65, no. 14, p. 144110, 2002.

[118] Li, D., Zbib, H., Sun, X., and Khaleel, M., "Predicting plastic flow and irradiation hardening of iron single crystal with mechanism-based continuum dislocation dynamics," *International Journal of Plasticity*, vol. 52, pp. 3–17, 2014.

[119] Li, M., Kirk, M., Baldo, P., Xu, D., and Wirth, B., "Study of defect evolution by tem with in situ ion irradiation and coordinated modeling," *Philosophical Magazine*, vol. 92, no. 16, pp. 2048–2078, 2012.

[120] Li-Qun, C., Chong-Yu, W., and Tao, Y., "Atomistic simulation of kink structure on edge dislocation in bcc iron," *Chinese Physics B*, vol. 17, no. 2, p. 662, 2008.

[121] Lisowski, P., Bowman, C., Russell, G., and Wender, S., "The los alamos national laboratory spallation neutron sources," *Nuclear Science and Engineering*, vol. 106, no. 2, pp. 208–218, 1990.

[122] Liu, X.-Y. and Biner, S., "Molecular dynamics simulations of the interactions between screw dislocations and self-interstitial clusters in body-centered cubic fe," *Scripta Materialia*, vol. 59, no. 1, pp. 51–54, 2008.

[123] Lucas, G. and Schäublin, R., "Helium effects on displacement cascades in α-iron," *Journal of Physics: Condensed Matter*, vol. 20, no. 41, p. 415206, 2008.

[124] Madec, R., Devincre, B., Kubin, L., Hoc, T., and Rodney, D., "The role of collinear interaction in dislocation-induced hardening," *Science*, vol. 301, no. 5641, pp. 1879–1882, 2003.

[125] Malerba, L., "Molecular dynamics simulation of displacement cascades in α-fe: a critical review," *Journal of nuclear materials*, vol. 351, no. 1, pp. 28–38, 2006.

[126] Mara, N., Bhattacharyya, D., Dickerson, P., Hoagland, R., and Misra, A., "Ultrahigh strength and ductility of cu-nb nanolayered composites.," *Mater. Sci. Forum*, vol. 633-634, pp. 647 – 653, 2010.

[127] Marian, J., Martinez, E., Lee, H.-J., and Wirth, B. D., "Micro/mesoscale computational study of dislocation-stacking-fault tetrahedron interactions in copper," *Journal of Materials Research*, vol. 24, no. 12, pp. 3628–3Z635, 2009.

[128] Marian, J., Wirth, B. D., Schäublin, R., Odette, G., and Perlado, J. M., "Md modeling of defects in fe and their interactions," *Journal of nuclear materials*, vol. 323, no. 2, pp. 181–191, 2003.

[129] Martin-Bragado, I., Rivera, A., Valles, G., Gomez-Selles, J. L., and Caturla, M. J., "Mmonca: An object kinetic monte carlo simulator for damage irradiation evolution and defect diffusion," *Computer Physics Communications*, vol. 184, no. 12, pp. 2703–2710, 2013.

[130] Masters, B., "Dislocation loops in irradiated iron," *Philosophical Magazine*, vol. 11, no. 113, pp. 881–893, 1965.

[131] Mayeur, J. R., Beyerlein, I. J., Bronkhorst, C. A., Mourad, H. M., and Hansen, B. L., "A crystal plasticity study of heterophase interface character stability of Cu/Nb bicrystals," *INTERNATIONAL JOURNAL OF PLASTICITY*, vol. 48, pp. 72–91, 2013.

[132] McDowell, D. L., "Evolving structure and internal state variables," Nadai Award Lecture, ASME IMECE, Dallas, TX, November 1997.

[133] McDowell, D. L., "Non-associative aspects of multiscale evolutionary phenomena," in *Proceedings 4th International Conference on Constitutive Laws for Engineering Materials* (Picu, R. and Krempl, E., eds.), pp. 54–57, Rensselaer Polytechnic Institute, 1999.

[134] McPhie, M., Capolungo, L., Dunn, A., and Cherkaoui, M., "Interfacial trapping mechanism of he in cu–nb multilayer materials," *Journal of Nuclear Materials*, vol. 437, no. 1, pp. 222–228, 2013.

[135] Menezes, S. and Anderson, D., "Wavelength-property correlation in electrodeposited ultrastructured Cu-Ni multilayers," *J. Electrochem. Soc.*, vol. 137, no. 2, pp. 440–444, 1990.

[136] Misra, A., Demkowicz, M., Zhang, X., and Hoagland, R., "The radiation damage tolerance of ultra-high strength nanolayered composites," *Jom*, vol. 59, no. 9, pp. 62–65, 2007.

[137] Misra, A., Hirth, J., and Hoagland, R., "Length-scale-dependent deformation mechanisms in incoherent metallic multilayered composites," *Acta Mater.*, vol. 53, no. 18, pp. 4817–4824, 2005.

[138] Misra, A., Hirth, J., and Kung, H., "Single-dislocation-based strengthening mechanisms in nanoscale metallic multilayers," *Philos. Mag. A.*, vol. 82, no. 16, pp. 2935–2951, 2002.

[139] Mohles, V. and Fruhstorfer, B., "Computer simulations of orowan process controlled dislocation glide in particle arrangements of various randomness," *Acta materialia*, vol. 50, no. 10, pp. 2503–2516, 2002.

[140] Mohles, V. and Nembach, E., "The peak-and overaged states of particle strengthened materials: computer simulations," *Acta materialia*, vol. 49, no. 13, pp. 2405–2417, 2001.

[141] Mohles, V., "Orowan process controlled dislocation glide in materials containing incoherent particles," *Materials Science and Engineering: A*, vol. 309, pp. 265–269, 2001.

[142] Monnet, G., "Mechanical and energetical analysis of molecular dynamics simulations of dislocation–defect interactions," *Acta Materialia*, vol. 55, no. 15, pp. 5081–5088, 2007.

[143] Monnet, G., Domain, C., Queyreau, S., Naamane, S., and Devincre, B., "Atomic and dislocation dynamics simulations of plastic deformation in reactor pressure vessel steel," *Journal of Nuclear Materials*, vol. 394, no. 2, pp. 174–181, 2009.

[144] Morgan, D., Van der Ven, A., and Ceder, G., "Li conductivity in li x mpo 4 (m= mn, fe, co, ni) olivine materials," *Electrochemical and solid-state letters*, vol. 7, no. 2, pp. A30–A32, 2004.

[145] Mott, N., "Mechanical strength and creep in metals," *Imperfections in nearly perfect crystals symposium*, pp. 173 – 197, 1952.

[146] Mott, N. and FRN, N., "Report of a conference on strength of solids," *Physical Society, London*, p. 1, 1948.

[147] Mousseau, N. and Barkema, G., "Traveling through potential energy landscapes of disordered materials: The activation-relaxation technique," *Physical Review E*, vol. 57, no. 2, p. 2419, 1998.

[148] Mura, T., "Continuous distribution of moving dislocations," *Philosophical Magazine*, vol. 8, no. 89, pp. 843–857, 1963.

[149] Mura, T., *Micromechanics of defects in solids*, vol. 3. 1982.

[150] Nabarro, F., "Dislocations in a simple cubic lattice," *Proceedings of the Physical Society*, vol. 59, no. 2, p. 256, 1947.

[151] Nembach, E., "Particle strengthening of metals and alloys," 1996.

[152] Nicol, A., Jenkins, M., and Kirk, M., "Matrix damage in iron," in *Materials Research Society Symposium Proceedings*, vol. 650, pp. R1–3, Cambridge Univ Press, 2001.

[153] Nix, W., "Yielding and strain hardening of thin metal films on substrates," *Scr. Mater.*, vol. 39, no. 4-5, pp. 545–554, 1998.

[154] Nix, W. D. and Cai, W., "Plasticity of bcc micropillars controlled by competition between dislocation multiplication and depletion," *Acta Materialia*, vol. 61, no. 9, pp. 3233–3241, 2013.

[155] Nogaret, T., Rodney, D., Fivel, M., and Robertson, C., "Clear band formation simulated by dislocation dynamics: Role of helical turns and pile-ups," *Journal of Nuclear Materials*, vol. 380, no. 1, pp. 22–29, 2008.

[156] Nomoto, A., Soneda, N., Takahashi, A., and Ishino, S., "Interaction analysis between edge dislocation and self interstitial type dislocation loop in bcc iron using molecular dynamics," *Materials transactions*, vol. 46, no. 03, pp. 463–468, 2005.

[157] Odette, G., "On the dominant mechanism of irradiation embrittlement of reactor pressure vessel steels," *Scripta metallurgica*, vol. 17, no. 10, pp. 1183–1188, 1983.

[158] Odette, G. and Lucas, G., "Embrittlement of nuclear reactor pressure vessels," *Jom*, vol. 53, no. 7, pp. 18–22, 2001.

[159] Oldenberg, O. and Sommers Jr, H., "The thermal reaction between hydrogen and oxygen iii. the temperature coefficient of the steady thermal reaction," *The Journal of Chemical Physics*, vol. 9, no. 5, pp. 432–438, 1941.

[160] Orowan, E., "The crystal plasticity. iii: about the mechanism of the sliding," 1934.

[161] Ortiz, C. and Caturla, M., "Simulation of defect evolution in irradiated materials: role of intracascade clustering and correlated recombination," *Physical Review B*, vol. 75, no. 18, p. 184101, 2007.

[162] Osetsky, Y. N. and Bacon, D. J., "An atomic-level model for studying the dynamics of edge dislocations in metals," *Modelling and simulation in materials science and engineering*, vol. 11, no. 4, p. 427, 2003.

[163] Osetsky, Y. N. and Bacon, D. J., "Atomic-scale mechanisms of void hardening in bcc and fcc metals," *Philosophical Magazine*, vol. 90, no. 7-8, pp. 945–961, 2010.

[164] Osetsky, Y. N., Stoller, R. E., Rodney, D., and Bacon, D. J., "Atomic-scale details of dislocation–stacking fault tetrahedra interaction," *Materials Science and Engineering: A*, vol. 400, pp. 370–373, 2005.

[165] Pan, E. and Yang, B., "Three-dimensional interfacial greens functions in anisotropic bimaterials," *Applied Mathematical Modelling*, vol. 27, no. 4, pp. 307–326, 2003.

[166] Pan, E. and Yuan, F., "Three-dimensional greens functions in anisotropic bimaterials," *International Journal of Solids and Structures*, vol. 37, no. 38, pp. 5329–5351, 2000.

[167] Patra, A. and McDowell, D. L., "Crystal plasticity-based constitutive modelling of irradiated bcc structures," *Philosophical Magazine*, vol. 92, no. 7, pp. 861–887, 2012.

[168] Peach, M. and Koehler, J., "The forces exerted on dislocations and the stress fields produced by them," *Physical Review*, vol. 80, no. 3, p. 436, 1950.

[169] Peierls, R., "The size of a dislocation," *Proceedings of the Physical Society*, vol. 52, no. 1, pp. 34–37, 1940.

[170] Pelzer, H. and Wigner, E., "The speed constansts of the exchange reactions," *Z Phys Chem B*, vol. 15, p. 445, 1932.

[171] Peters, B., Heyden, A., Bell, A. T., and Chakraborty, A., "A growing string method for determining transition states: Comparison to the nudged elastic band and string methods," *The Journal of chemical physics*, vol. 120, no. 17, pp. 7877–7886, 2004.

[172] Pfaundler, L., "Beiträge zur chemischen statik," *Annalen der Physik*, vol. 207, no. 5, pp. 55–85, 1867.

[173] Picu, R., Li, R., and Xu, Z., "Strain rate sensitivity of thermally activated dislocation motion across fields of obstacles of different kind," *Materials Science and Engineering: A*, vol. 502, no. 1, pp. 164–171, 2009.

[174] Pizzagalli, L., Beauchamp, P., and Jónsson, H., "Calculations of dislocation mobility using nudged elastic band method and first principles dft calculations," *Philosophical Magazine*, vol. 88, no. 1, pp. 91–100, 2008.

[175] Politano, O. and Salazar, J., "A 3d mesoscopic approach for discrete dislocation dynamics," *Materials Science and Engineering: A*, vol. 309, pp. 261–264, 2001.

[176] Porter, D. A., Easterling, K. E., and Sherif, M., *Phase Transformations in Metals and Alloys, (Revised Reprint)*. CRC press, 2011.

[177] Prieto-Depedro, M., Martin-Bragado, I., and Segurado, J., "An atomistically informed kinetic monte carlo model of grain boundary motion coupled to shear deformation," *International Journal of Plasticity*, vol. 68, pp. 98–110, 2015.

[178] Quapp, W. and Heidrich, D., "Analysis of the concept of minimum energy path on the potential energy surface of chemically reacting systems," *Theoretica chimica acta*, vol. 66, no. 3-4, pp. 245–260, 1984.

[179] Quek, S., Xiang, Y., Zhang, Y., Srolovitz, D., and Lu, C., "Level set simulation of dislocation dynamics in thin films," *Acta materialia*, vol. 54, no. 9, pp. 2371–2381, 2006.

[180] Queyreau, S., Monnet, G., and Devincre, B., "Slip systems interactions in α-iron determined by dislocation dynamics simulations," *International Journal of Plasticity*, vol. 25, no. 2, pp. 361–377, 2009.

[181] Queyreau, S., Monnet, G., and Devincre, B., "Orowan strengthening and forest hardening superposition examined by dislocation dynamics simulations," *Acta Materialia*, vol. 58, no. 17, pp. 5586–5595, 2010.

[182] Rao, S., Dimiduk, D., Parthasarathy, T., El-Awady, J., Woodward, C., and Uchic, M., "Calculations of intersection cross-slip activation energies in fcc metals using nudged elastic band method," *Acta Materialia*, vol. 59, no. 19, pp. 7135–7144, 2011.

[183] Ren, W. and Vanden-Eijnden, E., "Finite temperature string method for the study of rare events," *The Journal of Physical Chemistry B*, vol. 109, no. 14, pp. 6688–6693, 2005.

[184] Robach, J., Robertson, I., Lee, H.-J., and Wirth, B., "Dynamic observations and atomistic simulations of dislocation–defect interactions in rapidly quenched copper and gold," *Acta materialia*, vol. 54, no. 6, pp. 1679–1690, 2006.

[185] Robach, J., Robertson, I., Wirth, B., and Arsenlis, A., "In-situ transmission electron microscopy observations and molecular dynamics simulations of dislocation-defect interactions in ion-irradiated copper," *Philosophical Magazine*, vol. 83, no. 8, pp. 955–967, 2003.

[186] Rodney, D., Le Bouar, Y., and Finel, A., "Phase field methods and dislocations," *Acta materialia*, vol. 51, no. 1, pp. 17–30, 2003.

[187] Rosinski, S. T., *Effects of Radiation on Materials: 20th International Symposium*, vol. 1405. ASTM International, 2001.

[188] Scattergood, R. and Bacon, D., "The strengthening effect of voids," *Acta Metallurgica*, vol. 30, no. 8, pp. 1665–1677, 1982.

[189] Schmid, E., Boas, W., and Rawlins, F., "Kristallplastizität," *The Journal of Physical Chemistry*, vol. 39, no. 9, pp. 1248–1248, 1935.

[190] Schoeck, G., "The activation energy of dislocation movement," *physica status solidi (b)*, vol. 8, no. 2, pp. 499–507, 1965.

[191] Seeger, A., "Radiation damage in solids," *IAEA, Vienna*, vol. 1, p. 101, 1962.

[192] Shen, C., Li, J., and Wang, Y., "Finding critical nucleus in solid-state transformations," *Metallurgical and materials transactions A*, vol. 39, no. 5, pp. 976–983, 2008.

[193] Sheppard, D. and Henkelman, G., "Paths to which the nudged elastic band converges," *Journal of computational chemistry*, vol. 32, no. 8, pp. 1769–1771, 2011.

[194] Shi, X., Dupuy, L., Devincre, B., Terentyev, D., and Vincent, L., "Interaction of¡ 100¿ dislocation loops with dislocations studied by dislocation dynamics in α-iron," *Journal of Nuclear Materials*, vol. 460, pp. 37–43, 2015.

[195] Simonovic, D. and Sluiter, M. H., "Impurity diffusion activation energies in al from first principles," *Physical Review B*, vol. 79, no. 5, p. 054304, 2009.

[196] Singh, B., Horsewell, A., Toft, P., and Edwards, D., "Temperature and dose dependencies of microstructure and hardness of neutron irradiated ofhc copper," *Journal of Nuclear Materials*, vol. 224, no. 2, pp. 131–140, 1995.

[197] Sobie, C., Bertin, N., and Capolungo, L., "Analysis of irradiation hardening models using dislocation dynamics," *Metallurgical and Materials Transactions A*, vol. 46A, no. 8, pp. 3761–3772, 2015.

[198] Sobie, C., McDowell, D. L., Martinez, E., and Capolungo, L., "Scale transition using dislocation dynamics and the nudged elastic band method," *Submitted to Journal of the Mechanics and Physics of Solids*, 2016.

[199] Sobie, C., McPhie, M. G., Capolungo, L., and Cherkaoui, M., "The effect of interfaces on the mechanical behaviour of multilayered metallic laminates," *Modelling and simulation in materials science and engineering*, vol. 22, no. 4, p. 045007, 2014.

[200] Souidi, A., Hou, M., Becquart, C. S., and Domain, C., "Atomic displacement cascade distributions in iron," *Journal of nuclear materials*, vol. 295, no. 2, pp. 179–188, 2001.

[201] Spearot, D. and Dang, K. Private Communication, 2015.

[202] Spitzig, W. and Keh, A., "The effect of orientation and temperature on the plastic flow properties of iron single crystals," *Acta Metallurgica*, vol. 18, no. 6, pp. 611–622, 1970.

[203] Stein, D., Low, J., and Seybolt, A., "The mechanical properties of iron single crystals containing less than 5× 10- 3 ppm carbon," *Acta metallurgica*, vol. 11, no. 11, pp. 1253–1262, 1963.

[204] Stoller, R. E., Golubov, S. I., Domain, C., and Becquart, C., "Mean field rate theory and object kinetic monte carlo: a comparison of kinetic models," *Journal of Nuclear Materials*, vol. 382, no. 2, pp. 77–90, 2008.

[205] Stroh, A., "Dislocations and cracks in anisotropic elasticity," *Philosophical magazine*, vol. 3, no. 30, pp. 625–646, 1958.

[206] Stroh, A., "Steady state problems in anisotropic elasticity," *J. math. Phys*, vol. 41, no. 2, pp. 77–103, 1962.

[207] Swinburne, T., Dudarev, S., Fitzgerald, S., Gilbert, M., and Sutton, A., "Theory and simulation of the diffusion of kinks on dislocations in bcc metals," *Physical Review B*, vol. 87, no. 6, p. 064108, 2013.

[208] Szajewski, B. and Curtin, W., "Analysis of spurious image forces in atomistic simulations of dislocations," *Modelling and Simulation in Materials Science and Engineering*, vol. 23, no. 2, p. 025008, 2015.

[209] Takahashi, A., Chen, Z., Ghoniem, N., and Kioussis, N., "Atomistic-continuum modeling of dislocation interaction with y 2 o 3 particles in iron," *Journal of Nuclear Materials*, vol. 417, no. 1, pp. 1098–1101, 2011.

[210] Taylor, G. I., "The mechanism of plastic deformation of crystals. part i. theoretical," *Proceedings of the Royal Society of London. Series A, Containing Papers of a Mathematical and Physical Character*, pp. 362–387, 1934.

[211] Tench, D. and White, J., "Tensile properties of nanostructured Ni-Cu multilayered materials prepared by electrodeposition," *J. Electrochem. Soc.*, vol. 138, no. 12, pp. 3757–3758, 1991.

[212] Terentyev, D., Bacon, D., and Osetsky, Y., "Reactions between a 1/2111 screw dislocation and 100 interstitial dislocation loops in alpha-iron modelled at atomic scale," *Philosophical Magazine*, vol. 90, no. 7-8, pp. 1019–1033, 2010.

[213] Terentyev, D., Monnet, G., and Grigorev, P., "Transfer of molecular dynamics data to dislocation dynamics to assess dislocation-dislocation loop interaction in iron," *Scripta Materialia*, vol. 69, no. 8, pp. 578–581, 2013.

[214] Terentyev, D., Bonny, G., and Malerba, L., "Strengthening due to coherent cr precipitates in fe–cr alloys: Atomistic simulations and theoretical models," *Acta Materialia*, vol. 56, no. 13, pp. 3229–3235, 2008.

[215] Terentyev, D., Bacon, D., and Osetsky, Y. N., "Interaction of an edge dislocation with voids in α-iron modelled with different interatomic potentials," *Journal of Physics: Condensed Matter*, vol. 20, no. 44, p. 445007, 2008.

[216] Terentyev, D., Bonny, G., and Malerba, L., "Interplay of strengthening mechanisms in the interaction of a 1/2¡ 111¿ screw dislocation with cr precipitates in bcc fe: An atomistic study," *Nuclear Instruments and Methods in Physics Research Section B: Beam Interactions with Materials and Atoms*, vol. 267, no. 18, pp. 3155–3158, 2009.

[217] Terentyev, D., Grammatikopoulos, P., Bacon, D., and Osetsky, Y. N., "Simulation of the interaction between an edge dislocation and a¡ 100¿ interstitial dislocation loop in α-iron," *Acta Materialia*, vol. 56, no. 18, pp. 5034–5046, 2008.

[218] Terentyev, D. and Malerba, L., "Interaction of a screw dislocation with cu-precipitates, nanovoids and cu-vacancy clusters in bcc iron," *Journal of Nuclear Materials*, vol. 421, no. 1, pp. 32–38, 2012.

[219] Ting, T. and Lee, V.-G., "The three-dimensional elastostatic green's function for general anisotropic linear elastic solids," *The Quarterly Journal of Mechanics and Applied Mathematics*, vol. 50, no. 3, pp. 407–426, 1997.

[220] Topuz, A. I., "Dimension reduction of defect properties for application in 2d dislocation dynamics," *Computational Materials Science*, vol. 95, pp. 13–20, 2014.

[221] Tougou, K., Shikata, A., Kawase, U., Onitsuka, T., and Fukumoto, K.-i., "In-situ tem observation of dynamic interaction between dislocation and cavity in bcc metals in tensile deformation," *Journal of Nuclear Materials*, 2015.

[222] Uberuaga, B., Smith, R., Cleave, A., Montalenti, F., Henkelman, G., Grimes, R., Voter, A., and Sickafus, K., "Structure and mobility of defects formed from collision cascades in mgo," *Physical review letters*, vol. 92, no. 11, p. 115505, 2004.

[223] Ueda, Y., Lee, H., Ohno, N., Kajita, S., Kimura, A., Kasada, R., Nagasaka, T., Hatano, Y., Hasegawa, A., Kurishita, H., and others, "Recent progress of tungsten r&d for fusion application in japan," *Physica Scripta*, vol. 2011, no. T145, p. 014029, 2011.

[224] Ukai, S. and Fujiwara, M., "Perspective of ods alloys application in nuclear environments," *Journal of Nuclear Materials*, vol. 307, pp. 749–757, 2002.

[225] Van der Giessen, E. and Needleman, A., "Discrete dislocation plasticity: a simple planar model," *Modelling and Simulation in Materials Science and Engineering*, vol. 3, no. 5, p. 689, 1995.

[226] Van't Hoff, J., *Etudes de dynamique chimique*. Amsterdam: F. Mullet and Co., 1884.

[227] Vattré, A., Devincre, B., Feyel, F., Gatti, R., Groh, S., Jamond, O., and Roos, A., "Modelling crystal plasticity by 3d dislocation dynamics and the finite element method: the discrete-continuous model revisited," *Journal of the Mechanics and Physics of Solids*, vol. 63, pp. 491–505, 2014.

[228] Vaucorbeil, A., Sinclair, C., and Poole, W., "Dislocation glide through non-randomly distributed point obstacles," *Philosophical Magazine*, vol. 93, no. 27, pp. 3664–3679, 2013.

[229] Vegge, T., Rasmussen, T., Leffers, T., Pedersen, O., and Jacobsen, K. W., "Atomistic simulations of cross-slip of jogged screw dislocations in copper," *Philosophical magazine letters*, vol. 81, no. 3, pp. 137–144, 2001.

[230] Ventelon, L. and Willaime, F., "Core structure and peierls potential of screw dislocations in α-fe from first principles: cluster versus dipole approaches," *Journal of Computer-Aided Materials Design*, vol. 14, no. 1, pp. 85–94, 2007.

[231] Ventelon, L. and Willaime, F., "Generalized stacking-faults and screw-dislocation core-structure in bcc iron: a comparison between ab initio calculations and empirical potentials," *Philosophical Magazine*, vol. 90, no. 7-8, pp. 1063–1074, 2010.

[232] Ventelon, L., Wirth, B., and Domain, C., "Helium-self-interstitial atom interaction in α-iron," *Journal of nuclear materials*, vol. 351, no. 1, pp. 119–132, 2006.

[233] Verdier, M., Fivel, M., and Groma, I., "Mesoscopic scale simulation of dislocation dynamics in fcc metals: Principles and applications," *Modelling and Simulation in Materials Science and Engineering*, vol. 6, no. 6, p. 755, 1998.

[234] Vineyard, G. H., "Frequency factors and isotope effects in solid state rate processes," *Journal of Physics and Chemistry of Solids*, vol. 3, no. 1, pp. 121–127, 1957.

[235] Volterra, V., "Sur l'équilibre des corps élastiques multiplement connexes," in *Annales scientifiques de l'Ecole Normale superieure*, vol. 24, pp. 401–517, Société mathématique de France, 1907.

[236] Wang, H., Clausen, B., Capolungo, L., Beyerlein, I., Wang, J., and Tomé, C., "Stress and strain relaxation in magnesium az31 rolled plate: In-situ neutron measurement and elastic viscoplastic polycrystal modeling," *International Journal of Plasticity*, 2015.

[237] Wang, H. and Xiang, Y., "An adaptive level set method based on two-level uniform meshes and its application to dislocation dynamics," *International journal for numerical methods in engineering*, vol. 94, no. 6, pp. 573–597, 2013.

[238] Wang, H. and LeSar, R., "O (n) algorithm for dislocation dynamics," *Philosophical Magazine A*, vol. 71, no. 1, pp. 149–164, 1995.

[239] Wang, J., Hoagland, R., and Misra, A., "Mechanics of nanoscale metallic multilayers: From atomic-scale to micro-scale," *Scr. Mater.*, vol. 60, no. 12, pp. 1067–1072, 2009.

[240] Wang, Y., Misra, A., and Hoagland, R., "Fatigue properties of nanoscale Cu/Nb multilayers," *Scr. Mater.*, vol. 54, no. 9, pp. 1593–1598, 2006.

[241] Wang, Y. U., Jin, Y., Cuitino, A., and Khachaturyan, A., "Nanoscale phase field microelasticity theory of dislocations: model and 3d simulations," *Acta Materialia*, vol. 49, no. 10, pp. 1847–1857, 2001.

[242] Wang, Z. and Beyerlein, I., "An atomistically-informed dislocation dynamics model for the plastic anisotropy and tension–compression asymmetry of bcc metals," *International Journal of Plasticity*, vol. 27, no. 10, pp. 1471–1484, 2011.

[243] Weinan, E., Ren, W., and Vanden-Eijnden, E., "String method for the study of rare events," *Physical Review B*, vol. 66, no. 5, p. 052301, 2002.

[244] Wen, M. and Ngan, A., "Atomistic simulation of kink-pairs of screw dislocations in body-centred cubic iron," *Acta materialia*, vol. 48, no. 17, pp. 4255–4265, 2000.

[245] Weygand, D., Friedman, L., Van der Giessen, E., and Needleman, A., "Discrete dislocation modeling in three-dimensional confined volumes," *Materials Science and Engineering: A*, vol. 309, pp. 420–424, 2001.

[246] Wirth, B., Odette, G., Maroudas, D., and Lucas, G., "Dislocation loop structure, energy and mobility of self-interstitial atom clusters in bcc iron," *Journal of nuclear materials*, vol. 276, no. 1, pp. 33–40, 2000.

[247] Xiang, Y., Cheng, L.-T., Srolovitz, D. J., and Weinan, E., "A level set method for dislocation dynamics," *Acta Materialia*, vol. 51, no. 18, pp. 5499–5518, 2003.

[248] Xiao, X., Song, D., Xue, J., Chu, H., and Duan, H., "A size-dependent tensorial plasticity model for fcc single crystal with irradiation," *International Journal of Plasticity*, vol. 65, pp. 152–167, 2015.

[249] Xiong, L., Xu, S., McDowell, D. L., and Chen, Y., "Concurrent atomistic–continuum simulations of dislocation-void interactions in fcc crystals," *International Journal of Plasticity*, vol. 65, pp. 33–42, 2015.

[250] Xu, D. and Wirth, B. D., "Modeling spatially dependent kinetics of helium desorption in bcc iron following he ion implantation," *Journal of Nuclear Materials*, vol. 403, no. 1, pp. 184–190, 2010.

[251] Xu, H., Stoller, R. E., Osetsky, Y. N., Terentyev, D., and others, "Solving the puzzle of¡ 100¿ interstitial loop formation in bcc iron," *Physical review letters*, vol. 110, no. 26, p. 265503, 2013.

[252] Xu, Z. and Picu, R., "Thermally activated motion of dislocations in fields of obstacles: The effect of obstacle distribution," *Physical Review B*, vol. 76, no. 9, p. 094112, 2007.

[253] Yao, Z., Jenkins, M., Hernández-Mayoral, M., and Kirk, M., "The temperature dependence of heavy-ion damage in iron: A microstructural transition at elevated temperatures," *Philosophical Magazine*, vol. 90, no. 35-36, pp. 4623–4634, 2010.

[254] Yuan, F., Yang, S., and Yang, B., "Three-dimensional greens functions for composite laminates," *International journal of solids and structures*, vol. 40, no. 2, pp. 331–342, 2003.

[255] Zbib, H., Overman, C., Akasheh, F., and Bahr, D., "Analysis of plastic deformation in nanoscale metallic multilayers with coherent and incoherent interfaces," *Int. J. Plast.*, vol. 27, no. 10, SI, pp. 1618–1639, 2011.

[256] Zhang, R., Wang, J., Beyerlein, I., Misra, A., and Germann, T. C., "Atomic-scale study of nucleation of dislocations from fcc-bcc interfaces," *Acta Mater.*, vol. 60, no. 6-7, pp. 2855–2865, 2012.

[257] Zhu, T., Li, J., and Yip, S., "Atomistic study of dislocation loop emission from a crack tip," *Physical review letters*, vol. 93, no. 2, p. 025503, 2004.

[258] Zinkle, S. J. and Busby, J. T., "Structural materials for fission & fusion energy," *Materials Today*, vol. 12, no. 11, pp. 12–19, 2009.

[259] Zinkle, S. J. and Singh, B. N., "Microstructure of neutron-irradiated iron before and after tensile deformation," *Journal of nuclear materials*, vol. 351, no. 1, pp. 269–284, 2006.